UNIVERSITY OF CALIFORNIA,
IRVINE

The Changing Impacts of El Niño and Arctic Warming on Mid-latitude Climate Variability

DISSERTATION

submitted in partial satisfaction of the requirements
for the degree of

DOCTOR OF PHILOSOPHY

in Earth System Science

by

Yu-Chiao Liang

Dissertation Committee:
Professor Jin-Yi Yu, Chair
Professor Gudrun Magnusdottir
Professor Eric E. Saltzman

2018

To my parents, brother, and friends

TABLE OF CONTENTS

LIST OF FIGURES

LIST OF TABLES

ACKNOWLEDGMENTS

I would like to express my deepest appreciation to my advisor Professor Jin-Yi Yu for his mentoring and supports in all these years. Jin-Yi has a distinctive scientific view that continually encourages me to achieve research breakthrough. Without his guidance and persistent help this dissertation would not have been possible. Jin-Yi also gave me freedom to explore new research topics as well as encouraged me to cooperate with geoscientists from other institution, which I benefited greatly.

I thank my dissertation committee members Professor Eric Saltzman and Professor Gudrun Magnusdottir for their informative, constructive suggestions and comments to improve my thesis works. I also thank Professor Amir AghaKouchak and Professor Michael Pritchard being my PhD advancement committee members, and Professor Min-Hui Lo of National Taiwan University for his generous supports.

I acknowledge all of the professors with whom I took courses at University of California, Irvine: Professors Claudia Czimczik, Ellen Druffel, Gudrun Magnusdottir, Adam Martiny, Keith Moore, Michael Prather, François Primeau, Michael Pritchard, Eric Saltzman, Susan Trumbore, Jin-Yi Yu, and Charles Zender. I also thank professors and lecturer with whom I participated in teaching assistant: Professors Mathieu Morlighem, François Primeau, Michael Pritchard, and Jin-Yi Yu, and Lecturer Elizabeth Crook. I am grateful to Jaycee Chu, Morgan Sibley and other administrative staff of the department who are always willing to help.

Thanks to all the members in Jin-Yi's group that I have worked together: Mengyan Chen, Shih-Wei Fang, Shan He, Kewei Lyu, Houk Paek, Pengfei Tuo, Li Xu, and Yuhao Zhou. Thanks to my classmates Paul Levine, Guo Liu, Michael McCormick, Melinda Nicewonger, Scot Parker, Elizabeth Wiggins, Sungduk Yu, and Meng Zou.

Special thanks to Doctor Matthew Mazloff and Doctor Isabella Rosso of Scripps Institution of Oceanography, University of California, San Diego, with whom I cooperated for a project on Southern Ocean nitrate maps.

Many others have contributed to this dissertation in varying ways: Hrishi Chandanpurkar, Chu-Chun Chen, Professor Wei-Ting Chen, Mu-Hua Chien, Chin-Chieh Chou, John Emery, Chia-Wei Hsu, Zack Labe, Hossein Parishani, Adam Purdy, Hongchen Qin, Jessica Tsai, Professor Yu-Heng Tseng, Chunzai Wang, Fan Wang, Jenny Wang, Wenshan Wang, Ho-Hsuan Wei, Professor Chien-Ming Wu, Ren-Jie Wu, and Wen-Ying Wu.

I wish to thank my parents and brother for their continued supports throughout my life. Finally, I thank many friends at Irvine and Taiwan, who always show their generosities to support my work.

I want to thank the financial support provided by the University of California, Irvine (UCI), Nation Science Foundation's (NSF's) Climate and Large-scale Dynamics Program under Grants Atmospheric and Geospace Sciences-1233542 and 1505145 and by the NSF's Independent Research/Development program, and Ministry of Education of Taiwan. I also thank American Meteorological Society, American Geophysical Union, Royal Meteorological Society, and IOP Publishing, provided me permission to use previously publications as part of my dissertation. I also thank supercomputers Yellowstone and Cheyenne of NCAR, and Greenplanet of UCI offering computational resources providing me platform to conduct analyses and climate model simulations.

CURRICULUM VITAE

Yu-Chiao Liang

Education

2013-2018 Ph.D., Earth System Science, University of California, Irvine

2013 M.S., Earth System Science, University of California, Irvine

2005-2010 B.S., Atmospheric Sciences, National Taiwan University, Taiwan

Award

2014-2015 Government Scholarship for Study Abroad, Ministry of Education, Taiwan

Publications

- Liang, Y.-C., M. R. Mazloff, I. Rosso, S.-W. Fang, and J.-Y. Yu, 2018: A multi-variate Empirical Orthogonal Function method to construct nitrate maps in the Southern Ocean, *Journal of Atmospheric and Oceanic Technology* (under review).
- Liang, Y.-C. and J.-Y. Yu, 2018: Arctic warming intensifies the climate connectivity between the North Pacific and North Atlantic, *Geophysical Research Letters* (in preparation).
- Liang, Y.-C., J.-Y. Yu, E. S. Saltzman, and F. Wang, 2017: Linking the Tropical Northern Hemisphere pattern to the generation of the Pacific warm blob and Atlantic cold blob, *Journal of Climate,* 30, 9041-9057, doi:10.1175/JCLI-D-17-0149.1.
- Liang, Y.-C., C.-C. Chou, J.-Y. Yu, and M.-H. Lo, 2016: Mapping the Locations of Asymmetric and Symmetric Discharge Responses in Global Rivers to the Two Types of El Niño*, Environmental Research Letters*, 11, doi:10.1088/1748-9326/11/4/044012.
- Liang, Y.-C., J.-Y. Yu, M.-H. Lo, and C. Wang, 2015: The changing influence of El Niño on the Great Plains Low-Level Jet, *Atmospheric Science Letters*, 16, 512-517, doi:10.1002/asl.590.
- Liang, Y.-C., M.-H. Lo, and J.-Y. Yu, 2014: Asymmetric responses of land hydroclimatology to two types of El Niño in the Mississippi River Basin, *Geophysical Research Letters*, 41, 582-588, doi:10.1002/2013GL058828.

Presentations

Oral:

- Liang, Y.-C., M. R. Mazloff, I. Rosso, S.-W. Fang, and J.-Y. Yu (2018), A multi-variate EOF approach to construct nitrate maps in the Southern Ocean, *2018 Ocean Science Meeting*, Portland, OR, USA.

- Liang, Y.-C. and J.-Y. Yu, Arctic warming intensifies North Pacific-Atlantic ocean connectivity (2018), *Department of Atmospheric Sciences, National Taiwan University*, Taipei, Taiwan.

- Liang, Y.-C. and J.-Y. Yu (2017), Can Arctic warming intensify North Pacific-Atlantic oceanconnectivity? *2017 AGU Fall Meeting*, New Orleans, CA, USA.

- Liang, Y.-C. and J.-Y. Yu (2017), An atmospheric conducting mechanisms behind the synchronization of the Pacific and Atlantic blobs, *Department of Atmospheric Sciences, National Taiwan University*, Taipei, Taiwan.

- Liang, Y.-C., J.-Y. Yu, E. S. Saltzman, and F. Wang (2017), Synchronization of the Pacific and Atlantic Blobs via an Atmospheric Conductor Pattern, *Research Center for Environmental Changes, Academia Sinica*, Taipei, Taiwan.

- Liang, Y.-C., J.-Y. Yu, E. S. Saltzman, and F. Wang (2016), Synchronization of the Pacific and Atlantic Blobs via an Atmospheric Conductor Pattern, *2016 AGU Fall Meeting*, San Francisco, CA, USA.

- Liang, Y.-C., J.-Y. Yu, and M.-H. Lo (2016), The influences of changing El Niño on US hydroclimate, *Research Center for Environmental Changes, Academia Sinica*, Taipei, Taiwan.

- Liang, Y.-C., J.-Y. Yu, and M.-H. Lo (2015), The influences of changing El Niño on US hydroclimate, *Department of Atmospheric Sciences, National Taiwan University*, Taipei, Taiwan, Taipei, Taiwan.

Poster:

- Liang, Y.-C., C.-C. Chou, J.-Y. Yu, and M.-H. Lo (2015), Mapping the locations of asymmetric and symmetric discharge responses in global rivers to the two types of El Niño, *2015 AGU Fall Meeting*, San Francisco, CA, USA.

- Liang, Y.-C., J.-Y. Yu, and M.-H. Lo (2014), Distinct impacts of the two types of El Niño on the strength of Great Plains low-level jet, *2014 AGU Fall Meeting*, San Francisco, CA, USA.

- Liang, Y.-C., M.-H. Lo, and J.-Y. Yu (2013), Asymmetric responses of land water storage to two types of ENSO over the Mississippi river basin, *2013 AGU Fall Meeting*, San Francisco, CA, USA.

Teaching Experience

Teaching Assistant:

- Catastrophe (2016), *University of California, Irvine,* Lecturer Elizabeth Crook
- The Atmosphere (2016), *University of California, Irvine,* Lecturer Elizabeth Crook
- Data Analysis (2015), *University of California, Irvine,* Professor Mathieu Morlighem
- Earth's Atmosphere (2015), *University of California, Irvine,* Professor Jin-Yi Yu
- Climate Change (2015), *University of California, Irvine,* Professor Michael Pritchard
- Modeling the Earth (2014), *University of California, Irvine,* Professor François Primeau

ABSTRACT OF THE DISSERTATION

The Changing Impacts of El Niño and Arctic Warming on Mid-latitude Climate Variability

By

Yu-Chiao Liang

Doctor of Philosophy in Earth System Science

University of California, Irvine, 2018

Professor Jin-Yi Yu, Chair

Remote forcing associated with El Niño and Arctic warming are two mechanisms capable of producing variability in the mid-latitude climate of the Northern Hemisphere. Such variability can give rise to abnormal and extreme events in mid-latitudes that can greatly influence agriculture and socioeconomics in highly populated regions. However, the impacts may have changed over the past few decades as global warming or natural decadal variability altered El Niño and amplified Arctic warming. This dissertation uses statistical analyses and numerical model experiments to examine the changing impacts of El Niño and Arctic warming on mid-latitude climate variability.

The center of the warm sea surface temperatures (SSTs) associated with El Niño has shifted from the tropical Eastern Pacific (EP) to tropical Central Pacific (CP) during the most recent two to three decades. This dissertation finds this shift has resulted in changes in the impacts of El Niño events on North American hydroclimate. CP and EP El Niño events exert influences on the Mississippi River discharge and the Great Plains Low-Level-Jet (GPLLJ)

during boreal spring that are opposite in sign. Subsurface hydrological processes result in impacts on springtime Mississippi River discharge of the El Niño associated winter precipitation anomalies. The sea level pressure in the Gulf of Mexico and surface air temperature in the North America respond differently to the changing El Niño forcing, resulting in opposite impacts on the GPLLJ. The changing impacts of El Niño on the discharge from the world's top thirty river basins and their underlying mechanisms are also examined. These findings offer information that can help to develop new water management strategies to cope with the changing El Niño impacts.

Arctic warming began to accelerate in the early 1990s, resulting in an increase in the importance of Arctic forcing on the mid-latitude climate variability. This dissertation also demonstrates how changing Arctic conditions affect the inter-basin connection between extreme marine events in the North Pacific and North Atlantic. The marine heatwave event in the North Pacific during 2014-2015 (referred to as the Pacific warm blob) is found to be synchronized with a marine cold spell event in the North Atlantic (referred to as the Atlantic cold blob) via an atmospheric circulation pattern. This pattern is identified as the Tropical Northern Hemisphere (TNH) pattern and is characterized by a cross-basin structure that enables it to simultaneously induce the warm and cold blob signatures in the North Pacific and North Atlantic respectively. Such co-occurring blob events have a tendency to occur more frequently since the early-1990s, coinciding with the time when the Arctic warming began to accelerate. This dissertation further finds that the amplified Arctic warming enhances the cross-basin structure of the TNH pattern to increase the inter-basin connectivity between the two oceans. The relative importance of El Niño and Arctic warming to the Pacific-Atlantic climate connectivity is also discussed.

The findings of this dissertation contribute to a better understanding of how the forcing of mid-latitude climate variability has changed in recent decades and of the relative importance

of the tropical Pacific (i.e., El Niño) and Arctic (i.e., the amplified Arctic warming) forcings. The understanding gained has the potential to improve projections of climate variability in mid-latitudes, and in the development of new methodologies that use the tropical and Arctic conditions to predict mid-latitude extreme events.

CHAPTER1

Introduction

1.1 Mid-latitude Climate Variability

The Intergovernmental Panel on Climate Change (IPCC) Fifth Assessment report defines climate variability as the variations in the mean climate state on various spatial and temporal scales, but beyond the scope of individual weather events (IPCC, 2013). Previous studies have demonstrated the profound impacts produced by mid-latitude climate variability on ecosystems, agriculture, and socioeconomics across vast areas of the North American and Eurasian continents (e.g., IPCC, 2013; Shannon and Motha, 2015; Kim *et al.*, 2017). Variability in the Great Plains Low-Level-Jet (GPLLJ), for example, has been suggested to be partly responsible for the occurrence of the Dust Bowl over the central United States (U.S.) during the 1930s, which caused a severe economic depression and a massive westward population migration (Cook *et al.*, 2008; Hu *et al.*, 2018). More recently, the multi-year California drought during 2012-2015 and the severe flooding that followed during 2015-2016 were also attributed to mid-latitude climate variability (Swain, 2015). Therefore, it is necessary to better understand the causes of mid-latitude climate variability in order to improve our ability to better prepare for the occurrence of extreme events and associated hazards.

The leading modes of the mid-latitude climate variability have been extensively studied (e.g., Wallace and Gultzler, 1981) and their possible generation mechanisms are mostly well understood (Hoskins, 1983). Examples of major variability modes include the Arctic oscillation

(AO, Figure 1.1(a), Thompson and Wallace, 1998), the North Atlantic Oscillation (NAO, Figure 1.1(b), Barnston and Livezey, 1987), and the North Pacific Oscillation (NPO, not shown here, Rogers, 1981) that dominate the latitudinal vacillations of the polar and subtropical jet streams (Yu and Hartmann, 1993); as well as the Pacific North American (PNA, Figure 1.1(c), Wallace and Gultzler, 1981) and Tropical Northern Hemisphere (TNH, Figure 1.1(d), Barnston and Livezey, 1985) patterns that dominate the zonally asymmetric variability and have a structures that extend from tropics into mid-latitudes. The internal dynamics of the mid-latitude atmosphere has been suggested to be a major source of these variability modes. For example, the AO was suggested to arise from the interactions between mid-latitude jet streams and baroclinic waves (e.g., Yu and Hartmann, 1993), while the PNA pattern is the result of barotropic instability of the boreal winter mean state (see Chapter 16 in Vallis, 2017). Tropical forcing related to El Niño-Southern Oscillation (ENSO) has also been suggested to be an important forcing of these mid-latitude modes of variability. The PNA pattern, for example, can be excited as a Rossby wave response to ENSO forcing (Wallace and Gultzler, 1981; Trenberth *et al.*, 1998). The accelerated Arctic warming that has occurred in recent decades has revealed that Arctic forcing can also significantly impact mid-latitude climate variability, such as the AO, NAO, and NPO patterns that are associated with variations in the polar and subtropical jet streams (see the review article by Cohen *et al.*, 2014).

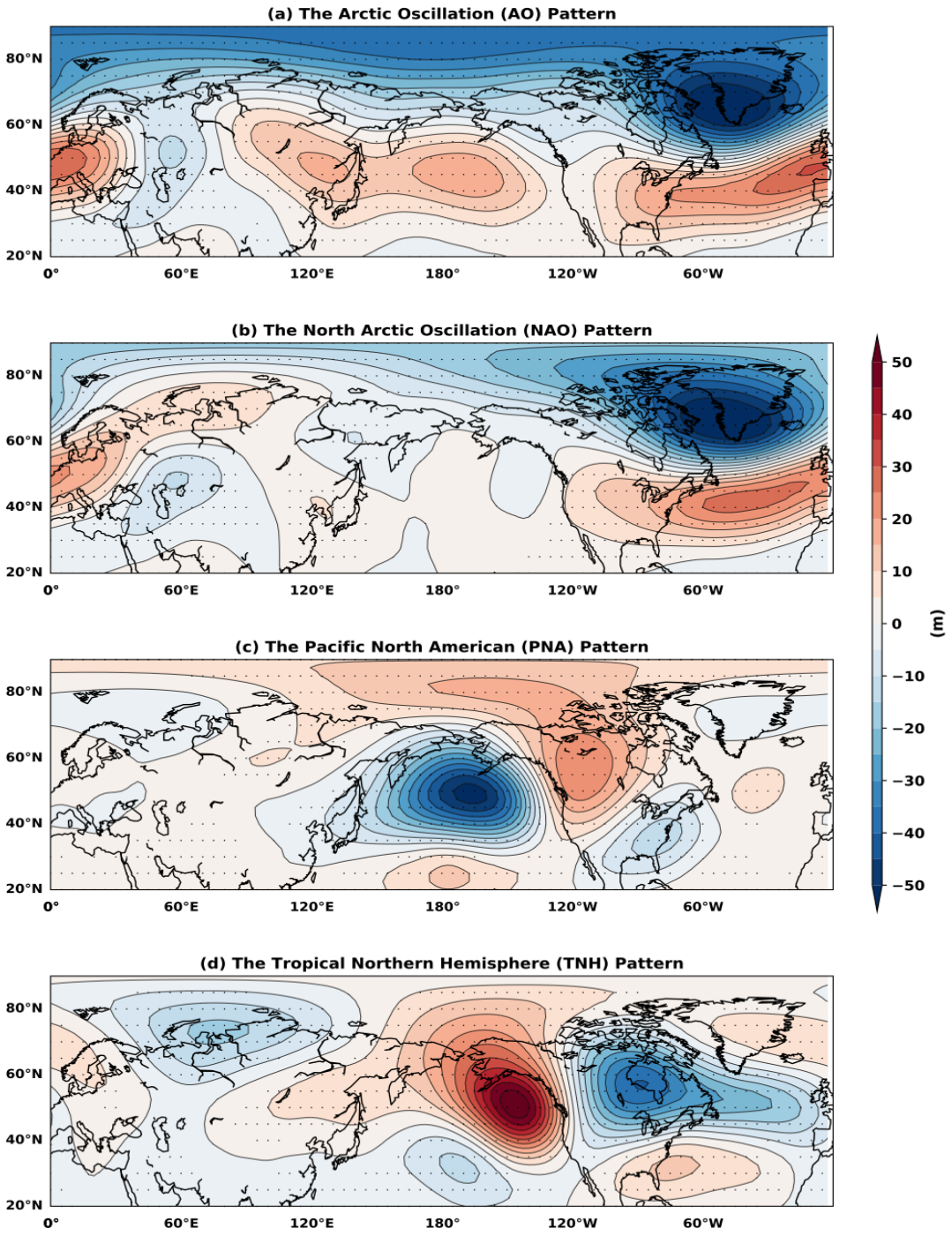

Figure 1.1 The 500-hPa geopotential height anomaly fields regressed onto (a) the Arctic Oscillation index, (b) North Atlantic Oscillation index, (c) Pacific-North American index, and (d) Tropical Northern Hemisphere index. The indices are downloaded from NOAA Climate Prediction Center website (see Section 4.3.3 for details).

1.2 Linking El Niño to Mid-latitude Climate Variability

El Niño is the most prominent tropical forcing exerting significant impacts on mid-latitude climate via altering large-scale atmospheric circulation patterns (Horel and Wallace, 1981; Hoerling *et al.*, 1997). This phenomenon is characterized by a warming of the sea surface in the tropical eastern-to-central Pacific that tends to occur quasi-periodically every two to seven years. When the El Niño occurs, it can disrupt typical atmospheric circulation patterns to impact global climate (e.g., Ropelewski and Halpert, 1986). Figure 1.2 shows the most well-known circulation pattern that enables the El Niño-induced warming in the tropical Pacific to affect North American climate. The higher-than-normal sea surface temperatures (SSTs; see red patch in Figure 1.2) of an El Niño event result in anomalous deep convection in the tropical Pacific that excites Rossby waves propagating poleward and eastward (pink and light blue patches in Figure 1.2) into North America. These waves can displace the location of the jet streams (red arrow line in Figure 1.2), changing the moisture transport and downstream precipitation patterns. The Rossby wave-induced geopotential height field anomalies (pink and light blue patches in Figure 1.2) can also modify local temperature fields (Ropelewski and Halpert, 1986). The large-scale atmospheric circulation patterns induced by El Niño can be the PNA (Figure 1.1(c)) or TNH patterns (Figure 1.1(d)) (Yu *et al.*, 2012a, calculation details can be found in Chapter 4.3.4). This is the conventional teleconnection framework used in many previous studies to understand how El Niño influences on mid-latitude climate (Yu *et al.*, 2012a; Yu and Zou, 2013; Liang *et al.*, 2014; Zou *et al.*, 2014; Liang *et al.*, 2015).

However, it has been increasingly recognized that El Niño properties have changed in recent decades (Ashok *et al.*, 2007; Yu and Kao, 2007; Kao and Yu, 2009; Kug *et al.*, 2009; and

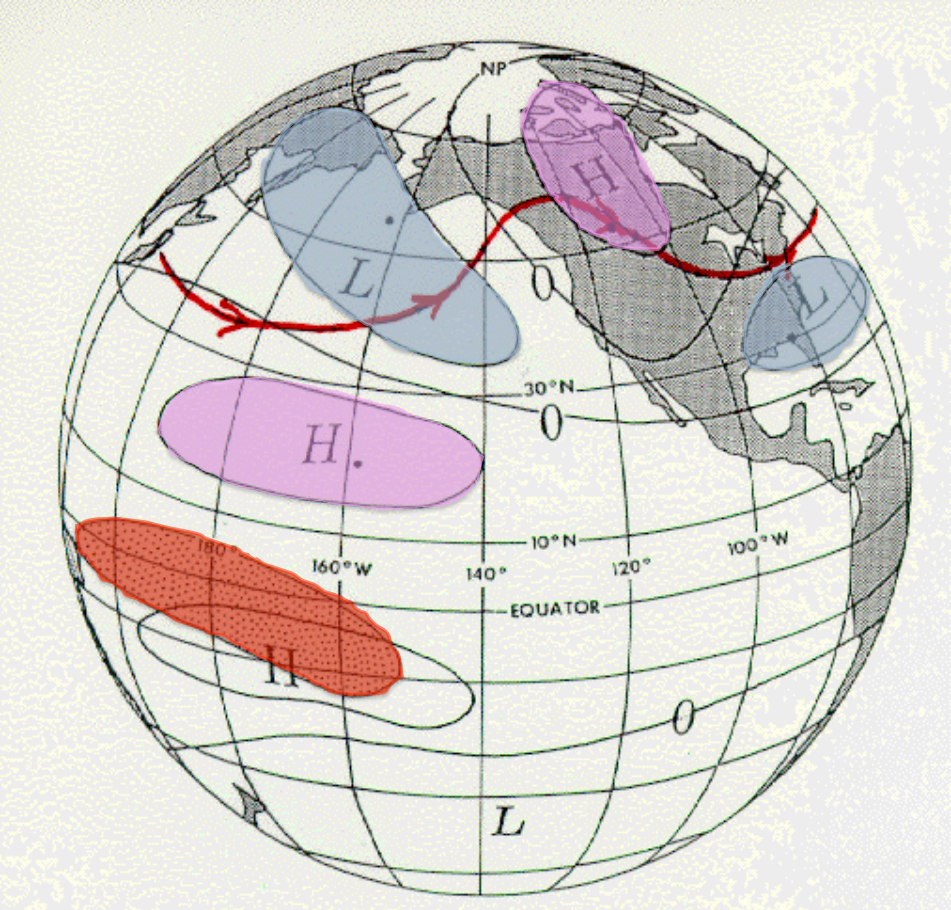

Figure 1.2 Schematic illustration of the hypothesized geopotential height anomaly pattern during boreal winter in response to warm sea surface temperature (SST) anomalies in equatorial Pacific modified from Figure 11 in Horel and Wallace (1981). The red patch indicates warm SST anomalies, while the pink and light blue patches the above- and below-normal geopotential height anomalies respectively. The red arrow line represents the mid-tropospheric streamline perturbed by the anomaly pattern with "trough" in the North Pacific and "ridge" over western Canada.

a U.S. CLIVAR Working group report by Capotondi *et al.*, 2015). The change of El Niño may be attributed to anthropogenic warming, decadal natural variability, or some combination of the two (Capotondi *et al.*, 2015). Since the early-1990s, the location of warmest waters associated with El Niño has moved from the tropical Eastern Pacific (EP) to the tropical Central Pacific (CP) (Yu *et al.*, 2012b; Yu and Kim, 2013). These two variants of El Niño are now referred to as the EP El

Niño and CP El Niño (Yu and Kao, 2007; Kao and Yu, 2009). The different locations of strongest SST anomalies result in different Rossby wave trains into the mid-latitudes to produce different climate impacts (Mo, 2010; Yu *et al.*, 2012a; Yu and Zou, 2013). Therefore, the El Niño impacts on mid-latitude climate variability should have also changed in recent decades as a result of the changing El Niño properties. While many studies have targeted El Niño impacts on winter and summer mid-latitude climate variability, this dissertation focuses particularly on the impacts on mid-latitude hydroclimate during boreal spring. These impacts include those on Mississippi River discharge and the Great Plains Low-Level-Jet. *A goal of this dissertation is to revise the conventional teleconnection framework that was developed primarily for the conventional EP El Niño in order to gain a better understanding of the changing impacts of El Niño on mid-latitude climate variability with a focus on boreal spring.*

1.3 Emerging Influences of Arctic Warming on Mid-latitude Climate Variability

The annual minimum in Arctic sea ice coverage has declined at an alarming rate of about eight thousand km^2/decade since 1990 (NASA Scientific Visualization Studio, https://svs.gsfc.nasa.gov/4435). Associated with this extensive sea ice loss, polar wintertime near-surface air temperatures have increased at a rate (about 0.167^oC/decade, see Figure 1.3) more than double of the rate of warming in lower latitudes (which is about 0.06 ^oC/decade, see Figure 1.3). This phenomenon is known as Arctic Amplification (AA, Manabe and Wetherald, 1975; Alexeev *et al.*, 2005; Serreze *et al.*, 2009). AA has been suggested to link to the polar vortex to breakdown as a result of polar cap height increases (Cohen *et al.*, 2014; Kim *et al.*, 2014; Cohen *et al.*, 2018), or a prominent weakening of the north-south temperature gradient that

could lead to an equatorward displacement of the polar jet stream and mid-latitude storm tracks (Francis and Vavrus, 2012; Cohen *et al.*, 2014; Screen, 2014; Francis and Vavrus, 2015). These Arctic changes have also been linked to the more frequent severe winters in the eastern U.S. and northern Eurasia (Cohen *et al.*, 2014; Mori *et al.*, 2014; Kug *et al.*, 2015; Overland *et al.*, 2015; Cohen *et al.*, 2018). As a consequence of the changes in the mean flow (i.e., the jet streams or

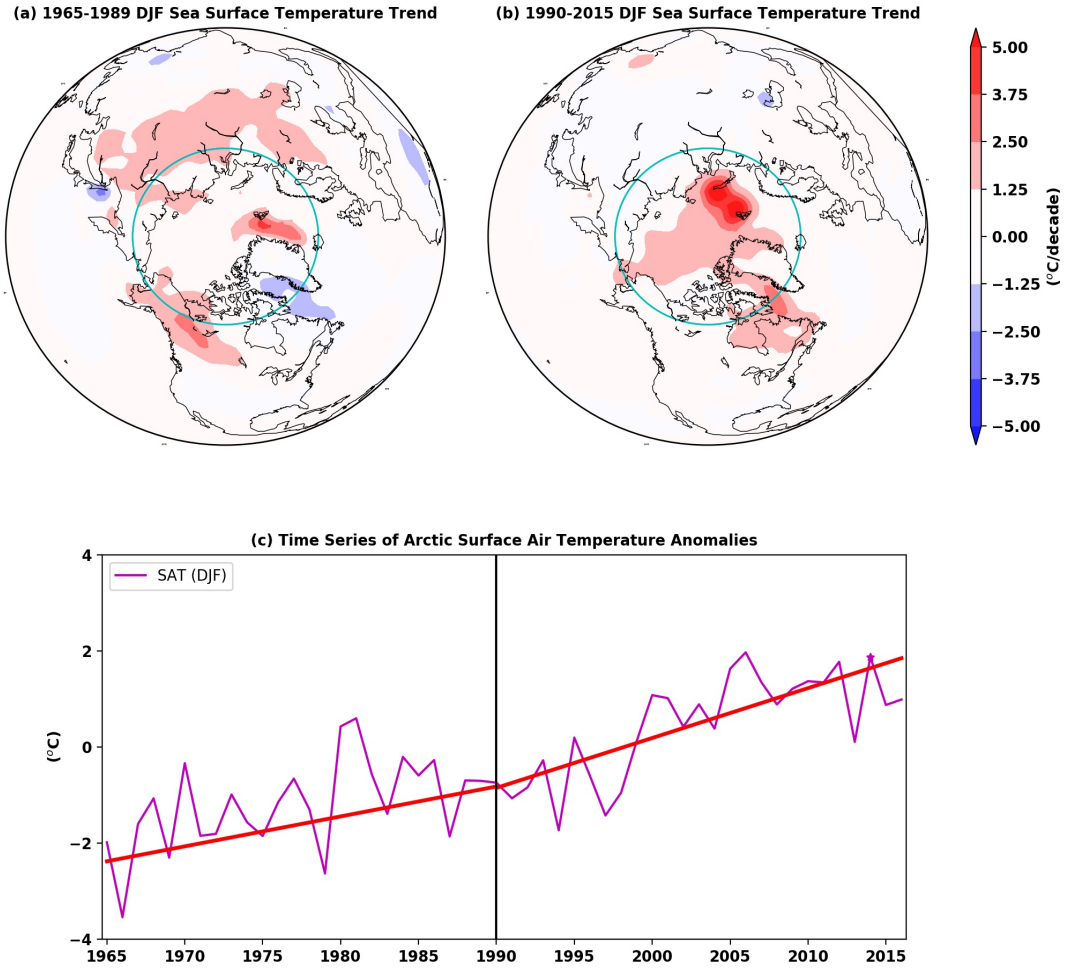

Figure 1.3 (a) Surface air temperature trend map during 1965-1989. (b) is similar to (a) but during 1990-2015. The cyan circles in (a) and (b) indicate the 65^{o}N parallel. (c) The time series of Arctic surface air temperature averaged north of 65^{o}N (magenta line) with the trends (red lines) before and after 1990. The data used is obtained from NCAR/NCEP reanalysis datasets.

polar vortex) and transient eddy activities (i.e., the winter storms), certain variability modes of atmospheric circulation in mid-latitude may become more dominant or their structures may change. For example, variations in snow cover over Eurasia have been suggested to modulate the amplitude and phase of the Arctic Oscillation/North Atlantic Oscillation (see Figures 1.1(a) and (b); Cohen *et al.*, 2012; Peings *et al.*, 2013; Nakamura, *et al.*, 2015). In this regard, the large-scale atmospheric circulation patterns provide the mechanism to transmit the influences of the changing Arctic conditions to mid-latitude climate variability.

While most previous studies have focused on the Arctic warming influences on mid-latitude extreme events over North America and Europe (e.g., California drought conditions, winter storms in Northeast U.S., and heavy precipitation in United Kingdom, Screen and Simmonds, 2014; Kug *et al.*, 2015; Swain *et al.*, 2016; Francis *et al.*, 2017; Kim *et al.*, 2017; Cohen *et al.*, 2018), little attention has been paid to the accelerated Arctic warming and how it may impact marine extreme events in mid-latitude oceans. *Another goal of this dissertation is to examine if the accelerated Arctic warming can influence mid-latitude climate variability.*

1.4 Pacific Warm Blob and Atlantic Cold Blob

Two extreme marine events in mid-latitudes that have recently been identified and attracted extensive attention are the Pacific warm blob (Bond *et al.*, 2015) and Atlantic cold blob (Henson, 2016). These terms refer to as the remarkably warm and cold water masses occasionally occurring over the northeastern (NE) Pacific and North Atlantic. Climatologist Nicholas Bond, in the monthly newsletter of the Office of the Washington State Climatologist for June 2014, was the first to use the term “blob” to describe the anomalous warm water mass that persisted during 2013-2015 in the NE Pacific (see a climate news review in Hannah, 2015).

At the peak of this blob event during the winter of 2014 and summer of 2015, the positive SST anomalies in the warming region reached as high as 2^{o}-3^{o}C and penetrated as deep as 180 m below the ocean surface (Figure 1.4, Bond *et al.,* 2015; Hu *et al.*, 2017). This Pacific warm blob event exerted pervasive impacts on the North American climate. Since then, this blob warming event in the NE Pacific has been widely discussed in the scientific community (e.g., 2014-2016 Pacific Anomalies Science and Technology Workshop 1 and 2, http://www.nanoos.org/resources/anomalies_workshop/workshop2.php).

One key reason why the blobs attracted so much attention was their prolonged durations. This 2013-2015 Pacific warm blob lasted more than two years, persisting from June of 2013 to the end of 2016. By June 2014, this patch of warm water has expanded its size to approximately 1,000 miles long and 1,000 miles wide (see Figure 1.4; Hannah, 2015), covering an ocean area about twice the size of Alaska State (570,641 $miles^2$). The warm water of the Pacific blob was nutrient depleted and exerted pervasive impacts on the marine biology and coastal ecosystems of the NE Pacific. Examples of the Pacific blob impacts include a profound species range shift in the Gulf of Alaska (Medred, 2014), dramatic changes in the marine productivity in the NE Pacific (Whitney, 2015; Siedlecki *et al.*, 2016), and a delay in the onset of the upwelling off California coasts (Peterson *et al.*, 2015; Zaba and Rudnick, 2016). The Pacific blob also altered springtime air temperatures (Bond *et al.*, 2015) and ozone concentration (Jaffe and Zhang, 2017) in the Pacific Northwest of the U.S.

Studies on the Pacific warm blob have so far mostly agreed that the warm blob during 2013-2015 was driven directly by an anomalous circulation pattern in the atmosphere – an

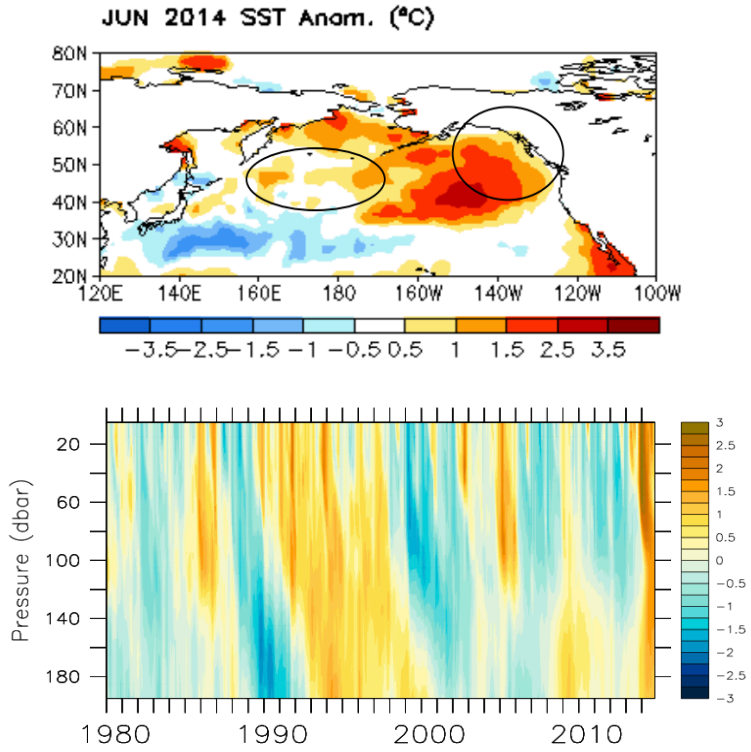

Figure 1.4 Top panel shows June 2014 SST deviations from 1981-2010 climatology values. This panel is adopted from NOAA's Ocean Briefing on July 2014, Page 22 (http://www.cpc.ncep.noaa.gov/products/GODAS/ocean_briefing_gif/global_ocean_monitoring_2014_07.pdf). Bottom panel shows the monthly temperature anomalies (normalized) from the surface to 200 m averaged over the area of 40°N-50°N, 150°W-135°W for the period of January 1980 through November 2014 adopted from Figure 1(a) in Bond *et al.* (2015).

unusually persistent ridge sitting over the NE Pacific (Seager *et al.*, 2014; Swain *et al.*, 2014; Wang *et al.*, 2014; Bond *et al.*, 2015; Hartmann, 2015; Seager *et al.*, 2015; Amaya *et al.*, 2016; Di Lorenzo and Mantua, 2016; Swain *et al.*, 2016; Hu *et al.*, 2017). This anomalous high pressure system is sometimes referred to as the "Ridiculously Resilient Ridge" (RRR, see Figure 1.5; Swain *et al.*, 2014; 2016). The RRR drives clockwise surface wind anomalies, weakening the prevailing surface westerlies, which reduced local surface evaporation and weakened cold ocean advection in the region to give rise to the Pacific blob warming. What is not yet fully

understood is the mechanism that causes this anomalous ridge, and why it persisted for such a long time. Several large-scale atmospheric circulation patterns are known to have an anomaly center close to the RRR region, including the PNA (Figure 1.1(c); Wallace and Gultzer, 1981) and TNH patterns (Figure 1.1(d); Mo and Livezey, 1986). As mentioned previously, these patterns can be excited by tropical forcing associated with El Niño and polar forcing associated with Arctic warming (Lee *et al.*, 2015). Further investigations are needed to uncover the roles and relative importance of El Niño and Arctic warming in driving this marine extreme phenomenon in the North Pacific.

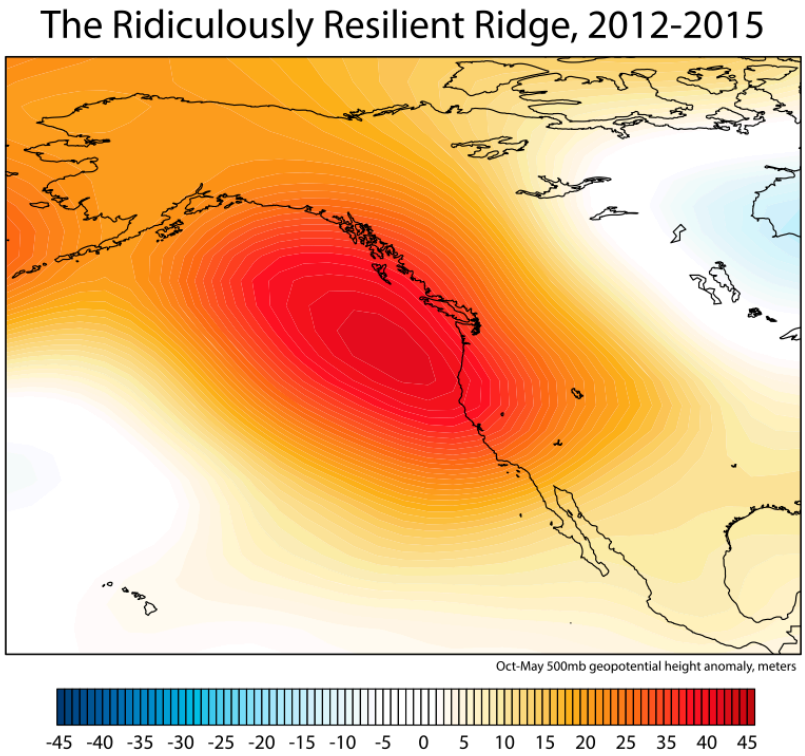

Figure 1.5 The Ridiculous Resilient Ridge as characterized by 500-hPa geopotential height anomalies over four consecutive years (October-May 2012, 2013, 2014, and 2015). The unit of the colorbar is meters. The figure is adopted from Figure 2 in Swain (2015).

As for the Atlantic cold blob, several mechanisms have been proposed to explain its generation, including the large-scale atmospheric circulation pattern associated with the North Atlantic Oscillation (Delworth *et al.*, 2016; Yeager *et al.*, 2016), the recent slowdown of the Atlantic meridional overturning circulation (Rahmstorf *et al.*, 2015; Robson *et al.*, 2016; Duchez *et al.*, 2016), and the melting of the Greenland ice sheet (Schmittner *et al.*, 2016). All these mechanisms consider the Atlantic cold blob to be a separate climate phenomenon from the Pacific warm blob. However, it is very interesting that the 2013-2015 Atlantic cold blob occurred during the same time as the 2013-2016 Pacific warm blob event (e.g., Figure 1.6). This temporal coincidence raises the possibility that the Atlantic and Pacific blob events may be related to each other through large-scale atmospheric circulation patterns. This possibility is examined in this dissertation.

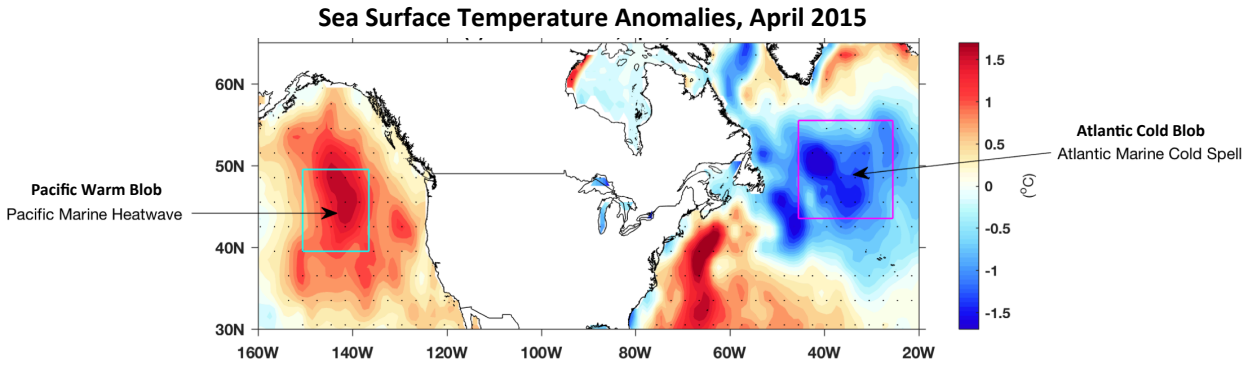

Figure 1.6 The sea surface temperature anomalies during April 2015. The light blue boxes delineate the Pacific blob region (40°-50°N, 150°-135°W) defined in Bond *et al.* (2015), whereas the pink boxes depict the Atlantic blob region (44°-56°N, 45°-25°W).

It is demonstrated in this dissertation that synchronized occurrences of Pacific warm blob and Atlantic cold blob have occurred more frequently after the ealy-1990s, which coincides with the time that the El Niño shifted from the EP to CP type and also the time that Arctic warming began to accelerate. *Third goal of this dissertation is to understand whether or not the changing impacts of the El Niño and Arctic warming may have affected the inter-basin connectively between the North Pacific and North Atlantic Oceans.*

1.5 Outline of the Dissertation

In this dissertation, statistical analyses and climate model experiments are conducted to study the changing influences of El Niño and Arctic warming on mid-latitude climate variability. The organization of this dissertation thesis is as follows:

In Chapter 2, the responses of the Great Plains Low-Level Jet to different types of El Niño events are examined. The possible mechanisms for these responses are investigated with a series of composite and statistical analyses. In contrast to previous studies mostly focused on different El Niño impacts on mid-latitude climate variability during boreal winter (Mo, 2010; Yu *et al.*, 2012a; Yu and Zou, 2013; Capotondi *et al.*, 2015), the findings in this chapter shed lights on the possibility that the changing El Niño also affects North American climate during spring via modulation of the Great Plains Low-Level Jet.

In Chapter 3, thorough analyses are conducted to examine the asymmetric responses of Mississippi River discharge to the two types of El Niño events and to explore how the changing El Niño type influences North American hydroclimate. Various hydroclimate variables, including precipitation, soil moisture, and subsurface water volume, are analyzed to understand the underlying mechanisms that enable the changing El Niño influences to evolve from boreal

winter to spring. Similar analyses are applied to the top thirty (in terms of drainage area) global river basins to construct a global mapping of river discharge responses to the changing El Niño. The findings provide information that can help global water management.

In Chapter 4, a new perspective on the generation mechanism of the Pacific warm blob is proposed using reanalysis products via a series of composite and statistical analyses. This new perspective focuses on the cross-basin (i.e., the North Pacific and North Atlantic) nature of the blob mechanism and is different from previous proposed blob generation mechanisms that focused on the physical processes within one ocean basin only. The finding provides a new way to consider and study the inter-basin climate connectivity between the North Pacific and North Atlantic.

Chapter 5 extends the findings from Chapter 4 to link the synchronized occurrences of the Pacific warm blob and Atlantic cold blob events to recent Arctic warming using both reanalysis datasets and climate model simulations. Future projections from climate models are also used to understand how the linkage between the Arctic forcing and the inter-basin connectivity may change under various warming scenarios.

Chapter 6 summarizes the main findings of this dissertation and discusses possible future research directions.

Appendix A describes the framework of the Empirical Orthogonal Functions (EOF) analysis used throughout the dissertation, and a side project that uses the EOF method to find out optimal ways to design an in situ observation network for better reconstructions of nutrient fields in Southern Ocean. Appendix B explains the procedure of performing Maximum Covariance Analysis that used in Chapters 4 and 5. Parts of the results in Chapters 2, 3, 4, and Appendix A are published works, each of which can be read independently.

CHAPTER2

Changing Influences of El Niño on the Great Plains Low-Level Jet

2.1 Abstract

The Great Plains low-level jet (GPLLJ) exerts a strong influence on the hydroclimate of the Great Plains of the United States (U.S.) during late spring and early summer. In this chapter, the El Niño influence on the summer GPLLJ according to the El Niño type is stratified and the influence is found to be dramatically different for the Eastern Pacific (EP) and Central Pacific (CP) types. While the CP El Niño induces negative sea level pressure anomalies over the Gulf of Mexico to drive anomalous northerly winds weakening the GPLLJ, the EP El Niño intensifies the GPLLJ by inducing anomalous surface air temperature gradient between the northeastern and southwestern U.S. The finding indicates that the El Niño impact on the GPLLJ may have changed since early 1990s, when the El Niño changed from the conventional EP type to the CP type. A weakened GPLLJ and less transport of heat and moisture from the Gulf of Mexico into the Great Plains can lead to a drier environment in the central U.S. during summer.

2.2 Introduction

The Great Plains of the United States (U.S.) contributes more than 40% of the total agro-economics in North America. The Great Plains low-level jet (GPLLJ) plays an important

role in modulating the transport of heat and moisture from the Gulf of Mexico into the region during boreal spring and summer. Several studies have attributed the 1988 drought and 1993 flood in the Mississippi Valley to the weakening and strengthening of the GPLLJ (Ting and Wang, 2006; Cook *et al.*, 2008). Variations in the strength of the GPLLJ and its associated moisture transport were also suggested to be a contributing factor for springtime tornado activity in the U.S. (Weaver *et al.*, 2012; Lee *et al.*, 2013). Therefore, understanding the climatic factors that modulate the strength of the GPLLJ is crucial for the hydroclimate and socioeconomics of North America.

Several large-scale factors play roles in influencing the GPLLJ. The alternate warming and cooling of sloping terrain of the eastern Rocky Mountains are one of the factors that contribute to the persistence of the GPLLJ (Bonner and Paegle, 1970). The GPLLJ has been considered to be a result of the westward extension of the North Atlantic subtropical high in the presence of monsoonal heating (Rodwell and Hoskins, 2001) and the blocking effect of the North American orography (Byerle and Paegle, 2003; Ting and Wang, 2006). Upper-level westerly jet streaks were also suggested to be important to the development of the GPLLJ (Uccellini, 1980; Byerle and Paegle, 2003; Mo and Berbery, 2004). Model experiments have shown that sea surface temperature (SST) changes in the tropical North Atlantic can induce GPLLJ variations (Wang *et al.*, 2007; Wang *et al.*, 2008). Variations in the Pacific SST were also considered important in causing GPLLJ variability (e.g. Trenberth and Guillemot, 1996). El Niño events have been suggested to be capable of influencing the GPLLJ strength in their decaying phase (Weaver and Nigam, 2008). Idealized general circulation model experiments further indicated that El Niño events favor a stronger GPLLJ (Weaver *et al.*, 2009).

Several studies have emphasized that there exist at least two types of El Niño (e.g. Larkin and Harrison, 2005; Kao and Yu, 2009): the conventional El Niño characterized by warm SST anomalies in the Eastern Pacific (EP) and the Central Pacific (CP) El Niño that develops mostly around the international dateline (Yu and Kao, 2007; Kao and Yu, 2009). These two types of El Niño have been shown to produce distinct impacts on the wintertime temperature and precipitation in the U.S. (Mo, 2010; Yu and Zou, 2013) and springtime discharge in the Mississippi River (Liang *et al.*, 2014 and see Chapter 3). Since El Niño has changed from the EP type to the CP type in recent decades (e.g. Larkin and Harrison, 2005; McPhaden *et al.*, 2011; Yu *et al.*, 2012b), the El Niño impacts on the central U.S. during spring/summer may have also changed via the modulation of the GPLLJ. In this chapter, the El Niño impacts on the GPLLJ according to its type are stratified.

2.3 Data and Methods

2.3.1 Near-surface Wind, Sea Level Pressure, Surface Air Temperature, and Precipitation Datasets

The 925-hPa meridional winds, sea level pressure (SLP), and surface air temperature (SAT), and precipitation fields are obtained from the National Center for Atmospheric Research/National Centers for Environmental Prediction (NCAR/NCEP) reanalysis dataset (Kalnay *et al.*, 1996). The reanalysis product is available from 1948 to 2010 with a horizontal resolution of 2.5^{o} longitude by 2.5^{o} latitude. In the chapter, anomalies are defined as the deviation from the 1948 to 2010 climatology.

2.3.2 Sea Surface Temperature Datasets

The sea surface temperature (SST) datasets used in this chapter are the National Oceanic and Atmospheric Administration (NOAA)'s Extended Reconstructed Sea Surface Temperature V3b dataset (Smith and Reynolds, 2003), and the Met Office Hadley Centre's Sea Ice and Sea Surface Temperature dataset (Rayner *et al.*, 2003).

2.3.3 CP and EP El Niño-Southern Oscillation Indices

This chapter also uses the EP and CP El Niño-Southern Oscillation (ENSO) indices, which are calculated from the National Oceanic and Atmospheric Administration (NOAA)'s Extended Reconstructed Sea Surface Temperature V3b dataset (Smith and Reynolds, 2003) using a regression-EOF (Empirical Orthogonal Functions) method (Kao and Yu, 2009). A total of twenty-one major El Niño events were identified during the analysis period based on the Ocean Niño Index (Trenberth and Stepaniak, 2001). The types of these El Niño events have been determined based on a "consensus method" developed by Yu *et al.* (2012a), in which three different identification methods are used to produce a "consensus" on the El Niño type (Table 2.1). The methods include (1) the EP/CP-index method (Kao and Yu, 2009), (2) the Niño method (Yeh *et al.*, 2009), and (3) El Niño Modoki index (EMI) method (Ashok *et al.*, 2007). If two of the three methods identify an El Niño event to be of the CP (EP) type, then the event is determined to be a CP (EP) El Niño event. Using this consensus method, eight of the twenty-one El Niño events were determined to be the EP El Niño events (1951-1952, 1969-1970, 1972-1973, 1976-1977, 1982-1983, 1986-1987, 1997-1998, and 2006-2007), while the other thirteen were determined to be CP El Niño events (1953-1954, 1957-1958, 1958-1959, 1963-1964, 1965-1966, 1968-1969, 1977-1978, 1987-1988, 1991-1992, 1994-1995, 2002-2003, 2004-2005, and 2009-2010). Note that whether or not the trend is removed does not affect the identification of the EP

and CP El Niño events. A more detailed description of the consensus method can be found in Yu *et al.* (2012a). These events are used to composite fields for the analyses in this chapter.

Table 2.1 Major El Niño events since 1950 and their types identified by the 'Consensus Method' from EP/CP-index method (Kao and Yu, 2009), the Niño Method (Yeh *et al.*, 2009), and the EMI Method (Ashok *et al.*, 2007). This table is adopted from Table 1 in Yu *et al.* (2012a).

		Type			
	El Niño Years	EP/CP method	Niño3/4 method	EMI method	Consensus
1	1951–52	EP	EP	EP	EP
2	1953–54	CP	CP	EP	CP
3	1957–58	CP	EP	CP	CP
4	1958–59	CP	CP	CP	CP
5	1963–64	CP	CP	CP	CP
6	1965–66	CP	EP	CP	CP
7	1968–69	CP	CP	CP	CP
8	1969–70	CP	EP	EP	EP
9	1972–73	EP	EP	EP	EP
10	1976–77	EP	EP	EP	EP
11	1977–78	CP	CP	CP	CP
12	1982–83	EP	EP	EP	EP
13	1986–87	CP	EP	EP	EP
14	1987–88	CP	CP	EP	CP
15	1991–92	CP	EP	CP	CP
16	1994–95	CP	CP	CP	CP
17	1997–98	EP	EP	EP	EP
18	2002–03	CP	EP	CP	CP
19	2004–05	CP	CP	CP	CP
20	2006–07	EP	EP	EP	EP
21	2009–10	CP	CP	CP	CP

2.4 Asymmetric Responses of the Great Plains Low-Level Jet to the Two Types of El Niño

The GPLLJ is characterized by strong low-level southerly winds (maximum wind speed is about 8 m/s) in the central U.S. during late spring/early summer (Ting and Wang, 2006; Cook *et al.*, 2008; Weaver and Nigam, 2008). Figure 2.1(a) shows the climatological values (1948-2010) of the May-June-July (MJJ) mean meridional winds at 925-hPa over the U.S. The low-level jet can be identified as the maximum in wind speeds over the Great Plains of the United States, which also extends southward to northeastern Mexico. The GPLLJ is particularly prominent in the Texas, Oklahoma, and south Kansas region; its magnitude decreases toward the north. The deviations of the composited meridional winds from the climatology are found to be statistically significant for the two types of El Niño only during their decaying phases (Figures 2.1 (b) and (c)) at the 90% level using a two-tailed Student's *t*-test. In contrast, the deviations during the developing phases do not pass the 90% level for the CP El Niño composite and only barely pass the test for the EP El Niño composite (Figure 2.2).

In this chapter, we focus only on El Niño's impacts during its decaying phase. During the decaying phase of the EP El Niño, the strength of the GPLLJ increases by as much as 0.5 m/s, which is about 6% of the climatological value. The strengthening of the GPLLJ is most obvious over Missouri and Arkansas, which is the northern portion of the GPLLJ. In contrast, the composite for the CP El Niño (Figure 2.1(b)) events shows a decrease in the meridional winds over the GPLLJ region. The decrease is particularly large over the southern portion of the GPLLJ, including Texas, Louisiana, and Arkansas. The strength of the GPLLJ weakens by about 0.5 m/s. Figure 2.1 indicates that the conventional view of a strengthening effect of El Niño on the GPLLJ (e.g. Weaver *et al.*, 2009) is true only for the EP type of El Niño. A distinct and opposite

effect is produced by the CP type of El Niño. Precipitation decreases (increases) are also found when CP (EP) El Niño events occur (Figure 2.3), which corresponds to a weakening (strengthening) of the GPLLJ. To make sure the results are not dependent on the reanalysis products used, the wind analyses using the ERA-Interim reanalysis product (Dee *et al.*, 2011) and the precipitation analysis using an observation-based precipitation dataset (Parameter-elevation Relationships on Independent Slopes Model (PRISM), Daly *et al.*, 2008) are repeated. Similar results are found (not shown), indicating that the features found here are robust across data products.

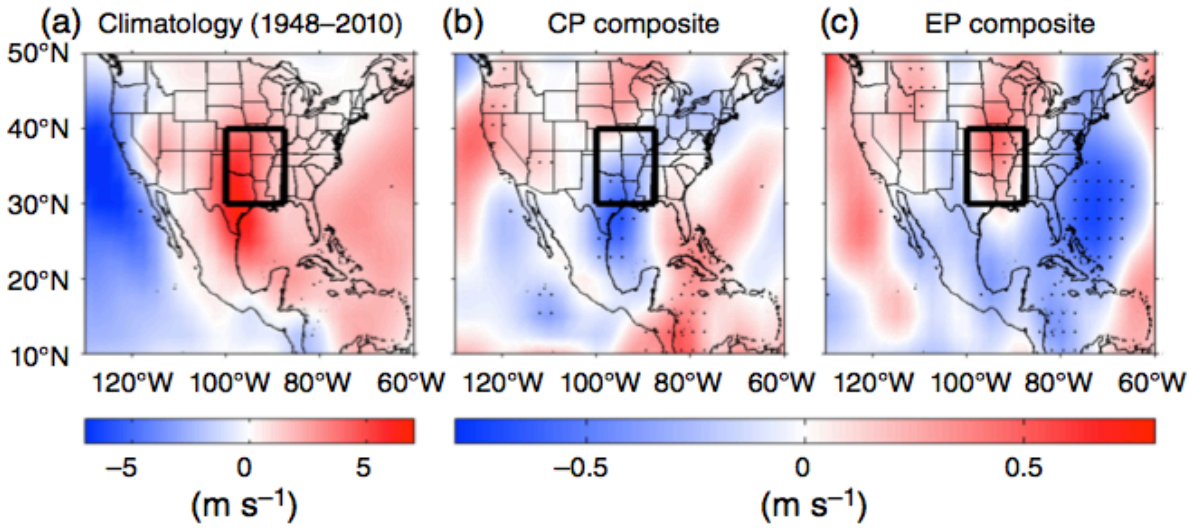

Figure 2.1 Meridional winds at 925-hPa during the May-June-July (MJJ) season: (a) the climatological values (1948-2010); (b) the anomalies composited from the thirteen CP El Niño events during their decaying phase; and (c) the anomalies composited from the eight EP El Niño events during their decaying phase. Statistically significant deviations are stippled. Boxes in the panels indicate the GPLLJ region, which is bounded in latitude by 30^{o} and 40^{o}N and in longitude by 87^{o} and 101^{o}W.

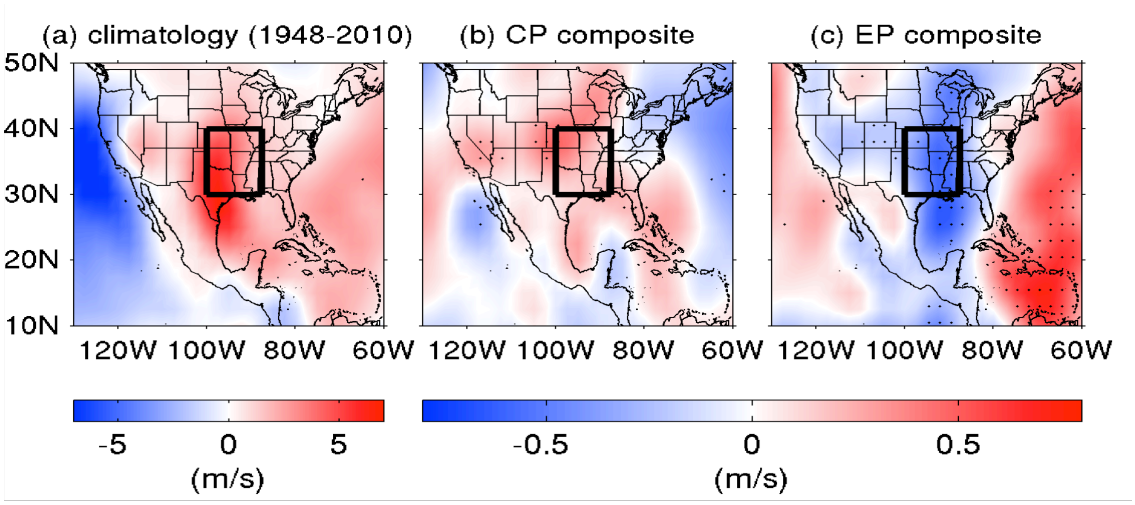

Figure 2.2 Similar to Figure 2.1 but during developing phase of CP and EP El Niño events.

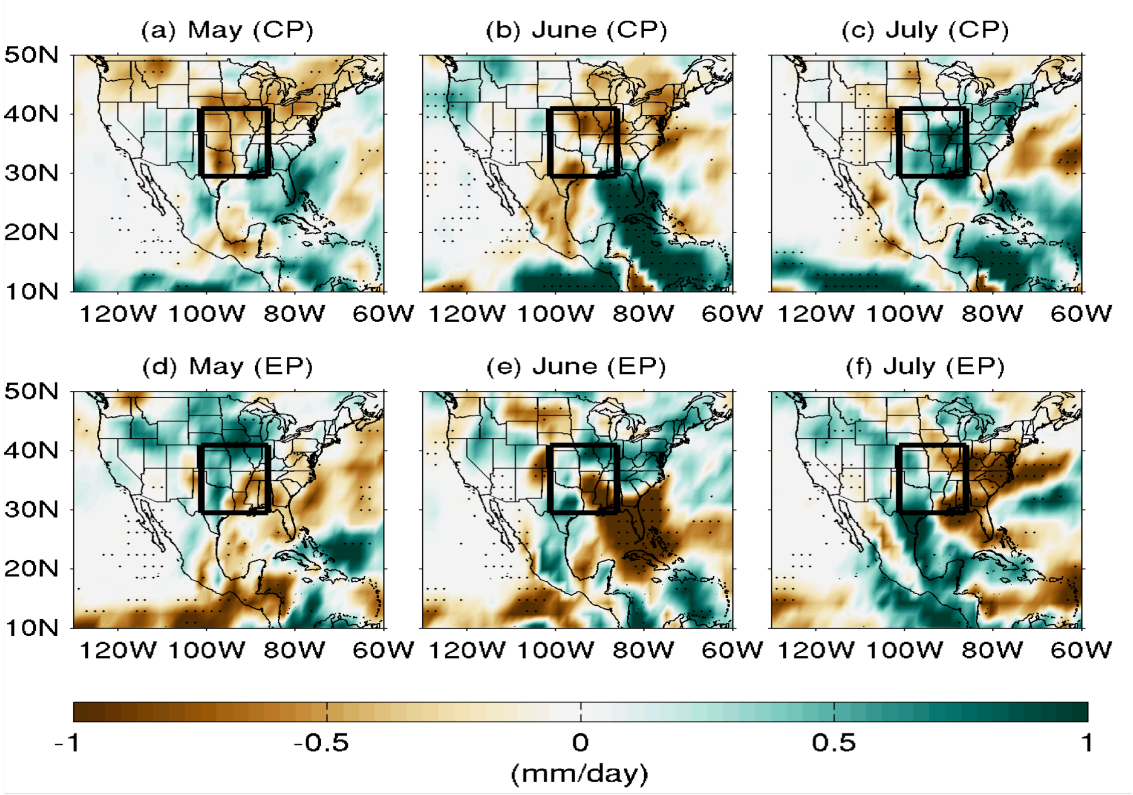

Figure 2.3 Precipitation anomalies during May, June, and July composted for the CP El Niño events (upper panels) and the EP El Niño events (lower panels) in their decaying phases. Statistically significant deviations are stippled.

To understand why the two types of El Niño produce opposite influences on the strength of GPLLJ, we examined the large-scale circulation features over the U.S. during the MJJ season. Figure 2.4 shows the MJJ-mean SLP anomalies composited for the two types of El Niño during their decaying phases. Associated with the CP El Niño (Figure 2.4(a)), significant negative SLP anomalies are found over the Gulf of Mexico and are accompanied by cyclonic wind anomalies. Northerly wind anomalies are produced in the GPLLJ region (indicated by a square box in the figure) to weaken the GPLLJ. A different SLP anomaly pattern is found in the composite for the EP El Niño (Figure 2.4(b)). The anomalies are characterized by a north-south dipole pattern over the U.S., which would have induced zonal wind anomalies rather than meridional wind anomalies. Instead, the region of GPLLJ (Figure 2.1(a)) is found farther south of the center of these SLP anomalies, indicating that the SLP anomaly dipole is not the mechanism to strengthen the GPLLJ. Therefore, the SLP anomalies induced by the EP El Niño do not seem to explain its strengthening effect on the GPLLJ.

The SAT anomaly pattern associated with the EP El Niño seems to be capable of explaining its strengthening effect on the GPLLJ better than the associated SLP anomaly pattern. As shown in Figure 2.5(b), negative SAT anomalies are observed to the west and southwest of the GPLLJ, while significant and positive SAT anomalies are observed to the north and northeast of the GPLLJ. The east-west dipole in the thermal structure results in a positive longitudinal temperature gradient ($dT/dx>0$), which induces a southerly jet anomaly according to the thermal wind balance. The thermal wind balance is applied to calculate the vertical wind shear in the lower troposphere from the horizontal surface temperature gradient. The vertical wind shear is then used to estimate the 925-hPa (i.e. the GPLLJ level) wind anomalies from the composite surface wind anomalies. As shown in Figure 2.6, the estimated 925-hPa wind anomalies for the

EP El Niño are similar to the composite 925-hPa wind anomalies over the central U.S. including the GPLLJ region. This analysis demonstrates that the strengthening of the GPLLJ at 925-hPa during the EP El Niño can be explained by the horizontal temperature gradient anomalies via the thermal wind balance. No such correspondence is found for the CP El Niño (not shown). The temperature anomaly pattern shown in Figure 2.5(b) is similar to that of typical EP El Niño impact on U.S. winter temperature reported by Yu *et al.* (2012a). Their work suggested that this southwest-to-northeast anomaly pattern is a result of the Tropical-Northern Hemisphere (TNH, see Chapter 4 for comprehensive description) wavetrain excited by the EP El Niño. Land hydrological processes (e.g. Liang *et al.*, 2014 and see Chapter 3) may be responsible for

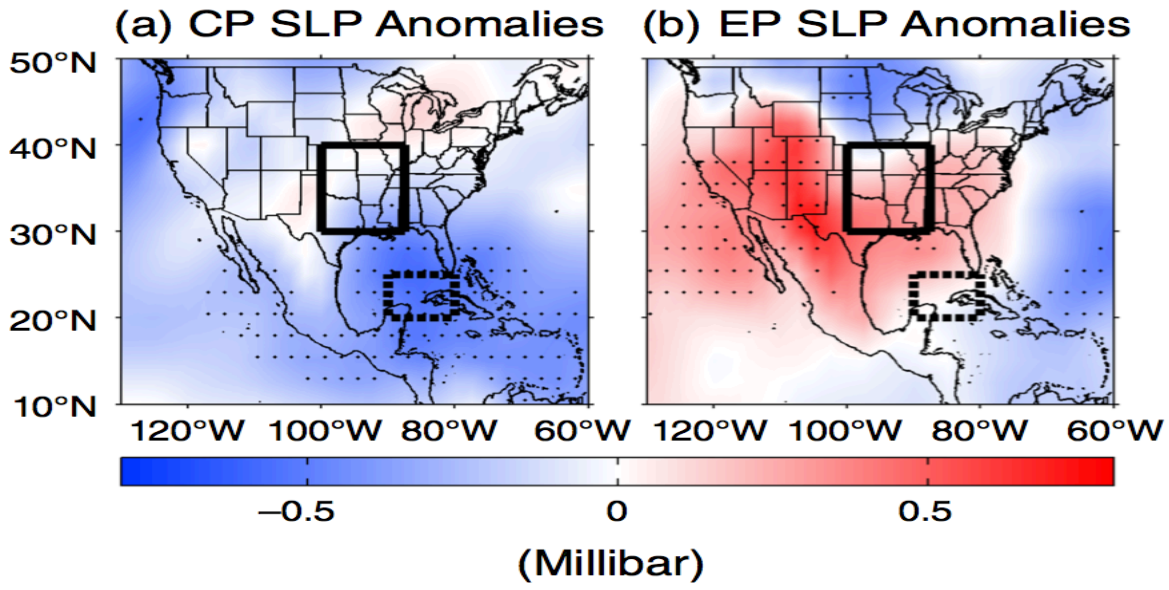

Figure 2.4 MJJ-mean sea level pressure anomalies composited for the (a) CP El Niño events and (b) the EP El Niño events during their decaying phases. The solid boxes are defined as in Figure 2.1. The dashed boxes are defined as the region bounded in latitude by 20^{o} and 25^{o}N and in longitude by 80^{o} and 90^{o}W. Statistically significant deviations are stippled.

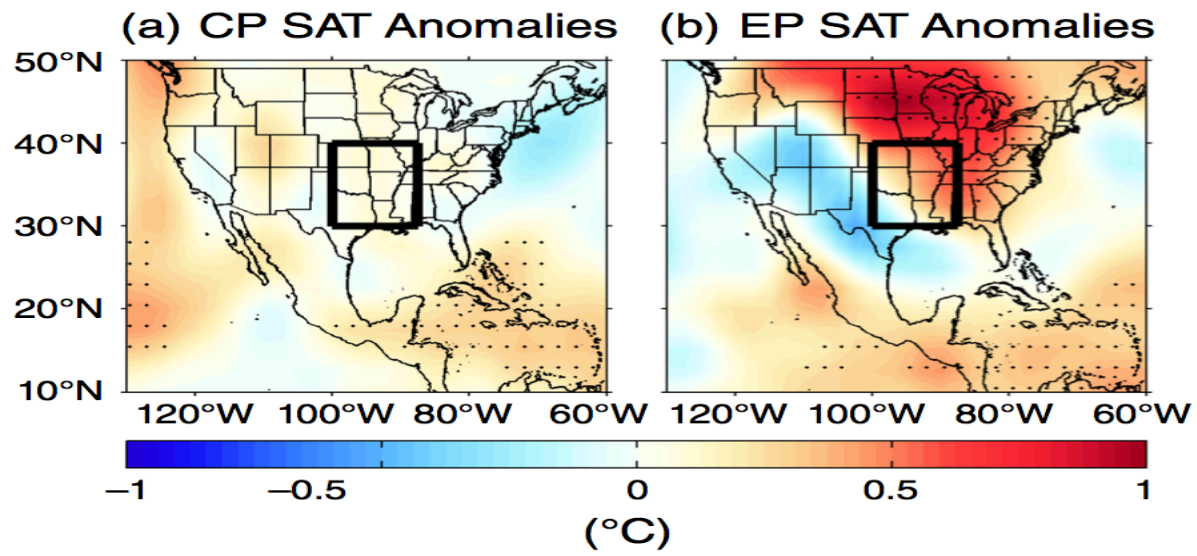

Figure 2.5 MJJ-mean surface air temperature anomalies composited for (a) the CP El Niño events and (b) the EP El Niño events during their decaying phases. The boxes are defined as in Figure 2.1. Statistically significant deviations are stippled.

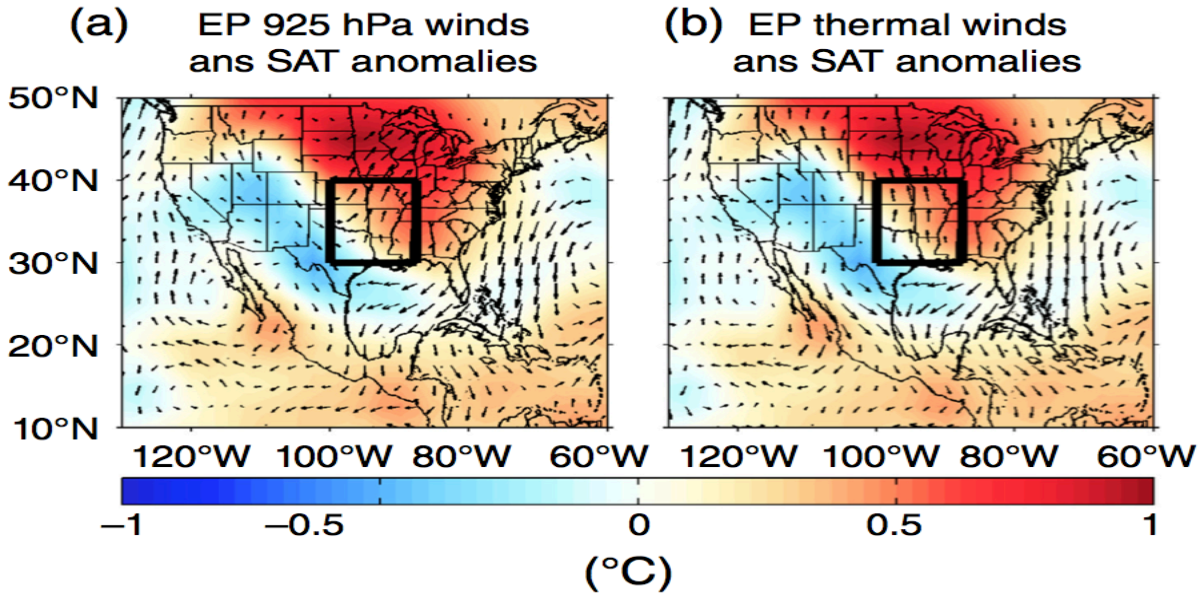

Figure 2.6 (a) MJJ-mean wind anomalies (vector) at 925hPa composited from the decaying phase of the EP El Niño. (b) MJJ-mean wind anomalies (vector) at 925 hPa estimated from the thermal wind balance during the decaying phase of the EP El Niño. Composite MJJ-mean surface air temperature (SAT) anomalies are shown as color shadings in both panels. The boxes are defined as in Figure 2.1.

sustaining the temperature anomalies from the winter season to the summer season. Local water management practices (such as irrigation) could affect the surface temperature pattern via modulations in the surface energy budget (Sacks *et al.*, 2009; Lo and Famiglietti, 2013) and result in changes in the strength of the low-level jet (Huber *et al.*, 2014). The induced southerly wind anomalies may also play an important role in contributing to the warming via moisture and heat transport from the southern part of the Great Plains and the Gulf of Mexico. Further analyses are required to better understand their impacts on sustained surface temperature anomalies.

In contrast, no significant surface temperature anomalies can be identified over the U.S. during the CP El Niño events (Figure 2.5(a)), which indicates that the CP El Niño impacts on the GPLLJ strength cannot be explained by the same thermal wind balance argument. The negative SLP anomalies identified over the Gulf of Mexico during CP El Niño events (Figure 2.5(a)) are found to be a prolonged dynamic response of the U.S. to the CP SST anomalies. In Figure 2.7, a lag correlation analysis between the wintertime (December-January-February) EP and CP ENSO indices and the SLP anomalies through winter to the following summer over the Gulf of Mexico is performed (region indicated by the dashed square box in Figure 2.4(a) and (b)). As shown in Figure 2.7, both the CP and EP ENSO indices have negative correlation coefficients (between −0.6 and −0.5) with the Gulf of Mexico SLP anomalies during the winter, and the negative correlations weaken in the following seasons. The decaying correlation indicates that the ENSO influences on the Gulf of Mexico SLPs decreases during the decaying phase of El Niño events. However, the correlation coefficient decreases more slowly for the CP ENSO index (blue line) than for the EP El Niño index (red line). In MJJ, the correlation coefficient with the CP El Niño is about -0.35. This value is still statistically significant at the 95% level, while the correlation

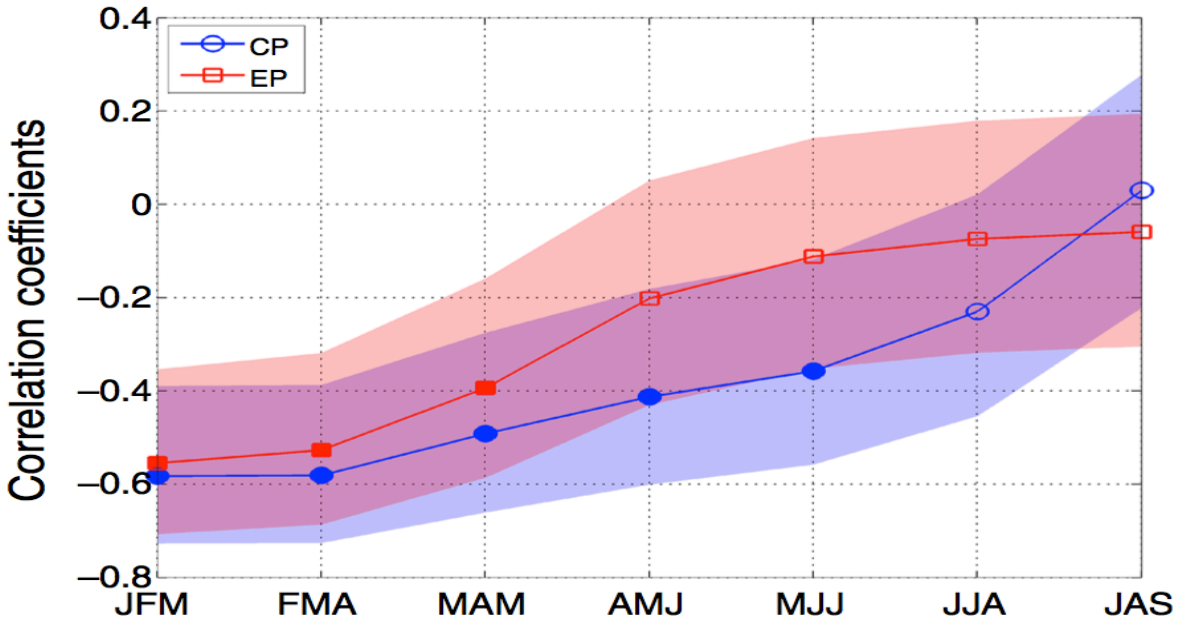

Figure 2.7 Correlation coefficients between the CP and EP ENSO indices and the SLP anomalies averaged in a region between 20°–25°N and 80°–90°W (i.e. the dashed square boxes in Figure 2.4 (a) and (b)). Filled symbols indicate statistically significant points with *p*-value less than 0.05. The shaded area indicates 95% confidence interval for coefficients.

with the EP ENSO index has already plunged to about -0.1. This analysis suggests that the winter CP El Niño SST anomalies have a more prolonged impact on the SLP fields over the Gulf of Mexico than that for the EP El Niño.

To further confirm the opposite influence produced by the two types of El Niño on the strength of the GPLLJ, we examined the strength during the MJJ season for each of the twenty-one El Niño events after 1950. The GPLLJ strength is quantified by a GPLLJ index, which is defined as the meridional winds averaged in the box shown in Figure 2.1(a). Figure 2.8 shows that the deviation of this index from its climatological value for all the El Niño events analyzed in this chapter. Ten of the thirteen (77%) CP El Niño events show a weakening of the GPLLJ, while six of the eight (75%) EP El Niño events show a strengthening of the GPLLJ. After the late 1980s, it is obvious that the frequent occurrence of CP El Niño events leads to a weakening

of the GPLLJ, except during the 2009-2010 El Niño event. Noted that three CP El Niño events (1958-1959, 1963-1964, and 2009-2010) and two EP El Niño (1972-1973 and 2006-2007) produced impacts on the GPLLJ that are opposite from those suggested by the composite analyses.

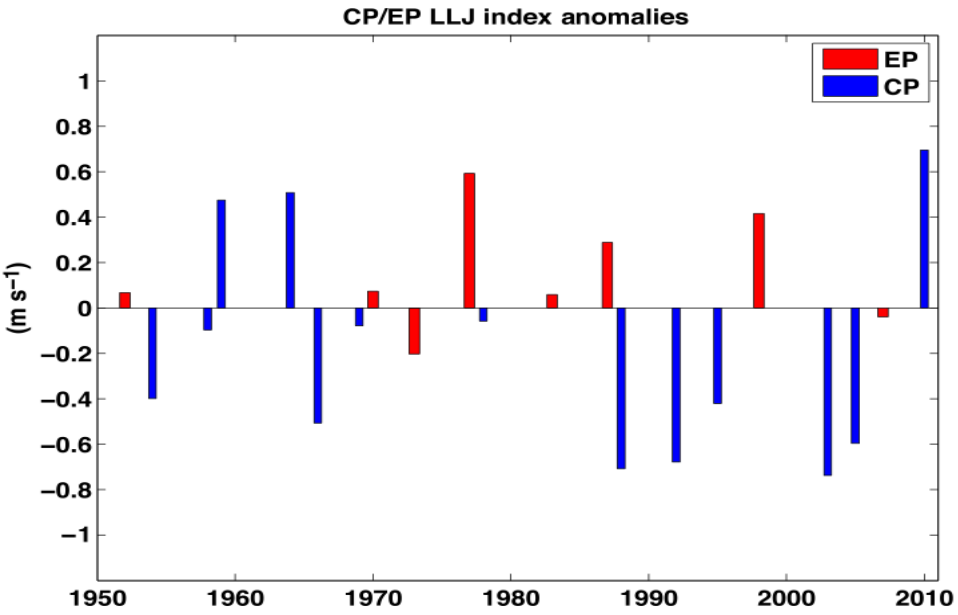

Figure 2.8 Values of the GPLLJ index (see text for its definition) calculated for the twenty-one major El Niño events after 1950. The blue bars indicate CP El Niño events, and the red bars indicate EP El Niño events.

To discuss the possible causes for these exceptional events, the SST anomalies averaged from these "exceptional" CP and EP El Niño events (Figure 2.9) are compared to the SST anomalies averaged from the "normal" CP and EP El Niño events (Figure 2.10). The biggest differences occur in the eastern equatorial Pacific, where the exceptional CP and EP El Niño events have large negative SST anomalies. This difference indicates that the rapid decay of these particular El Niño events is a reason why this group of events produces different impacts on the

GPLLJ than the normal group of the El Niño events. In addition, large SST anomalies are also found in the North Pacific during the exceptional EP El Niño events and in the North Atlantic during the exceptional CP El Niño events, which suggest that oceanic forcing outside the tropical Pacific may disrupt or even overcome El Niño's influences on the GPLLJ. Earlier studies have already demonstrated these ocean influences on U.S. summer climate (e.g., Wang *et al*., 2007; Wang *et al*., 2008; Weaver *et al*., 2009). These results illustrate some potential causes for the irregularity in the GPLLJ index in Figure 2.8.

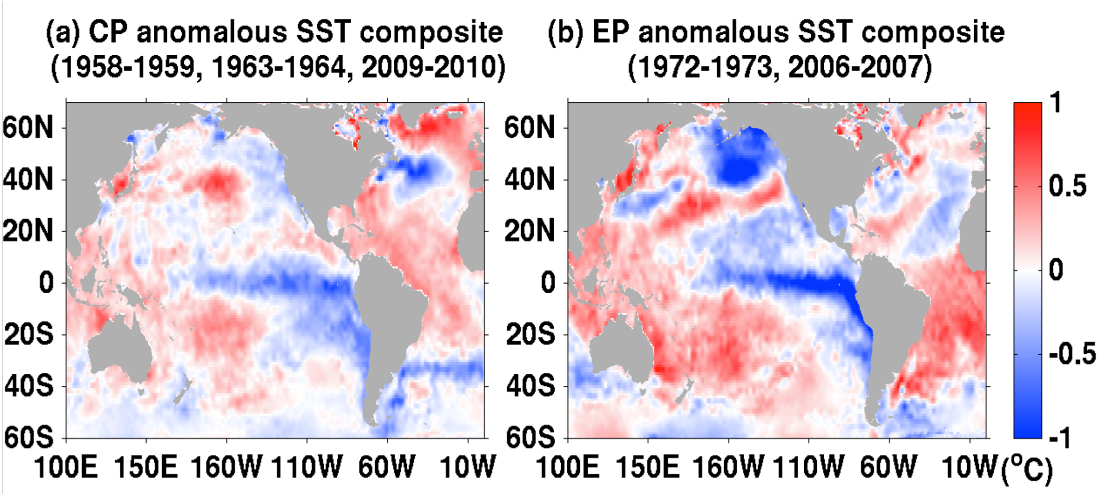

Figure 2.9. MJJ-mean SST anomalies averaged from (a) the three "exceptional" CP El Niño events (1958-1959, 1963-1964, and 2009-2010) and (b) the two "exceptional" EP El Niño events (1972-1973 and 2006-2007).

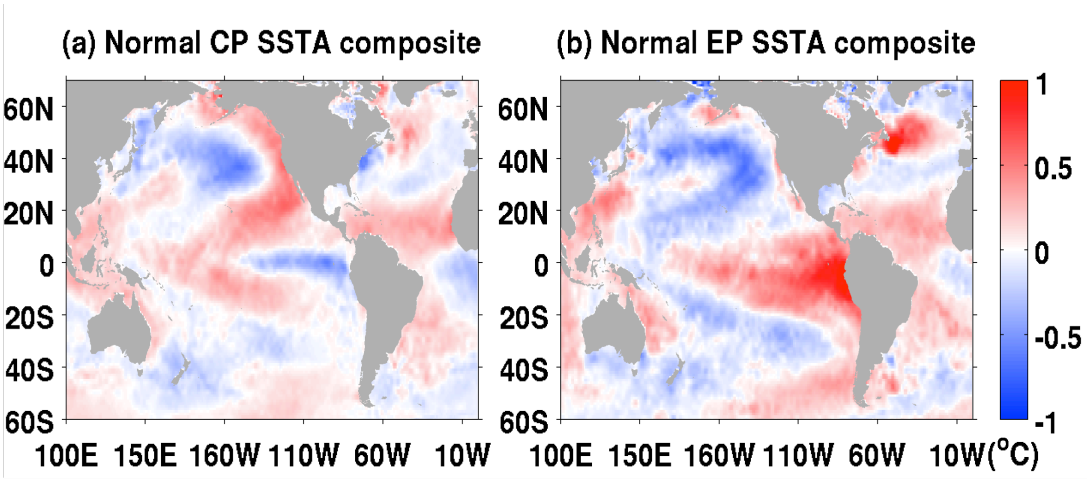

Figure 2.10. MJJ-mean SST anomalies averaged from (a) the "normal" CP El Niño events (i.e., excluding the 1958-1959, 1963-1964, and 2009-2010 exceptional events) and (b) the "normal" EP El Niño events (i.e., excluding the 1972-1973 and 2006-2007 exceptional events).

2.5 Summary and Discussion

In this chapter, statistical evidences show that the two types of El Niño can produce opposite impacts during their decaying phases on the strength of the GPLLJ during late spring and early summer. In contrast to the EP El Niño that tends to intensify the GPLLJ via establishing air temperature gradient between northeastern and southwestern U.S., the CP El Niño induces negative sea level pressure anomalies over the Gulf of Mexico to drive northerly winds to weaken the GPLLJ. The results imply that the El Niño impacts of the GPLLJ may have changed since the early 1990s as the El Niño type has changed from EP type to CP type. The influences of the CP El Niño on the GPLLJ are also found to persist longer into late spring season than those induced by the El Niño, implying that El Niño SST anomalies may become more valuable in predicting boreal springtime U.S. climate variability if the El Niño event flavors CP type than EP type.

The finding has several implications for understanding, predicting, and projecting the U.S. summer climate. In 1988, a severe drought damaged the agroeconomics in the central U.S. and cost approximately $40.0 (61.6, adjusted to 2002 value) billion dollars (Ross and Lott, 2003). The northward displacement of the jet stream and positive upper-level height anomalies above the Great Plains were considered to be causes for the drought (Basara *et al.*, 2013). Any studies that have attributed this drought event to El Niño have not been reported. According to the 'consensus El Niño type' identified by Yu *et al.* (2012a), 1988 was the decaying period of the 1987-1988 CP El Niño. The results indicate that this CP El Niño event had the potential to contribute to the reduction in strength of the MJJ GPLLJ, which may have weakened the moisture transport from the Gulf of Mexico into the Great Plains. This may have been a contributing factor for the severe drought in 1988.

Recent studies have indicated that the GPLLJ has become stronger and migrated northward since 1979, leading to an increasing trend in the precipitation in the central and northern Great Plains but a significant reduction in rainfall in the Southern Plains (Barandiaran *et al.*, 2013). General circulation model simulation results have suggested that global warming may amplify the GPLLJ in the future mainly due to a westward extension of a stronger North Atlantic subtropical high (Cook *et al.*, 2008). This study suggests that the strengthening effect caused by global warming may be partially offset by the CP El Niño that has been suggested to occur more frequently in a warmer climate (e.g. Yeh *et al.*, 2009; Kim and Yu, 2012).

The impacts of the CP El Niño SST anomalies on the Great Plains via SLP changes reported here imply that El Niño SST anomalies may become more useful in predicting summertime U.S. climate as El Niño changes from the EP type to the CP type.

CHAPTER3

Asymmetric Responses of North American Hydroclimate to the Two Types of El Niño

3.1 Abstract

El Niño events play important roles in influencing North American hydroclimate. This chapter shows that the two types of El Niño events, the Central Pacific (CP) El Niño and Eastern Pacific (EP) El Niño, have opposite effects on boreal spring soil hydrology in the Mississippi River Basin (MRB). Above-normal spring (March) precipitation during the EP El Niño years leads to higher soil water levels during the subsequent two to three months in the central and western MRB. In contrast, the CP El Niño events induce below-normal spring precipitation that causes lower soil water levels over the Ohio-Mississippi Valley during the following one or two months. As a result, a springtime asymmetric response to the different types of El Niño occurs in the Mississippi River discharge and soil water storage. Subsurface hydrological storage processes are found to be essential to extend the El Niño's influence in the MRB to late spring. As the location of El Niño events has gradually shifted from the EP to the CP during the recent two decades (i.e., after the early-1990s), the findings indicate that an El Niño event has the tendency to induce drier hydrological conditions, to pose water shortages or severe drought, and to threaten the agricultural water supplies in the central United States.

In addition, the discharge asymmetric (and symmetric) responses of global rivers to the two types of El Niño are mapped in this chapter to offer an overview of which rivers may need new projection techniques and management strategies in response to the changes in El Niño type during recent decades.

3.2 Introduction

River discharge plays an important role in global water and biogeochemical cycles. For the water cycle, the discharge serves as the main water outflux in the terrestrial water balance (Dai and Trenberth, 2002) and contributes to the long-term water balance of the global oceans (Oki and Kanae, 2006). For the biogeochemical cycle, river discharge delivers great amounts of nutrients and dissolved minerals and organics into the ocean that have large impacts on biogeochemical processes in coastal and reef regions (Boyer *et al.*, 2006). Fluctuations in river discharge, therefore, have significant impacts on the global water and biogeochemical cycles, as well as on global socioeconomics and human activities (Milly *et al.*, 2005; Iles and Hegerl, 2015; Pal *et al.*, 2015).

The Mississippi River Basin (MRB) has the largest drainage basin in North America (Figure 3.1), covering an area of approximately 3.2×10^6 km^2, which is about 41% of the contiguous United States (U.S.). The freshwater resources in the MRB support the extensive agricultural activity in the central U.S. Therefore, it is important to understand surface and groundwater hydrology in the MRB and how they respond to climate variation and change (Goolsby et al. 1999). The El Niño–Southern Oscillation (ENSO) can significantly influence temperature and precipitation throughout the U.S. (e.g., Ropelewski and Halpert, 1986; Rogers and Coleman, 2004; Kurtzman and Scanlon, 2007), including the MRB. Previous observational

and modeling studies (e.g., Kahya and Dracup, 1993; Twine *et al.*, 2005; Dai *et al.*, 2009) found a close connection between ENSO and MRB discharge. Twine *et al.* (2005), for example, analyzed observational data and model simulations to show that El Niño events increase springtime river discharge in MRB; and Dai *et al.* (2009) explored a long-term river flow dataset and confirmed that El Niño events tend to enhance the Mississippi River discharge.

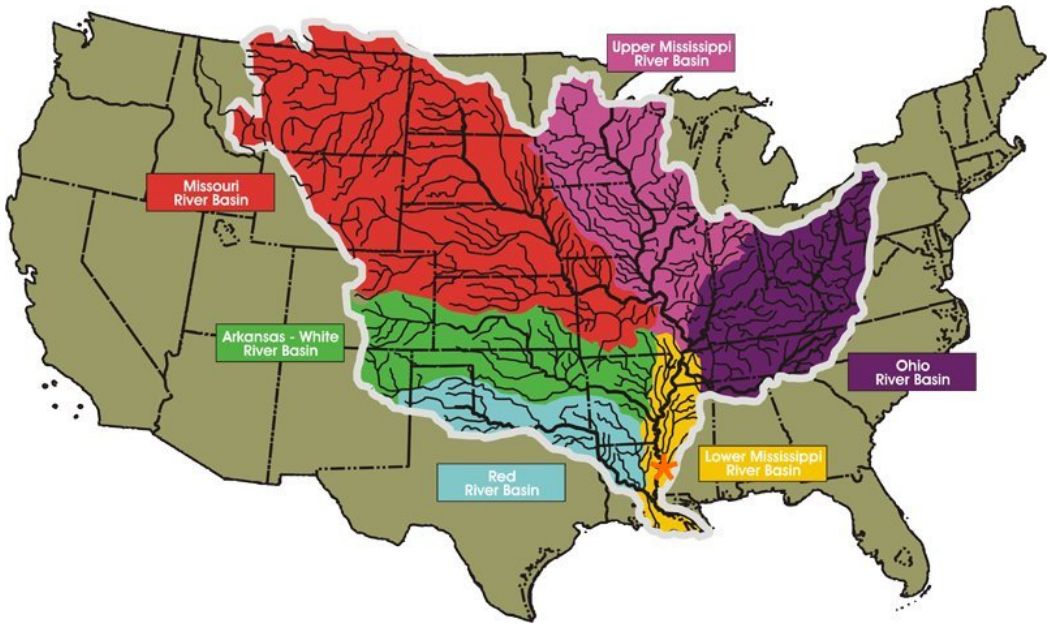

Figure 3.1 The drainage area of the Mississippi River Basin (MRB). Different color shadings denote sub-basins of MRB. The orange star symbol represents the location of gauge observation at Vicksburg, Mississippi. The map is downloaded from news posted on Linkedin (https://www.linkedin.com/pulse/great-news-mississippi-river-coming-from-south-dakota-browning).

ENSO-induced precipitation anomalies can affect the water storage in soil moisture and groundwater, which can significantly influence hydrological processes in the MRB. Based on the available global soil moisture dataset, Entin *et al.* (2000) found a lag of two to three months in soil moisture storage in response to the precipitation anomalies. Chen and Kumar (2002) further illustrated the relationship between ENSO and hydrological variables, including soil water storage and river discharge. Using a modeling approach, Lo and Famiglietti (2010) demonstrated that subsurface hydrological processes can affect the timing of soil moisture storage, thus play important roles in preserving the precipitation signals in terrestrial water storage (soil moisture and groundwater) and influencing river discharge in the subsequent months or seasons in the MRB.

Many studies have suggested that there are two types of El Niño-Eastern Pacific (EP) El Niño and Central Pacific (CP) El Niño (e.g., Yu and Kao, 2007; Ashok *et al.*, 2007; Kao and Yu, 2009; Kug *et al.*, 2009). The EP El Niño is characterized by positive sea surface temperature (SST) anomalies extending from the South American coast westward along the equator. In contrast, positive SST anomalies can evolve mostly in the central Pacific around the international dateline, forming the CP El Niño (Kao and Yu, 2009). The formation and mechanism of CP and EP El Niño have been examined by a series of analyses in two leading empirical orthogonal function (EOF, see Appendix 1 for details) patterns of SST anomalies in the tropical Pacific (Ashok *et al.*, 2007; Kao and Yu, 2009; Kug *et al.*, 2009). These two types of El Niño can lead to different convection patterns and atmospheric responses (Mo, 2010; Yu *et al.*, 2012a; Yu and Zou, 2013), resulting in distinct impacts on regional and global climate (Li *et al.*, 2011; Karori *et al.*, 2013). Over the U.S., Mo (2010) and Yu and Zou (2013) found that CP El Niño events

induce negative precipitation anomalies along the Ohio-Mississippi Valley during late winter, while EP El Niño events produce wet anomalies in the central U.S.

Although previous studies have investigated the statistical relationship between hydrological processes and El Niño, few studies have considered El Niño's effects on soil water storage together with river discharge for the CP and EP El Niño types separately. Because the location of El Niño has the tendency to shift from the EP to the CP during the recent few decades (Ashok *et al.*, 2007; Kug *et al.*, 2009; Yu *et al.*, 2012b), it is crucial to understand whether or not these two types of El Niño produce different impacts on the hydroclimate (e.g., river discharge and soil water storage) in the MRB.

Since the impacts of El Niño outreach to almost every corner of the world, it is desirable to obtain an overview of how world river discharges responds to the two types of El Niño. A method is developed in this chapter to map these responses for top thirty global river basins during the developing, mature, and decaying phases of different types of El Niño. Corresponding precipitation conditions are also analyzed to reveal the possible mechanism producing these global river discharge responses.

3.3 Data, Model, and Methods

3.3.1 River Discharge Dataset

The Global River Flow and Continental Discharge Data Set from Dai *et al.* (2009) is used for analysis in this chapter, which provides river discharge data for the world's 925 largest rivers primarily based on gauge observations. There are two versions of this discharge dataset available: one uses model simulations (the National Center for Atmospheric Research Community Land Model) to fill data gaps (as described in Dai *et al.*, 2009) and the other does not use the gap

filling. The non-filling data set is used in this chapter and is downloaded from http://www.cgd.ucar.edu/cas/catalog/surface/dai-runoff/coastal-stns-Vol-monthly.updated-oct2007.nc. For the MRB hydroclimate study, the Mississippi River discharge data is used from this dataset. For global river mappings, the thirty of the world's largest rivers are selected according to the size of their drainage areas (based on the data from Oki and Sud, 1998; http://hydro.iis.u-tokyo.ac.jp/~taikan/ TRIPDATA/TRIPDATA.html). Large rivers in high-latitude regions are not considered because El Niño's impacts on their discharges tend to be interrupted by pulse-like seasonal irregularities (not shown) related to the spring snowmelt. Large rivers that show discontinuities or large gaps in their data are also excluded. The thirty rivers selected are listed in Figure 3.2, together with the availability of their discharge data during the 1950-2006 analysis period. These selected rivers are numbered in Figure 3.2 based on their rankings in terms of drainage area. The drainage areas, the locations, and the names of the corresponding gauge stations for each of the thirty rivers are listed in Table 3.1. The total area of the investigated river basins is roughly 3.7445×10^7 km^2, about 25% of the total land area. The river discharge anomalies are defined as the deviations from the 1950 to 2006 climatology.

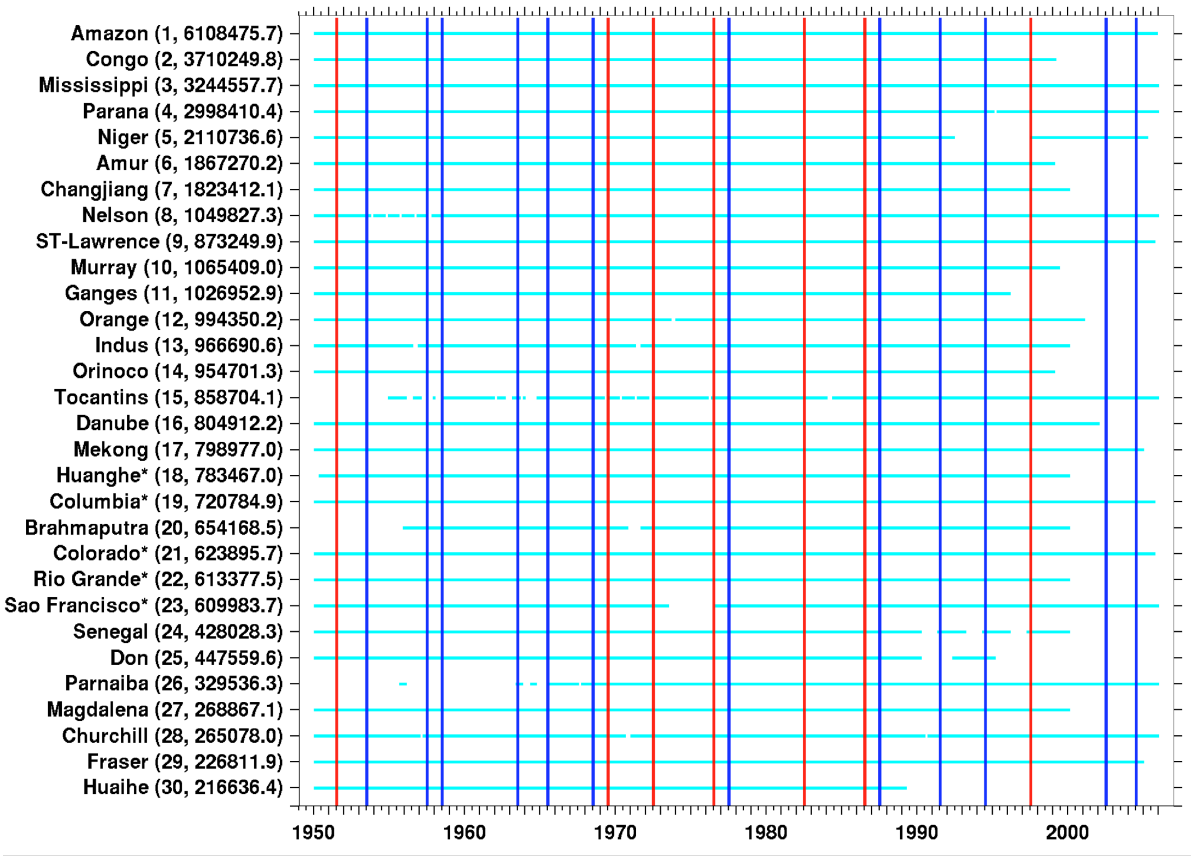

Figure 3.2 The availability of discharge data (horizontal light-blue bars) for the thirty rivers with the largest drainage areas. The drainage area ranking is based on Oki and Kanae (2006) and the discharge data originated from Dai *et al.* (2009). The second number in the parenthesis indicates the river basin area (km^2). The vertical red and blue lines mark the years of the EP and CP El Niño events, respectively, according to Yu *et al.* (2012b). The '*' symbol after the river name denotes that this river may be influenced by human interventions.

Table 3.1 Summary of top thirty rivers according to the size of drainage area.

River Name	Drainage Area (km^2)	Station/Country	Longitude	Latitude
(1) Amazon	6,108,475.7	Obidos/Brazil	55.51W^o	1.95S^o
(2) Congo	3,710,249.8	Kinshasa/Congo	15.3E^o	4.3S^o
(3) Mississippi	3,244,557.7	Vicksburg/USA	90.91W^o	32.31N^o
(4) Paraná	2,998,410.4	Timbues/Argentina	60.71W^o	32.67S^o
(5) Niger	2,110,736.6	Lokoja/Nigeria	6.7667E^o	7.8N^o
(6) Amur	1,867,270.2	Komsomolsk/Russia	137E^o	50.53N^o
(7) Changjiang	1,823,412.1	Datong/China	117.62E^o	30.77N^o
(8) Nelson	1,049,827.3	Bladder/Canada	97.92W^o	54.77N^o
(9) ST-Lawrence	873,249.9	Cornwall ON/USA	74.74W^o	45N^o
(10) Murray	1,065,409.0	Euston Weir/Australia	142.76E^o	34.6S^o
(11) Ganges	1,026,952.9	Farakka/India	88.13E^o	24.55N^o
(12) Orange	994,350.2	Vioolsdrift/S. Africa	17.63E^o	28.78S^o
(13) Indus	966,690.6	Kotri/Pakistan	68.3E^o	25.36N^o
(14) Orinoco	954,701.3	Pte Angostu/Venezuela	63.6W^o	8.15N^o
(15) Tocantins	858,704.1	Tucurui/Brazil	49.67W^o	3.76S^o
(16) Danube	804,912.2	Ceatal Izma/Romania	28.73E^o	45.22N^o
(17) Mekong	798,977.0	Pakse/Laos	105.8E^o	15.11N^o
(18) Huanghe*	783,467.0	Gaocung/China	114.92E^o	35.23N^o
(19) Columbia*	720,784.9	Dalles/USA	121.17W^o	45.61N^o
(20) Brahmaputra	654,168.5	Bahadurabad/Bangladesh	89.67E^o	25.18N^o
(21) Colorado*	623,895.7	Hoover Dam AZ-NV/USA	114.74W^o	36.02N^o
(22) Rio Grande*	613,377.5	Matamoros/USA	97.45W^o	25.88N^o
(23) Sao Francisco*	609,983.7	Traipu/Brazil	36.99W^o	9.98S^o
(24) Senegal	428,028.3	Dagana/Senegal	15.5W^o	16.52N^o
(25) Don	447,559.6	Razdorskaya/Russia	40.65E^o	47.53N^o
(26) Parnaiba	329,536.3	Porto Formo/Brazil	42.37W^o	3.46S^o
(27) Magdalena	268,867.1	Calamar/Colombia	74.92W^o	10.25N^o
(28) Churchill	265,078.0	Red Head Rapids/Canada	94.62W^o	58.12N^o
(29) Fraser	226,811.9	Hope/Canada	121.45W^o	49.38N^o
(30) Huaihe	216,636.4	Bengbu/China	117.37E^o	32.94N^o

Human interventions on river discharge have become an important issue that attracted much attention. Dam construction, for example, has been found to affect the seasonality of downstream river discharge in many studies (Cowell and Stoudt, 2002; Ye *et al.*, 2003; Iles and Hegerl, 2015), and can also decrease the amplitude of annual river discharge (Iles and Hegerl, 2015). One extreme example demonstrated in Iles and Hegerl (2015) is the dam effect on the discharge in Nile River (see Section 3 and Figure S2 in their Supplementary Information). The Aswan Dam not only reduced the seasonality and the annual discharge amplitude of the Nile River, but also flattened the interannual variability beginning around 1965 when the first phase of dam construction was completed. Human interventions like this may contaminate the river discharge data, reducing its usefulness for studies of the natural variability induced by El Niño events.

To investigate whether there are significant human interventions in our dataset, the time series of river discharge for each of the thirty rivers are examined by looking for significant changes. Figure 3.3 shows the annual-mean (a, blue line) and monthly (b, red line) time series of the river discharge since 1950 for all the thirty rivers selected for this study. The annual-mean river discharge is calculated according to the water year (i.e. October(0)-September(1)). The five rivers (out of 30; 17%) may suffer from the dam effect due to significant decreases in their annual discharge cycle. These five rivers are: Huanghe, Columbia, Colorado, Rio Grande, and Sao Francisco. The dam effect on these rivers is also reflected in their annual discharge values, except for the Columbia River. For example, the magnitude of annual Rio Grande discharge became small and stayed at low after 1992, indicating its interannual variability may be damped out by upstream dam construction. These rivers also have high values (larger than 20) of the Regulation Index (RI, Nilsson *et al.*, 2005), which is a measure of the ratio of the live capacity of

all dams within a river basin to its annual discharge. It is noticed that from Figure 3.3 rivers with large drainage areas, such as the Amazon, Congo, Mississippi Rivers, and Amur, tend to be less influenced by the dam effect and have low RI values (less than 20). Therefore, human interventions may affect the river discharge data from the Huanghe, Columbia, Colorado, Rio Grande, and Sao Francisco Rivers but have little to no effect on rivers with large drainage areas. These five rivers are marked with a '*' symbol in the table and figures throughout this chapter to caution that the results may be altered by the human interventions.

3.3.2 Soil Moisture and Precipitation Datasets

To examine the land hydrological processes responsible for the variations in river discharge and their relationships with atmospheric forcing associated with different types of El Niño, monthly soil moisture and precipitation (including rainfall and snowfall) from 1950 to 2006 are obtained from Global Land Data Assimilation System version 2 (GLDAS2) dataset (Rodell *et al.*, 2004). The atmospheric forcings in GLDAS2 are based on Sheffield *et al.* (2006). There are four soil layers in the GLDAS2 data set with the lower boundaries at 10 cm, 50 cm, 100 cm, and 200 cm, respectively. The soil moisture and precipitation anomalies are defined as the deviations from the 1950 to 2006 climatology. Also used for MRB precipitation dataset is the Parameter-elevation Regressions on Independent Slopes Model (http://prism.oregonstate.edu).

For global precipitation maps NOAA's PRECipitation REConstruction over Land (PREC/L, http://www.esrl.noaa.gov/psd/data/gridded/data.precl.html) dataset is used, which provides precipitation rates (in mm/day) from 1948 to 2015 with a 1×1 horizontal resolution over global continents (Chen *et al.*, 2002).

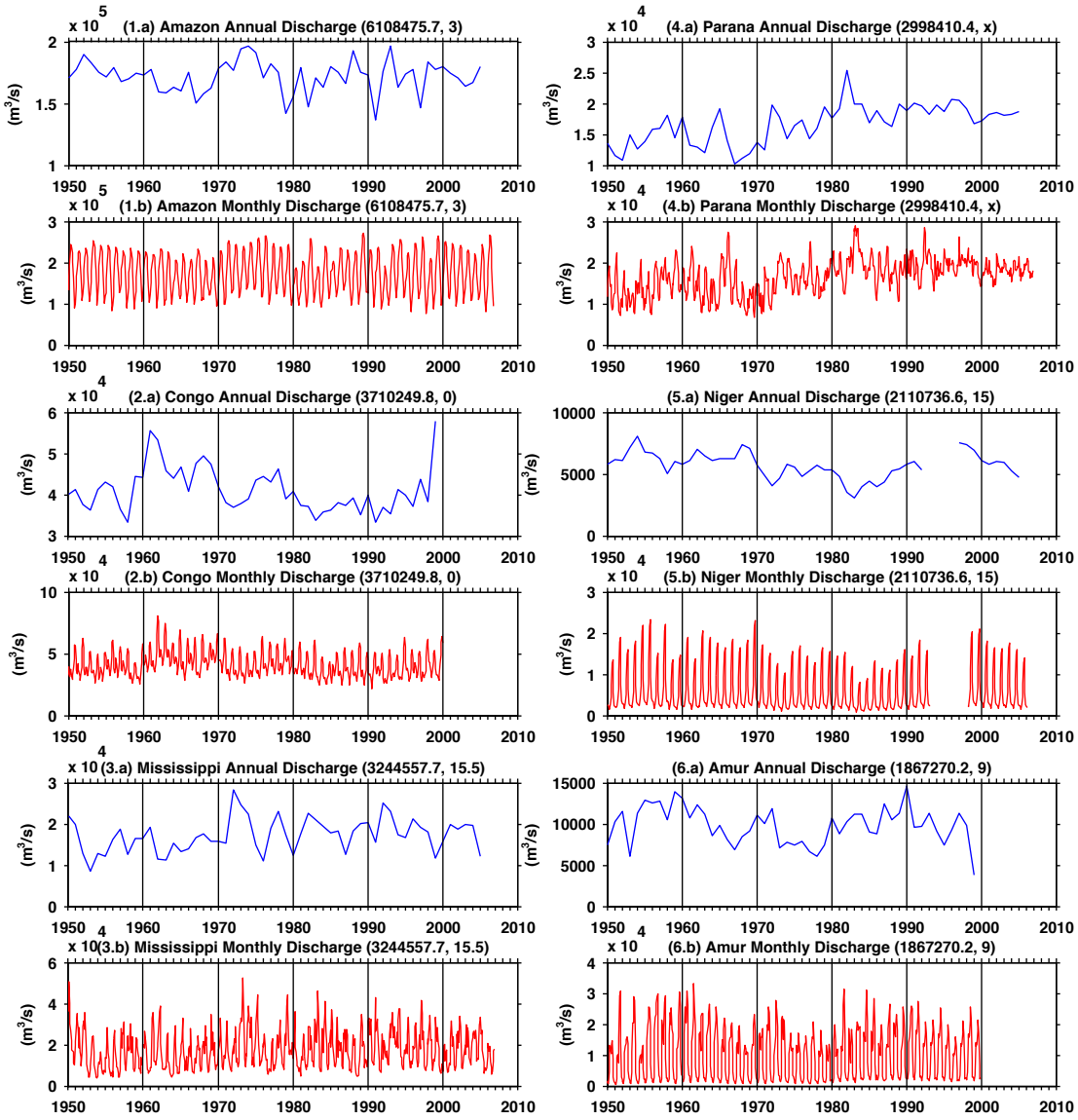

Figure 3.3 Time series of top thirty rivers selected in this chapter. The monthly discharge is delineated by red lines while the annual-averaged discharge are denoted by blue lines. The annual-averaged river discharge is calculated according to the water year (i.e. October(0)-September(1)). The first number in title parenthesis is the drainage area in the unit of km^2, and the second number is the Regulation Index (Nilsson *et al.* 2005). The '*' symbol after the river name denotes that this river may be influenced by human interventions.

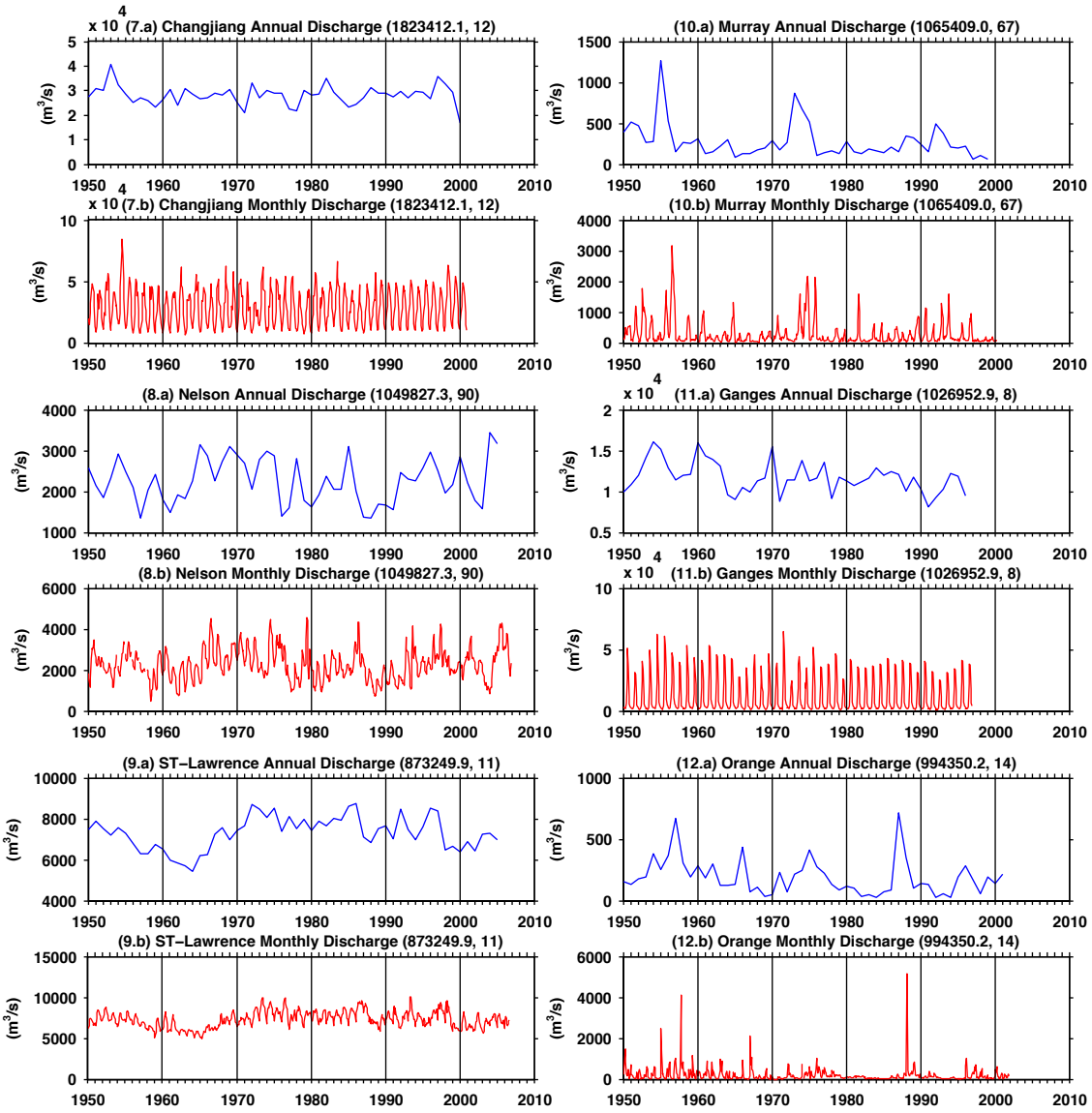

Figure 3.3 Continued.

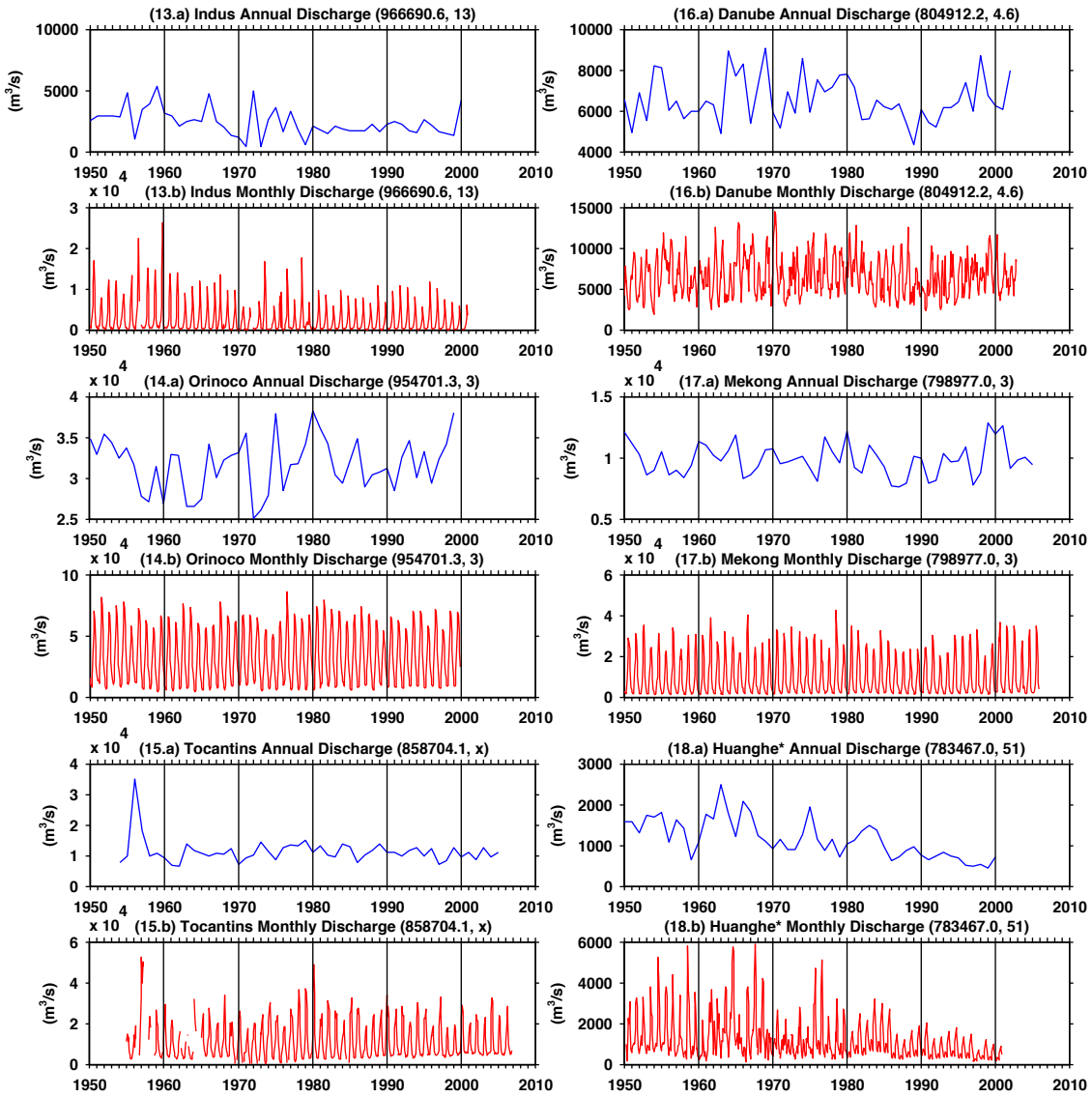

Figure 3.3 Continued.

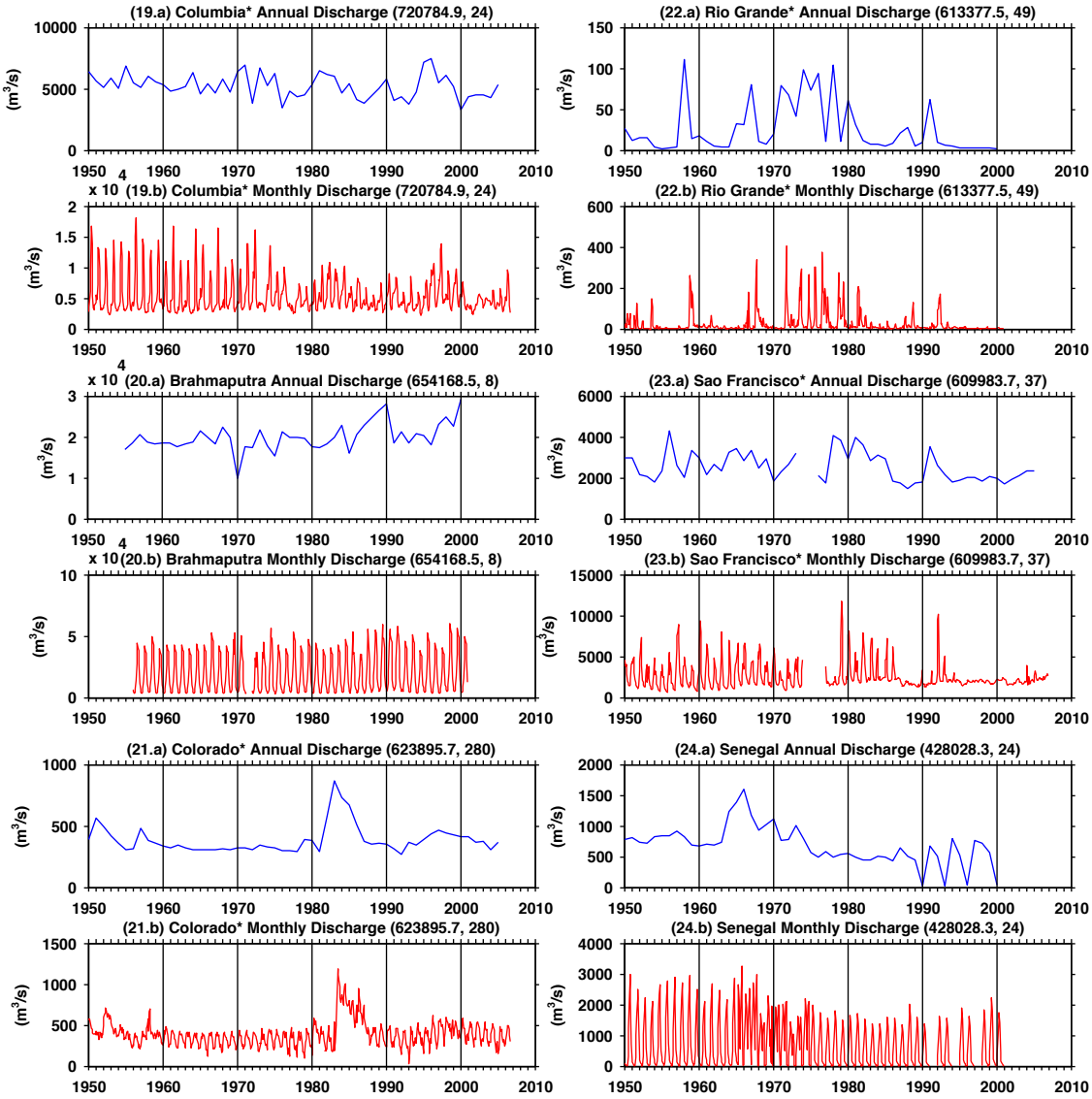

Figure 3.3 Continued.

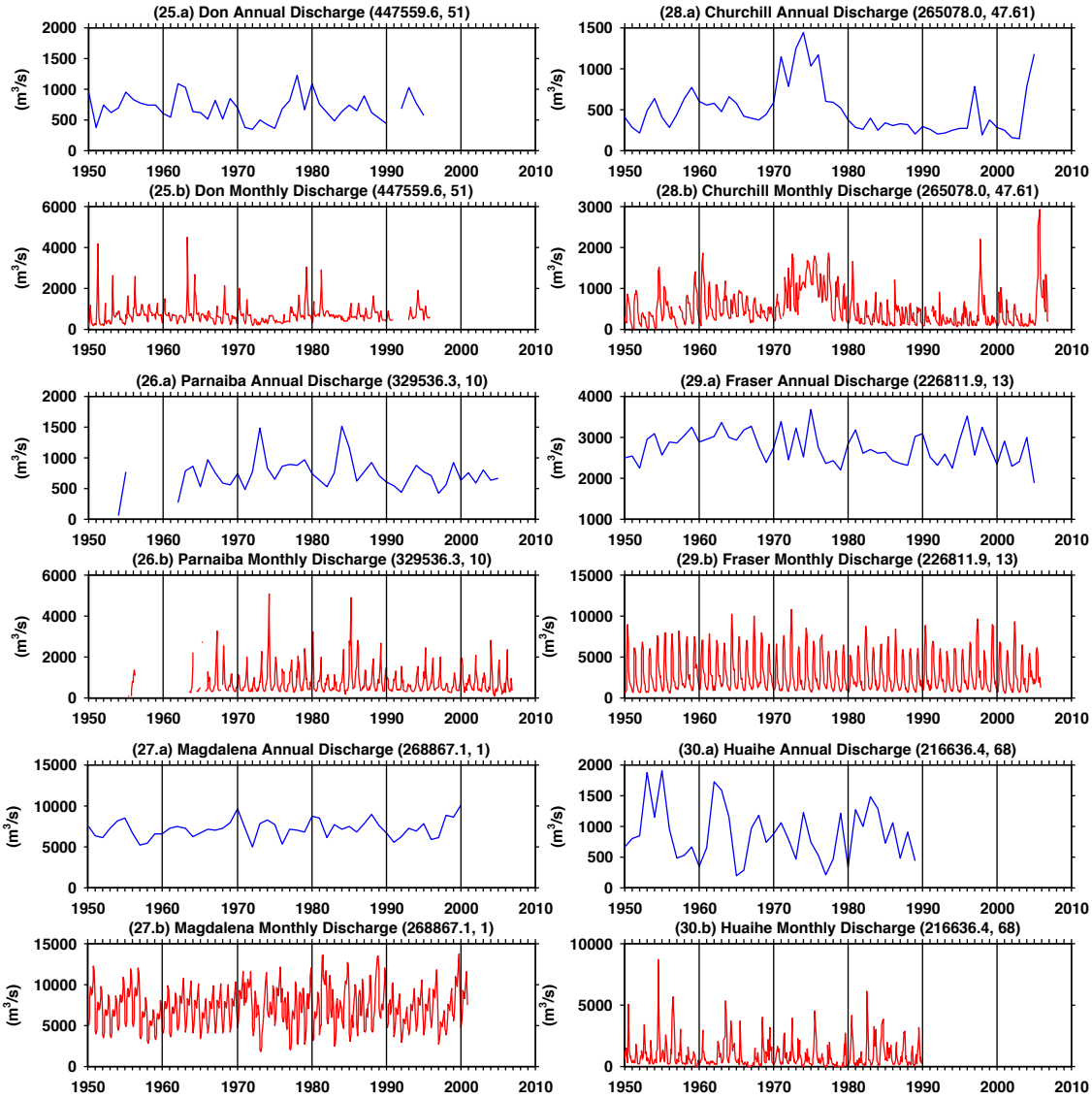

Figure 3.3 Continued.

3.3.3 Community Land Model Version 4 (CLM4)

The offline CLM4 simulation is driven by observed precipitation and other atmospheric forcings (downloaded from http://dods.ipsl.jussieu.fr/igcmg/IGCM/BC/OOL/OL/CRU-NCEP) without the inclusion of any anthropogenic influences, such as the dam effect. The CLM4 simulation is performed using prescribed forcing for the period 1950 to 2006. In this chapter, the observational river discharge results are used to compare the results obtained from the river discharge dataset with those obtained using the discharges simulated by an offline CLM4 simulation results. The comparisons can indicate whether the anthropogenic influences affect the river discharge data.

3.3.4 CP and EP El Niño Types

There are several different identification methods to determine whether an El Niño event is of the EP type or the CP type. Yu *et al.* (2012a) combined three different methods to define a "consensus El Niño type" for the major El Niño events occurring after 1950. These methods are the EP/CP-index method from Kao and Yu (2009), the Niño3 versus Niño4 method from Yeh *et al.* (2009), and the El Niño Modoki method from Ashok *et al.* (2007). During our analysis period, seven EP El Niño events (1951-1952, 1969-1970, 1972-1973, 1976-1977, 1982-1983, 1986-1987, and 1997-1998) and 12 CP El Niño events (1953-1954, 1957-1958, 1958-1959, 1963-1964, 1965-1966, 1968-1969, 1977-1978, 1987-1988, 1991-1992, 1994-1995, 2002-2003, and 2004-2005) are identified for analyses. These CP and EP El Niño events are indicated in Figure 3.2 and are used to construct discharge and precipitation composites for analysis. The lifecycle of El Niño is divided into three phases: the developing phase (i.e. May(0)-September(0)), the mature phase (i.e. October(0)-February(1)), and the decaying phase (i.e. March(1)-July(1)). Here, (0)

means the calendar year that an El Niño event begins to develop, and (1) denotes the year immediately following.

3.3.5 Asymmetric Response (AR) and Symmetric Response (SR) of River Discharge

To determine if a river basin produces an SR pattern or an AR pattern to the two types of El Niño is as follows. If the composite discharge anomalies are of the same sign for more than three months in one El Niño phase (i.e., for more than 50% of the phase), that river basin is regarded as producing an SR pattern to the two types of El Niño during that particular El Niño phase. If during three months or more in that phase, the EP composite anomalies are above-normal while the CP composite anomalies are below-normal, the river basin is considered to produce an 'AR+' pattern. Conversely, the reversed anomaly situation is referred to as an 'AR-' pattern.

3.3.6 Statistical Analysis

To test the statistical significance of the discharge anomalies composited for the two types of El Niño, a two-tailed Student's *t*-test is performed. Due to the limited numbers of EP and CP Niño events available for the composites, the test is applied to the composite anomalies averaged in the developing, mature, and decaying phases of the El Niño. The null hypothesis of the test is that the phase-averaged discharge anomalies are zero at the 90% significance interval. If the composite anomalies for a particular phase pass the significance test for either the EP or CP El Niño, we consider the discharge anomalies during that phase for that river to be statistically significant.

3.4 Asymmetric Responses of Mississippi River Discharge

The Mississippi River discharge (at Vicksburg, Mississippi) is first examined using the global river discharge data set from Dai *et al.* (2009). The monthly river discharge from January to June after El Niño events reach their peak intensities are composited based on the seven EP El Niño and twelve CP El Niño events. The composites are shown and compared in Figure 3.4 with the discharge climatology. Figure 3.4 shows that the discharge climatology (black solid line) increases from January, reaches its peak in April, and then gradually declines. During the EP El Niño (blue solid line), the MRB discharge is significant above normal after March. During the CP El Niño (red solid line), the river discharge is below normal throughout January to June, and the largest difference occurs in April, about 20% less than the climatological volume. In contrast, the largest difference during the EP El Niño occurs in May, about 28% more than the climatological value. These two types of El Niño cause the MRB discharge to fluctuate in a range of about half of the climatological discharge amount, which is profound. If the El Niño impact is not stratified according to the El Niño type, the discharge composite for all the nineteen El Niño events is near or moderately below normal (see the green solid line in Figure 3.4). This pattern differs from findings from previous studies (e.g., Twine *et al.*, 2005) and most likely results from the calculation method used here which includes more CP El Niño events occurring in the recent decades.

Figure 3.4 also shows that the negative discharge anomalies produced by the all El Niño composite are at most only half of the anomalies produced by the CP El Niño. The analysis indicates that a stronger and clearer impact of El Niño on the MRB discharge can be demonstrated when the El Niño type is considered. Also, the difference in discharge between the

two types of El Niño are found to be most statistically significant in March, April, and May, indicating that the two types of El Niño produce the most different impacts on the springtime MRB discharge. It is noted that the MRB discharge during the developing phase of El Niño is also investigated but no significant difference between the CP and EP El Niño is found (not shown).

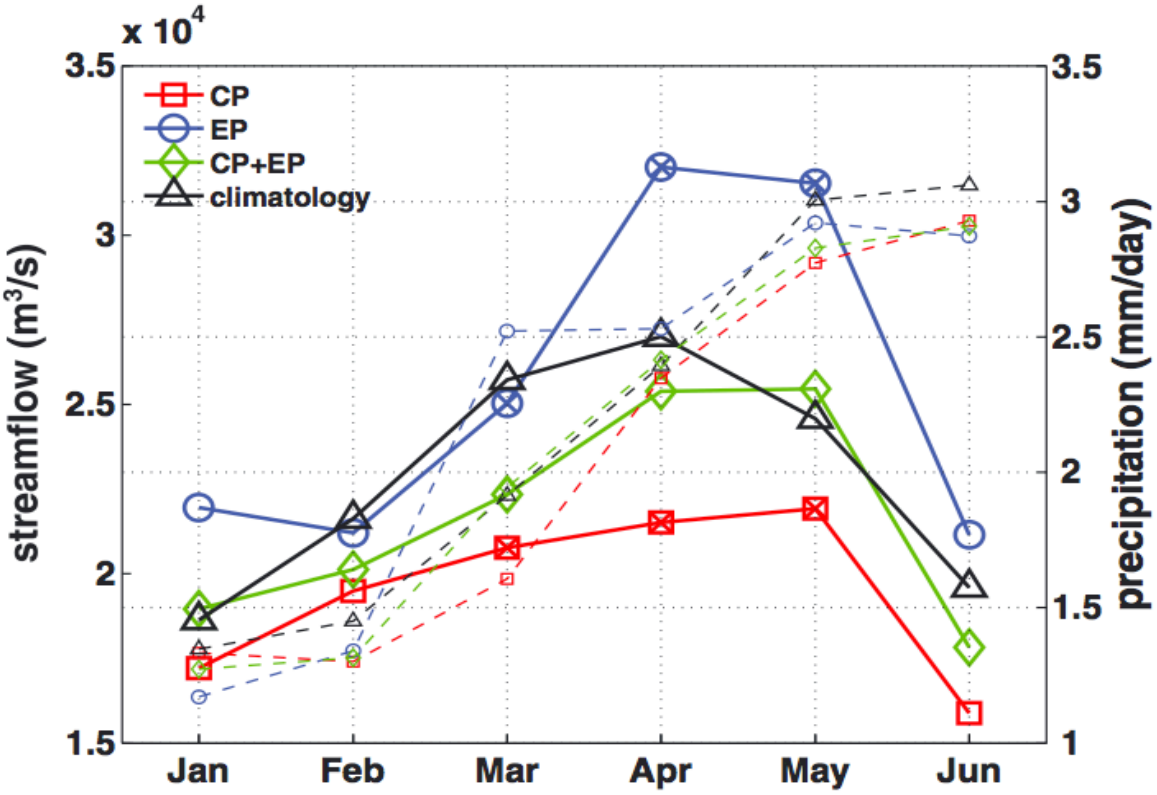

Figure 3.4 Monthly Mississippi River discharge gauged at Vicksburg, USA. The climatology discharges calculated from 1950 to 2006 are shown by the black line, while the discharges are shown in red for the CP El Niño composite, in blue for the EP El Niño composite, and in green for the all-El Niño composite. The "cross" indicates that the difference in discharge between the CP and EP El Niño composites is statistically significant. The dashed lines show area-averaged precipitation in MRB.

The asymmetric response of the river discharge between the CP and EP El Niño years is likely to be related to the patterns of precipitation and the evolution of total soil water storage in the MRB. The area-averaged precipitations (dashed lines in Figure 3.4) have revealed the linkage between precipitation and the MRB discharge, in which, the most significant change in precipitation is in March, and the most significant change in discharge is in April and May. To understand how the asymmetric river discharge responses are produced, the evolutions of the monthly precipitation and total soil moisture anomalies from GLDAS2 dataset are examined in Figure 3.5. The regions where the anomalies are 90% statistically significant are dotted. Similar results (not shown) are obtained when the analysis is repeated with another precipitation data from the Parameter-elevation Regressions on Independent Slopes Model (http://prism.oregonstate.edu). The strongest precipitation anomalies in the MRB are observed in early spring (March through April), when above-normal precipitations first prevail over most of the central MRB and then move to eastern MRB. In late winter (January and February), negative precipitation anomalies are observed over the Ohio-Mississippi Valley and in late spring and earlier summer (May and June) over the southern MRB, but their magnitudes are relatively small and confined to specific areas.

When EP El Niño occurs, the total soil moisture (sum of the four soil layers above 200 cm depth) anomalies show an overall wetness in the MRB from January to June (Figures 3.5(g)–3.5(l)). The wet soil anomalies in January and February are in fact associated with the positive precipitation anomalies that occur during the late autumn and earlier winter of the previous year (i.e., the developing phase of El Niño; results not shown). The largest soil moisture anomalies are observed in the western MRB from March to May, which occur up to two months after the largest precipitation anomalies are produced in the region. Wet soil anomalies actually can still

be found in the MRB until June. The evolution of precipitation in Figures 3.5(a)–3.5(f) and soil moisture in Figures 3.5(g)–3.5(l) indicate that there is a two to three month lag in total soil moisture response to the above-normal precipitation anomalies induced by the EP El Niño in the MRB.

During the CP El Niño, a different picture emerges when the evolution of precipitation and soil moisture anomalies are examined. First of all, negative precipitation anomalies (Figures 3.5(m)–3.5(r)) persist throughout January to June in the MRB. The negative anomalies have the largest magnitudes from February to March, which is consistent with the finding of Yu and Zou (2013) that the CP El Niño produces a stronger winter drying effect over the Ohio-Mississippi River valley than the EP El Niño does. They attributed this enhanced drying effect of the CP El Niño to the more southward displacement of the tropospheric jet streams that steer the movements of winter storm over the U.S. The second difference appears in the lagged response of the total soil moisture to the precipitation anomalies. As can be seen from Figures 3.5(s)-3.5(x), below-normal soil moisture were accumulated in the MRB during the CP El Niño, which is expected from the below normal precipitation induced by the CP El Niño. Besides, a shorter lag relationship between the soil moisture anomalies and the precipitation anomalies is observed, reflecting the weaker precipitation anomalies in magnitude during the CP El Niño. Statistically, significant dry soil moisture anomalies in the MRB are observed only in March and April, despite the relative large negative precipitation anomalies in February and March. Apparently in the MRB, dry precipitation anomalies have a less-persistent impact on soil moisture than the impact produced by the wet precipitation anomalies during the EP El Niño.

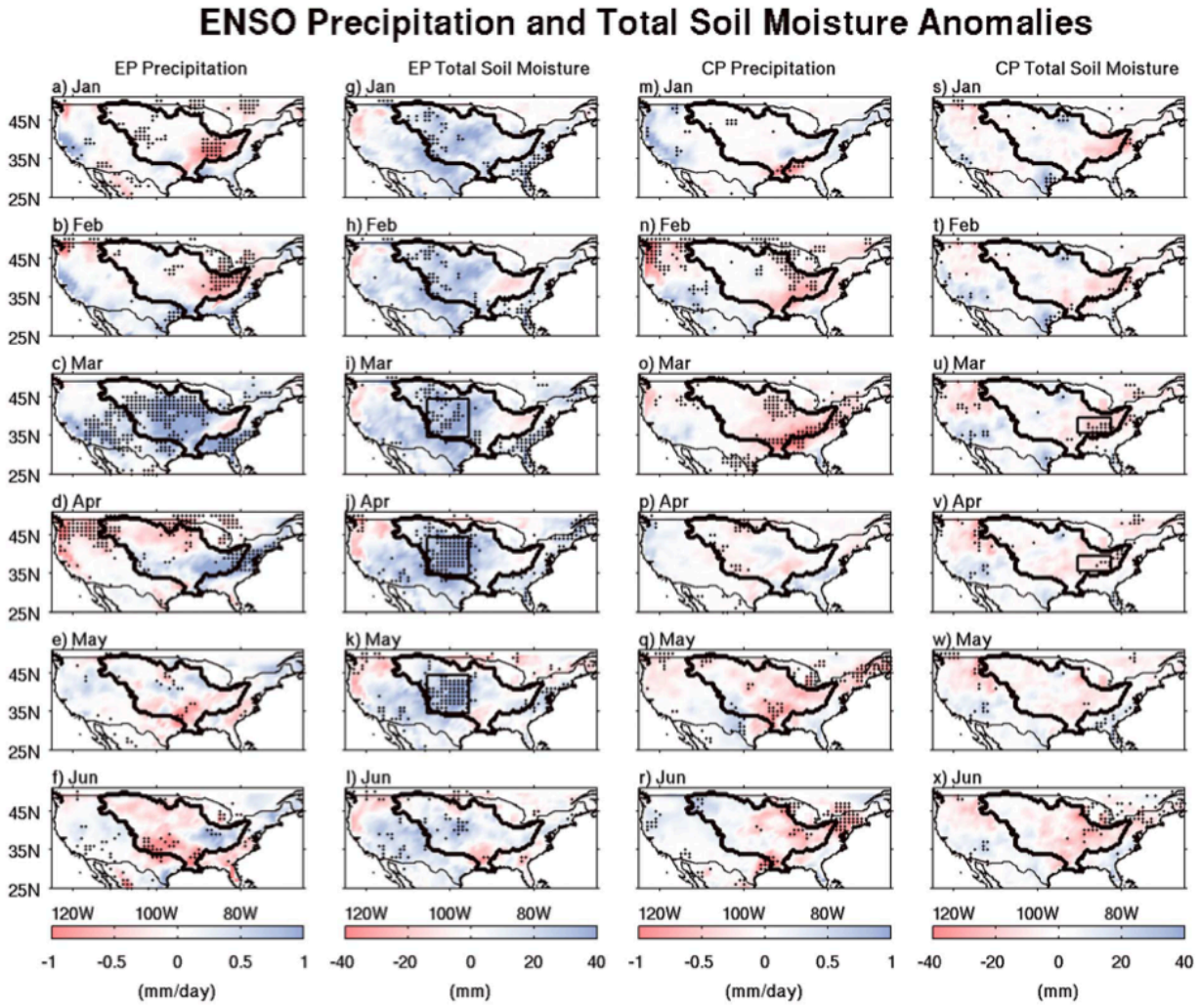

Figure 3.5 January to June precipitation (millimeter/day) and total soil moisture (millimeter) anomalies during the EP and CP El Niño. The two left columns show the composited for the CP El Niño events (for (a–f) precipitation anomalies and for (g–l) total soil moisture anomalies), and the two right columns show the composite for the CP El Niño (for (m–r) precipitation anomalies and for (s–x) total soil moisture anomalies). Statistically, significant results are dotted. The thick black line delineates the boundary of MRB. The rectangular boxes in Figures 3.5(i)–3.5(k) cover 95°–105°W and 34°–45°N, while the ones in Figures 3.5(u)–3.5(v) cover 80°–90°W and 35°–40°N.

3.5 Subsurface hydrological processes

To illustrate the relationship between precipitation anomalies in March and total soil water storage in the subsequent months, the correlations between the March precipitation anomalies and the total soil moisture anomalies are compared from March to June. The correlation is calculated in a rectangular box in 95°-105°W and 34°-45°N for the EP El Niño composite and a box in 80°-90°W and 35°-40°N for CP El Niño composite as indicated in Figures 3.5(i) and 3.5(u), respectively. As shown in Figure 3.6(a), the correlation coefficient for the EP El Niño composite increases from March to May, implying that the water from the intense positive precipitation anomalies in March is stored and accumulated in the central and western MRB, corresponding to the lag response of total soil water storage shown in Figure 3.6. On the other hand, the positive correlation coefficients for the CP El Niño composite only increase from March to April, reflecting a lag of about one month after the maximum negative precipitation anomaly occurs in March. In other months the correlation coefficient becomes weaker, implying fewer impacts from the weak negative precipitation anomalies during CP El Niño.

In addition to the total soil moisture, which soil depth the precipitation anomalies can impact the soil moisture is also considered. Figure 3.6(b) shows the correlation coefficients between the March precipitation anomalies and soil moisture anomalies at different soil layer depths during the EP El Niño. The figure indicates that the positive precipitation anomaly in March penetrates to the surface soil layers in April, including layer L1 (0-10 cm) and L2 (10-40 cm). In May, the influence of precipitation anomalies is no longer confined to surface soil layers but reaches layer L4 (100-200 cm). Deep soil layers are known to play an important role in producing lagged responses to atmospheric forcing, which significantly affects the slow response

component of river discharge (or groundwater flow) (e.g., Niu *et al.*, 2005; Yeh and Eltahir, 2005; Lo *et al.*, 2008). The vertical penetration of water in the soil can be viewed as a transport of precipitation signals from surface to deeper layers, showing the restoration of El Niño signals in the land memory effect. Similar vertical propagation of soil water can be seen in CP El Niño in Figure 3.6(c), but the signal cannot persist longer than one month because of the relative weaker negative precipitation anomalies. Also, the dry precipitation anomalies can only penetrate to the layer of L2 during the CP El Niño.

Above analyses of the soil moisture storage explain why the MRB discharge responds differently to the two types of El Niño. During EP El Niño events, positive precipitation anomalies in early spring can penetrate to a deep layer of soil to enhance soil water storage in April and May over the central and western MRB. This two to three months lagged increase in the total soil water storage is then reflected as an increase in the MRB discharge. On the other hand, CP El Niño events cause negative precipitation anomalies that penetrate only to a shallower layer of soil in the eastern portion of MRB with a shorter lag of one to two months. The decreased content in the total soil water storage then leads to reduced discharge rate in the subsequent one–two months. Evaporation and the snow melt effect can also contribute to changes in discharge when CP and EP El Niño events occur. However, the region of significant snow melt in the U.S. occurs outside the northern MRB, and the evaporation is relatively small during the spring season; hence, they have limited effects on the results shown in this chapter.

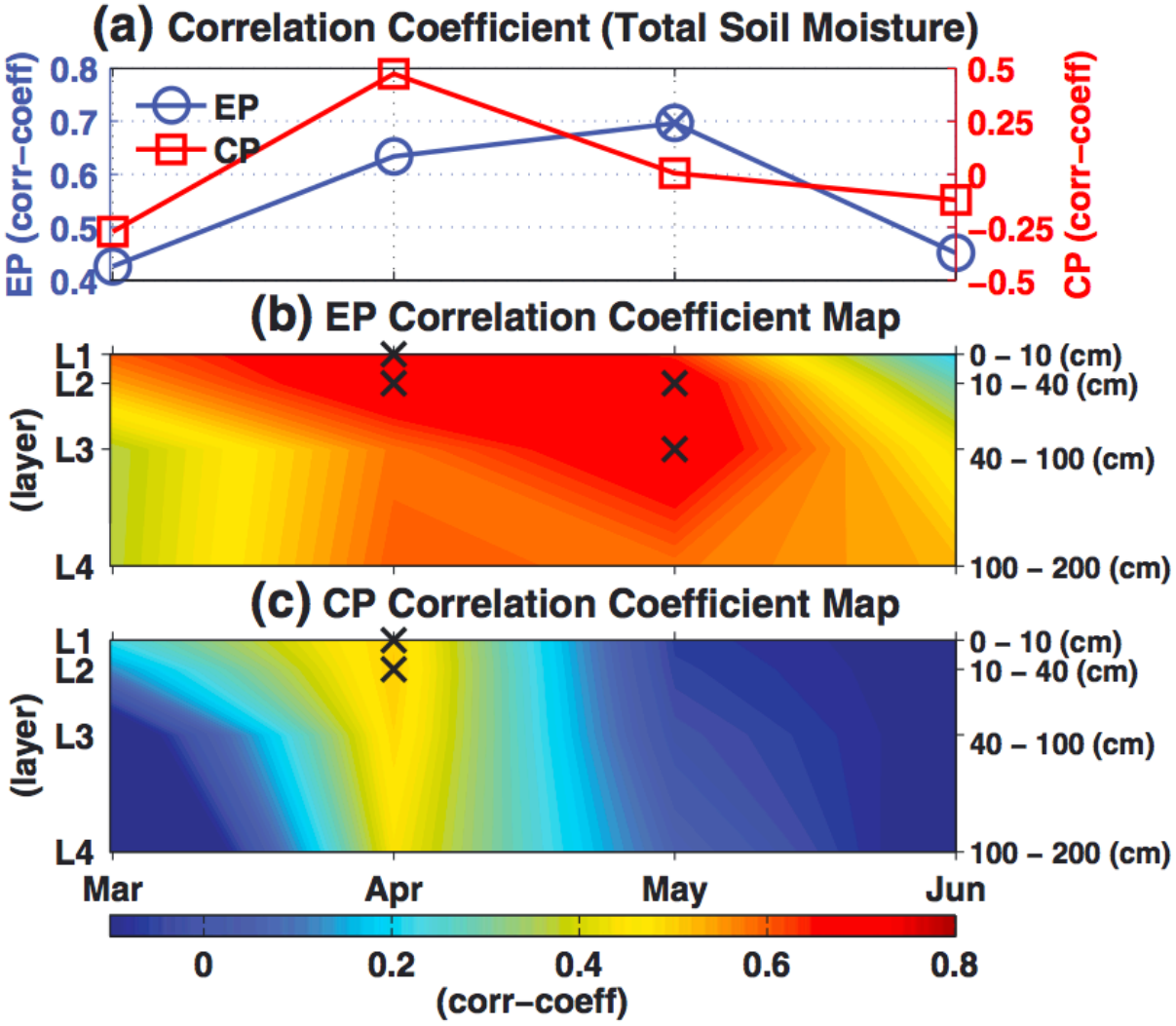

Figure 3.6 (a) Correlation coefficients between March precipitation anomalies and total soil moisture anomalies in the subsequent months calculated from the CP El Niño composite (red squares with respect to right, red y-axis) and the EP El Niño composite (blue circles with respect to left, blue y-axis). Correlation coefficients between March precipitation anomaly and soil moisture anomalies in different layers are shown in (b) the EP El Niño composite and in (c) the CP El Niño composite. The regions chosen for all these calculations are shown in Figure 3.5(i) for the EP El Niño and in Figure 3.5(u) for the CP El Niño. The symbol "cross" (X) shown in Figures 3.6(a), 3.6(b), and 3.6(c) denotes the significant point with p value less than 0.1.

3.6 Mapping Reponses of Global River Discharge to Two Types of El Niño

3.6.1 Response Patterns of River Discharge to the Two Types of El Niño

To stratify the global river responses to the two types of El Niño, Figure 3.7 shows the discharge anomalies composited for the EP and CP El Niño for each of the thirty selected rivers. The significance tests indicate that, among the ninety total phases (i.e., thirty rivers times three El Niño phases per river), fifty-seven of them have discharge anomalies that pass the 90% two-tailed significance test. Based on this, a large fraction (i.e., 57 out of 90; 63%) of the discharge anomalies in Figure 3.7 is considered statistically significant.

At first glance, four rivers (i.e., the Danube, Mekong, Murray, and Parnaiba) in Figure 3.7 show an obvious and persistent SR pattern to the two types of El Niño throughout the El Niño lifecycle: their discharge anomalies in the EP and CP composites always (or almost always) have the same signs. Below-normal discharge is found in these rivers during El Niño years, regardless of the El Niño type. Another five rivers show an obvious and persistent AR pattern; these are the Mississippi, ST-Lawrence, Churchill, Niger, and Don rivers. For the first three, their discharge is mostly above normal during the EP El Niño but below normal during the CP El Niño (i.e., AR+). In contrast, the last two rivers (the Niger and Don) have above normal discharge during the CP El Niño but below normal discharge during the EP El Niño (i.e., AR-). For the remaining twenty-one rivers, their composite anomalies fluctuate among SR, AR+, and AR- during various phases of the El Niño lifecycle.

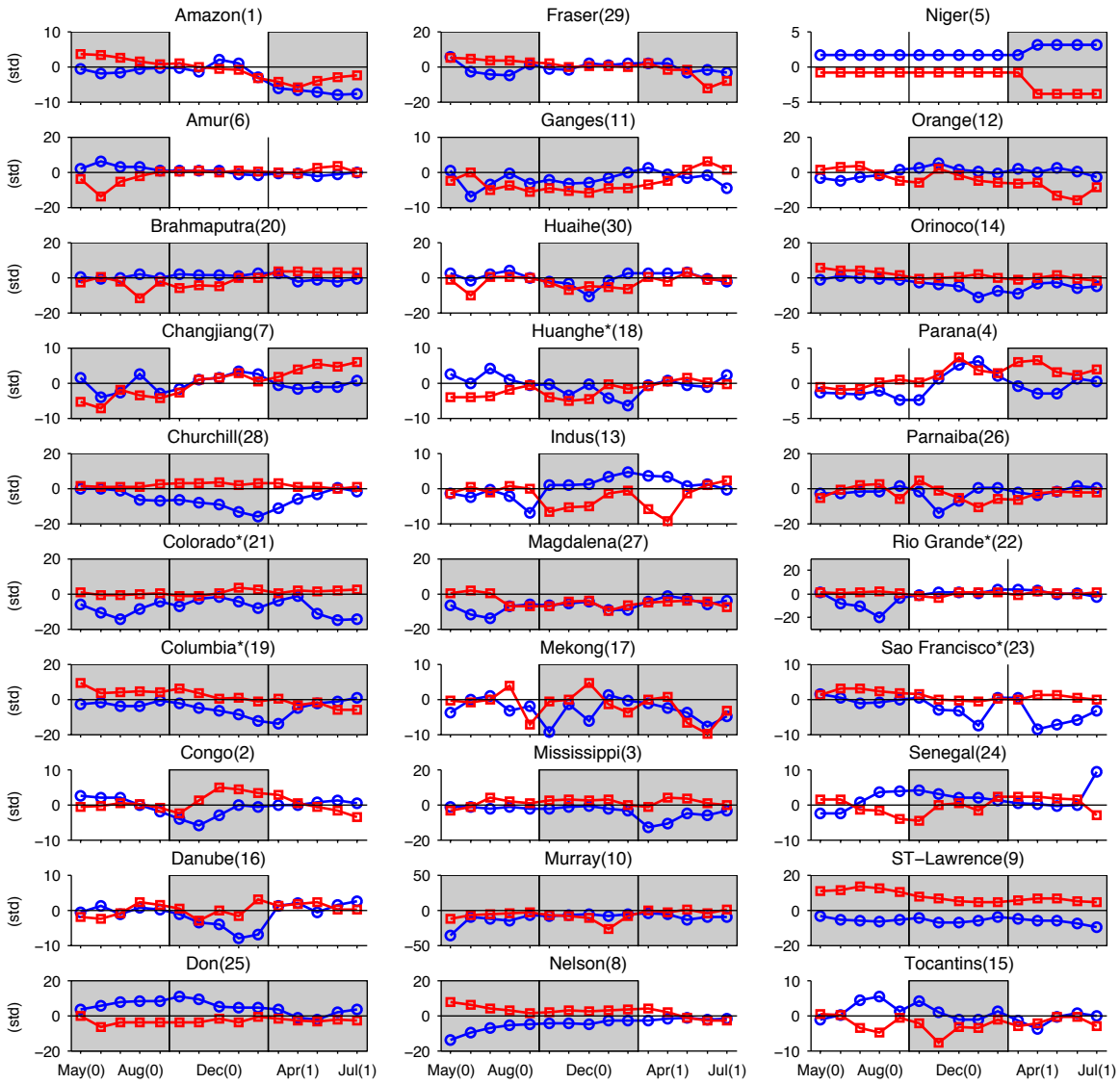

Figure 3.7 Composite monthly discharge anomalies for the EP El Niño (red) and CP El Niño (blue) for the thirty selected rivers. The discharge anomalies have been normalized by the standard deviation of the discharge calculated for that particular river basin for each particular calendar month. The normalization was performed to account for the fact that the magnitude of discharge variations varies from basin to basin. Rivers are listed in alphabetical order. The number in the parenthesis denotes the ranking of the drainage area size as shown in Figure 3.2. The values shown are the discharge anomalies from zero in each river basin. Gray areas indicate the one or both of the CP and EP averaged discharge anomalies (to zero) in that phase pass the 90% significance level of a two-tailed Student's *t*-test. Note that the y-axis scale is different for each river basin. The '*' symbol after the river name denotes that this river may be influenced by human interventions.

3.6.2 Global Mapping of the Response Patterns

In order to examine whether there is a geographical dependence of the river discharge response to the two types of El Niño, Figure 3.8 shows the global distribution of the SR, AR+, and AR- patterns during the developing, mature, and decaying phases of the El Niño. The response pattern in each phase is determined using the method described in Chapter 3.3.5. Based on Figure 3.8, the response patterns are more uniform and persistent over North America, where the AR+ response pattern appears in most river basins and the response pattern does not change through the various phases of El Niño. Therefore, large rivers in North America tend to produce above-normal discharge during the EP type of El Niño but below-normal discharge during the CP type. This AR pattern indicates that El Niño type is important to the discharge variations for most large rivers in North America.

The global map in Figure 3.8 also reveals systematic response patterns in other continents. In South America, the response pattern is relatively simple. A majority of the rivers exhibit the AR+ pattern in the developing phase and the SR pattern for the rest of the El Niño lifecycle. This result indicates that the El Niño type should be considered for the South American rivers only in the developing phase. For the Danube River in Central Europe and the Murray River in Eastern Australia, the SR pattern persists throughout all three El Niño phases. Apparently, the discharge anomalies in these two river basins are not sensitive to El Niño type. The Don River in Eastern Europe, however, shows a persistent AR- pattern throughout the El Niño lifecycle.

The response patterns are more complicated for rivers in Asia and Africa, where the patterns tend to vary not only during different phases of the El Niño lifecycle but also from river to river. Nevertheless, some general tendencies can be identified from Figure 3.8. During the developing and mature phases (Figures 3.8(a) and 3.8(b)), the SR pattern dominates the river

basins in Asia, indicating that the El Niño type probably matters little for the discharge variations during these two phases. During the decaying phase, the AR+ pattern dominates in Asia (Figure 3.8(c)). As for Africa, the response is most consistent during the decaying phase of the El Niño, where the AR- pattern prevails for rivers in Africa as well as the Indus River.

To verify that the response patterns identified in Figure 3.8 are not due to possible measurement errors or human interventions, we conducted a forced model simulation with the CLM4 (Oleson *et al.*, 2010) to produce a river discharge dataset free of human interventions (see Chapter 3.3.3 for the details of the simulation). This CLM4 simulation is driven by the observed precipitation and other atmospheric forcings from 1901 to 2014; we only use the 1950–2006 simulated river discharge for analysis. In the simulation, no anthropogenic influence is included. The same mapping analyses are repeated using the simulated river discharge data, which show that the response patterns identified (Figure 3.9) are largely consistent with those identified from the observed discharge dataset (Figure 3.8), particularly for large river basins in the North and South Americas, Northeastern Asia, and Northern India.

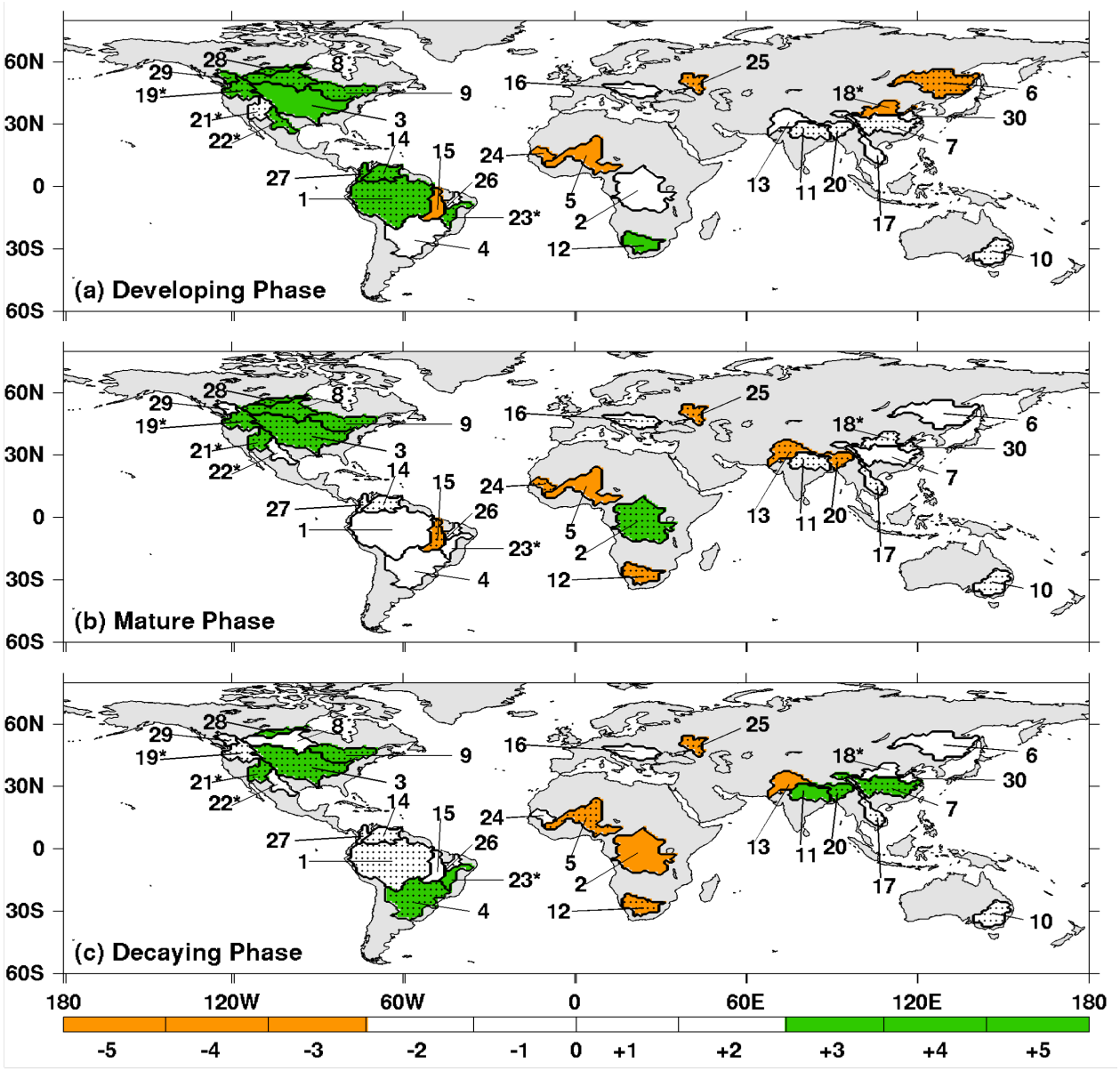

Figure 3.8 Discharge response patterns for global rivers during (a) the developing phase (May(0)-September(0)), (b) the mature phase (October(0)-February(1)), and (c) the decaying phase (March(1)-July(1)) of El Niño. The colors indicate the different response patterns for the thirty selected rivers: white for SR, green for AR+, and brown for AR-. The black numbers correspond to the river basins listed in Figure 3.2. The '*' symbol after the number denotes that this river may be influenced by human interventions. The numbers under the colorbar represent the number of months in each phase showing an asymmetric response. The negative (positive) sign in front of the numbers indicates the AR- (AR+) response pattern. '0' implies a symmetric response. Discharge anomalies in each phase of EP and CP El Niño that pass 90% Student's *t*-test following Figure 3.7 are stippled.

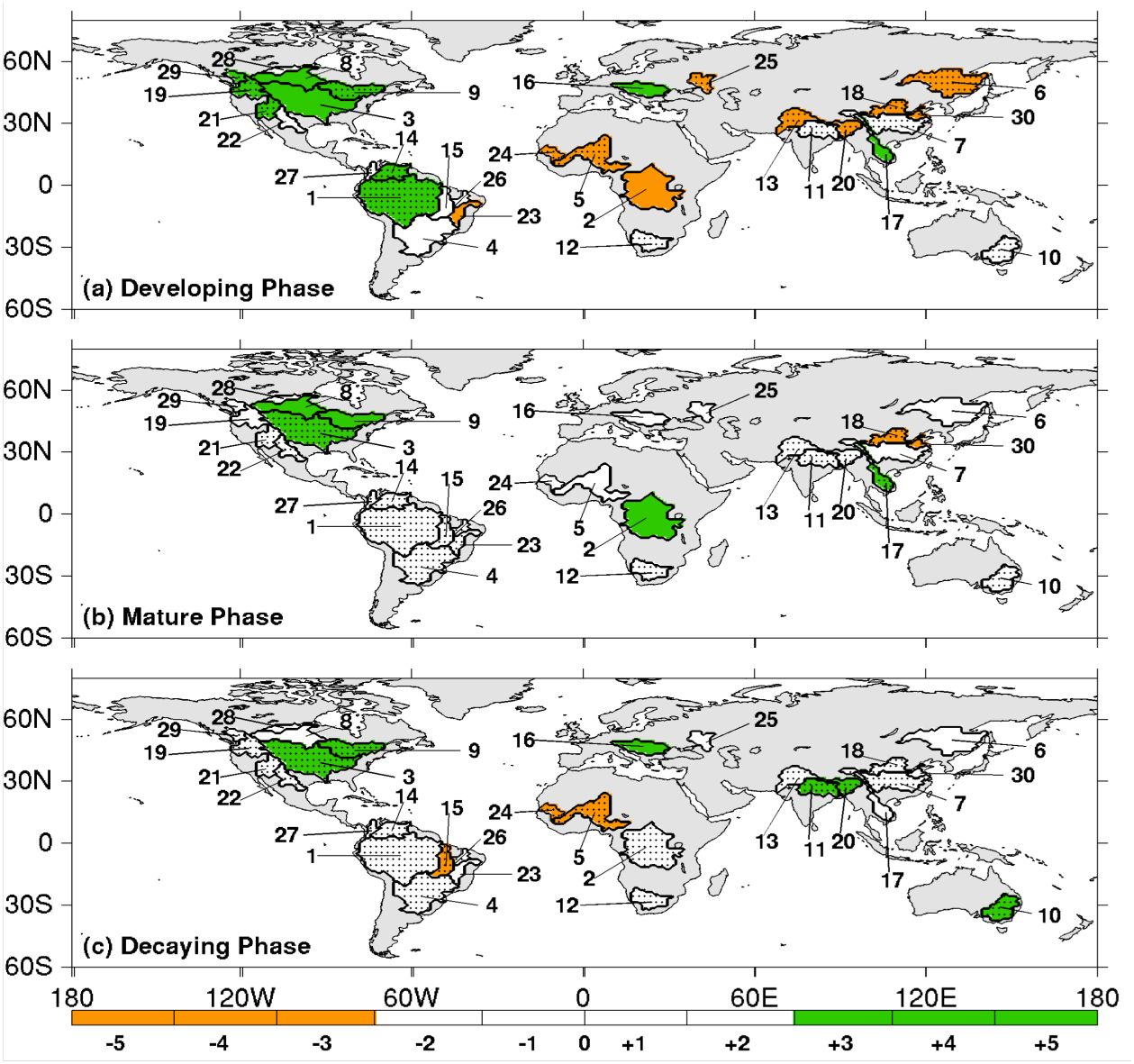

Figure 3.9 Similar to Figure 3.8 but using CLM4 simulation river discharge data.

3.6.3 The Linkage between River Discharge and Precipitation

Precipitation has been identified as the major freshwater input into a river basin (Gerten *et al.*, 2008, Milliman *et al.*, 2008, Dai *et al.*, 2009). To examine the possible relationship between precipitation and discharge anomalies during the three phases of El Niño, Figure 3.10 displays the phase-averaged precipitation anomalies in each river basin separately for the two types of El Niño. When the signs of precipitation anomalies match the signs of discharge anomalies for both types of El Niño in one phase, that phase is marked with a '(v)' symbol. Taking the Amur River as an example, its discharge response pattern can be explained by the precipitation anomalies in all three phases. The Amur River basin experiences below-normal precipitation during the developing phase of the EP El Niño but above-normal precipitation during the CP El Niño. This is consistent with the AR- discharge anomaly pattern identified in Figure 3.8(a) for the developing phase. For the mature and decaying phases, the SR patterns shown in Figures 3.8(b) and 3.8(c) can also be explained by the identically signed precipitation anomalies as seen in Figure 3.10.

Examining the symbols in Figure 3.10, we find seventeen rivers (57%) show consistent discharge and precipitation variations during at least two phases of El Niño. For these rivers, the discharge response patterns may be explained by the precipitation anomalies within the river basins during the two types of El Niño. These seventeen rivers are: the Amazon, Amur, Brahmaputra, Changjiang, Churchill, Danube, Fraser, Ganges, Huaihe, Indus, Magdalena, Mekong, Mississippi, Murray, Niger, Orinoco, and Paraná. It is worth noting that this group includes almost all the largest-drainage rivers on every continent, such as the Mississippi for North America, the Amazon for South America, and the Changjiang for East Asia. Due to their large drainage areas, it is reasonable that their discharge variations have strong linkages to

variations in the precipitation within the river basins. The only exception is the Congo River, which is the largest river in Africa but whose discharge response patterns cannot be explained by local precipitation anomalies. For other rivers, the inconsistencies between the discharge and precipitation anomalies may be due to time lags between these two variables caused by land surface processes (e.g. Lo and Famiglietti, 2010). Dettinger and Diaz (2000) found that the lags between peaks of precipitation and river discharge can vary from one geographic location to another. The results presented in Figure 3.10 provide a first-order linkage between El Niño-induced precipitation and river discharge, further studies considering lagged responses are required to fully elucidate the precipitation-discharge relationships, which remain for future works.

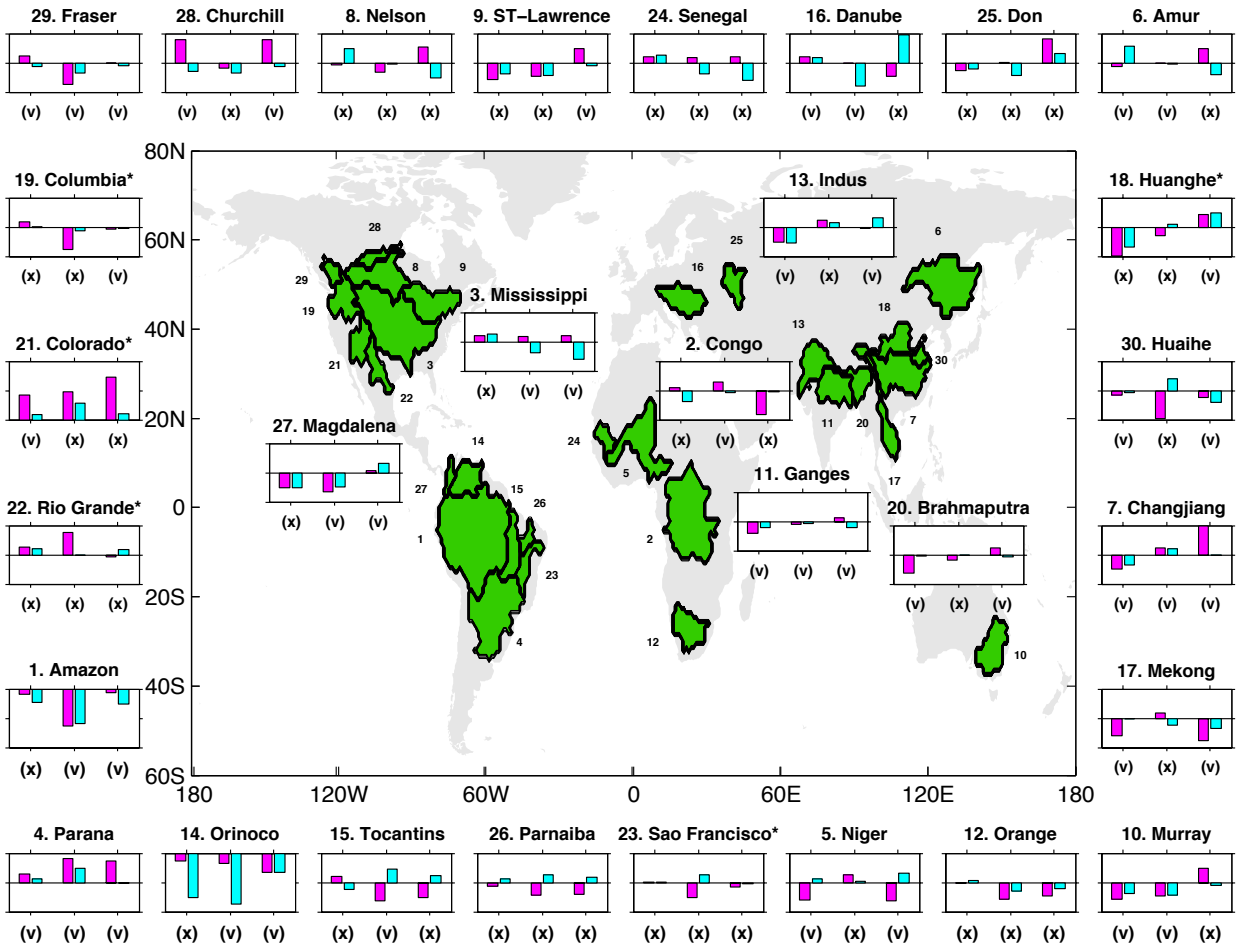

Figure 3.10 Composite precipitation anomalies for the EP (pink bars) and CP (light blue bars) El Niños during their developing (left-most pair of bars), mature (middle pair), and decaying phases (right-most pair). The bar shows precipitation anomalies, calculated by averaging precipitation anomalies in each phase. The check '(v)' indicates that the sign of precipitation anomalies matches the sign of the discharge anomalies, whereas the check '(x)' indicates that the signs do not match. The '*' symbol after the river name denotes that this river may be influenced by human interventions.

3.7 Summary and Discussion

The El Niño and La Niña have been found to cause asymmetric responses of tropical precipitation along the equator (Chou and Lo, 2007). This chapter further shows that even in the same warm phase of ENSO, changes in the location of El Niño can cause significantly different responses in soil water storage and discharge in the MRB. Eltahir and Yeh (1999) discussed the nonlinear behavior of groundwater discharge on aquifers water level, which can explain the mechanism of soil water restoration. Without land subsurface hydrological storage, the impacts of EP/CP El Niño cannot persist from earlier spring (or late winter), when El Niño events typically peak and their impacts on the U.S. are the strongest, to the subsequent seasons. These findings indicate that including the role of the memory of subsurface land hydrological processes in future empirical or numerical modeling studies (e.g., Lo and Famiglietti, 2011) will be necessary to better explore the relationships analyzed in this chapter.

The location of El Niño has gradually shifted from the eastern Pacific to the central Pacific during the recent two decades. Yu and Zou (2013) have already shown that the altered atmospheric circulation tends to enhance negative precipitation anomalies in the MRB when CP El Niño occurs. This study further indicates that the negative precipitation anomalies can decrease the total soil water content in the western MRB (Figure 3.11), which can lead to a reduced river discharge in the Mississippi River. Consistent results are also found in offline simulations with the Community Land Model version 4 using the same GLDAS2 atmospheric forcings, indicating that our results are model-independent (Figure 3.9). Although in general, the strength of CP El Niño is not as strong as that of EP El Niño, the overall drier land conditions and reduced river discharge could pose water shortages or severe drought and threaten agricultural water supplies in the central U.S., which greatly affect North American hydroclimate.

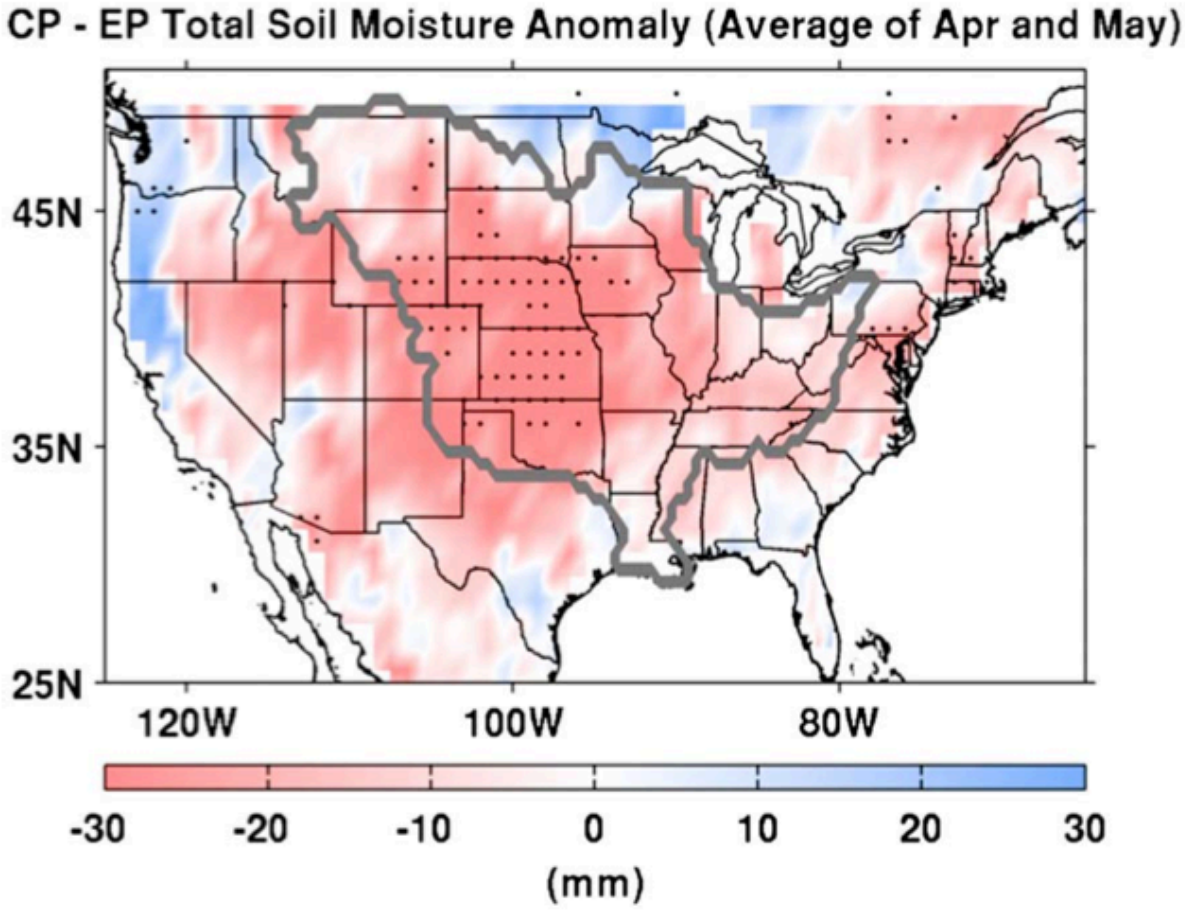

Figure 3.11 Difference in total soil moisture (averaged from April to May) between CP El Niño and EP El Niño. Statistically significant results are dotted.

The global distributions of asymmetric and SRs in river discharge to the EP and CP types of El Niño during their developing, mature and decaying phases are also mapped in this chapter. A few conclusions can be drawn from this work. It is found that the discharge response patterns tend to be geographically dependent. Large rivers on the American continents show more persistent and simple response patterns throughout the various phases of the El Niño lifecycle, which are possibly caused by different atmospheric teleconnection patterns induced by different types of El Niño. The Mississippi River basin, for example, Liang *et al.* (2014), have offered a

mechanism to explain the AR+ pattern, which involves the excitation of the Pacific North American pattern or the Tropical Northern Hemisphere pattern (Yu *et al.*, 2012b; Zou *et al.*, 2014) by the two types of El Niño, and results in different impacts on precipitation and land-hydrology processes (Lo and Famiglietti, 2010).

On the other hand, rivers in Asia and Africa show complex response patterns that vary from river to river and from phase to phase. It is well-known that El Niño events can induce Indian Ocean SST variations that can persist into the decaying phase of El Niño via Indian Ocean dynamics and local ocean–atmosphere coupling (e.g. Wang *et al.*, 2000; Xie *et al.*, 2009). Such an extended or delayed El Niño influence appears to be stronger during the EP El Niño than during the CP El Niño (see Figure 4 of Yu *et al.*, 2017). This difference may cause the rivers in Africa and parts of the India to respond differently to the two types of El Niño in their decaying phases. In addition, Kao and Yu (2009) have shown that, during the decaying phase, CP El Niño SST anomalies diminish locally in the CP while the EP El Niño SST anomalies retreat to the South American Coast. These very different locations of the SST anomalies can affect the Pacific Walker circulation and the regional Hadley circulation differently, leading to ARs in Asian rivers. The Danube River in Central Europe and the Don River in Eastern Europe, and the Murray River in Eastern Australia show persistent responses throughout different phases of El Niño. Future studies are required to understand why their response patterns are not sensitive to different flavors of the El Niño.

Local precipitation variations within the river basins are one important factor determining the discharge response pattern for rivers that have large drainage areas. For some other rivers, the discharge response patterns cannot be explained solely by local precipitation variations. Other factors, such as the lagged response of discharge to precipitation, volcanic

eruptions (Iles and Hegerl, 2015), and the dam effect (see Chapter 3.3.1 for discussions), need to be invoked. While we did not identify these factors explicitly, we are able to identify a group of rivers whose discharge variations are linked to precipitation variations and another group whose precipitation and discharge variations show less consistent patterns. This identification highlights the location of rivers whose discharge variation mechanisms require further study.

It has been reported that El Niño changed from the EP to the CP type in the early 1990s (Yu *et al.*, 2012b; Yu *et al.*, 2015). The mapping produced in this chapter offers an overview of which global rivers may have experienced changes in their discharge variation patterns during the past two decades. By considering the El Niño type, the El Niño impacts on river discharge can be more accurately identified. For example, the El Niño impacts in the river basins that produce the AR patterns may be mistakenly considered insignificant if the impacts from the two types of El Niño are lumped together. New or different strategies may be needed to project and manage their discharge in the coming decades if the CP type of El Niño continues to dominate. Traditional ways of utilizing climate predictions (i.e., seasonal El Niño forecasts) for river flow management and agriculture planning may have to be revised.

It should be cautioned that the discharge data analyzed in this chapter may still be influenced by human interventions and measurement errors in unidentified means. Although we have made efforts to reduce the possible impacts via screening the data and repeating the analyses with a model simulation, the findings reported here should be taken with the data limitations and caveats in mind.

CHAPTER4

Synchronization of the Pacific Warm Blob and Atlantic Cold Blob

4.1 Abstract

During 2013-2015, prolonged near-surface warming in the northeastern Pacific was observed and has been referred to as the Pacific warm blob. In this chapter, statistical analyses are conducted to show that the generation of the Pacific warm blob is closely related to the tropical Northern Hemisphere (TNH) pattern in the atmosphere. When the TNH pattern stays in its positive phase for extended periods of time, it generates prolonged blob events primarily through anomalies in surface heat fluxes and secondarily through anomalies in wind-induced ocean advection. Five prolonged (>24 months) blob events are identified during the past six decades (1948-2015), and the TNH-blob relationship can be recognized in all of them. Although the Pacific decadal oscillation and El Niño also induce an arc-shaped warming pattern near the Pacific blob region, they are not responsible for the generation of Pacific blob events. The essential feature of Pacific blob generation is the TNH-forced Gulf of Alaska warming pattern. This study further finds that the atmospheric circulation anomalies associated with the TNH pattern in the North Atlantic can induce sea surface temperature variability akin to the so-called Atlantic cold blob, also through anomalies in surface heat fluxes and wind-induced ocean advection. As a result, the TNH pattern serves as an atmospheric conducting pattern that

connects some of the Pacific warm blob and Atlantic cold blob events. This conducting mechanism has not previously been explored.

4.2 Introduction

The term 'Pacific warm blob' (Bond *et al.*, 2015) was coined to refer to the remarkably warm water mass in the northeastern (NE) Pacific that persisted during 2013-2015. At its peaks during the winter of 2014 and summer of 2015, the positive sea surface temperature (SST) anomalies in the warming region reached as high as 2^{o}-3^{o}C and penetrated as deep as 180 meters below the ocean surface (Bond *et al.*, 2015; Hu *et al.*, 2017). This patch of warm water then propagated from the Gulf of Alaska toward the coastal regions, resulting in an arc-shaped warming off the North American coasts during the following winter (Amaya *et al.*, 2016; Di Lorenzo and Mantua, 2016; Gentemann *et al.*, 2017). This Pacific warm blob event exerted pervasive impacts on coastal ecosystems, North American climate, and air quality. Examples of the Pacific blob impacts include a profound species range shift in the Gulf of Alaska (Medred, 2014), dramatic changes in the marine productivity in the NE Pacific (Whitney, 2015; Siedlecki *et al.*, 2016), a delay in the onset of the upwelling off California coasts (Peterson *et al.*, 2015; Zaba and Rudnick, 2016), and altered springtime air temperatures (Bond *et al.*, 2015) and ozone concentration (Jaffe and Zhang, 2017) in the Pacific Northwest of the United States (U.S.). Intensive efforts have been expended on attempts to understand the causes of this unusual marine heatwave phenomenon (Di Lorenzo and Mantua, 2016).

Studies of the 2013-2015 Pacific warm blob event have largely agreed that the warming was generated by an unusually persistent ridge system in the atmosphere over the NE Pacific region (Seager *et al.*, 2014; Swain *et al.*, 2014; Wang *et al.*, 2014; Bond *et al.*, 2015; Hartmann,

2015; Seager *et al.*, 2015; Amaya *et al.*, 2016; Di Lorenzo and Mantua, 2016; Swain *et al.*, 2016; Hu *et al.*, 2017). This anomalous high-pressure system can induce clockwise surface wind anomalies that work against the prevailing surface westerlies to reduce local surface evaporation and weaken cold ocean advection in the NE Pacific, giving rise to the Pacific warm blob (Bond *et al.*, 2015). Atmospheric circulation patterns that have an anomaly center close to or encompassing the location of this anomalous ridge are possibly involved in the generation of the Pacific blob. A list of such patterns includes at least the Pacific-North American (PNA) pattern (Wallace and Gutzler, 1981), the North Pacific Oscillation (NPO) pattern (Rogers, 1981), and the tropical Northern Hemisphere (TNH) pattern (Mo and Livezey, 1986). Among them, the NPO and PNA patterns have been invoked to explain how the Pacific blob evolved from the Gulf of Alaska (GOA) warming pattern to the arc-shaped (ARC) warming pattern during the 2013-2015 event (Amaya *et al.*, 2016; Di Lorenzo *et al.*, 2016; Di Lorenzo and Mantua, 2016). The possible role of the TNH pattern has not been examined in past Pacific blob studies.

Concurrent with the 2013–2015 Pacific warm blob event, a region of persistently below-normal SSTs was observed in the North Atlantic. This cooling event is referred to as the Atlantic cold blob (Henson, 2016) or the Atlantic warming hole (Rahmstorf *et al.*, 2015) to emphasize the fact that this is the most prominent area in global oceans that has cooled in the face of a prevailing warming trend in global oceans (Henson, 2016; Robson *et al.*, 2016). The Atlantic cold blob was also suggested to affect downstream European climate (Duchez *et al.*, 2016). Several mechanisms have been proposed to explain the generation of the Atlantic cold blob, including atmospheric forcing associated with the North Atlantic Oscillation (NAO; Delworth *et al.*, 2016; Yeager *et al.*, 2016), an ocean circulation change linked to the Atlantic meridional overturning circulation (AMOC; Rahmstorf *et al.*, 2015; Robson *et al.*, 2016; Duchez

et al., 2016), and the melting of the Greenland ice sheet (Schmittner *et al.*, 2016). The general perspective of the scientific community at this point is to consider the Atlantic and Pacific blobs as two separate phenomena that are driven by different mechanisms. However, the coincident occurrence of the 2013-2015 Atlantic cold blob and Pacific warm blob events raises the possibility that some fraction of such Atlantic and Pacific blob events may be linked by atmospheric circulation patterns that have a cross-basin structure (i.e., from North Pacific to North Atlantic). If such a pattern exists, it can serve as a mechanism to induce climate connectivity between the North Pacific and North Atlantic sectors, some of which may be manifested as the co-occurrence of Pacific and Atlantic blob events.

In this chapter, reanalysis products are analyzed to show that the atmospheric circulation pattern associated with the generation of the Pacific blob closely resembles the TNH pattern. The mechanisms through which the TNH pattern generates the Pacific warm blob and the roles of the Pacific decadal oscillation (PDO) and El Niño-Southern Oscillation (ENSO) play in the evolution of the Pacific warm blob are discussed. The possible connection between the Pacific blob and the Atlantic blob events is then examined. Some implications for the Pacific-Atlantic climate connectivity and the possible mechanisms that give rise to the TNH pattern are also discussed.

4.3 Data and Methods

4.3.1 Atmospheric Datasets

In this chapter, Atmospheric wind fields, 200-hPa, 500-hPa, and 700-hPa geopotential heights (hereafter Z200, Z500 and Z700 respectively), and sea level pressure (SLP) are from the National Centers for Environmental Prediction (NCEP)-National Center for Atmospheric

Research (NCAR) reanalysis dataset (Kalnay *et al.*, 1996). Anomalies during the analysis period (1948-2015) are defined as deviations from the 1981-2010 climatology. These fields can be downloaded from the NCEP–NCAR reanalysis dataset website (http://www.esrl.noaa.gov/psd/data/gridded/data.ncep.reanalysis.derived.html). The linear trends are removed from these fields before performing the analyses. Similar results are obtained when these trends are retained (not shown).

4.3.2 Oceanic Datasets

The SST data used in this chapter are from the Hadley Centre Sea Ice and Sea Surface Temperature dataset (Rayner *et al.*, 2003) and can be downloaded from the Met Office Hadley Centre Observations Datasets (http://www.metoffice.gov.uk/hadobs/hadisst/data/download.html). Mixed layer temperatures, surface heat fluxes, and ocean currents are from the NCEP Global Ocean Data Assimilation System (GODAS, Behringer *et al.*, 1998). GODAS products can differ from real observations due to the assimilation framework that includes model simulation results (Xue *et al.*, 2011; Kumar and Hu, 2012). However, they are capable of capturing the general features of surface oceanic conditions and are used here to study the blob generation. Anomalies during the analysis period (1948-2015) are defined as deviations from the 1981-2010 climatology. The linear trends are removed from these fields before performing the analyses. Similar results are obtained when these trends are retained (not shown). The net surface heat flux and ocean currents are downloaded from the NOAA GODAS website (http://www.esrl.noaa.gov/psd/data/gridded/data.godas.html).

4.3.3 Climate Indices

Several indices are used in this chapter for analyses. Following Bond *et al.* (2015), the Pacific blob index is calculated as the SST anomalies averaged within the box bounded by 40°-50°N and 150°-135°W. This blob box encompasses the 'point' used in Amaya *et al.* (2016) to delineate the Pacific blob warming feature and is also covered by the two boxes used in the blob study of Di Lorenzo and Mantua (2016) to depict SST pattern shifts during 2014-2015. The Atlantic cold blob index is defined as minus one (e.g., -1) times the SST anomalies averaged within the box bounded by 44°-56°N and 45°-25°W, which is close to the SST cooling region studied by Rahmstorf *et al.* (2015). This index is used to characterize the Atlantic cold blob variability. The Niño-3.4 index is used to represent ENSO activity. Monthly indices for PNA, NAO, and TNH patterns were downloaded from the NOAA Climate Prediction Center (http://www. cpc.ncep.noaa.gov/data/teledoc/telecontents.shtml). The PDO index is obtained from NOAA's Earth System Research Laboratory website (https://www.esrl.noaa. gov/psd/data/correlation/pdo.data). The NPO index is calculated as the second-leading principal component of SLP anomalies over the North Pacific sector following Yu and Kim (2011).

4.3.4 The TNH Pattern and the TNH Index

The TNH pattern has been identified as an important atmospheric circulation mode of the Northern Hemisphere (NH) winter season in many studies (Esbensen, 1984; Mo, 1985; Mo and Livezey, 1986; Barnston and Livezey, 1987; Panagiotopoulos *et al.*, 2002; Franzke and Feldstein, 2005; Peng and Kumar, 2005). The TNH circulation anomalies are suggested to produce anomalous surface temperatures and precipitation throughout the North American continents, subtropical North Pacific, and North Atlantic (for a comprehensive description, see http://www.cpc.ncep.noaa.gov/data/teledoc/tnh.shtml). Correlation-based analyses were first

used to identify the TNH mode (e.g., Mo, 1985; Mo and Livezey, 1986), but these methods can suffer from difficulties in separating the TNH mode from other atmospheric circulation modes, especially when they co-occur. To avoid the possible mixture of different modes, a rotated empirical orthogonal function (REOF) analysis was also used to better distinguish the TNH mode from others (e.g., Mo and Livezey, 1986; Barnston and Livezey, 1987). The TNH mode was identified in Barnston and Livezey (1987) as the fourth mode in January (explaining 9.8% of the total variance), the sixth mode in February (explaining 7.4% of the total variance), the ninth mode in November (explaining 4.9% of the total variance), and the ninth mode in December (explaining 6.3% of the total variance). These studies indicate that it is reasonable to identify the TNH pattern using the REOF method despite the fact that the pattern appears as a higher mode and explains less than 10% of the total variance.

In this chapter, the same REOF method of Barnston and Livezey (1987) are applied to monthly Z700 anomalies in the NH (20^{o}-90^{o}N) to identify the TNH pattern. The TNH pattern is identified as the ninth REOF mode, explaining 4.96% of the total variance, and its corresponding principal component is used as the TNH index in this chapter. A strong trend in the TNH index is not found and similar results can be obtained when applying the REOF analysis to the nondetrended Z700 fields. Our calculation is applied to all the data rather than just the NH winter months used in previous studies. To ensure our TNH calculation is correct, we first compared our TNH index to the NH winter (December–January-February (DJF)) values of the TNH index provided by NOAA's Climate Prediction Center. We found the correlation coefficients between them to be high for all three winter months (i.e., 0.74 for December, 0.86 for January, 0.86 for February, and 0.82 for the DJF average). Then the wintertime Z500 anomalies regressed onto NOAA's TNH index (Figures 4.1(a)-(d)) are compared to those regressed onto ours (Figures

4.1(e)-(h)) and find their pattern correlations to be high (i.e., 0.73 for December, 0.91 for January, 0.87 for February, and 0.92 for DJF average) over the study region (20^{o}-80^{o}N, 120^{o}E–20^{o}W). Lead-lagged regression analyses of Z700, Z500, and Z200 anomalies with these two indices also reveal similar temporal evolutions (not shown).

The seasonality in the TNH pattern by repeating the REOF analysis is also examined to each of the four seasons (Figures 4.1(i)-(l)). The TNH mode appears as the fifth mode in spring (explaining 7.35% of the total variance), the eighth mode in summer (explaining 4.98% of the total variance), the fifth mode in autumn (explaining 7.41% of the total variance), and the sixth mode in winter (explaining 8.06% of the total variance). This analysis confirms that the TNH pattern exists throughout the year and that it is strongest during winter/spring and weakest during summer.

To determine statistical significance in our correlation analysis, the effective number of degrees of freedom ($\tilde{N}$) is calculated following Bretherton *et al.* (1999):

$$\tilde{N} = N \bullet (1 - r_x r_y)/(1 - r_x r_y), \qquad (1)$$

where N is the sample size of the original time series, r_x and r_y are the lag-1 autocorrelations of the time series x and y that are being correlated. If correlation analysis is applied to filtered time series, the r_x and r_y are replaced by the lag-1 autocorrelations of the filtered time series x and y.

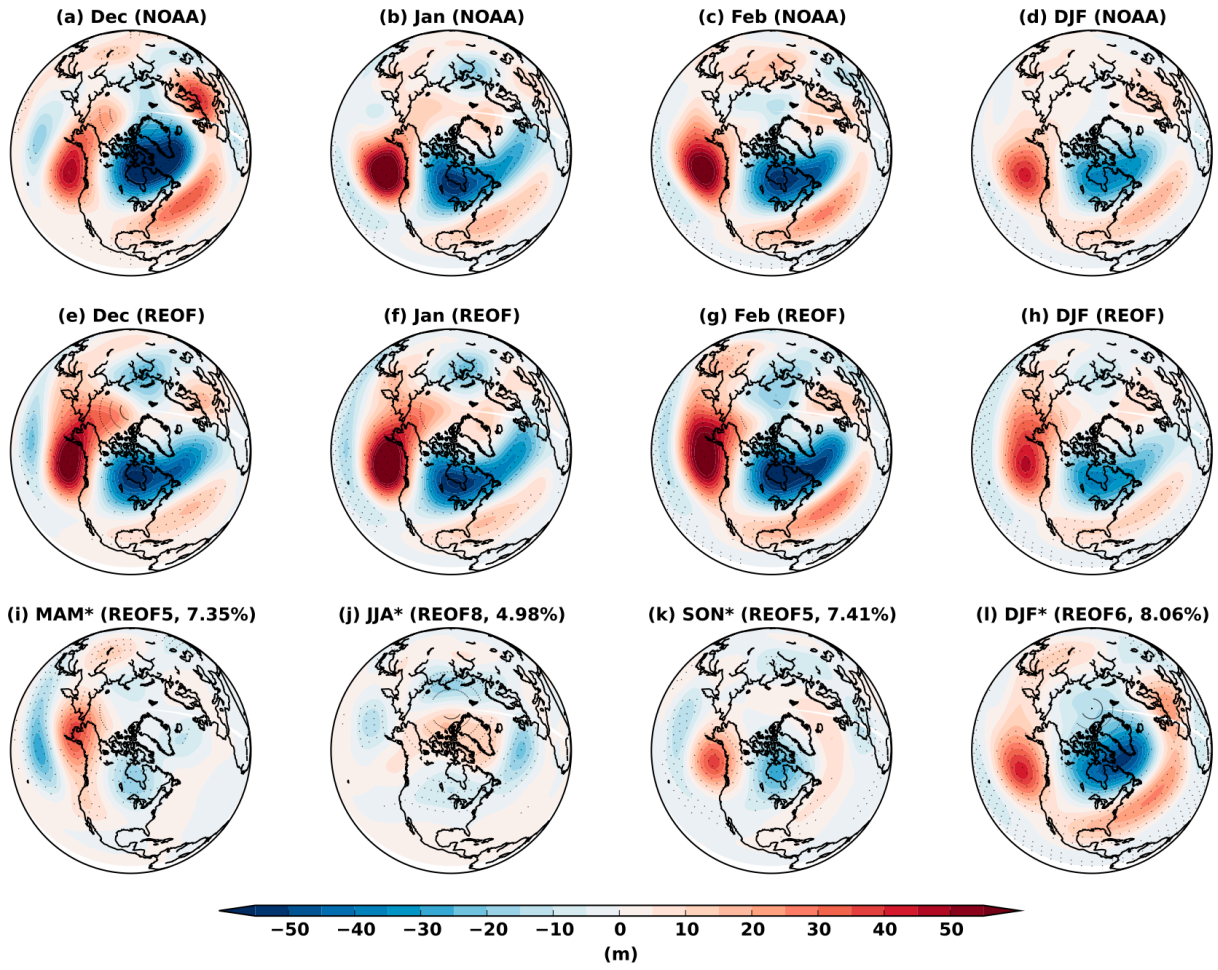

Figure 4.1 The 500-hPa geopotential height (Z500) anomalies regressed onto NOAA's TNH index for (a) December, (b) January, (c) February, and (d) the DJF average. (e)-(h) As in (a)-(d), but for our TNH index. (i)-(l) Regressed Z500 anomalies onto PCs derived from rotated EOF analysis separately for the different seasons. The numbers in the titles of (i)-(l) are the explained variance associated with each rotated EOF mode. The stippling indicates that the regression values are statistically significant (i.e., have *p* values less than 0.05).

4.4 The Relationship between the Tropical Northern Hemisphere (TNH) pattern and the Pacific Warm Blob

To investigate which large-scale atmospheric circulation pattern is closely associated with the Pacific blob, the Z500 anomalies are regressed onto the Pacific blob index. This regression pattern (Figure 4.2(a)) closely resembles the Z500 pattern regressed onto the TNH index (Figure 4.2(b)), both of which are characterized by a wave train structure with anomaly centers emanating from the subtropical Pacific and passing through the anomalous ridge region in the NE Pacific and a meridional dipole structure extending zonally from North American continents to the North Atlantic. In contrast, the PNA and NPO patterns (Figures 4.2(e) and (g)) show geographical features differing from the blob-regressed pattern. In the North Pacific sector, the wave train structure in the blob-regressed pattern is distinct from the meridional dipole structures in the PNA or NPO patterns. In the North Atlantic sector, the zonally elongated structure is absent in the PNA pattern and is almost orthogonal to the dipolar structure of the NPO pattern. To further verify the spatial similarities/differences, pattern correlation coefficients are calculated between the regressed Z500 pattern onto the Pacific blob index and those regressed onto the TNH, PNA, or NPO indices over the North Pacific-Atlantic sector (20^{o}-80^{o}N, 120^{o}E-20^{o}W). The pattern correlation coefficient for the TNH pattern (0.83) is much larger than those for the PNA (0.15) or NPO (0.48) patterns. Comparing the blob- and TNH-regressed SST anomaly patterns (Figures 4.2(e) and (f)), we also found both to be associated with large SST anomalies near the Pacific blob region that resemble the GOA warming pattern observed during the 2013-2015 blob event (e.g., Amaya *et al.*, 2016; Di Lorenzo and Mantua, 2016), but different from the PNA- and NPO-regressed SST anomalies (Figures 4.2(g) and (h)). It is obvious that the TNH pattern, not the PNA or NPO pattern, is the large-scale atmospheric circulation pattern

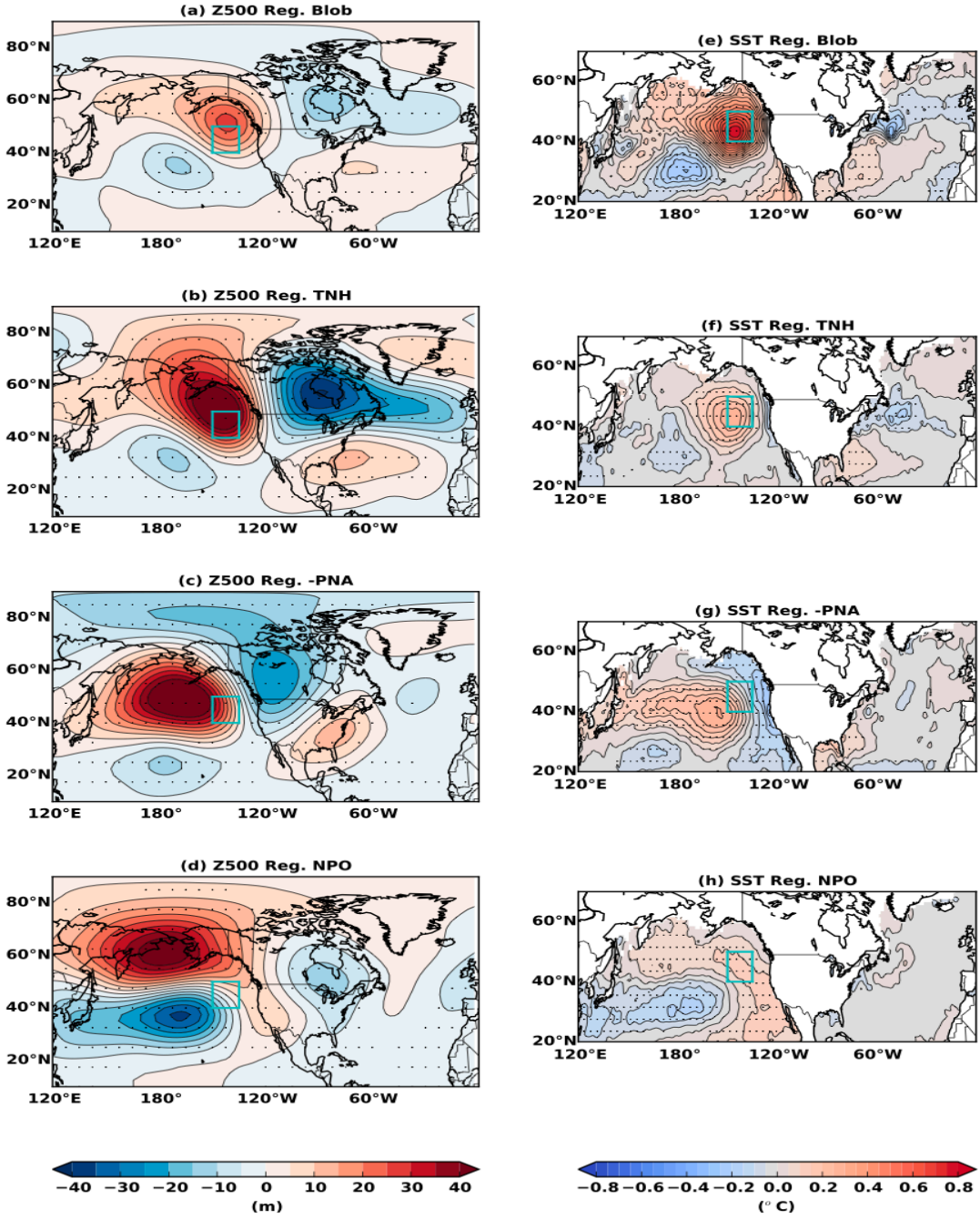

Figure 4.2 Regression maps of 500-hPa geopotential height (Z500) anomalies onto the (a) Pacific blob index, (b) TNH index, (c) negative PNA index, and (d) NPO index. Regression maps of SST anomalies onto the (e) Pacific blob index, (f) TNH index, (g) negative PNA index, and (h) NPO index. Contour intervals are 5 m in (a)-(d) and 0.05°C in (e)-(h). The light blue boxes delineate the Pacific blob region (40°-50°N, 150°-135°W) defined in Bond *et al.* (2015). The stippling indicates that the regression values are statistically significant (i.e., have *p* values less than 0.05).

closely associated with the Pacific blob. It is noted that there are some differences in magnitude between the TNH- and blob-regressed SST patterns, which reflects the fact that other processes may affect the SST variability in the Pacific blob region.

Then the temporal evolutions of the TNH pattern are compared to the Pacific blob indices in Figure 4.3(a). The warm phase of the Pacific blob largely coincides with the positive phase of the TNH pattern. A one-year low-pass filter is applied to smooth the indices in Figure 4.3(a) to better illustrate their evolution and to remove high-frequency fluctuations. The lead-lagged correlation analysis between the original unfiltered indices in Figure 4.3(b) shows that the maximum correlation coefficient (0.42) occurs when the TNH index leads the Pacific blob index by one month. This relation indicates that it is the TNH pattern that forces the Pacific blob rather than the other way around. The lead-lagged correlation coefficients of the PNA and NPO indices with the Pacific blob index (Figure 4.3(b)) are also calculated and found them to be much smaller than the correlation coefficients between the TNH and Pacific blob indices.

The close association between the TNH pattern and the Pacific blob can be further verified by a first-order auto-regressive (AR1) model, a widely used tool for quantifying the ocean response to forcing from the atmosphere in the North Pacific (e.g., Newman *et al.*, 2003; Schneider and Cornuelle, 2005; Johnstone and Mantua, 2014; Di Lorenzo and Mantua, 2016). Following these previous studies, A Pacific blob index is constructed according to the AR1 model formulation as follows:

$$Blob_{t+1} = \alpha \bullet TNH_t + \beta \bullet Blob_t + \varepsilon_t, \qquad (2)$$

where the *TNH* and *Blob* terms on the right-hand side denote the TNH forcing and the blob SST damping, and ε_t represents uncorrelated Gaussian-type random noise. The coefficient α (0.42) is obtained by regressing the Pacific blob index (i.e., $Blob_{t+1}$) against the TNH index with one-

month lag time (i.e., TNH_t). The coefficient β (0.77) is calculated by regressing the Pacific blob index, after removing the TNH information (i.e., $Blob_{t+1}$ - $\alpha \bullet TNH_t$), against the original Pacific blob index with one-month lag time (i.e., $Blob_t$). As shown in Figure 4.3(c), the reconstructed blob index matches the original blob index reasonably well with a high correlation coefficient of 0.78. This result indicates that about 61% of the Pacific blob variability can be accounted for by the TNH forcing and adds additional support to our suggestion that the TNH pattern can force the Pacific blob.

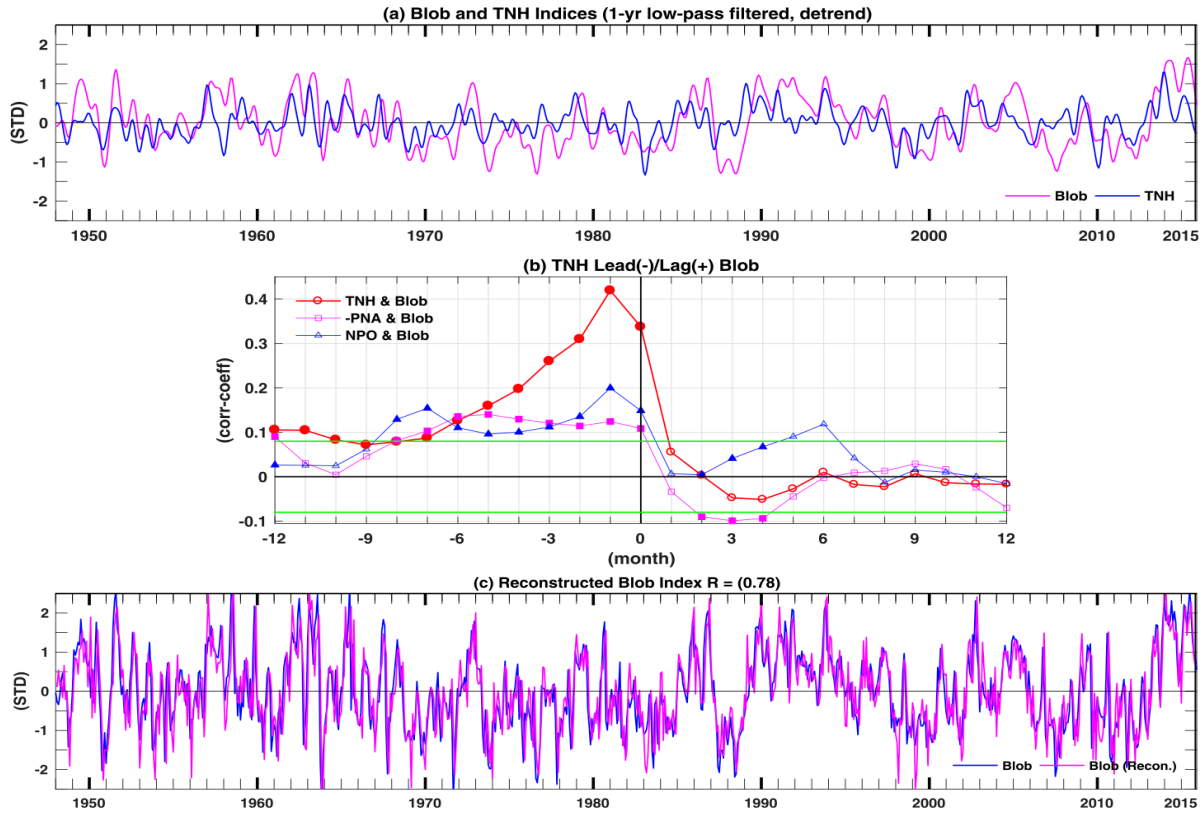

Figure 4.3 (a) Temporal evolution of the Pacific blob and TNH indices during the period 1948-2015. (b) The lead-lagged relationships between the TNH (-PNA and NPO) and Pacific blob indices. The solid (open) marks denote correlation coefficients that have *p* values smaller (larger) than 0.05. The green lines in (b) delineate the 95% significance levels by considering the effective sample sizes determined based on Eq. (1). (c) The AR1 model-reconstructed Pacific blob index (pink) including the TNH forcing term as described in Eq. (2), and the original blob index (blue). Note that the lead-lagged correlation coefficients and reconstructed blob index are calculated using unfiltered time series.

To uncover the mechanisms by which the TNH pattern forces the Pacific blob, an ocean mixed layer heat budget analysis (similar to that per- formed in Bond *et al.*, 2015) is performed over the North Pacific domain (see Figure 4.4). The monthly values of the mixed layer temperature tendency (dT_m/dt), net surface heat fluxes (SHF, positive downward), and horizontal ocean advection are calculated, and then regressed them onto the TNH index and the time tendency of the blob index (i.e., dBlob/dt). When determining the ocean advection, the ocean current velocity and potential temperature are integrated from ocean surface to the bottom of the mixed layer, and then the horizontal temperature gradient and its dot product with the integrated velocities are calculated. The regressed dT_m/dt patterns are characterized by the GOA warming pattern with a center in the Pacific blob region and a cooling band along the U.S. West Coast that extends toward the subtropical Pacific (Figures 4.4(a) and (d)). These regions of warming and cooling tendencies largely coincide with positive and negative SHF anomalies (Figures 4.4(b) and (e)). The positive SHF anomalies in the Pacific blob region are associated with near-surface wind anomalies regressed onto the TNH index and dBlob/dt (pink arrows in Figures 4.4(b) and (e)), both of which are dominated by clockwise near-surface wind anomalies relating to the anomalous ridge. The southern and eastern branches of the clockwise wind anomalies weaken the prevailing westerlies, decrease the SHF, and produce a warming tendency. Further examination on the TNH-regressed horizontal ocean advection anomalies (Figure 4.4(c)) show that warm anomalies, induced by the anomalous easterly winds, also contribute to the warming tendency (0.069^{o}C month^{-1}) in the Pacific blob region, but are only about one-third as large as the SHF-induced warming (0.21^{o}C month^{-1}). The vertical heat exchange at the bottom of the mixed layer (i.e., entrainment), estimated by the wind stress curl and found slightly negative anomalies induced in the Pacific blob region is also examined (not shown). These results are

consistent with those in Bond *et al.* (2015) and indicate that the TNH-induced entrainment anomalies are relatively weak. This mixed layer heat budget analysis suggests that the TNH pattern forces the Pacific blob primarily through anomalies in SHF and secondarily through anomalies in wind-induced ocean advection.

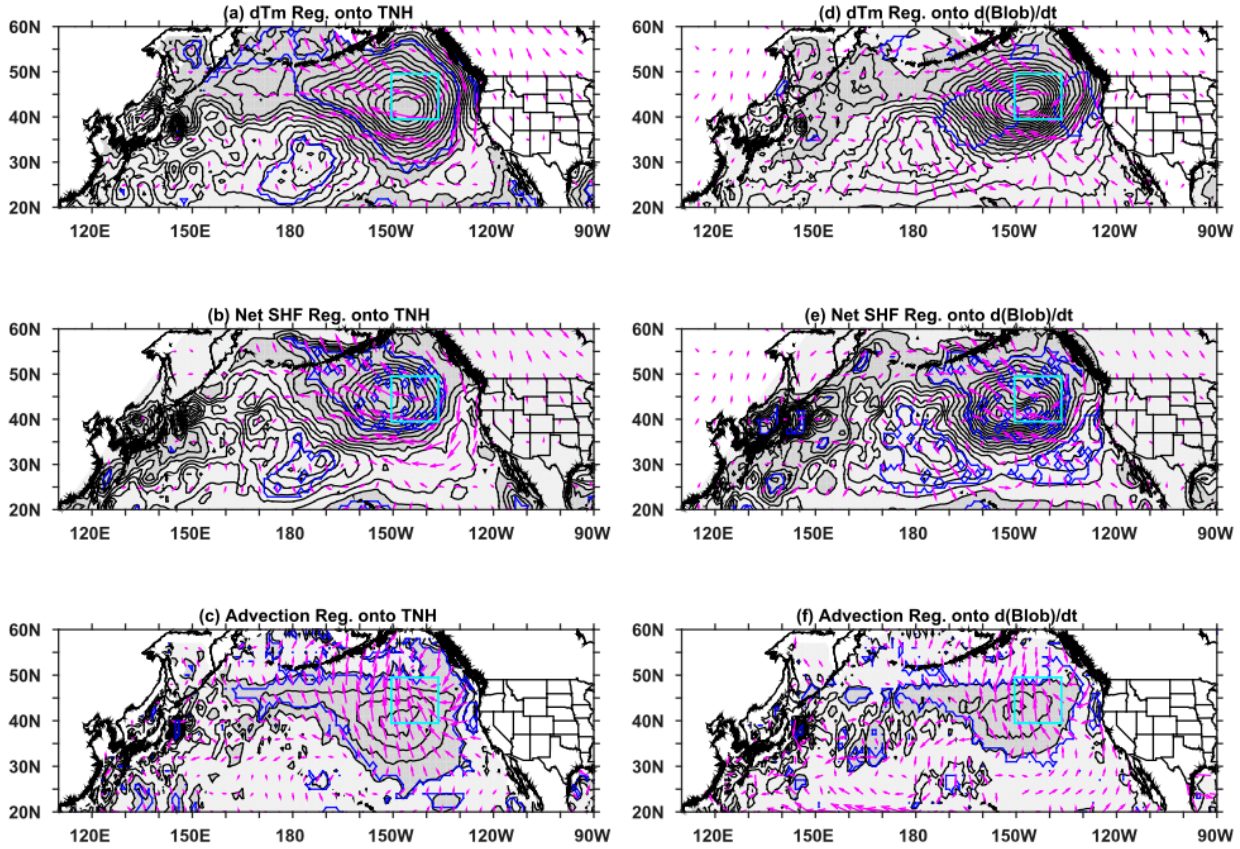

Figure 4.4 (a) The mixed layer temperature tendency (dT_m/dt), (b) the net SHFs (positive into the ocean), and (c) the horizontal ocean advection regressed onto the TNH index. (d)-(f) As in (a)-(c), but values are regressed onto the time tendency of the Pacific blob index (i.e., *d*Blob/*dt*). Contour intervals are 0.01°C month^{-1}. The shaded regions represent positive values while the unshaded areas represent negative values. The pink arrows in (a), (b), (d), and (e) are the regressed 1000-hPa wind anomalies while those in (c), (f) are the regressed 5-m ocean current anomalies. The light blue boxes delineate the Pacific blob region (40°-50°N, 150°-135°W) defined in Bond *et al.* (2015). The blue contour lines indicate the 95% significance level.

It is noticed that from Figure 4.3(a) that, when the 2013-2015 Pacific blob warming occurs, the TNH pattern has the tendency to stay in its positive phase for a similar period of time. To investigate this phase consistency between the TNH and Pacific blob indices, a phase analysis is performed to explicitly identify the periods when the Pacific blob index has positive values (blue shading) and the periods when the TNH index has positive values (pink bars) during 1948-2015 (Figure 4.5(a)). For a majority of the periods when the Pacific blob index stays in its positive phase, the TNH index also stays in its positive phase. Particular attention is paid to the periods when Pacific blob warming lasts exceptionally long (similar to the 2013-2015 event), defined as a prolonged Pacific blob event having warming for at least twenty-four months. Five such prolonged events (including the 2013-2015 event) during 1948-2015 can be identified, and they account for 19% of the total number of the positive blob periods (Figure 4.5(b)). These five prolonged blob events occurred during July 1956-October 1958, August 1961-August 1964, February 1985-January 1987, April 1989-March 1995, and March 2013-December 2015. After marking all these events (the red numbers in Figure 4.5(a)), the TNH index is found locked into its positive phase through a major portion of each event. These results indicate that locking the TNH pattern into its positive phase for an extended period plays a critical role in forcing prolonged Pacific blob events. The blob intensity also shows in Figure 4.5(c) the mean, maximum, and minimum values of the blob index during these prolonged blob events. All prolonged events this chapter selected have strong intensity (means >0.8 and maxima >1.5 standard deviations), with the 2013-2015 event being the strongest.

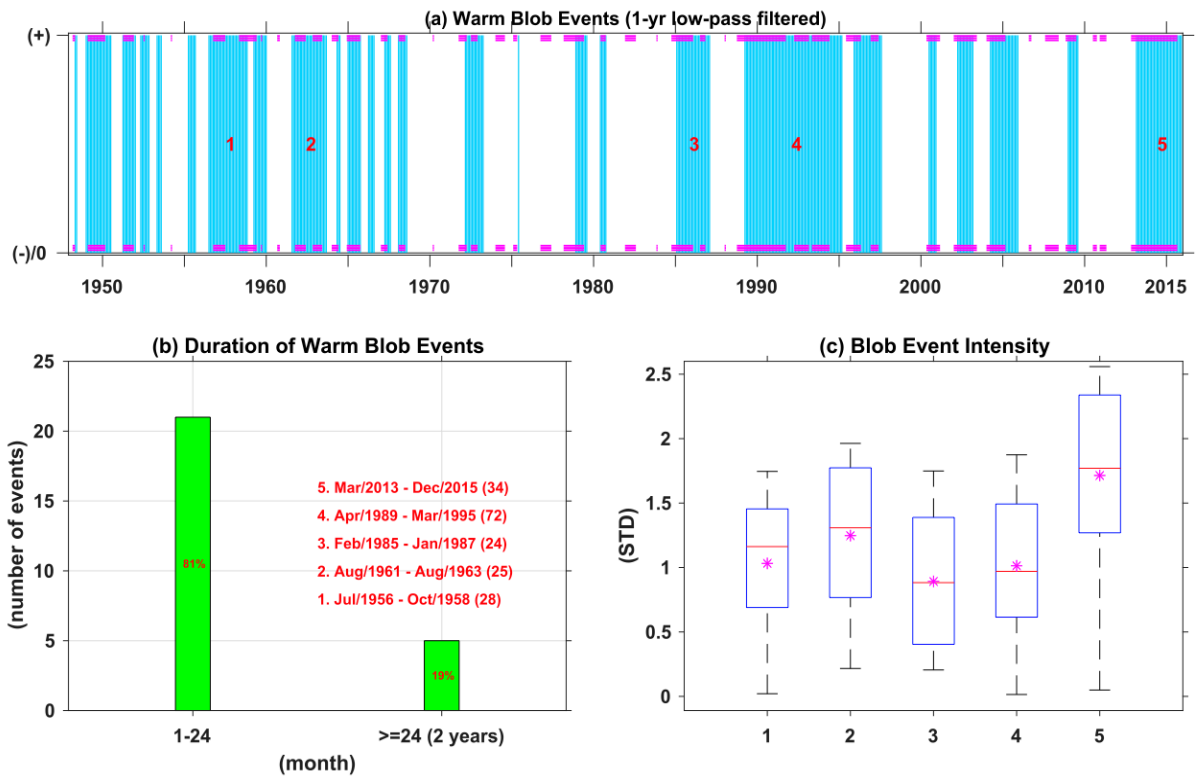

Figure 4.5 (a) Phase analysis of the Pacific blob and the TNH indices. The light blue (white) shadings indicate the positive (negative) phase of the blob index. The pink bars indicate the positive phase of the TNH index, and the red numbers represent the five prolonged Pacific warm blob events. (b) Duration analysis of the positive values of the Pacific blob index. In (b), the values on the y axis represent the number of events, the numbers inside the bars indicate the percentage of these Pacific warm blob events, the exact starting and ending dates of events having duration times larger than two years are listed above the right bar, and the values in the parentheses represent the exact duration in months. (c) Box-and-whisker plot for the SST anomalies for each prolonged Pacific blob event. The top and bottom of the blue box denote the 75th and 25th percentiles of the blob SST samples, the red line represents the median of the blob SST anomalies, the pink star is the mean of the blob SST anomalies, and the top and bottom of the whisker dashed lines are the highest and lowest blob SST anomalies in each event. The indices used here are 1-yr low-pass filtered.

To better illuminate the SST evolutions and the TNH phase-locking feature during the five prolonged blob events, Figure 4.6 shows Hovmöller diagrams for the SST anomalies averaged between 40°N and 50°N. The values of the TNH index during these events are shown next to the Hovmöller diagram. It is clearly shown that the TNH index stays mostly in its positive phase during these events, which is also shown by the positive mean TNH values. The 2013-2015 event has the highest mean TNH value (1.09), followed by the 1961-1963 (0.65), the 1985-1987 (0.57), the 1989-1995 (0.56), and the 1956-1958 (0.16) events. These positive TNH means correspond well to the positive mean values of the blob index during these events, which provides additional support for a close association between the TNH phase-locking and prolonged blob events.

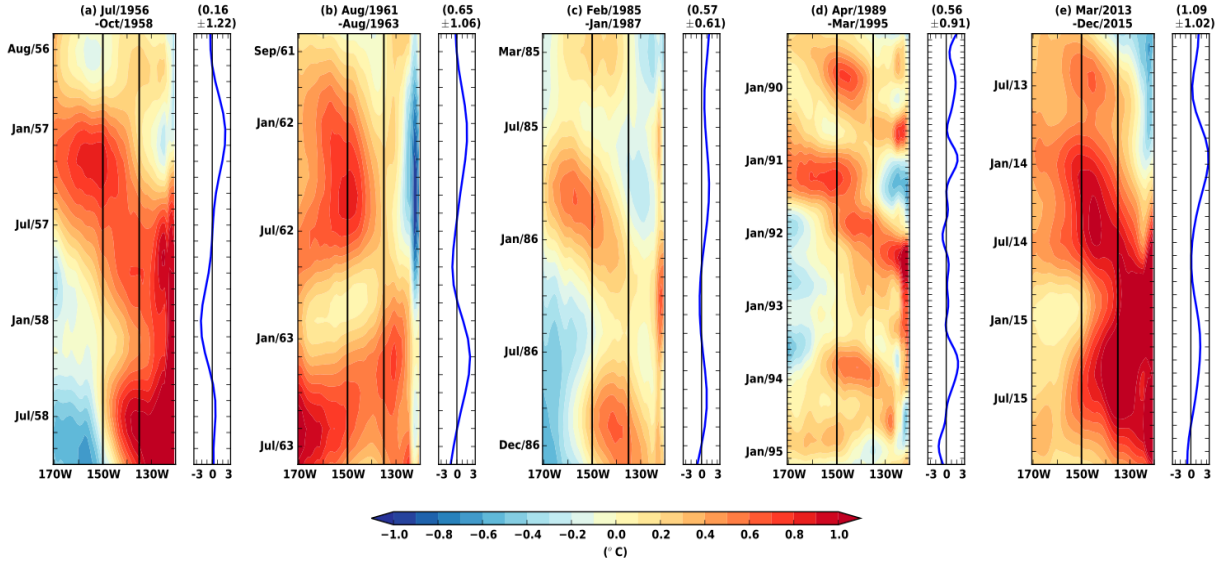

Figure 4.6 Hovmöller diagrams for the SST anomalies averaged between 40°N and 50°N after application of a one-year low-pass filter. The vertical black lines represent the longitudes of the Pacific blob boundaries (i.e., 150°W and 135°W). The one-year low-pass-filtered TNH indices during these events are shown by the blue lines next to the Hovmöller diagrams. The first value in the parentheses indicates the mean of the TNH index over each event, while the value after the ''±'' sign is the standard deviation over each event.

4.5 The Relationships of the Pacific Warm Blob to Pacific Decadal Oscillation (PDO) and El Niño-Southern Oscillation (ENSO)

The PDO and ENSO can also produce SST anomalies near the Pacific blob region (Mantua *et al.*, 1997; Alexander *et al.*, 2002; Newman *et al.*, 2003). To examine the possible relationships of the Pacific blob to PDO and ENSO, a covariance-based EOF analysis on SST anomalies is performed in the North Pacific region (17^{o}-60^{o}N, 120^{o}-100^{o}W). The first EOF mode (EOF1; explains 27.6% of total variance; Figure 4.7(a)) resembles the PDO SST pattern, characterized by a cooling in the central North Pacific and a band of warming along the North American coasts resembling the ARC SST pattern. The principal component of EOF1 mode (PC1) follows closely with the PDO index during the analysis period (Figure 4.7(c)) with a high correlation coefficient between them (0.85), in contrast to the low correlation coefficient between PC1 and the Pacific blob index (0.07). The EOF2 mode (explains 18.2% of total variance; Figure 4.7(b)) is characterized by SST anomalies in the NE Pacific that resembles the GOA pattern with its anomaly center appearing inside the Pacific blob box. The PC2 is found evolving closely with the Pacific blob index (Figure 4.7(d)) with a correlation coefficient of 0.70. This EOF analysis clearly shows that the Pacific blob is not associated with the PDO and is a separate dynamical entity.

One important signature shown in EOF1 mode is the band of warming off North American coasts that is similar to the ARC warming pattern observed in the 2013-2015 Pacific blob event. As mentioned, SST anomalies during that blob event involved a shift from a GOA warming pattern to an ARC warming pattern (Amaya *et al.*, 2016; Di Lorenzo *et al.*, 2016; Di Lorenzo and Mantua, 2016). Is such a shift a necessary component of Pacific blob generation?

To answer this question, the evolution of the SST anomalies in the five prolonged blob events are analyzed (Figure 4.8), and only two of them (the 1957-1958 and 2014-2015 events) exhibit a shift from the GOA to ARC warming pattern. It is noted that these two blob events were accompanied by El Niño conditions in the tropics. Therefore, El Niño possibly triggers the ARC-to-GOA shift in the prolonged blob events, as has been suggested by several recent studies (e.g., Amaya *et al.*, 2016; Di Lorenzo *et al.*, 2016; Di Lorenzo and Mantua, 2016), but is not a necessary mechanism for Pacific blob generation.

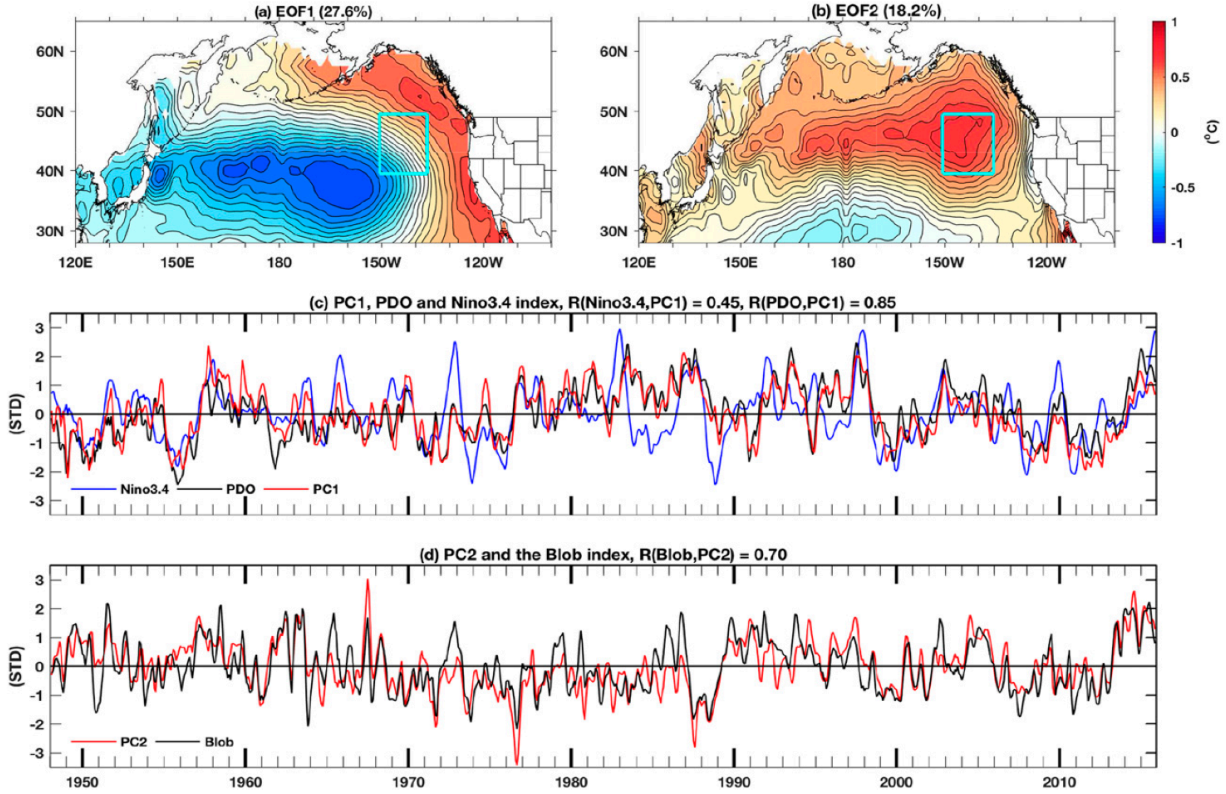

Figure 4.7 (a), (b) The loading coefficient patterns for the first and second EOF modes of the North Pacific SST variability, where the units have been converted to 8C using their corresponding eigenvalues. The light blue boxes in (a) and (b) delineate the Pacific blob region (40°-50°N, 150°-135°W) defined in Bond *et al.* (2015). Contour intervals are 0.18°C. (c) The evolution of the principal component of the first EOF mode (i.e., PC1), the PDO index, and the Niño3.4 index. (d) The evolution of the principal component of the second EOF mode (i.e., PC2) and the Pacific blob index. Time series in (c) and (d) are averaged using a three-month window.

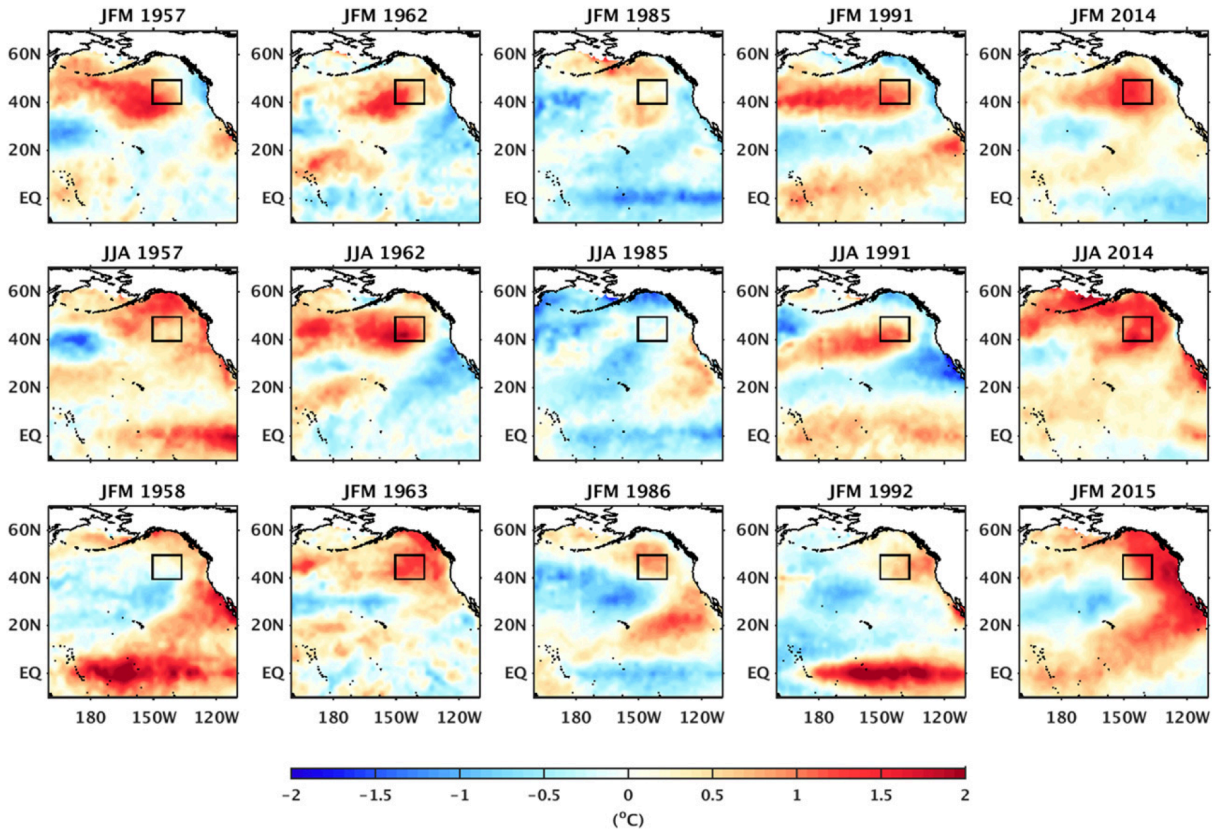

Figure 4.8 The SST anomalies averaged in winter (JFM) and summer (JJA) seasons for the five prolonged blob events. The black boxes delineate the Pacific blob region (40°-50°N, 150°-135°W) defined in Bond *et al.* (2015).

4.6 The Relationship between the TNH pattern and the Atlantic Cold Blob

An interesting feature of the TNH pattern is that its anomaly structures crossing both the North Pacific and North Atlantic (Figure 4.2(b)). This implies that when the TNH pattern stays in its positive phase for an extended period of time to force a Pacific warm blob event, it may also force SST variability in the North Atlantic. This possibility is revealed by the TNH-regressed SST anomaly pattern (Figure 4.2(f)), where statistically significant negative SST anomalies are found in the North Atlantic. The location of the cold anomalies is close to where the Atlantic cold blob was observed during 2014-2015 (Henson, 2016), as shown in the SST anomalies averaged in this event (Figure 4.9(a)). Such Atlantic cold blobs are also observed in the SST anomalies averaged in the other four prolonged Pacific warm blob events (Figures 4.9(b)-(e)), although the intensity of the Atlantic blob is weaker in the 1956-1958 event. The co-occurrence of Pacific warm blob and Atlantic cold blob in these five events reveals that the TNH pattern may serve as a conducting mechanism to connect some of them.

Figure 4.10(a) exhibits that the TNH and the Atlantic cold blob indices have a tendency to follow each other during the analysis period. The lead-lag correlation analysis shows that the one-year low-pass-filtered TNH index has the largest correlation coefficient (0.37) with the filtered Atlantic blob index when the former leads the latter by four months (Figure 4.10(b)), which is longer than the two-month lead time found between the filtered TNH and Pacific blob indices. A two-month lead time is also found in the lead-lag correlation analysis between filtered Pacific blob and the Atlantic blob indices. These lead-lagged relations likely reflect the fact that the mean mixed layer is deeper in the Atlantic blob region (118.7 m) than in the Pacific blob region (48.1 m), indicating the TNH pattern requires more time to induce Atlantic cold blob than

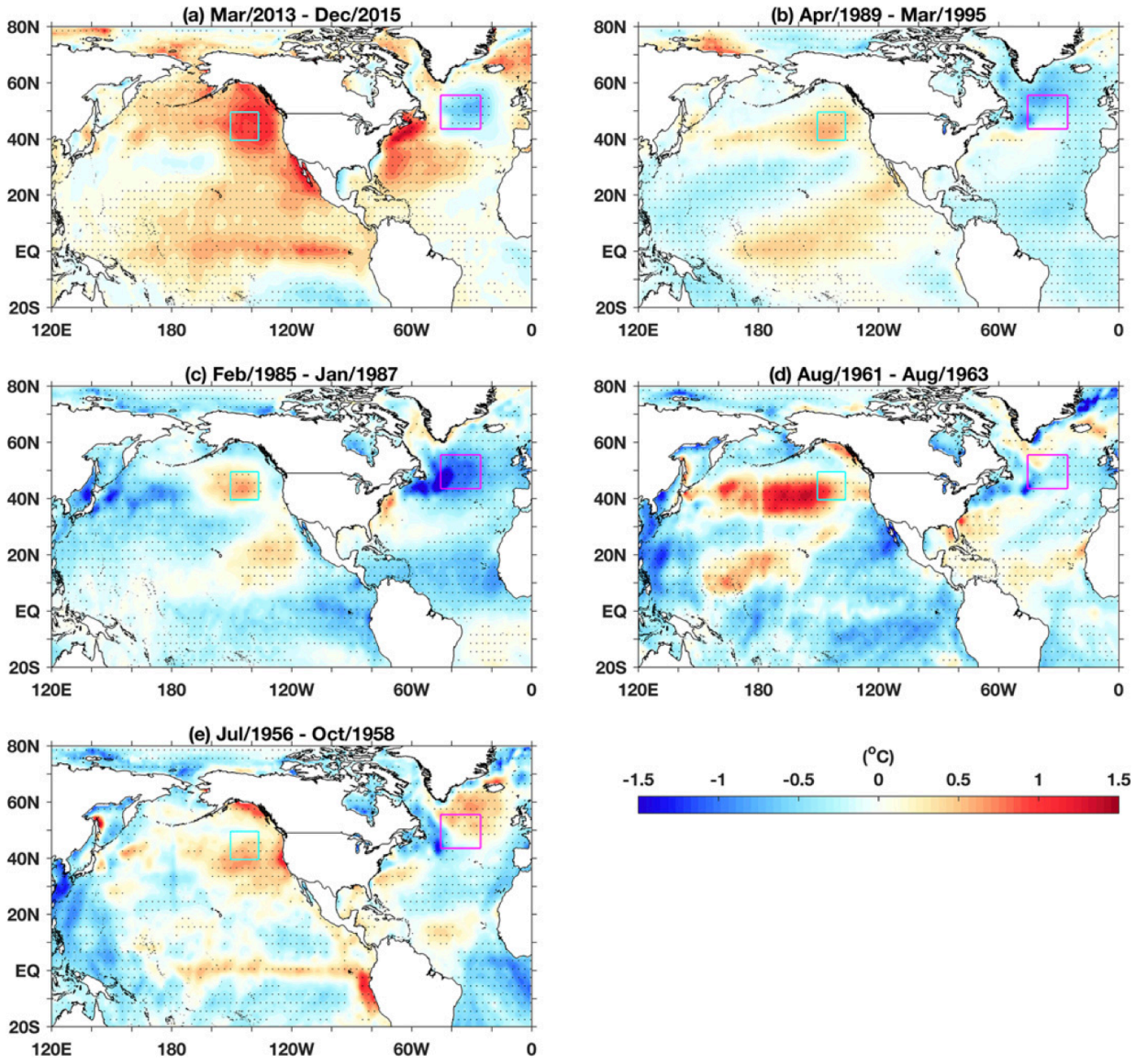

Figure 4.9 Composited SST anomalies for the five prolonged blob events: (a) March 2013-December 2015, (b) April 1989-March 1995, (c) February 1985-January 1987, (d) August 1961-August 1963, and (e) July 1956-October 1958. The light blue boxes delineate the blob region (40°-50°N, 150°-135°W) defined in Bond *et al.* (2015), whereas the pink boxes depict the Atlantic cold region (44°-56°N, 45°-25°W). The stippling indicates that the composite anomalies are statistically significant at the 95% level according to the Student's two-tailed *t*-test.

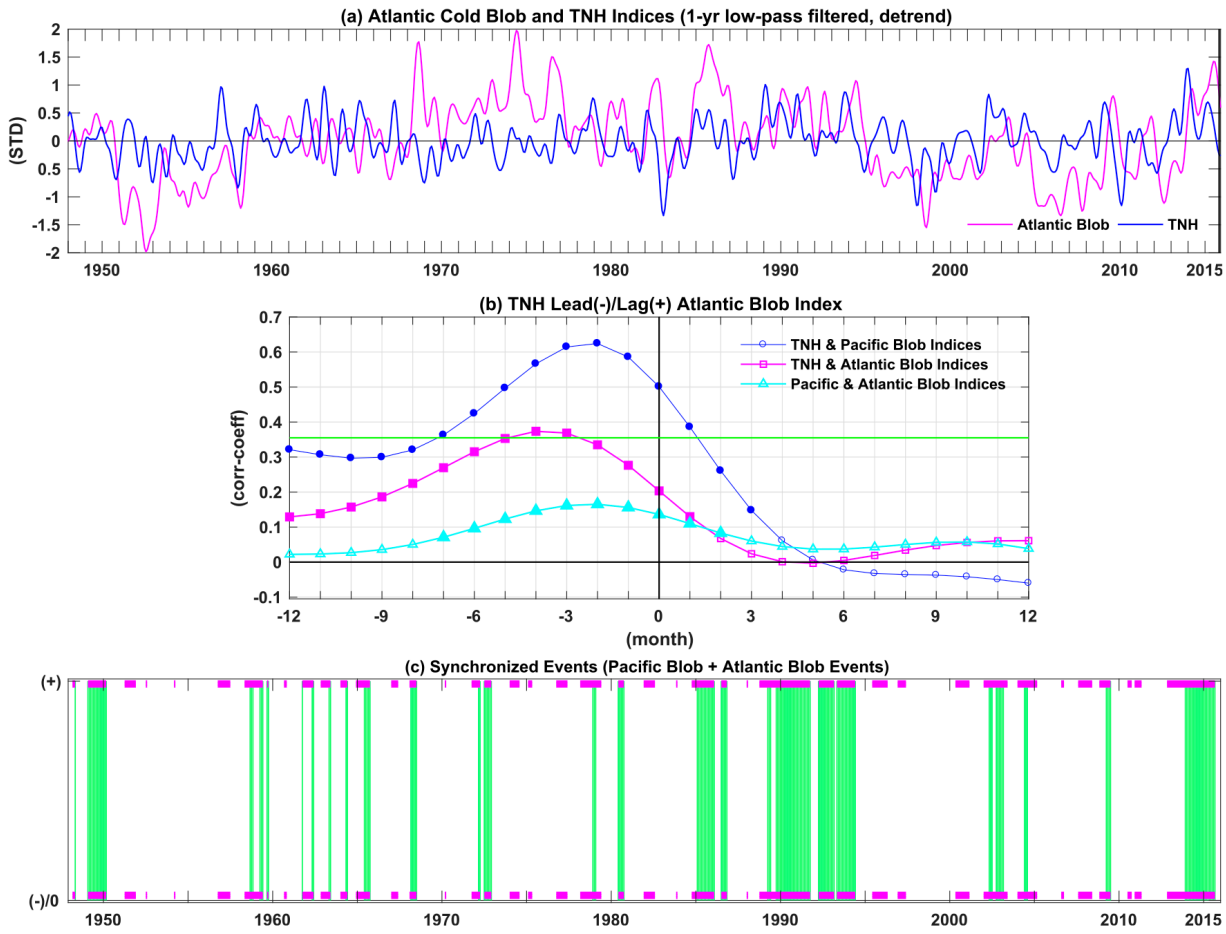

Figure 4.10 (a) Temporal evolution of the Atlantic cold and TNH indices during the period 1948-2015. (b) The lead-lagged relationships between the TNH, Atlantic blob, and Pacific blob indices. The solid (open) marks denote correlation coefficients that have *p* values smaller (larger) than 0.05. Note that the lead-lagged correlation coefficients are calculated using filtered time series. The green lines in (b) delineate the 95% significance levels by considering the effective sample sizes determined based on Eq. (1). (c) Phase analysis for the occurrences of the Pacific warm blob and Atlantic cold blob events. The light green shading indicates the positive phases of both the Pacific blob and Atlantic cold indices. The pink bars indicate the positive phase of the TNH index. The indices used for the phase analysis are one-year low-pass filtered.

Pacific warm blob. Figure 4.10(b) also reveals that the correlation coefficients between the TNH and the Pacific blob indices are higher than those between the TNH and the Atlantic blob indices, which implies that the TNH pattern accounts for more SST variability in the Pacific blob region than that in the Atlantic blob region. Other major forcing mechanisms also exist for the Atlantic cold blobs, such as those associated with the NAO, the AMOC, and the Greenland ice sheet melting (Delworth *et al.*, 2016; Yeager *et al.*, 2016; Rahmstorf *et al.*, 2015; Robson *et al.*, 2016; Duchez *et al.*, 2016; Schmittner *et al.*, 2016). The results indicate that the TNH forcing is an additional, rather than an exclusive, explanation for the generation of the Atlantic blob.

To further examine the connection between Pacific and Atlantic blobs, Figure 4.10(c) shows that the periods when positive values of the Pacific blob index coincide with positive values of the Atlantic blob index (green shading). Also shown in Figure 4.10(c) are the periods when the TNH pattern stays in its positive phase (pink bars). The Pacific warm blob events have co-occurred with Atlantic cold blob events several times during the analysis period, mostly when the TNH pattern persistently stayed in its positive phase. Among them, 1985-1987, the early 1990s, and 2013-2015 are the three longest periods when the Pacific and Atlantic blobs are synchronized. The evidence suggests that the TNH pattern is able to connect some of the prolonged Pacific warm blobs and Atlantic cold blobs. A mixed layer heat budget analysis over the North Atlantic (Figure 4.11) confirms that the TNH pattern forces the Atlantic blob cooling mainly via anomalies in SHF (-0.18^{o}C/month) and secondarily via anomalies in horizontal ocean advection (-0.026^{o}C/month).

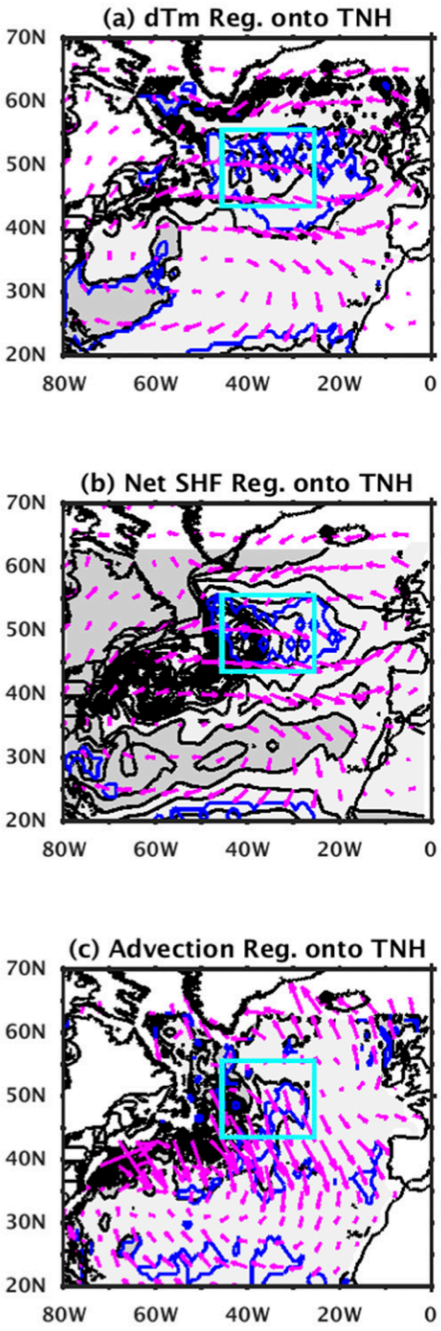

Figure 4.11 (a) The mixed layer temperature tendency (dT_m/dt), (b) the net SHFs (positive into the ocean), and (c) the horizontal ocean advection regressed onto the TNH index. Contour intervals are 0.018^{o}C month^{-1}. The shaded regions represent positive values while the unshaded areas represent negative values. The pink arrows in (a) and (b) are the regressed 1000-hPa winds anomalies while those in (c) are the regressed 5-m ocean current anomalies. The light blue boxes depict the Atlantic cold region (44^o-56^{o}N, 45^o-25^{o}W). The blue contour lines indicate 95% significance level.

To assess the importance of the TNH pattern in establishing the climate connectivity between the North Pacific and North Atlantic, a maximum covariance analysis (MCA; Wallace *et al.*, 1992) is performed to the Z500 and SST anomalies over these two oceans during the analysis period. These MCA modes are calculated by assuming the Z500 field leads the SST field by one month as shown in Figure 4.12(b). The first MCA (MCA1) mode (explains 42% of the squared covariance; Figures 4.12(a) and (b)) is characterized by a Z500 anomaly pattern similar to the PNA pattern (Figure 4.12(c)) and an SST anomaly pattern similar to the ARC warming pattern (Figure 4.12(a)). The correlation coefficients between the MCA1 PCs and the PNA and PDO (Niño3.4) indices are 0.72 and 0.80 (0.44), respectively. The MCA1 mode is related to the PDO or ENSO and their associated atmospheric circulation patterns. This mode has large anomalies over the Pacific sector but small anomalies over the Atlantic sector and contributes little to the climate connectivity between the North Pacific and North Atlantic. In contrast, the second MCA (MCA2) mode (explains 22% of the squared covariance; Figures 4.12(c) and (d)) is characterized by Z500 and SST anomalies crossing both the North Pacific and North Atlantic. Its Z500 pattern closely resembles the TNH pattern with a pattern correlation coefficient of 0.78 and a Z500 PC correlation coefficient of 0.66 with the TNH index. The SST anomaly pattern of MCA2 mode is characterized by a warming center in the Pacific blob region and a cooling center in the Atlantic blob region (Figure 4.12(d)). Its SST PC has high correlation coefficients with both the Pacific blob index (0.64) and the Atlantic blob index (0.76). This MCA mode suggests 1) that the connection between the Pacific blob and Atlantic blob is the second leading atmosphere–ocean coupled mode in the North Pacific-Atlantic sector and 2) that the TNH pattern is the key atmospheric circulation pattern to establish the climate connectivity between the two oceans.

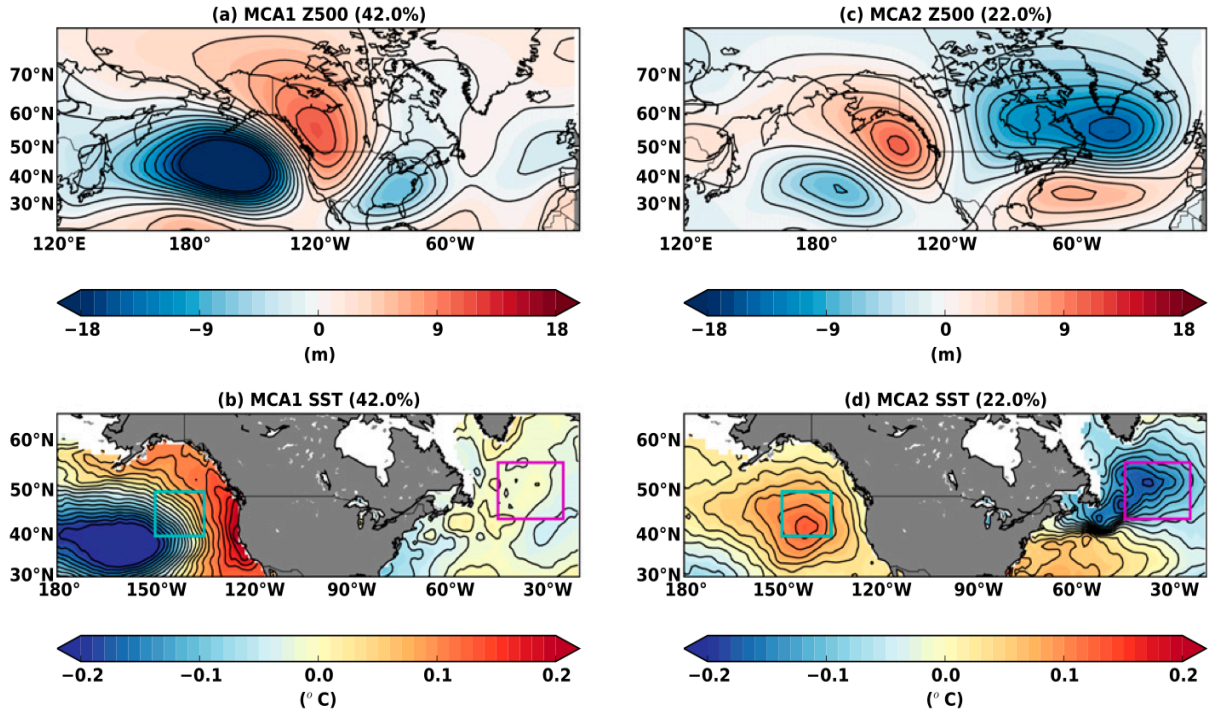

Figure 4.12 The two leading modes of an MCA analysis of the combined Z500 (20°-90°N, 120°E-0°) and SST (30°-65°N, 180°-20°W) anomalies in the North Pacific-Atlantic Oceans with the Z500 field leading the SST field by one month. (a), (b) The Z500 and SST patterns associated with the first leading MCA mode. (c), (d) The patterns associated with the second leading mode. The number in the parentheses of each panel represents the percentage of squared covariance between Z500 and SST fields explained by the MCA mode. The light blue boxes delineate the Pacific blob region (40°-50°N, 150°-135°W) defined in Bond *et al.* (2015), whereas the pink boxes depict the Atlantic cold region (44°-56°N, 45°-25°W).

4.7 Summary and Discussion

In this chapter, the TNH pattern is argued to be the principle atmospheric circulation pattern involved in the generation of the Pacific warm blob. Prolonged warm blob events occurred together with extended episodes of positive phases of this atmospheric circulation pattern. The TNH-blob relationship is verified by performing statistical analyses and case studies of the five prolonged Pacific warm blob events during the analysis period (1948-2015). The shift from a GOA warming pattern to an ARC warming pattern is also found not a necessary feature of Pacific blob generation. This shift occurs if an El Niño develops during a Pacific blob event, such as during the 2013-2015 Pacific warm blob event. The core part of the Pacific warm blob is the GOA warming pattern, which is closely tied to the TNH forcing. EOF analysis demonstrated that the Pacific warm blob is not part of the PDO or ENSO and is a separate dynamical entity.

The cross-basin structure of the TNH pattern is further shown to be capable of forcing the SST variability in both the Pacific blob and Atlantic blob regions. As a result, some of the Pacific warm blob events occurred together with some of the Atlantic cold blob events. This connection between the Pacific warm blob and Atlantic cold blob appears as a leading covariability mode in the North Pacific-Atlantic sector. Three of the five prolonged Pacific warm blob events were accompanied by prolonged Atlantic cold blob events. It is important to note that the TNH contribution to the generation of the Pacific warm blob is larger than its contribution to the generation of the Atlantic cold blob. Factors other than the TNH pattern, such as the NAO, the AMOC, and Greenland ice sheet melting, are also important in the generation of Atlantic cold blob events. These factors may weaken the apparent connection between the Pacific and Atlantic blobs. The connection can be better revealed if focusing on the TNH pattern and its associated oceanic SST covariability.

The results further raise a number of unanswered questions. For example, what causes the TNH pattern to stay in its positive phase for an extended period of time? Previous studies have suggested the TNH (or TNH-like) pattern may be triggered by tropical forcing mechanisms, such as the El Niño (Mo and Livezey, 1986; Barnston *et al.*, 1991; Yu *et al.*, 2012; Yu and Kim, 2011; Yu and Zou, 2013; Zou *et al.*, 2014), the quasi-biennial oscillation (Barnston *et al.*, 1991), the propagation of the wave activity initiated from the western tropical Pacific Ocean (Wang *et al.*, 2014; Lee *et al.*, 2015; Seager and Henderson, 2016; Hu *et al.*, 2017), and the internal dynamics in the atmosphere (Kumar *et al.*, 2013; Seager *et al.*, 2014; Xie and Zhang, 2017). Also, recent warming in the Arctic regions has been suggested to exert strong impacts on mid-latitude weather and climate by altering large-scale atmospheric circulation patterns (Cohen *et al.*, 2012, 2014; Kim *et al.*, 2014; Peings and Magnusdottir, 2014; Deser *et al.*, 2015; Lee *et al.*, 2015; Overland *et al.*, 2015, 2016; Yu *et al.*, 2017). Thus, forcing related to certain tropical Pacific Ocean or polar conditions may be potential factors for the phase-locking of the TNH pattern. Extensive investigations on the underlying dynamics of the TNH pattern are clearly warranted in future research, given its importance as a mechanism for connecting the climate of the North Pacific and Atlantic Oceans. Chapter 5 focuses on how the recent Arctic warming impacts on the spatial structure of the TNH pattern and associated influences on the climate connectivity between North Pacific and North Atlantic. In addition, it is noticed that the linear trends for the Pacific and Atlantic blob indices, when calculated using the nondetrended SST anomalies, are 0.007^{o}C/year and -0.004^{o}C/year, respectively. The trends, although small, may produce cumulative warming large enough to affect the characteristics of the Pacific and Atlantic blobs or their relationships with large-scale atmospheric circulation patterns in recent decades. This possibility also needs to be explored.

CHAPTER5

Arctic Warming Intensifies Pacific-Atlantic Climate Connectivity

5.1 Abstract

The amplified Arctic warming during recent decades may have altered the large-scale atmospheric circulations and thus exerted profound influences on mid-latitude extreme events and climate. Previous studies focused on the circulation pattern associated with the Arctic Oscillation in the atmosphere to suggest the atmospheric pathway that enables the Arctic warming to affect mid-latitude extreme events. In this chapter, observational datasets and model experiments are used to show that the Arctic warming can alter another atmospheric circulation pattern - the Tropical Northern Hemisphere (TNH) pattern - to connect ocean variability in the North Pacific and North Atlantic. The intensified North Pacific-Atlantic climate connection is manifested as a co-occurrence of the Pacific warm blob and Atlantic cold blob events. These events have co-occurred more frequently since 1990 when Arctic warming began to accelerate. The Arctic warming may have also emerged to surpass the tropical forcing (associated with the El Niño-Southern Oscillation) to become the dominant controlling factor in intensifying the Pacific-Atlantic climate connectivity. Ensemble experiments with a coupled climate model project that the Arctic warming can further expand the TNH cross-basin structure under greenhouse gas forcing to strengthen the North Pacific-Atlantic climate connectivity. While the

Arctic climate is expected to become warmer in the future and cause an ice-free Arctic in boreal summer that could open new routes for marine commercial shipping, our findings suggest that the ice-free Arctic may also open new prediction "routes" that will enable us to use North Pacific conditions to predict North Atlantic climate variations and vice versa.

5.2 Introduction

The rate of increase in Arctic surface air temperatures (SATs) during recent decades is two-to-three times larger than that observed in lower latitudes (Cohen *et al.*, 2014; Screen and Simmonds, 2010; Pithan and Mauritsen, 2014; Wang *et al.*, 2017). This amplified Arctic warming may be capable of altering mid-latitude jet stream locations and stationary wave activity in the troposphere and stratosphere, which in turn affect mid-latitude climate (Francis and Vavrus, 2012; Cohen *et al.*, 2014; Kim *et al.*, 2014; Overland *et al.*, 2016; Francis *et al.*, 2017). Changes in the mid-latitude atmospheric circulation have been suggested to contribute to the increasing occurrence of extreme events (Francis and Vavrus, 2012; Cohen *et al.*, 2014; Kim *et al.*, 2014; Mori *et al.*, 2014; Screen and Simmonds, 2014; Wallace *et al.*, 2014; Kug *et al.*, 2015; Overland *et al.*, 2016; Francis *et al.*, 2017; Cheung *et al.*, 2018). A greater than 4^{o}C increase in the SATs of the East Siberian-Chukchi Sea (ES-CS) region during the boreal winter of 2013-2014 (Figure 5.1(a) and star sign in Figure 5.1(b)), for example, may have induced a persistent ridge over the western United States (U.S.) and a trough over the eastern U.S. to exacerbate wildfires and drought conditions in California, and severe winter storms and cold spells in the eastern U.S. (Kug *et al.*, 2015; Francis *et al.*, 2017).

Marine extreme events were also observed in the mid-latitude oceans during 2013-2014 (Bond *et al.*, 2015; Di Lorenzo and Mantua, 2016; Henson, 2016; Yeager *et al.*, 2016). A large

patch of warm water that was 3^{o}C warmer than normal was observed in the Northeastern Pacific (Figure 5.1(a)) and was referred to as the Pacific warm blob (Bond *et al.*, 2015) or as the Pacific marine heatwave (Di Lorenzo and Mantua, 2016). During about the same time, a distinctive cooling event developed in the North Atlantic (Figure 5.1(a)) that is referred to as the Atlantic cold blob (Henson, 2016) or the Atlantic marine cold spell. These two blob events exerted widespread stresses on fisheries, marine ecosystems, and downstream regional environments (Bond *et al.*, 2015; Di Lorenzo and Mantua, 2016; Henson, 2016; Yeager *et al.*, 2016, Jaffe and Zhang, 2017; Hobday, *et al.*, 2016; Duchez *et al.*, 2016). However, most studies of Arctic warming impacts on mid-latitude climate and extreme events did not investigate the possibility that these two marine blob events occurred together not by accident but as a result of Arctic warming.

While many studied the Pacific warm blob and the Atlantic cold blob as two separate phenomena, my recent study (Liang *et al.*, 2017 and see Chapter 4) suggested that these two blob events can be forced simultaneously by an atmospheric circulation pattern - the Tropical Northern Hemisphere (TNH) pattern (Mo and Livezey, 1986). The TNH pattern is unique in its cross-basin structure that extends from the North Pacific to North Atlantic (see Figure 4.2(b)). Therefore, the TNH pattern can induce sea surface temperature (SST) anomalies simultaneously in the areas where the Pacific and Atlantic blob events were observed during 2013-2015 (Liang *et al.*, 2017 and see Chapter 4). Prolonged (i.e., durations longer than twelve months) Pacific warm blob and Atlantic cold blob events have occurred together eight times since 1948, all of which occurred when the TNH pattern was locked into its positive phase for an extended period. Interestingly, six of the events occur after 1990 (Liang *et al.*, 2017 and see Chapter 4), which is also the time when Arctic warming began to accelerate (Cohen *et al.*, 2014). Such a coincidence

motivates this study to examine if the amplified Arctic warming has modified the TNH cross-basin structure to increase the connectivity between the North Pacific and North Atlantic.

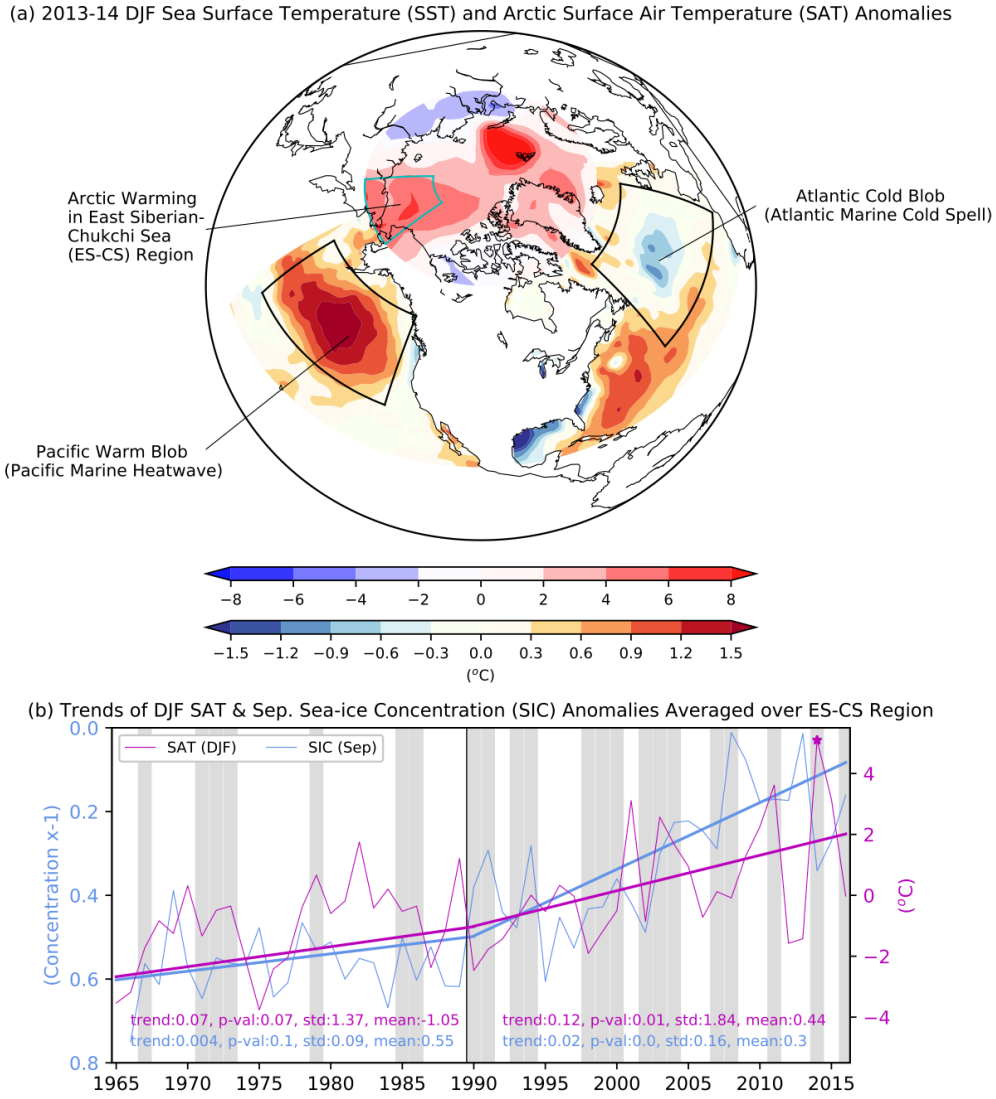

Figure 5.1 (a) 2013-2014 December-January-February (DJF) SST anomalies in the North Pacific and North Atlantic regions (20°N-65°N and 180°-360°), and SAT anomalies in the Arctic region (60°N-90°N). (b) the linear trends of Arctic SAT and SIC anomalies averaged over the ES-CS region (cyan box in (a)) during the period 1965-1989 and the period 1990-2015. The original SAT and SIC time series (magenta and light blue curves) are also shown in (b). The grey shading indicates the boreal winters during which the SST anomalies averaged over the North Pacific (North Pacific black box in (a)) and the North Atlantic (North Atlantic black box in (a)) are out-of-phase (i.e., one value is positive, the other is negative).

5.3 Data, Model, and Methods

5.3.1 Reanalysis Datasets

The SST and sea-ice concentration (SIC) datasets are from the Hadley Centre Sea Ice and Sea Surface Temperature data set (http://www.metoffice.gov.uk/hadobs/hadisst/data/download.html, Rayner *et al.*, 2003); atmospheric wind fields, SAT, and geopotential heights are from the National Center for Atmospheric Research/National Centers for Environmental Prediction (NCAR/NCEP) reanalysis dataset (http://www.esrl.noaa.gov/psd/data/gridded/data.ncep.reanalysis.derived.html, Kalnay *et al.*, 1996) and ECMWF website (http://apps.ecmwf.int/datasets/data/interim-full-moda/levtype=sfc/, Berrisford *et al.*, 2011). Mixed-layer temperatures, surface heat fluxes (positive downward), and ocean currents are from the NCEP Global Ocean Data Assimilation System (GODAS, https://www.esrl.noaa.gov/psd/data/gridded/data.godas.html, Behringer *et al.*, 1998). Anomalies are defined as the deviations of averaged December-January-February (DJF) fields from their 1981-2010 climatology values.

5.3.2 Climatic Indices

Several indices are used in the analyses. The ES-CS SAT index is used to describe the Arctic SAT fluctuations in the ES-CS region and is calculated as the DJF-mean SAT anomalies averaged within a box bounded by 65^{o}N-80^{o}N and 160^{o}E-160^{o}W (see the cyan box in Figure 5.1(a)), following recent studies (Kug *et al.*, 2015; Sung *et al.*, 2016; Kim *et al.*, 2017). A DJF TNH index is calculated following the rotated Empirical Orthogonal Function (EOF, see Appendix 1 for details) method described in the previous studies (e.g., Barnston and Livezey, 1987). A thorough comparison between our TNH index and NOAA's TNH index can be also be

found in Liang *et al.* (2017) and Chapter 4.3.4. The Pacific North-American (PNA), North Atlantic Oscillation (NAO), and Arctic Oscillation (AO) indices are downloaded from NOAA's CPC websites (http://www.cpc.ncep.noaa.gov/data/teledoc/telecontents.shtml, http://www.cpc.ncep.noaa.gov/products/precip/CWlink/daily_ao_index/ao.shtml). The Pacific Decadal Oscillation (PDO) index is obtained from NOAA's Earth System Research Laboratory website (https://www.esrl.noaa.gov/psd/data/correlation/pdo.data). The Niño3.4 index is calculated as the SST anomalies averaged in a box bounded by 5^{o}S-5^{o}N and 170^{o}W-120^{o}W and represents El Niño-Southern Oscillation (ENSO) activity. The Pacific blob index is calculated as the SST anomalies averaged within the box bounded by 33^{o}N-55^{o}N and 175^{o}W-129^{o}W, whereas the Atlantic blob index within the box bounded by 40^{o}N-59^{o}N and 52^{o}W-10^{o}W times minus one. They are used to represent the SST variability in the Northeast Pacific and North Atlantic respectively.

5.3.3 Maximum Covariance Analysis (MCA)

The MCA is used in this chapter to determine the first three leading atmosphere-ocean coupled variation modes in the North Pacific-Atlantic sector. MCA is applied on the DJF Z500 anomalies in the region 20^{o}N-90^{o}N and 0^{o}-360^{o}, and SST anomalies in 30^{o}N-65^{o}N and 180^{o}W-0^{o}. The MCA extracts the co-variation signals in two fields by organizing their covariance. Detailed description on the MCA algorithm used and its implementation can be found in Appendix B.

5.3.4 Atmospheric General Circulation Model (AGCM) Ensemble Modeling

Forced AGCM simulations are conducted using the Community Atmosphere Model version 5 (CAM5, Gent *et al.*, 2011). The control simulations are forced with climatological

global SST and SIC values (Figures 5.2(a) and (b)), which are constructed using 1870-2009 SST and SIC datasets from Hadley centre. The experiment simulations use +1^{o}C SST and -10% SIC anomalies in the ES-CS region with linear smoothing in the boundary regions in all seasons. All simulations are run for ninety years and initialized by a 20-year run with climatology SST and SIC forcings. We only adopt idealized forcings with uniform SST and SIC anomalies added throughout seasons. More realistic forcings considering geographic distribution and seasonality will be conducted in future studies. The forty ensemble simulations are conducted by randomly selecting the start year in the ninety-year simulation and using the following forty-year results. The CAM5 is downloaded from UCAR/NCAR's Community Earth System Model (CESM) website (http://www.cesm.ucar.edu/models/). More details and comprehensive documents can be found the website and documents there.

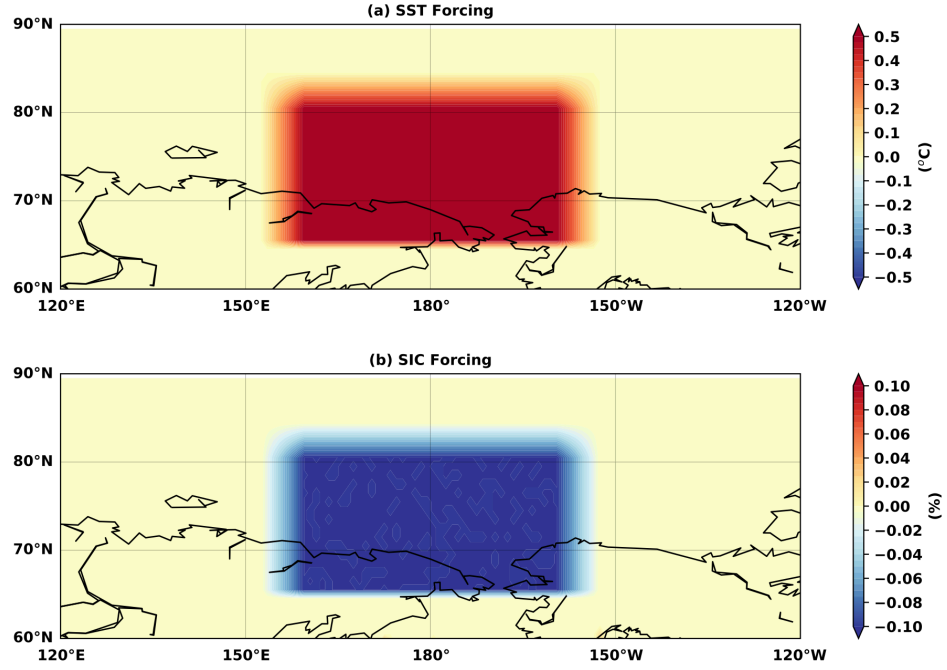

Figure 5.2 (a) SST forcing for AGCM experimental simulation. (b) SIC forcing for AGCM experimental simulation.

5.3.5 CESM-Large Ensemble (CESM-LE) data availability

Forty members of the CESM-LE simulations are used in this chapter during 1920-2080 under RCP8.5 greenhouse scenario (Kay *et al.*, 2015) downloaded from NOAA's ESRL website (https://esrl.boulder.noaa.gov/psd/repository/entry/show?entryid=7d47f9bd-7e09-4254-a178-6f94febe5b1e). Historical radiative forcing is used to force each ensemble member for the period 1920-2005 and RCP8.5 radiative forcing for 2006-2080. Comprehensive descriptions can be found on UCAR/NCAR's CESM website (http://www.cesm.ucar.edu/projects/community-projects/LENS/).

5.3.6 Statistical Analyses

Statistical tests for regression coefficients in the anomalous fields are performed using the *F*-test. If the corresponding *p* value is less than 0.05, the coefficient is regarded as statistically significant. The 95% level of the two-tailed Student's *t*-test is used for the composite anomalies.

5.4 Effects of Arctic Warming on the Spatial Structure of the TNH pattern

The Arctic changes before and after 1990 are comparing by the trends in DJF (i.e., December- January-February mean) SAT anomalies averaged over the ES-CS region (magenta lines in Figure 5.1(b)), which has been identified as a hotspot due to the dramatic changes in the SATs and sea-ice extents there (Kug *et al.*, 2015). The trend increases by about 1.7 times from 0.07^{o}C/year during 1965-1989 to 0.12^{o}C/year during 1990-2015, consistent to the fact that the

rate of Arctic-wide warming increased rapidly after 1990 (Cohen *et al.*, 2014; Pithan and Mauritsen, 2014; Kug *et al.*, 2015; Screen and Simmonds, 2010). Accompanying the amplified warming is a rapid decline in September SIC, which was decreased at a rate that is about 3.8 times greater after 1990 (cyan lines in Figure 5.1(b)) than before. These results show that the Arctic climate in the ES-CS region has undergone significant changes since the early 1990s.

DJF SST anomalies of opposite sign in the Northeast Pacific and North Atlantic (the black boxes in Figure 5.1(a)), where the Pacific and Atlantic blob events were observed in 2013-2014, also tend to co-occur more frequently after 1990 (light grey shadings in Figure 1(b)). The temporal correlation coefficient (hereafter R_t) between the Pacific and Atlantic blob indices increases from 0.16 (0.01 with linear trends removed) during 1965-1989 to 0.38 (0.45 with linear trends removed) during 1990-2015. The enhanced correlation coefficient verifies that the marine warming/cooling events in these two ocean basins have become more synchronized after Arctic warming accelerated. Further correlation analyses to illustrate the intensified Pacific-Atlantic climate connectivity are conducted in Section 5.5.

To illustrate the role of the TNH pattern plays in the atmospheric circulations, an Empirical Orthogonal Function (EOF) analysis on the 500-mbar geopotential height (Z500 hereafter) anomalies is performed over the Northern Hemisphere (NH; 20^{o}N-90^{o}N and 0^{o}-360^{o}E). The second leading EOF mode (EOF2), explaining 16% of the total variance, resembles the TNH pattern. Their close resemblance is corroborated by the fact that the pattern correlation coefficient (hereafter R_p) between Z500 anomalies regressed onto the PC of EOF2 mode (hereafter *PC2*) and those regressed onto the TNH index is as high as 0.96. *PC2* and the TNH index also evolve similarly (Figure 5.3) and are highly correlated (R_t = 0.90). The EOF analyses indicate that the TNH pattern is the second leading variation mode in the NH atmospheric

circulation. On the other hand, the first EOF mode (EOF1), explaining 25% of the total variance, shows a north-south dipole anomaly pattern that resembles the structure of AO (AO, Yu and Hartmann, 1993; Thompson and Wallace, 1998). The pattern correlation coefficient (hereafter R_p) between the Z500 anomalies regressed onto the PC of EOF1 mode (hereafter PC1) and those regressed onto the AO index is 0.98, and the R_t between the PC1 and the AO index is 0.94. The EOF analyses indicate that the TNH pattern is the second leading variation mode in the wintertime NH atmospheric circulation, with the AO being the first.

To examine the possible differences in the TNH pattern between warm and cold Arctic conditions, the conditional regression analyses are performed considering *PC2* for warm and cold Arctic periods, which are determined by positive and negative phases of the detrended ES-CS SAT index. In total thirty-eight DJF during 1979-2015 (i.e., thirty-six DJF-mean winters plus the means of January-February, 1979, and December, 2015), the ES-CS SAT index is found in its positive phase seventeen times (see orange bars in Figure 5.3), whereas in its negative phase twenty-one times (see light blue bars in Figure 5.3). During warm periods, the zonally-elongated structure of the TNH pattern extends further into the eastern North Atlantic and there is a westward shift of the center of the anomalous ridge over the Northeast Pacific (Figure 5.4(a)). In contrast, the TNH anomalies contract in both Pacific and Atlantic sector during cold periods, resulting in a structure that is more confined to the North American continent (Figure 5.4(b)). The difference map between the regressed Z500 anomalies during the warm and cold periods clearly reveals this TNH expansion effect of the Arctic warming (Figure 5.4(c)). Similar results can be obtained with linear trend retained (not shown), and by repeating the analyses with NOAA's DJF TNH index and the ECMWF reanalysis datasets (Figures 5.5 and 5.6). These

regression analyses indicate that Arctic warming (particularly in the ES-CS region) may enhance the cross-basin characteristics of the TNH pattern.

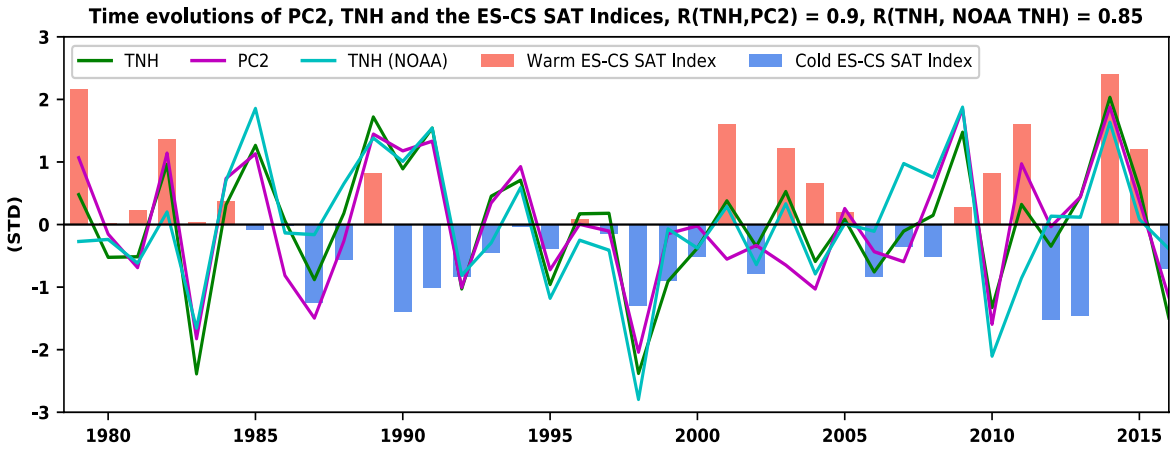

Figure 5.3 Time evolutions of *PC2*, the TNH indices and the ES-CS SAT index during 1979-2015. The green curve is the TNH index derived following a previous study (Barnston and Livezey, 1987), the cyan curve the TNH index download from NOAA's CPC website, the magenta line the *PC2*. The bars represent the ES-CS SAT index. The orange color denotes that the ES-CS SAT index in its positive phase, while light blue color in its negative phase.

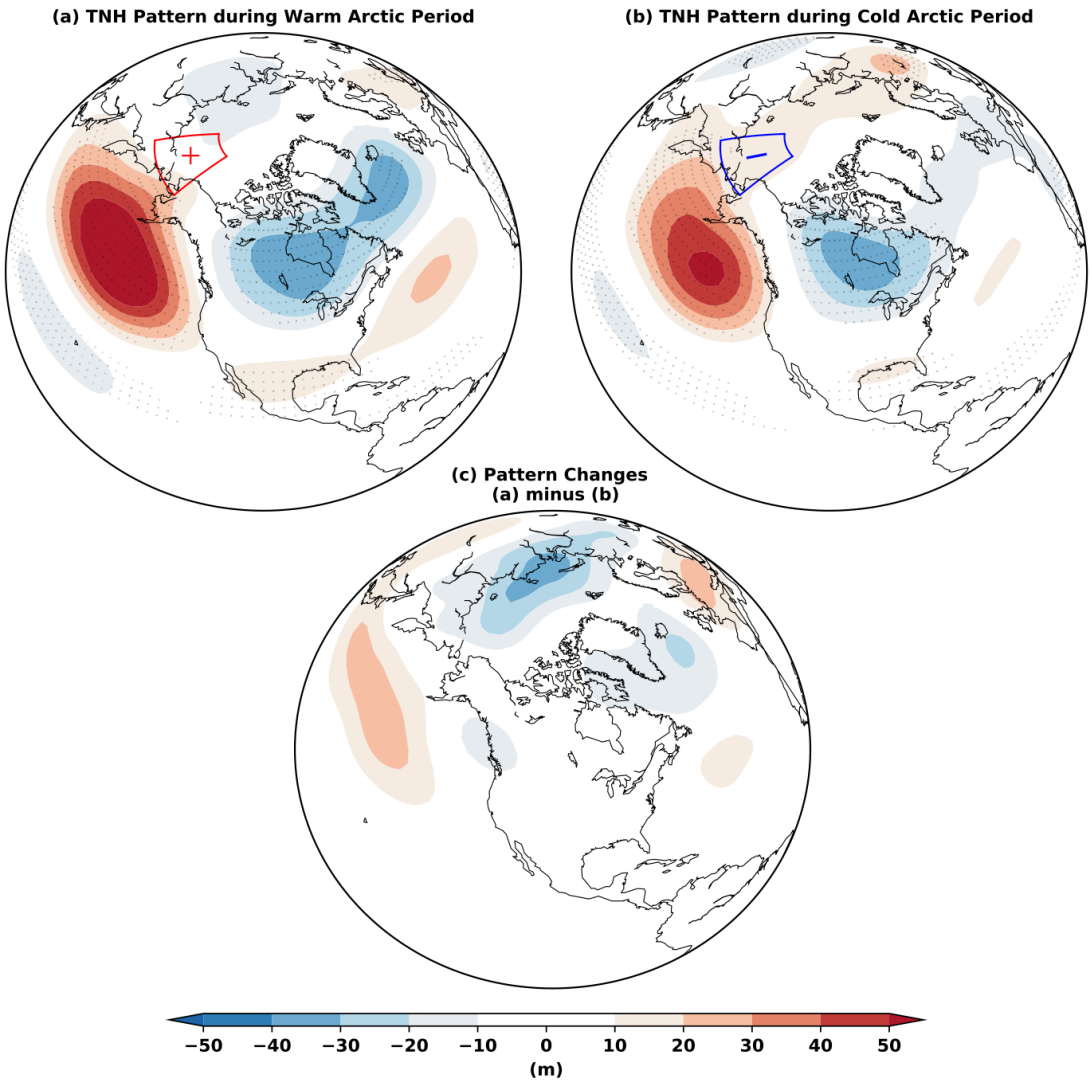

Figure 5.4 (a) regressed DJF Z500 anomalies onto the *PC2* during the period when the value of the ES-CS SAT index is positive. (b) is similar to (a), but when the value of the ES-CS SAT index is negative. The red and blue boxes in (a) and (b) boxes depict the ES-CS region (65°N-80°N and 160°E-160°E) in warm and cold phases respectively. The stippling denotes that the regression has statistical significance with *p*-value less than 0.05. (c) Z500 difference map determined as the regressed anomalies in (a) minus those in (b).

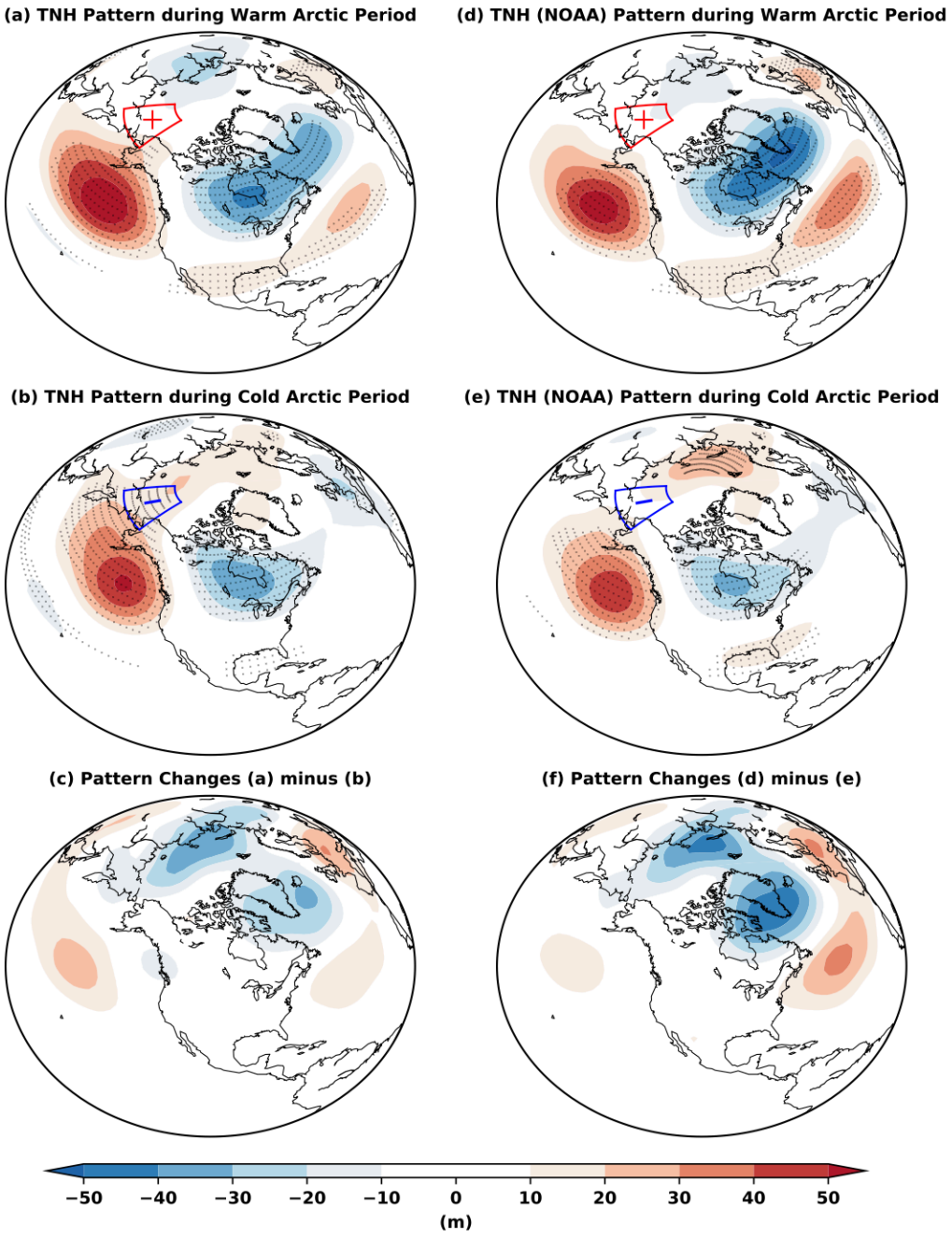

Figure 5.5 The TNH patterns during warm Arctic and cold Arctic periods using our TNH index and NOAA's TNH index. (a)-(c) as in Figures 5.3(a)-(c) but using the TNH index derived following a previous study (Barnston and Livezey, 1987). (d)-(f) as in Figures 5.3(a)-(c) but using the TNH index downloaded from NOAA's CPC website. The stippling denotes that the regression has statistical significance with *p*-values less than 0.05.

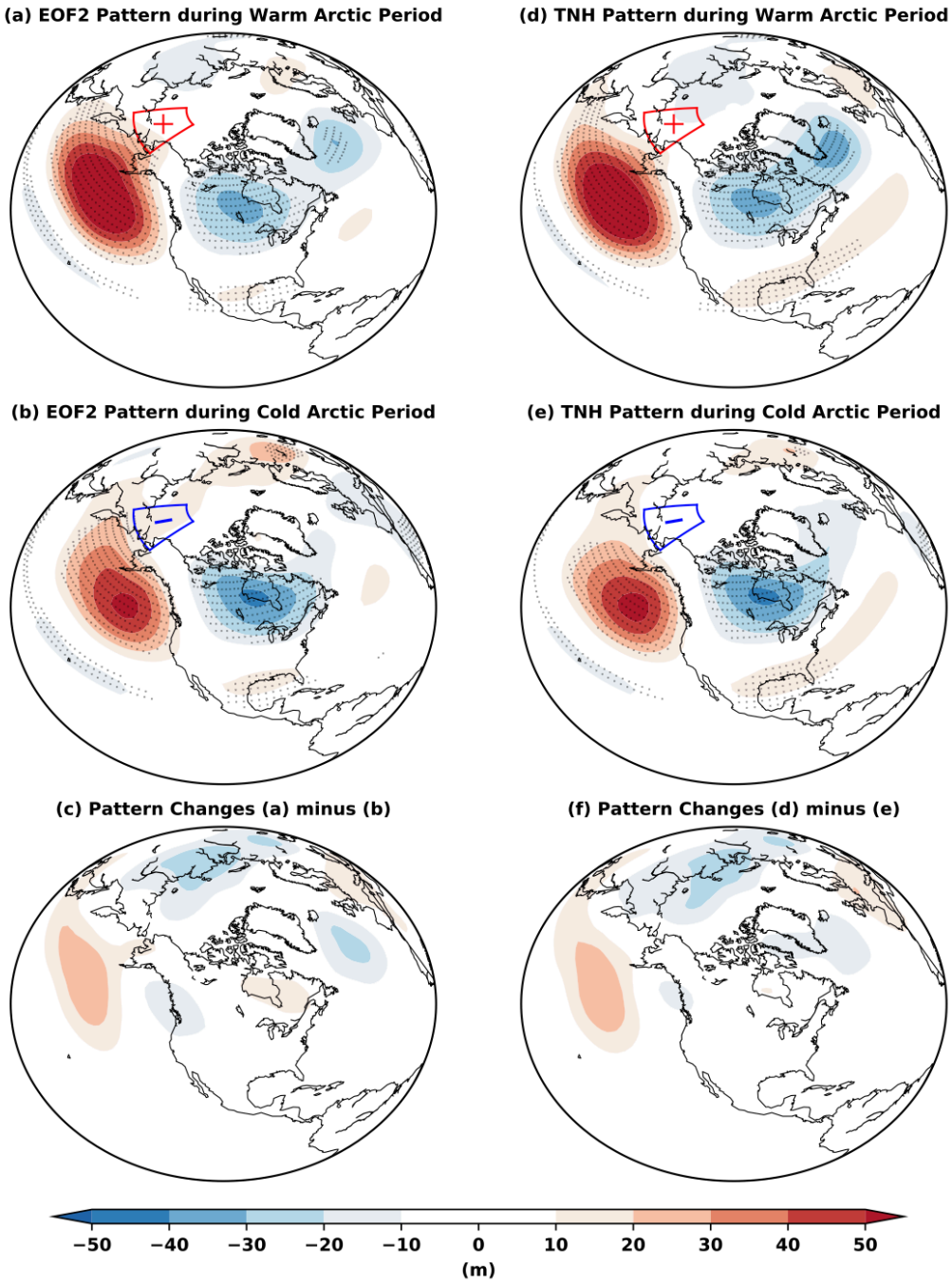

Figure 5.6 The TNH patterns during warm Arctic and cold Arctic periods using ECMWF reanalysis datasets. (a)-(c) as in Figs. 2(a)-(c) but regressed onto *PC2* using ECMWF reanalysis datasets. (d)-(f) as in Figs. 2(a)-(c) but using the TNH index derived following a previous study (Barnston and Livezey, 1987) with ECMWF reanalysis datasets. The stippling denotes that the regression has statistical significance with *p*-values less than 0.05.

An ocean mixed-layer heat budget analyses shows that the expanded TNH pattern can induce SST anomalies simultaneously in the Pacific and Atlantic blob regions via surface heat fluxes and horizontal ocean advection. Figure 5.7 shows the mixed layer temperature tendency (dT_m/dt), net surface heat fluxes (SHF, positive downward), and wind-induced horizontal ocean advection, regressed onto *PC2* during warm and cold Arctic periods. Comparing Figure 5.7(a) with Figure 5.7(d), the warm Arctic periods tend to induce stronger negative values of dT_m/dt over a wider area of the North Atlantic than the cold Arctic periods. This cooling tendency can be largely explained by stronger near-surface westerly anomalies that extend further to the east (the pink arrows in Figure 5.7(a)) during warm Arctic periods. The anomalous winds, superimposed onto the climatological Atlantic westerlies, increase latent and sensible heat fluxes into the atmosphere resulting in negative net SHF anomalies (Figure 5.7(b)). The anomalous westerlies also induce, via Ekman transport, southeastward surface ocean currents (the pink arrows in Figure 5.7(c)) that act on the climatological mixed layer temperature gradient resulting in negative anomalies in the horizontal ocean advection (Figure 5.7(c)). Both the SHF and ocean advection mechanisms contribute to the negative temperature tendency in the North Atlantic. In contrast, Arctic cooling induces weaker negative dT_m/dt because of the reduced net SHF and ocean advection anomalies generated by the weaker westerly wind anomalies associated with the contracted TNH structure (Figures 5.7(d)-(f)). In the Pacific sector, similar but opposite mechanisms enable the anti-cyclonic wind anomalies of the TNH pattern to give rise to positive anomalies in dT_m/dt (Figures 5.7(a)-(c)). It is noted that the dT_m/dt positive anomaly center shifts southward during warm Arctic period mainly due to wind-induced ocean advection, reminiscent of the shifted center of the anomalous TNH-associated ridge. Other mechanisms (not shown), such as vertical mixing (i.e. entrainment) and radiative processes, have been suggested by other

studies to play secondary roles compared to the effects of net SHF and wind-induced ocean advection (Bond *et al.*, 2015). The above analyses indicate that the extended atmospheric circulation pattern associated with warming in the ES-CS region could induce stronger oceanic anomalies in the North Pacific and North Atlantic simultaneously, which intensifies their climate connectivity.

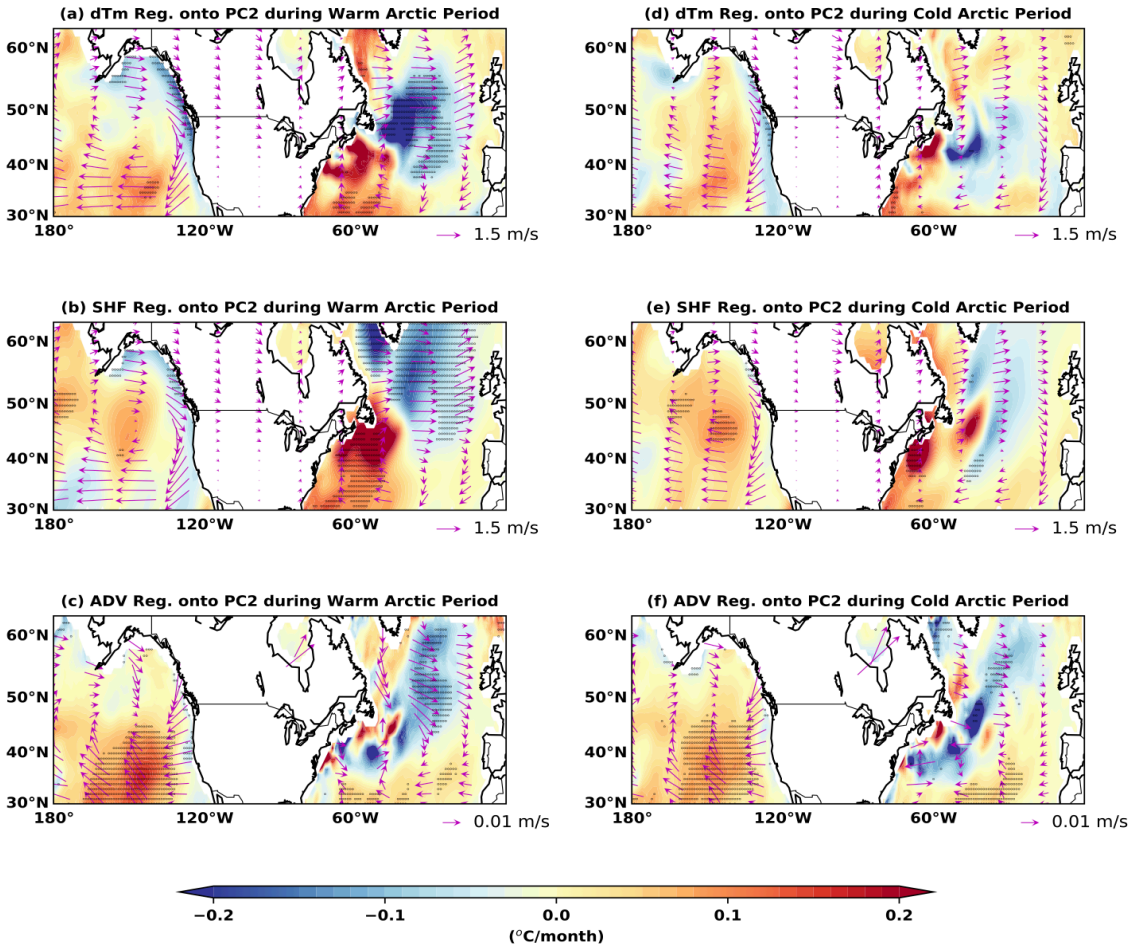

Figure 5.7 (a) the mixed layer temperature tendency (dT_m/dt); (b) the net surface heat fluxes (SHF; positive downward into the ocean); and (c) the horizontal ocean advection regressed onto the *PC2* during warm Arctic period. (d)-(f) are similar to (a)-(c) but regressed onto *PC2* during cold Arctic period. The pink arrows in (a), (b), (d), and (e) are the regressed 1000-hPa winds anomalies while those in (c) an (f) are the regressed surface (averaged from surface to 5-meter depth) ocean current anomalies. The stippling denotes that the regression has statistical significance with *p*-values less than 0.05.

To determine whether or not the expanded TNH pattern can be induced solely by Arctic warming, forced AGCM (CAM5) experiments are conducted. The same EOF and conditional regression analyses on the Z500 anomalies are repeated from the control AGCM ensemble (forty members), which was forced with climatological SST and SIC. No evident TNH expansion effect can be found (Figure 5.8(a)). However, the TNH expansion effect appears in the ensemble AGCM experiment, which was forced with SST and SIC anomalies in the ES-CS region only (Figure 5.8(b)). These AGCM experiment results confirm that the expanded TNH pattern is a robust response of the NH atmospheric circulation to the Arctic warming in the ES-CS region.

The 1920-2080 projections from a forty-member ensemble produced by the CESM-LE simulations using historical (1920-2005) and the RCP8.5 (2006-2080) greenhouse scenario are also examined. The TNH pattern exhibits a particularly prominent expansion in its cross-basin structure during 2041-2080 when greenhouse forcing is strong (Figure 5.8(d)), whereas no evident expansion effect occurs during 1966-2005 when less greenhouse forcing is present (Figure 5.8(c)). The results suggest that stronger Arctic warming in the future could favor the extended cross-basin structure of the TNH pattern, leading to even closer North Pacific-Atlantic climate connectivity.

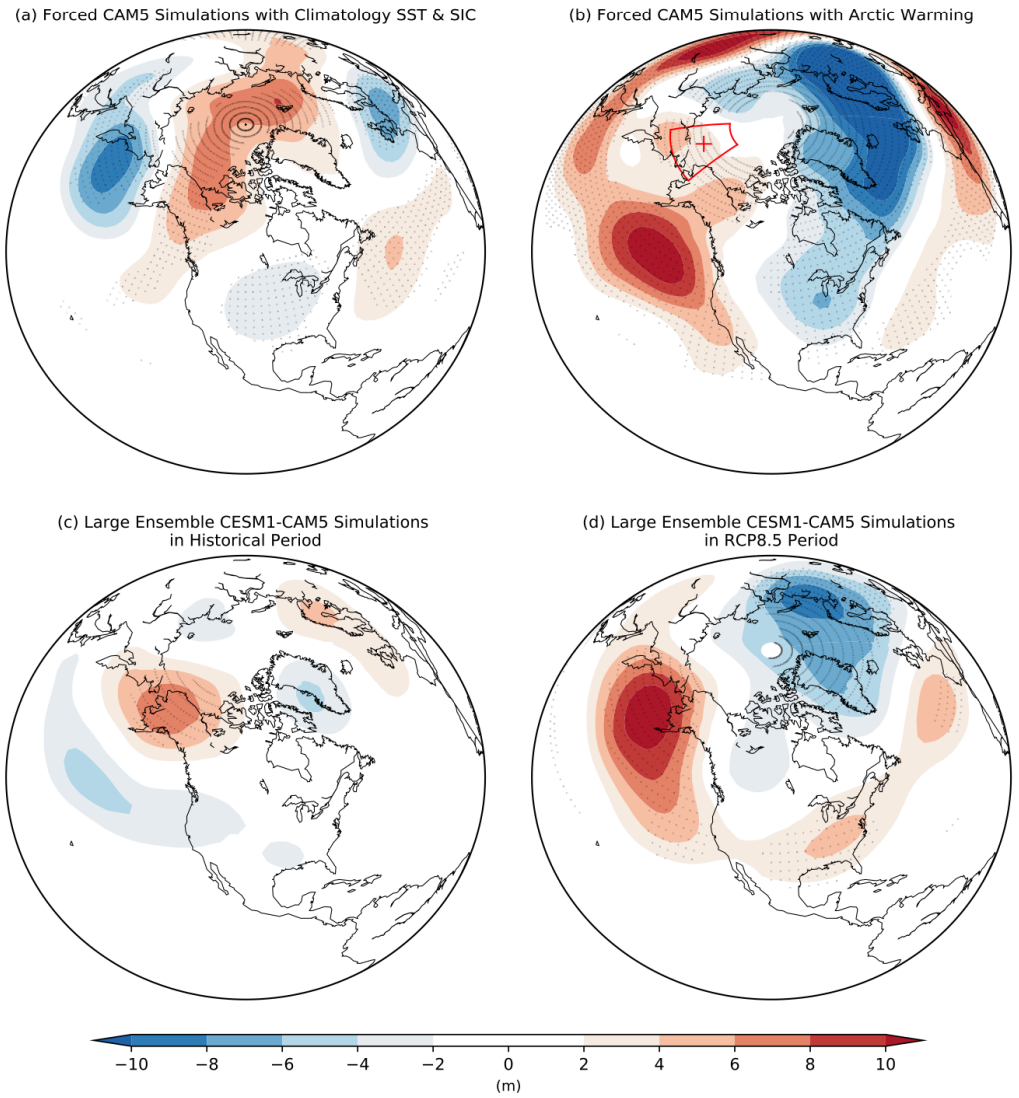

Figure 5.8 The TNH expansion effect in global climate model simulations. As in Figure 5.3(c). but using (a) AGCM (CAM5) simulations forced with climatology SST and SIC boundary condition, (b) AGCM (CAM5) simulations forced with additional SST and SIC anomalies in the ES-CS region, (c) CESM-LE simulations during 1966-2005, and (d) CESM-LE simulations during 2041-2080. The red box in (b) depicts the ES-CS region (65^{o}N-80^{o}N and 160^{o}E-160^{o}E) where additional SST and SIC anomalies are prescribed. The stippling denotes that the difference value has statistical significance with *p*-value less than 0.05.

To quantify the impacts of Arctic warming on the North Pacific-Atlantic climate connectivity, MCA is applied to the combined DJF Z500 and SST anomaly fields over the North Pacific-Atlantic sector (Figure 5.9). The first MCA mode, explaining 51.5% of the squared covariance, is the PDO-related mode. Its atmospheric circulation pattern resembles the PNA pattern (Wallace and Gutzler, 1981) that is related to PDO (Newman *et al.*, 2003), while its SST anomaly pattern is characterized by an arc-shaped warming along the North American west coast (Figure 5.9(a)). High R_t values are found between the MCA1 PC in Z500 field (hereafter Z500 PC) and the PNA index (0.74) and between the MCA1 PC in SST field (hereafter SST PC) and the PDO index (0.85). The second MCA mode, explaining 24.0% of the squared covariance, represents the AO/North Atlantic Oscillation (NAO)-related mode (Yu and Hartmann, 1993; Thompson and Wallace, 1998) and is characterized by a north-south Z500 anomaly pattern over both Pacific and Atlantic sectors (Figure 5.9(b)). The R_t value between the MCA2 Z500 PC and the AO (NAO) index is 0.76 (0.80). The third MCA (MCA3) mode, explaining 10.5% of the total squared covariance, is characterized by a TNH pattern (Figure 4.2(b)) in the atmosphere and SST anomalies in the oceans (Figure 5.9(c)) that resemble those associated with Pacific and Atlantic blob events (Figure 5.1(a)). The MCA3 PC in Z500 field (hereafter Z500 PC) has a high R_t (0.77) with the TNH index, and its PC in SST field (hereafter SST PC) also has high R_t (0.74 and 0.61) with the Pacific blob and Atlantic blob SST indices. The MCA3 mode implies that the co-occurrence of the two blobs induced by the TNH pattern is an important atmosphere-ocean coupled mode in the North Pacific-Atlantic sector. This mode is referred to as the North Pacific-Atlantic Connectivity (NPAC) mode. It is also found that the ES-CS SAT index has a higher R_t with the Z500 PC (0.54) of this NPAC mode than with the corresponding PCs of the first and second MCA modes (0.14 and 0.27), which are related to the AO and PDO, respectively. While

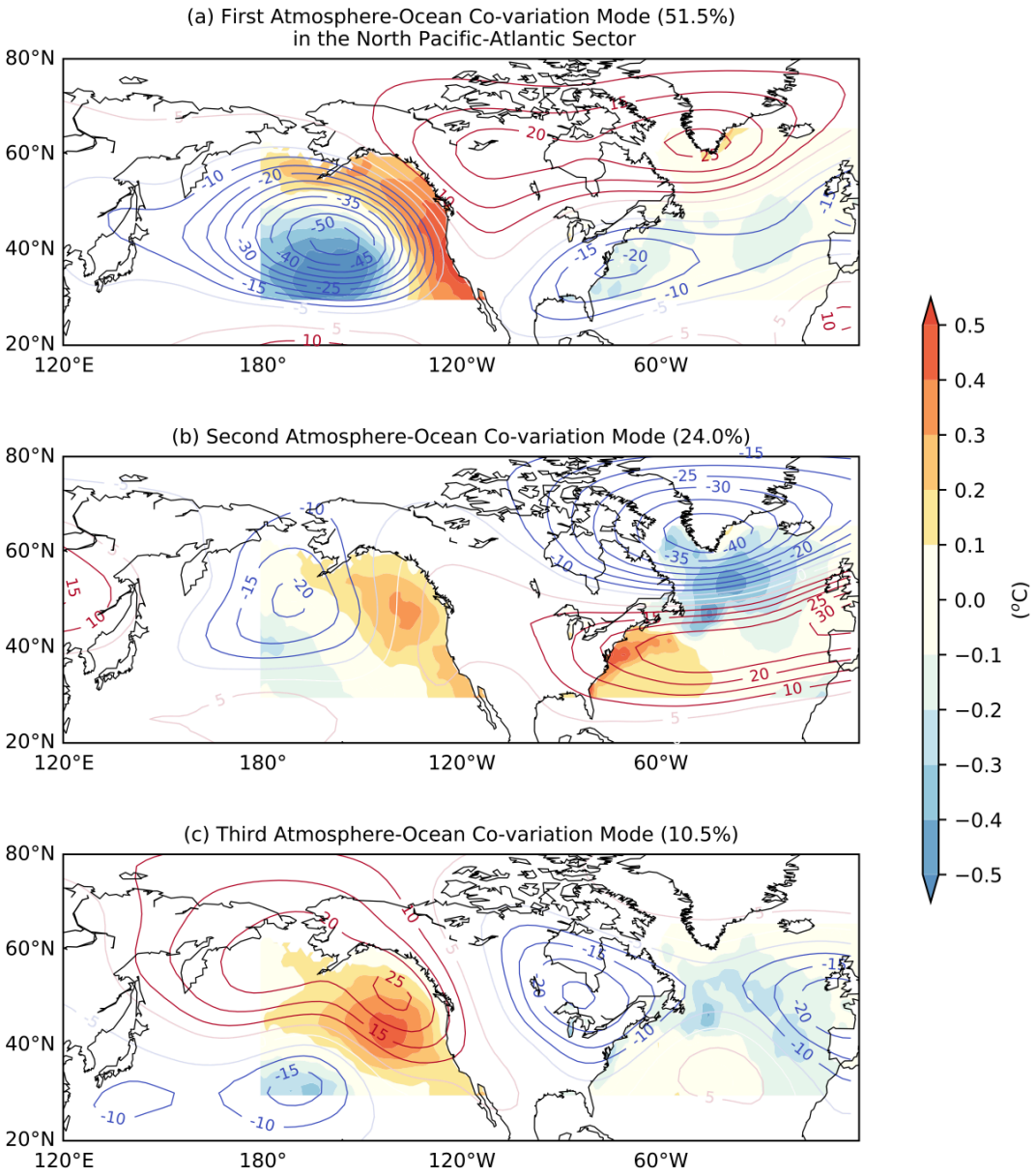

Figure 5.9 The first three leading atmosphere-ocean coupled modes with combined DJF Z500 and SST anomalies in the North Pacific-Atlantic sector. The Z500 domain is between 20°N-90°N and 120°E-0°, while the SST domain between 30°N-65°N and 180°-0°. (a), (b), and (c) represent the Z500 and SST patterns of first, second, and third MCA modes respectively.

previous studies have emphasized the role of the AO in linking accelerated Arctic warming to mid-latitude climate extremes (Cohen *et al.*, 2014), the results show that the TNH pattern is one of the bridging mechanisms that enable the Arctic warming to intensify the North Pacific-Atlantic climate connectivity.

It is also found that ENSO can affect the PDO-related mode due to the significant R_t (0.57 and 0.53) between Niño3.4 index and the MCA2 SST and Z500 PCs. In contrast to the fact that the R_t between the ES-CS SAT index and MCA3 Z500 (SST) PC increases from 0.25 (-0.08) during 1960-1989 to 0.68 (0.47) during 1990-2015, the R_t between the Niño3.4 index and the MCA1 Z500 (SST) PC remains almost unchanged (0.55 (0.56) and 0.53 (0.60)). Thus, the Arctic warming likely surpasses the tropical ENSO forcing to contribute more to the intensification of the North Pacific-Atlantic connectivity in recent decades.

5.5 Summary and Discussion

The results suggest that the Arctic warming may open a new route for climate prediction as the climate connectivity between the North Pacific and Atlantic intensifies. While a number of previous works have focused on Arctic warming impacts on mid-latitude extreme and climate through mechanisms such as the AO (Cohen *et al.*, 2014) and considered the PDO (Wallace and Thompson, 2002), ENSO (Alexander *et al.*, 2002), and Atlantic multi-decadal variability (Vecchi and Delworth, 2017) to be the most important modes for Pacific-Atlantic climate connections, this dissertation work identifies the NPAC mode as a key coupled atmosphere-ocean mode that can enhance the Pacific-Atlantic climate connectivity as the Arctic warms. The NPAC mode consists of a zonally asymmetric TNH circulation pattern in the atmosphere and the co-occurrence of the Pacific warm and Atlantic cold blobs in the oceans. Climate model projections

further suggest that this mode results in stronger Pacific-Atlantic climate connections in the future. The stronger connectivity may enable us to use climate conditions in one ocean to predict the surface ocean variability in the other basin. Therefore, we may be able to establish an inter-basin prediction framework to better monitor and predict the co-occurrence of extreme marine events in mid-latitude oceans.

This chapter addresses the impacts of the Arctic climate variability on the North Pacific-Atlantic climate connectivity. However, we also notice the interannual variability of the Arctic SAT is also changing before and after the early-1990s. Further analyses are needed to illuminate the portion of internall variability contributes to the intensified Pacific-Atlantic climate connectivity. In addition, the tropical forcing may also play an important role. A recent study proposed that the ENSO activity is capable of extending its impacts on the North Pacific further into the North Atlantic and even Europe via tropospheric and stratospheric pathways (Jiménes-Esteve and Domeisen, 2018). A previous study also showed that the PNA-NAO linkage becomes stronger in recent decades, suggesting the forcing from tropical Pacific could influence the Pacific-Atlantic climate connectivity (Pinto *et al.*, 2011). These suggest that that further analyses are required to understand the importance of the forcings from tropical Pacific compared to those from Arctic.

Furthermore, many studies have shown that our climate system has undergone a regime shift since the early 1990s (Yu and Paek, 2015; Wang *et al.*, 2017) and have attributed the shift to the Pinatubo volcanic eruption (Church *et al.*, 2005) or the phase change in the Atlantic multi-decadal variation mode (Vecchi and Delworth, 2017). The findings in this chapter suggest that Arctic forcing may be another contributor to the early 1990s climate regime shift.

CHAPTER6

Conclusions and Future Research Directions

6.1 Summary of Results

In this Dissertation, the changing impacts of El Niño and Arctic warming on mid-latitude climate variability are examined using multiple reanalysis products and state-of-the-art climate models.

Chapter 2 discusses the possible changing impacts of El Niño events on the Great Plains Low-Level Jet (GPLLJ), which is characterized by prominent southerly winds in the central United States (U.S.) during boreal spring. The GPLLJ plays important roles in modulating the hydroclimate of the central U.S. due to its capability to transport moisture and heat from the Gulf of Mexico into the U.S. Great Plains. Reanalysis datasets are analyzed in Chapter 2 to stratify the asymmetric responses of the GPLLJ to Eastern Pacific (EP) El Niño and Central Pacific (CP) El Niño events. While the EP El Niño tends to intensify the GPLLJ via establishing air temperature gradient between northeastern and southwestern U.S., the CP El Niño induces negative sea level pressure anomalies over the Gulf of Mexico that drive northerly wind anomalies that weaken the GPLLJ. The results from Chapter 2 indicate that the El Niño impacts on the GPLLJ may have changed since the early 1990s, as the El Niño changed from the EP to CP type. The influences of the CP El Niño on the GPLLJ are further found to persist longer than those induced by the EP El Niño, implying that CP El Niño SST anomalies may become more useful in predicting boreal springtime U.S. climate variability than EP El Niño SST anomalies.

Chapter 3 shows that asymmetric responses to the two types of El Niño also exist in Mississippi River discharge during boreal spring. Long-term river discharge data and multiple reanalysis datasets are used in the chapter. EP El Niño events are found to induce above-normal spring (March in particular) precipitation within the Mississippi River Basin (MRB), which results in higher soil water content during the subsequent two to three months in the central and western upper MRB. On the other hand, CP El Niño events tend to result in below-normal springtime precipitation that causes deficit in soil water over the Ohio-Mississippi Valley during the following one or two months. Subsurface hydrological storage processes are responsible for the different persistence of the anomalous soil water observed in the MRB between the two El Niño types. The results from Chapter 3 indicate that the more-frequently occurring CP El Niño events in recent and possibly future decades can produce a drier condition, threatening the water supplies in the central U.S.

Chapter 3 also presents a global mapping of the locations of river basins where asymmetric and symmetric responses in discharge occur in response to the two El Niño types during the developing, mature, and decaying phases of El Niño. The river discharge responses largely reflect precipitation responses to the two types of El Niño. Possible human interventions, such as the dam effect, on the El Niño-induced discharge changes are also assessed in this chapter with land surface model simulations driven only by natural forcing. The findings provide information that can help government agencies throughout the world determine whether or not they should revise their traditional methods of applying El Niño conditions to predict river discharge and to plan their water management.

In Chapter 4, the Tropical Northern Hemisphere (TNH) pattern, characterized by a wave train structure in the North Pacific and a zonal oscillation (north-south dipole) structure in the

North Atlantic, is found to be the principal atmospheric circulation pattern responsible for the generation of the Pacific warm blob. Using reanalysis datasets, statistical analyses and case studies of five prolonged Pacific warm blob events (i.e., Jul/1956-Oct/1958, Aug/1961-Aug/1963, Feb/1985-Jan/1987, Apr/1989-Mar/1995, Mar/2013-Dec/2015), it is confirmed that prolonged Pacific warm blob events tend to co-occur during extended periods when the TNH pattern was locked in its positive phase. The TNH pattern generates warm and cold blob events via inducing anomalies in surface heat fluxes and horizontal ocean advections. Although the Pacific Decadal Oscillation (PDO) and El Niño can also induce the arc-shaped warming part of the Pacific warm blob, the core warming part (i.e., the Gulf-of-Alaska warming) of the Pacific blob is tied closely to the TNH pattern. An Empirical Orthogonal Function (EOF) analysis further confirms that the Pacific blob is a dynamic mode independent from PDO or ENSO. In addition, the cross-basin structure of the TNH pattern is found capable of inducing cooling in the North Atlantic resembling the so-called Atlantic cold blob. Therefore, the TNH pattern serves as a conducting mechanism to simultaneously induce out-of-phase SST anomalies in the North Pacific and North Atlantic that resemble the Pacific warm blob and Atlantic cold blob. The TNH-blobs relationship discovered in this chapter implies that climate variability in the North Pacific and North Atlantic can be inter-connected. This inter-basin climate connectivity is further verified with a Maximum Covariance Analysis (MCA).

Chapter 5 extends the findings from Chapter 4 to examine the contribution of the changing Arctic climate to the North Pacific-Atlantic climate connectivity. Based on the reanalysis datasets, the Arctic warming particularly in the East Siberian-Chukchi Sea (ES-CS) region is found to expand the spatial structure of the TNH pattern, which is identified as the second leading EOF mode of the atmospheric circulation variability (next to the Arctic

Oscillation). The expanded TNH pattern induces stronger out-of-phase SST anomalies in both the North Pacific and North Atlantic, which intensifies the Pacific-Atlantic climate connectivity. When the Arctic warming began to accelerate after 1990, this intensified inter-basin connection is manifested as a more frequent co-occurrence of the Pacific warm blob and Atlantic cold blob events. The Arctic warming has also surpassed the tropical forcing associated with ENSO to become a more important factor in intensifying the Pacific-Atlantic climate connectivity after the 1990. Forced atmospheric general circulation model simulations were conducted to verify that it is the additional Arctic warming in the ES-CS region that causes the expansion of the TNH pattern. Coupled climate model projections suggest that the Arctic warming should be more capable of expanding the TNH cross-basin structure under strong greenhouse gas forcing (RCP8.5 scenario) than current climate state (historical scenario).

Overall, the results from Chapters 4 and 5 indicate that the accelerated Arctic changes during recent decades have rendered the Arctic forcing more capable of influencing mid-latitude climate variability.

6.2 Implications for Future Research

6.2.1 Changing Impacts of Other Tropical Oceans on the Mid-latitude Climate Variability

In addition to the changes in the central location of ENSO SST anomalies discussed in Chapters 2 and 3, changes in the SST variation patterns in the tropical Western Pacific (WP) (Wang *et al.*, 2014; Lee *et al.*, 2015) and Indian Ocean (IO) (Seager and Henderson, 2016) may also produce different impacts on the mid-latitude climate variability. Whether or not these changing tropical ocean conditions tend to induce certain types of teleconnection patterns, such

as the TNH pattern, to enhance or weaken their impacts on the mid-latitude climate variability is yet to be understood. I propose in future works to use multiple reanalysis products to first investigate the possible relationships between these tropical ocean variations and mid-latitude climate, and identify what are the underlying mechanisms responsible for establishing these tropical-mid-latitude linkages. I also propose to design a series of numerical experiments, including forced and coupled climate model simulations, with different SST tropical forcings to verify the findings in reanalysis datasets.

6.2.2 The TNH dynamics

The results shown in Chapters 4 and 5 indicate that it is important to understand the underlying dynamics of the TNH pattern. Based on previous studies examining the dynamics of the large-scale atmospheric circulation patterns, such as Pacific Northern American pattern (Wallace and Gutzler, 1981) and Arctic Oscillation (Hoskins, 1983), it is reasonable to consider the TNH dynamics in the context of stationary wave dynamics due to its nature of long persistence. The known sources of the stationary waves are orographic forcing (e.g., Himalaya and Rockies), diabetic heating (e.g., surface temperature contrast over land and sea), and their interactions with transient eddies (e.g., eddy (wave)-mean flow interaction). In addition, since the Arctic warming is suggested to modify above-mentioned mid-latitude dynamics (see a review article by Cohen *et al.*, 2014), exploring how the Arctic warming impacts on them and quantify their relative importance will also advance the understanding of the TNH dynamics. To comprehensively understand each of these possible factors in generating the TNH pattern and how the Arctic warming may interfere with them require elaborated analyses and well-designed

numerical experiments. These proposed works would be the possible future research directions arising from this dissertation.

6.2.3 Using Polar Sea Ice Condition to Monitor Synchronized Pacific and Atlantic Blobs

Based on the findings from Chapters 4 and 5, I plan in future works to explore the possibility of developing an empirical model that uses the Arctic conditions, particularly the sea-ice conditions in the East-Siberian Chukchi Sea region, and the identified physical processes to predict the co-occurrences of the marine extreme events in the North Pacific and North Atlantic. I propose to use NASA satellite observations, global climate models, and multiple reanalysis datasets to attempt initiating the framework. NASA satellite observations will be used because they cover both the polar and mid-latitude oceans with high horizontal resolutions since 1980s. The empirical model will first be built based on the analysis results of observational datasets and then calibrated by the results from numerical simulations. If this empirical model can be built and validated, substantial prediction potentials may be realized for the prediction of the co-occurrence of extreme Pacific and Atlantic blob events.

6.2.4 The Possible Role of Poleward Energy Transport in Modulating Arctic-mid-latitude Interactions

As mentioned in Chapters 1.4 and 5, the global warming signal has been found to be strongest in the near-surface air temperatures (SATs) over the Arctic regions (Graversen *et al.*, 2008; Screen and Simmonds, 2010; Screen *et al.*, 2012), and is referred to as Arctic Amplification (AA, Graversen *et al.*, 2008; Cohen *et al.*, 2014; Pithan and Mauritsen, 2014). The

cause of the AA is generally considered attributed to the sea-ice-albedo feedback, which chains the wider open water due to the sea-ice melting, the more absorption of incoming solar radiation, and the resultant warmer Arctic SATs (Winton, 2006; Serreze and Barry, 2011; Screen *et al.*, 2012). However, this climate feedback relies on the incoming solar radiation, which unlikely works during Arctic perpetual night seasons (e.g., December, January, and February). Many studies have investigated the complimentary mechanisms to maintain this amplified Arctic warming (Gillett *et al.*, 2008; Graversen *et al.*, 2008; Shindell and Faluvegi, 2009; Screen *et al.*, 2012; Stroeve *et al.*, 2012; Pithan and Mauritsen, 2014; Lee *et al.*, 2017).

Among them, the poleward energy transports carried out by the large-scale atmospheric circulations into the Arctic Circle were emphasized (Graversen *et al.*, 2008; Woodgate *et al.*, 2010; Yang *et al.*, 2010; Screen *et al.*, 2012; Zhang, 2015; Screen and Francis, 2016; Lee *et al.*, 2017). For example, Graversen *et al.* (2008) suggested that the poleward atmospheric energy transports are responsible for a significant portion of the Arctic warming in boreal winter seasons, which were later quantified by Yang *et al.* (2010) that the increases of the energy transports (with a rate of 0.32 ± 1.09 W m^{-2} $decade^{-1}$) result in about 50% of the Arctic warming trend in decadal time scale during the last thirty years. Yang *et al.* (2010) further linked the variations of the poleward energy transports to the Arctic Oscillation (Thompson and Wallace, 1998), revealing the possibility that the large-scale atmospheric circulation patterns can relate to the energy transports into the Arctic region.

The other pathway to transport energy from the North Pacific into the Arctic region is through the Bering Strait, which is characterized by a narrow gateway approximately 50 m deep and 85 km wide (Woodgate *et al.*, 2012). On interannual time scales, in situ measurements (i.e., 7-mooring array deployed since 2007, see Figure 1 in Woodgate *et al.*, 2012) reveal that the

oceanic heat fluxes into the Arctic area through the Bering Strait reached the highest value in 2007-2008 (about 5.5×10^{20} J) and lead to significant sea-ice retreat in latter seasons (Woodgate *et al.*, 2012). On the decadal time scale, a series of global climate model simulations suggested that additional heat transport through the Bering Strait can contribute to a reduction of the Arctic sea-ice particularly in the East-Siberian Chukchi Sea region (Zhang, 2015).

Motivated by these studies, I hypothesize that the modification of the TNH pattern due to the Arctic warming as that discussed in Chapter 5 may also affect the poleward energy transports both through atmospheric and oceanic pathways. If the altered TNH pattern favors the increases in the poleward energy transports, it may amplify the existing Arctic warming and exacerbate the Arctic sea-ice melting. Combining these processes may form a positive climate feedback between the mid-latitude climate variability and Arctic region, and intensify the Arctic-mid-latitude interactions. Validating this hypothesis will enhance our understanding of the changes in interactions among, mid-latitude oceans extratropical atmosphere, and cryosphere in the climate system under global warming, and will improve our ability to predict changing Arctic climate.

Appendix A

Empirical Orthogonal Function Analysis

A.1 Introduction

The Empirical Orthogonal Function (EOF) analysis is a statistical tool widely used in the atmospheric, oceanographic, and climate research. The EOF technique was first developed in the social science studies in the early-1900 (e.g., Pearson, 1902), and later introduced by mathematical statistician Harold Hotelling as principal component analysis (PCA, Hotelling, 1933) in statistics and computer science, which is the more common name for the EOF analysis. About a decade later the EOF method was used in meteorological analysis but only for smoothing and prediction purposes (Obukho, 1947; Fukuoka, 1951). Meteorologist Edward Lorenz (Lorenz, 1956) was the first to call this technique the EOF analysis, and since then the EOF analysis started to gain its popularity in geoscience, including atmospheric sciences and oceanography, for exploring data structure and dynamical mode reduction (Hannachi *et al.*, 2007). The EOF method obtained the name Karhunen-Loève basis function in the 1970s (Loève, 1978), aiming for feature extraction in applied mathematics (Fukunaga and Koontz, 1970). In recent decades, the EOF analysis was applied to global atmospheric and oceanic observations to extract large-scale variability modes (e.g., Bjerknes, 1969; Wallace and Gutzler, 1981; Pavan *et al.*, 2000; Wallace and Thompson, 2002), climate model simulations (e.g., Kim and North, 1999; Kim and Yu, 2012), and geoscience mapping tasks (Smith *et al.*, 1996; Kaplan *et al.*, 1997; Alvera-Azcárate *et al.*, 2007; Nikolaidis *et al.*, 2014; Liang *et al.*, 2018).

In this dissertation, the EOF analysis is used in Chapters 2, 3, and 5 for calculating the CP and EP indices following Kao and Yu (2009), in Chapter 4 for examining the SST variability and identifying leading SST variation mode in the North Pacific sector, and in Chapter 5 for investigating leading large-scale atmospheric circulation variability mode in both reanalysis datasets and climate model simulations. A side project applying the EOF method to construct Southern Ocean nitrate maps is introduced in A.4.

A.2 Mathematical Formatting

The original goal of the EOF analysis is to decompose a continuous time-space field (*X(t, **s**)*) into paired functions representing temporal and spatial information ($c_i(t),\ u_i(\boldsymbol{s})$) based on the observed temporal variance. The mathematical formulation is

$$X(t, \boldsymbol{s}) = \sum_{i=1}^{K} c_i(t)\, u_i(\boldsymbol{s}), \qquad \text{(A. 1)}$$

where *K* is the number of modes determined in the decomposition, t and $\boldsymbol{s}$ denote time and spatial position vector respectively (My own impression is that this idea is rooted in the separation of variables to solve a simple ordinary differential equation or a partial differential equation, and/or in Fourier decomposition). In other words, the EOF technique aims at searching a new linear combination of original data that can capture most of the observed temporal variance (Hannachi *et al.*, 2007). In various literatures, the spatial information is called the EOF mode or the PC loadings, while the time information is named the principal component (PC), the EOF expansion coefficients, or the EOF amplitude (see Hannachi *et al.*, 2007; Monahan *et al.*, 2009 for reviews). In this dissertation, I adopt the terminology the 'EOF mode' and 'PC' to represent the spatial structure and time information respectively.

In order to describe the procedures to perform the decomposition and obtain the EOF modes and corresponding PCs in a concise fashion, I adopt matrix and vector notations. The time-space field (*X(t, **s**)*), therefore, can be represented as the matrix form:

$$X = \begin{pmatrix} x_{11} & x_{12} & \cdots & x_{1n} \\ x_{21} & x_{22} & \cdots & x_{2n} \\ \vdots & \vdots & \vdots & \vdots \\ x_{m1} & x_{m2} & \cdots & x_{mn} \end{pmatrix} \qquad \text{(A.2)}$$

where x_{ij} is a data component of *X* at discrete time *i* and spatial grid *j*. The column direction denotes the time advancement at one specific grid of the spatial domain, while the row assigns the spatial grids at a specific time. It is noted that in this dissertation, the monthly climatology values are removed from each component of *X*, so the x_{ij} represents the anomaly field in the following steps.

To find the EOF modes and corresponding PCs based on the temporal covariance, the covariance information from *X* has to be well treated and formulated. Following many review papers and statistical textbooks (e.g., von Storch, 1995; von Storch and Zwiers, 1999; Jolliffe, 2002; Hannachi *et al.*, 2007), the general and convenient way to formulate the covariance of *X* is to calculate its covariance matrix in the form of:

$$S = \frac{1}{m} X^T X \qquad \text{(A.3)}$$

Then the attempt to find the EOF modes and corresponding PCs can be converted mathematically to solve an optimization problem, in which a unit-length vector ($\boldsymbol{u}$) maximizes the variability of *X*. The optimization problem can be formulated as:

$$\max(\boldsymbol{u}^T S \boldsymbol{u}), \text{ subject to } \boldsymbol{u}^T \boldsymbol{u} = 1. \qquad \text{(A.4)}$$

$\boldsymbol{u}$ in Equation (A.4), therefore, can be solved as a eigenvalue problem:

$$S\boldsymbol{u} = \lambda \boldsymbol{u^T} \tag{A.5}$$

The *i*'th EOF mode is then determined by the *i*'th eigenvector $\boldsymbol{u_i}$, and the corresponding eigenvalue λ_i can be obtained by:

$$\lambda_i = \boldsymbol{u}_i^T S \boldsymbol{u}_i = \frac{1}{m} \boldsymbol{u}_i^T X^T X \boldsymbol{u}_i = \frac{1}{m} \|X\boldsymbol{u}_i\|^2, \tag{A.6}$$

which is a measure of the temporal variance of *X* for the *i*'th EOF mode. Here, the first K EOF modes are obtained according to (A.1) depending on the rank of eigenvalues and sorted them in decreasing order. Therefore the first EOF mode has the largest eigenvalue and explains most temporal variance, while the *K*'th EOF mode has the smallest eigenvalue and explains least temporal variance. It is note that the EOF modes are orthogonal with each other due to the properties of the eigenvectors derived from the linear system formulated as (A.5), i.e., $\boldsymbol{u_i u_j^T} = 0$ when $i \neq j$.

To show the relative importance of each EOF mode, the *i*'th eigenvalue is usually converted to *i*'th explained variance, which is defined as:

$$\frac{\lambda_i}{\sum_{p=1}^{K} \lambda_p} \times 100\% \tag{A.7}$$

The time information, i.e., the PC, is then determined by projecting anomaly field *X* onto the corresponding EOF mode. The *i*'th PC is calculate as:

$$PC_i = X\boldsymbol{u}_i \tag{A.8}$$

So the *i*'th eigenvalue λ_i represents the variance of *i*'th PC according to (A.6). Trivially, the PCs are also orthogonal to each other by the fact that $PC_i PC_j^T = X\boldsymbol{u}_i \left(X\boldsymbol{u}_j\right)^T = X\boldsymbol{u}_i \boldsymbol{u}_j^T X^T = 0$ when $i \neq j$.

Considering the computational efficiency to deal with a large dataset, a powerful tool of linear algebra called the singular value decomposition (SVD, Gulub and van Loan, 1996) can be also used to obtain the EOF modes, the PCs, and the explained variances. In the framework of SVD, the data matrix *X* can be decomposed as:

$$X = A\Lambda U^T \tag{A.9}$$

where *A* and *U* are unitary matrices that mean UU^T and AA^T are identity matrices. Λ is called the singular matrix of *X* and has only diagonal elements in decreasing order. It can be shown that the *U*, *A*, and Λ are relating to the EOF modes, PCs, and corresponding eigenvalues. Based on (A.3) and (A.9). the covariance matrix can written as:

$$S = \frac{1}{m}X^T X = \frac{1}{m}\,(A\Lambda U^T)^T A\Lambda U^T = \frac{1}{m}U\Lambda^T A^T A\Lambda U^T = \frac{1}{m}U\Lambda^2 U^T, \tag{A.10}$$

where $\Lambda^2 = \Lambda^T\Lambda$. Comparing (A.5) and (A10) can get the *i*'th row vector of *U* is $\boldsymbol{u_i}$ and the *i*'th eigenvalue λ_i is equal to the *i*'th element of Λ^2/m. Projecting anomaly field *X* onto *U* again obtains the corresponding PC. The algorithm and details of applying the SVD to derive the EOF modes, PCs, and the explained variances are referred to Hannachi *et al.* (2007).

As for the statistical significance of the EOF modes, there is no complete theory. A common method is tempting to measure the uniqueness of each EOF mode. If one EOF mode is unique, its characteristic should be prominent enough to distinguish it from other modes. For this purpose, a rule of thumb proposed by North *et al.* (1982) in determining the 95% confidence level to help distinguish each EOF mode from each other is estimated as:

$$\Delta\lambda_i \approx \lambda_i\sqrt{\frac{2}{m^*}} \tag{A.11}$$

m^* is the effective sample size that can be calculated following Thiébaux and Zwiers (1984):

$$m^* = m\left(1 + 2\sum_{k=1}^{m-1}\left(1 - \frac{k}{m}\right)\rho(k)\right)^{-1}, \qquad (A.12)$$

where $\rho(k)$ is the autocorrelation of the test time series.

In Python, '*numpy*' package offers the SVD function (see https://docs.scipy.org/doc/numpy-1.13.0/reference/generated/numpy.linalg.svd.html) that I use in the dissertation when performing the EOF analysis. I also compare results to those calculated from an EOF Python library, called '*eofs*' (Dawson, 2016; and see http://ajdawson.github.io/eofs/index.html) and to those calculated by solving the eigenvalue problem formulated in Equation (A.5). The same results can be obtained using any of these methods.

To demonstrate these procedures, I apply the EOF analysis on the 500-hPa geopotential height (Z500 hereafter) anomalies within the North Hemisphere domain (20^oN-90^oN) during 1979-2015 obtained from the National Center for Atmospheric Research/National Centers for Environmental Prediction (NCAR/NCEP) reanalysis website (http://www.esrl.noaa.gov/psd/data/gridded/data.ncep.reanalysis.derived.html, Kalnay *et al.*, 1996). I use the monthly Z500 values with linear trend removed. A square cosine weighting along latitude for Z500 anomaly values at each grid is performed before conducting the EOF analysis.

Figure A1 shows the explained variances of the first fifty EOF modes (blue dots) following Equation (A.7) and the 95% confidence intervals (red whiskers) estimated based on Equation (A.11). The explained variance by the first EOF mode is about 14.3% of the total variance, which is much larger than the variances explained by the other EOF modes. This result together with the fact that the upper whisker of the second EOF mode does not overlap with the

lower whisker of the first EOF mode indicate that the first EOF mode can be distinguished from other modes. In contrast, the third EOF mode, for example, is not separable from the fourth EOF mode because their explained variances are similar and confidence intervals are overlapped. In this regard, only the first and second EOF modes are possibly separated from other modes. I only discuss the first and second EOF modes in later discussion.

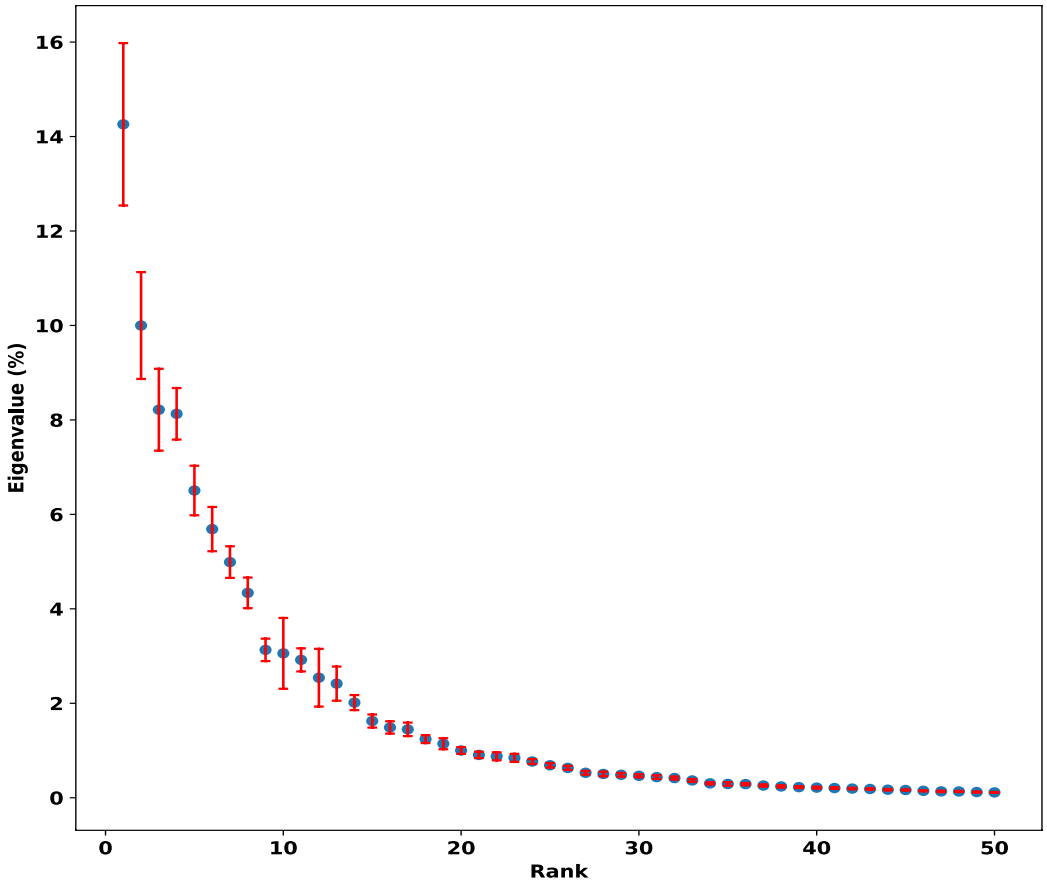

Figure A1 The explained variances of the first fifty EOF modes (blue dots) and their corresponding 95% confidence intervals (red whiskers). The EOF analysis is performed on monthly Z500 anomalies field over Northern Hemisphere domain (20°N-90°N) during 1979-2015.

Figure A2 shows the first two EOF modes, which explain about 14.3% and 10.0% of total variance as shown in Figure A1. The first EOF mode resembles the Arctic Oscillation (Thompson and Wallace, 1998), which is characterized by north-south dipole anomaly structure with centers of action in the south Greenland, northern France, and North Pacific. The second EOF mode, on the other hand, shows a wave-train structure circulating mid-latitude regions. In the Eastern Hemisphere (i.e., from Europe to Eurasia) the large-scale wave has approximately wavenumber-3 structure, while in the Western Hemisphere (i.e., from the North Pacific to North America) wavenumber-2 structure appears. This wavy structure may reflect the combination of large-scale Rossby waves with different wavelength in mid-latitude regions. It is noted that a positive Z500 anomaly center appears in lower latitude in the North Pacific, which may be related to tropical forcing mechanisms, such as El Niño-Southern Oscillation (ENSO).

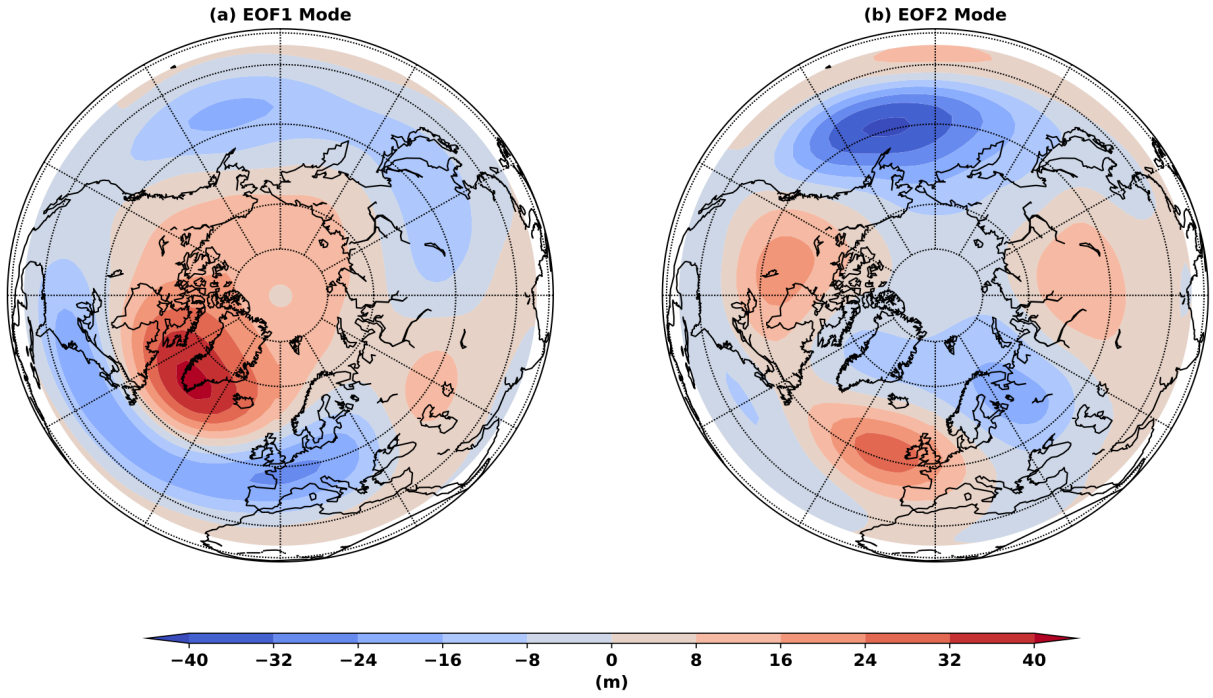

Figure A2 The first (a) and the second (b) EOF modes of monthly Z500 anomalies in the Northern Hemisphere domain (20°N-90°N). The EOF values are converted to original unit by the total variance and eigenvalues.

Figure A3 shows the PCs of the first and second EOF modes (PC1 and PC2 hereafter). They are uncorrelated due to the orthogonality of different PC, which is clearly shown in Figure A4(a) at zero-lag correlation coefficient calculated between PC1 and PC2. The lead-lag correlation coefficient analysis further shows that no strong lead-lag relationship is found between PC1 and PC2 because the correlation coefficient values are small (-0.2 < Corr. < 0.2). The autocorrelations of PC1 and PC2 indicate that the first EOF mode persist longer (about one month) than the second EOF mode (Figure A4(b)). The source of this difference is hard to explain here because of the limited analyses. However, as mentioned in previous discussion that the second EOF mode may relate to ENSO, the longer persistence may be induced by ENSO activity.

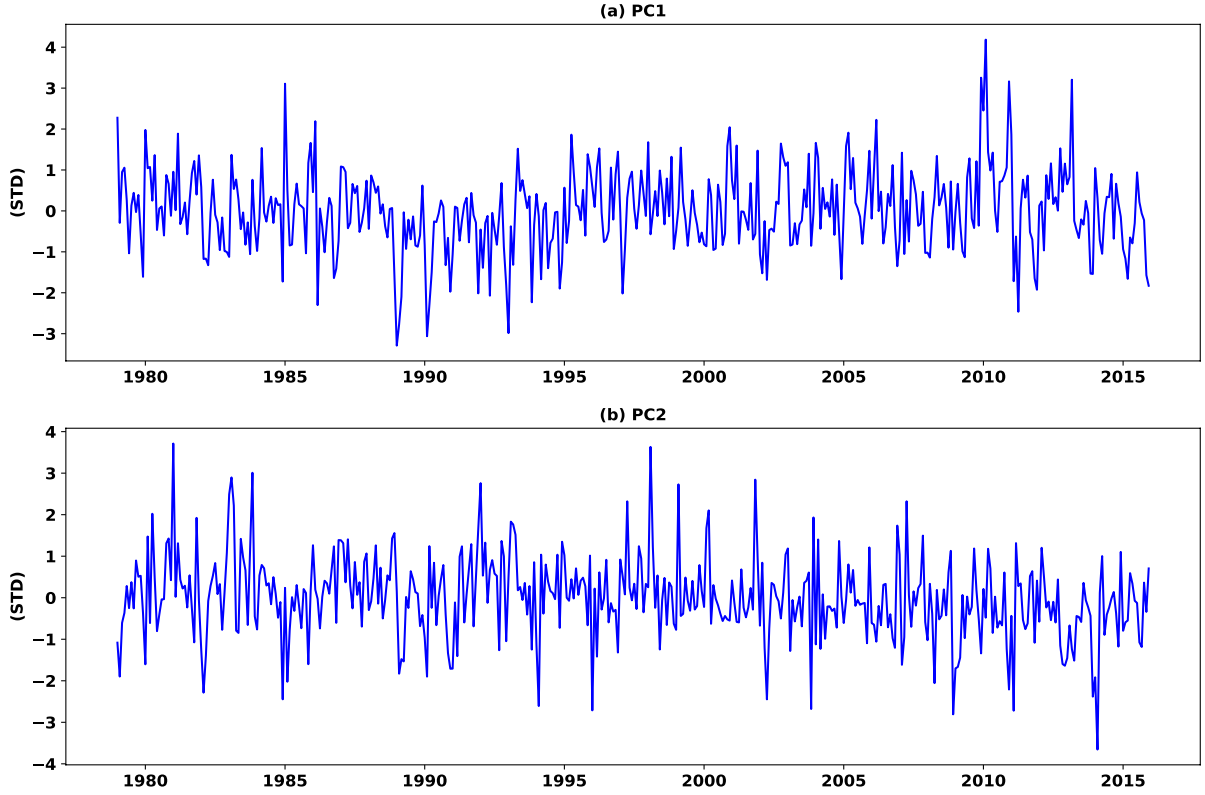

Figure A3 The PCs of the first (a) and second (b) EOF modes during 1979-2015.

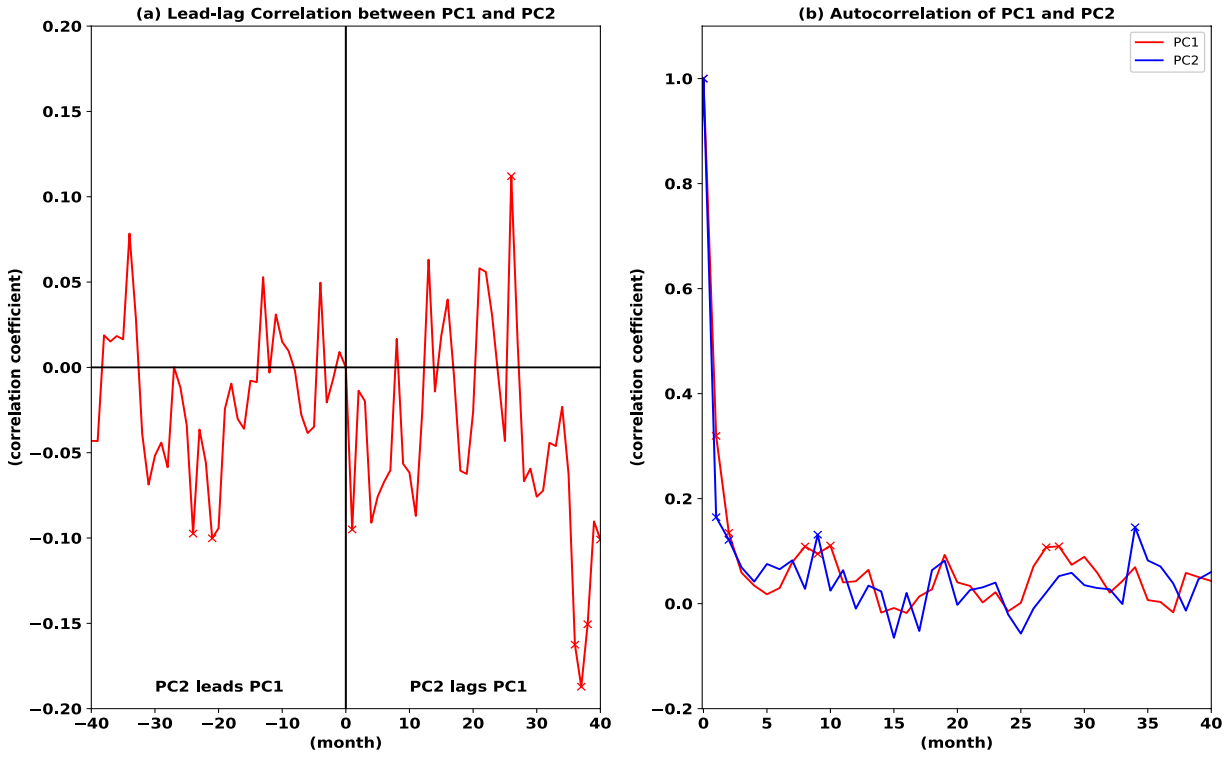

Figure A4 (a) the lead-lag correlation coefficients between PC1 and PC2. The negative values in the x-axis indicate the correlation coefficients calculated as PC2 leads PC1 by that number of month, while the positive values indicate those calculated as PC2 lags PC1. (b) the autocorrelations of PC1 and PC2. The 'X' sign means the correlation coefficient is statistical significant with 95% level.

A.3 Rotated Empirical Orthogonal Function Analysis

To properly interpret the results of EOF analysis is a challenging task due to the strict mathematical restriction on the orthogonality of both the EOF modes and PCs. It is still debating that the large-scale pattern shown in one EOF mode can represent a physical mode of variability in the atmosphere or ocean (Hannachi *et al.*, 2007; Monahan *et al.*, 2009). For example, despite the fact that the first EOF mode shown in Figure A2(a) has spatial structure of the Arctic Oscillation, their relationship requires further validation. A method based on rotation of the EOF modes is developed to help resolve this difficulty. The REOF analysis started to apply in

atmospheric science in the early 1980s (Horel, 1981; Richman, 1981; Jolliffe, 1987), although it has been used earlier in social science studies, known as factor rotation method (Carroll, 1953; Kaiser, 1958).

The goal of the rotated EOF (REOF) technique, therefore, is to ease the strict mathematical constrains on the orthogonality of the EOF modes that enables the REOF modes have the ability to better represent the observed physical mode of variability. This can be achieved by finding a matrix R to construct the REOF modes in the sense of the linear combination of the original EOF modes:

$$B = U_K R, \tag{A.13}$$

where U_K represents the first K leading EOF modes as a matrix form. Then R can be found by solving an optimization problem:

$$max f(B = U_K R), \text{ subject to } RR^T = I \tag{A.14}$$

where f is the rotation criterion and I is the identity matrix. A well-known rotation algorithm, called VARIMAX (Kaiser, 1958) attempts to maximize the variance of the square of B, so Equation (A.14) can be formulated as:

$$max\left(f(B) = \sum_{j=1}^{K}\left(n\sum_{i=1}^{n} b_{ij}^4 - \left(\sum_{i=1}^{n} b_{ij}^2\right)^2\right)\right), \tag{A.15}$$

where b_{ij} is the element of B. In general, the REOF modes would appear as more simple spatial patterns compared to the original EOF modes as the maximization process has the tendency to extract more localized and simple structures. Cautions performing the REOF method are referred to the discussion in Dommenget and Latif (2002).

In Chapters 4 and 5 when calculating the TNH pattern and index, I adopt the VARIMAX rotation method with the first ten normalized EOF modes (i.e., $K = 10$). I use NCAR Command

Language's function 'eofunc_varimax_Wrap' to perform the VARIMAX calculation. The documentary of this function can be found in NCAR Command Language's official website (https://www.ncl.ucar.edu/Document/Functions/Contributed/eofunc_varimax_Wrap.shtml).

In Figure A5, I show the first ten REOF modes adopting the VARIMAX method using the first ten EOF modes from the fifty modes described in A.2. The Z500 anomaly centers of the REOF modes become more localized. For example, the anomaly north-south dipole structure of the first REOF mode locates only in the North Atlantic rather than extending toward other basins, such as the North Pacific and Eurasia (Figure A2(a)). The results reflect the effect of REOF method. Localized structure can also found in other lower-order modes. Whether they are corresponding to any physical modes of variability in the atmosphere requires further investigations. Details of how to identify the TNH mode can be found in Chapter 4.3.

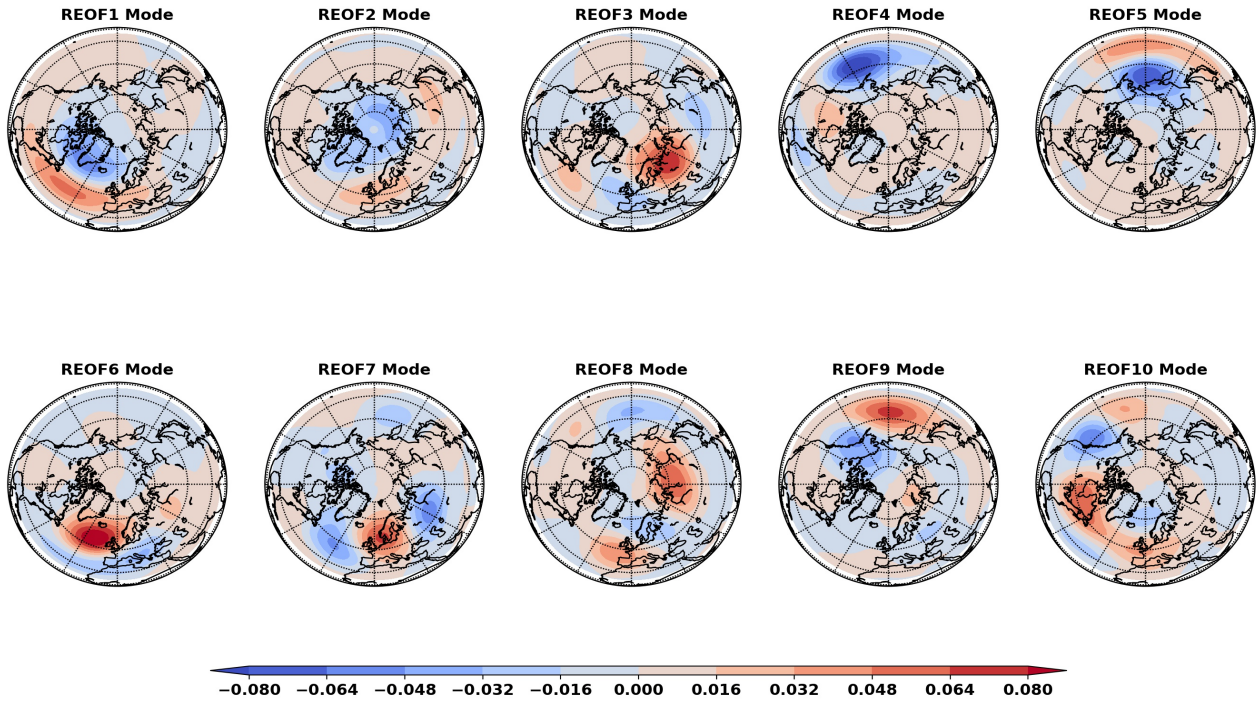

Figure A5 The first ten REOF modes of the Z500 anomalies in the North Hemisphere domain obtained using VARIMAX method. (20°N-90°N). The values of the color shadings are the original REOF values without scaling.

A.4 An Application for Southern Ocean Nitrate Mapping

A side project cooperated with Doctor Matthew Mazloff and Doctor Isabella Rosso of Scripps Institution of Oceanography assesses the capability of the EOF analysis to construct Southern Ocean (SO) nitrate maps. The goal of this study is to inform the skill of constructed SO nitrate maps using varying data sampling strategies. The mapping method adopts multi-variate EOF (MEOF) method – based on the EOF method but incorporating different variables. The salinity, potential temperature (temperature hereafter), and nitrate (N-S-T) fields are sampled from a state-of-the-art biogeochemical general circulation model simulation. Synthetic N-S-T datasets are created by sampling modeled N-S-T fields in specific SO regions, either determined by random selection or by selecting regions over a certain threshold of nitrate temporal variances. The first five hundred MEOF modes, determined by their capability to reconstruct the original N-S-T fields, are projected onto these synthetic N-S-T data to construct time-varying nitrate maps. Normalized root-mean-square errors (NRMSE) are calculated between the constructed nitrate maps and the original modeled fields for different sampling strategies. The ability to obtain the spatiotemporal nitrate features by sampling according to nitrate temporal variances outperforms random sampling. A K-means cluster method that considers the N-S-T combined variances to identify key regions to insert data is most effective in reducing the mapping errors. These findings are further confirmed by a series of mapping error analyses that also address the significance of data sampling density. And the results provide a sampling framework to prioritize the deployment of biogeochemical Argo floats for constructing nitrate maps. Here, the capability of he MEOF method to construct SO nitrate maps are introduced. Details are referred to Liang *et al.* (2018).

A 4.1 Biogeochemical General Circulation Model

The biogeochemical general circulation model (GCM) used in this study to provide the reference nitrate, salinity, and temperature fields is the MITgcm (Marshall *et al.*, 1997) coupled to the modified Biogeochemistry with Light, Iron, Nutrient, and Gases (BLING) model (Galbraith *et al.*, 2010). A sea ice component is also included (Losch *et al.*, 2010). This biogeochemical GCM setup has been applied to estimate SO dynamical and biogeochemical states (Verdy and Mazloff, 2017). The model domain is 78^{o}S to 30^{o}S at 1/3^{o} resolution with a Mercator projection, and then the resolution telescopes to a coarser resolution from 30^{o}S to the equator. The vertical z-coordinate grid has 52 layers with varied thickness from about 4 m at the surface to 400 m at depth. The bathymetry is derived from ETOPO1 (Amante and Eakins, 2009). For this work an analysis domain spanning 64.8^{o}S to 30.4^{o}S, and subsample the model on a Mercator grid with 2^{o} resolution in longitude and approximately 1.1^{o} in latitude are considered. The sample spacing ranges from 96 km at 64.8^{o}S to 190 km at 30.4^{o}S.

The biogeochemical component, adapted from the original BLING model (Galbraith *et al.*, 2010), includes nitrogen cycling and phytoplankton dynamics (Verdy and Mazloff, 2017). Evolutions and interactions of eight prognostic tracers (i.e., inorganic/organic forms of nitrogen and phosphorus, dissolved inorganic carbon (DIC), alkalinity, oxygen, and iron) are calculated in the model representing important biogeochemical processes, such as the conversion between DIC and organic matters, phytoplankton evolution, and net community production (Verdy and Mazloff, 2017; Rosso *et al.*, 2017).

A number of datasets are utilized to initiate and to force the biogeochemical GCM. The atmospheric state is obtained from ECMWF ERA-interim reanalysis products (Dee *et al.*, 2011). The initial biogeochemical tracer fields are derived from the GLODAPv2 climatology (Lauvset

et al., 2016; Key *et al.*, 2015), the World Ocean Atlas 2013 climatologies (Garcia *et al.*, 2014a; Garcia *et al.*, 2014b), and coupled model simulation with BLING version 2 (communication between E. Galbraith and M. Mazloff). The river and Antarctic freshwater discharge are derived from continental freshwater products of Dai and Trenberth (2002) and Hammond and Jones (2016). The model is run for 130 years with a time step of one hour by looping the 2005 to 2014 forcing conditions. Monthly averaged fields are output for diagnostics. The N-S-T fields in last 60 years at 100 m depth are only used, which is approximately the average depth of nutrocline in the SO (not shown). The simulated N-S-T fields are used as the reference N-S-T fields in the following analyses. The N-S-T anomaly fields are calculated by subtracting the monthly mean fields over the 60-year analysis period, thus representing the departure from the seasonal cycle.

A 4.2 The MEOF Method

The MEOF method is adopted to construct SO nitrate maps. Here the procedures of the MEOF calculation are summarized. First of all, the N-S-T anomaly fields are dived by their total (spatial and temporal) standard deviations and transformed into a data matrix X in the form of:

$$\begin{bmatrix} N_{1,1} & N_{1,2} & \cdots & \cdots & N_{1,n} \\ \vdots & \vdots & \cdots & \cdots & \vdots \\ N_{m,1} & N_{m,2} & \cdots & \cdots & N_{m,n} \\ S_{1,1} & S_{1,2} & \cdots & \cdots & S_{1,n} \\ \vdots & \vdots & \cdots & \cdots & \vdots \\ S_{m,1} & S_{m,2} & \cdots & \cdots & S_{m,n} \\ T_{1,1} & T_{1,2} & \cdots & \cdots & T_{1,n} \\ \vdots & \vdots & \cdots & \cdots & \vdots \\ T_{m,1} & T_{m,2} & \cdots & \cdots & T_{m,n} \end{bmatrix}, \qquad \text{(A.16)}$$

where m represents the grid points of the reference N-S-T fields with land points cropped and n the total time steps. Then the SVD on X to isolate the MEOF modes and PCs:

$$UDV^T = X, \qquad (A.17)$$

where D is a diagonal matrix, in which the diagonal elements (i.e., D_{ii}) represent the eigenvalues according to the rank in amplitude (from largest to smallest), and the superscript T means transpose of the matrix. The MEOF modes are obtained from U and PCs are calculated by the projection of X onto U. As we have 720 time records, 720 MEOF modes can be obtained. A schematic chart to clarify the details of the MEOF calculation is shown in Figure A6 (Step 1).

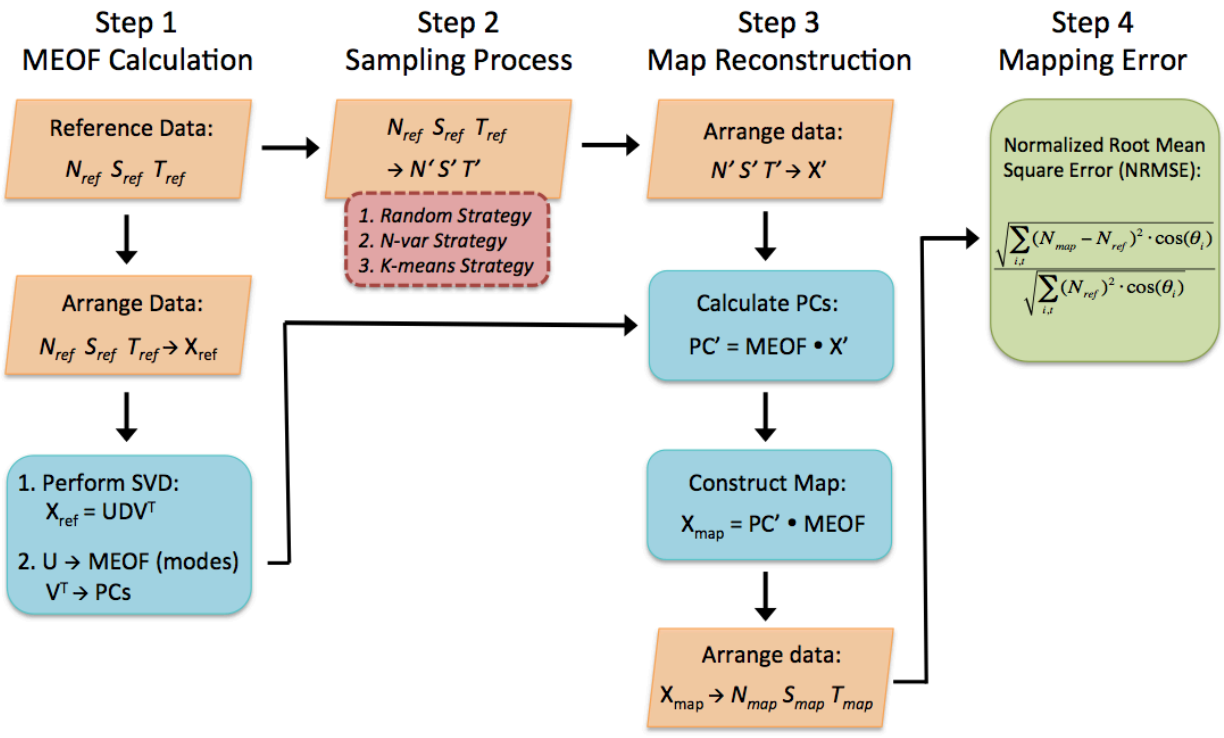

Figure A6 Schematic of the MEOF mode calculation, sampling processes, and map construction.

Figure A7 demonstrates the spatial patterns of the leading five MEOF modes, which combine to explain 36% of the total combined N-S-T variance. The N-S-T patterns of the first MEOF mode capture important features, and show resemblances with each other at low latitudes (see the first column panels in Figure A7), particularly at the confluence of Brazil and Malvinas Currents, and in the downstream regions where the positive nitrate anomalies and out-of-phase salinity and temperature anomalies are collocated. In contrast, the N-S-T patterns do not resemble each other in higher latitudes. In the Bellingshausen-Amundsen Sea regions (green boxes in the first column panels in Figure A7) the anomaly pattern of strong positive temperature signals differs from those of moderate negative nitrate and salinity patterns. These latitude-dependent similarities and differences seem to be the general features of the other four MEOF modes (shown in second to fifth column panels in Figure A7) and other lower-order MEOF modes (not shown).

To evaluate the relationships between the number of MEOF modes and the capability to reproduce the reference nitrate anomaly field, the snapshots of the mapped nitrate anomalies for one random August in the biogeochemical GCM simulation from using the first five MEOF modes to using total 720 MEOF modes are shown in Figures A8(a)-(e). The more MEOF modes are used to construct the SO nitrate maps, the more detailed features of nitrate anomalies are manifested. Taking the anomalies at the Brazil-Malvinas confluence and its downstream regions as an example, when only five MEOF modes are used, the reproduced nitrate anomalies show two parallel, out-of-phase anomaly bands, extending from coastal region into South Atlantic sector (Figure 8(a)). In contrast, the meandering structures of nitrate anomalies become more evident when using more MEOF modes (Figures 8(b)-(e)).

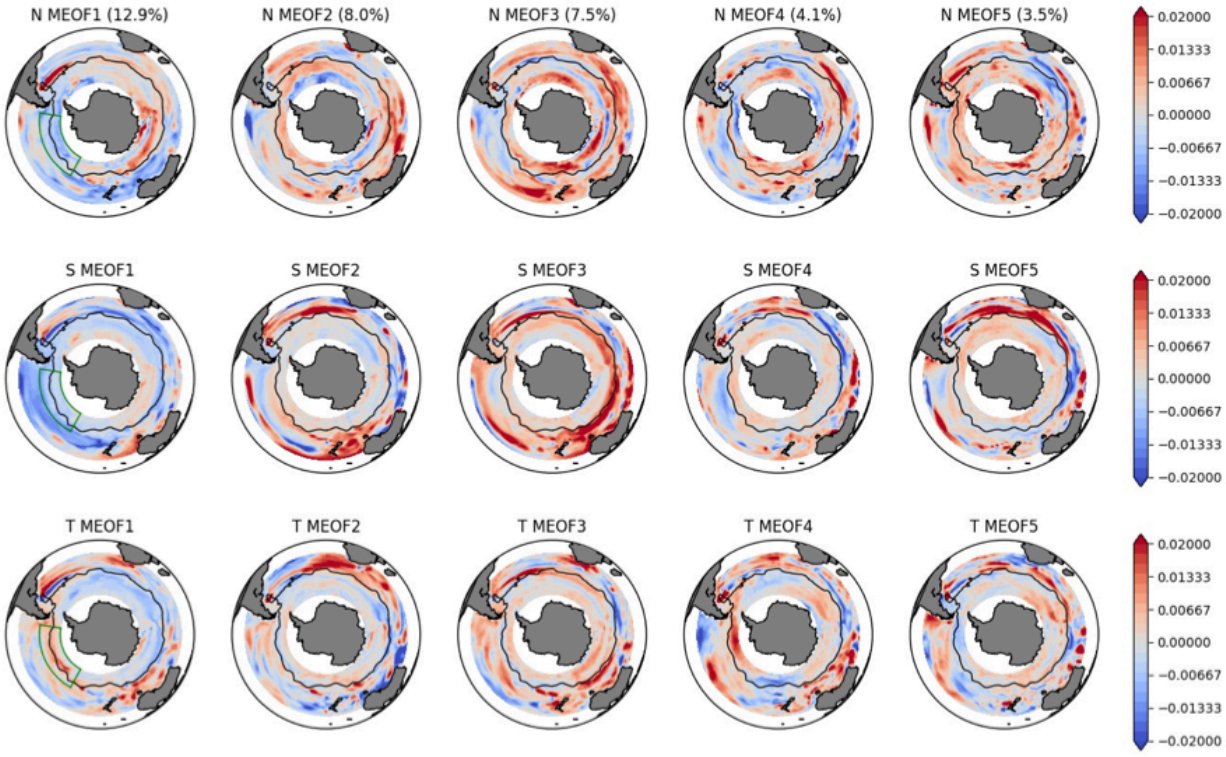

Figure A7 The first five leading MEOF modes. The maps shown from top to bottom are the spatial patterns of the MEOF modes associated with nitrate, salinity, and temperature fields. The green boxes (150°W-80°W, 65°S-50°S) in the first column denote the Bellingshausen-Amundsen Sea regions. The black curve circling low-latitude oceans represents Subantarctic Front according to Orsi *et al.* (1995).

The capability of capturing the details can be quantified by examining the NRMSEs between the mapped nitrate anomaly field (N_{map}) and the reference nitrate field (N_{ref}). The NRMSE for nitrate maps is defined as:

$$NRMSE = \frac{\sqrt{\sum_{i,t}\left(N_{map} - N_{ref}\right)^2 \cdot \cos\theta_i}}{\sqrt{\left(N_{map}\right)^2 \cdot \cos\theta_i}}, \qquad (A.18)$$

where t,i indicate time step and spatial grid point respectively, and θ_i is the latitude at grid i in radian unit. Figure 8(f) shows the nitrate NRMSEs with increasing number of MEOF modes

used in recovering the reference nitrate anomaly field (cyan line). The first five MEOF modes result in about 0.81 NRMSE (36% variance explained), which is greatly reduced to about 0.092 (99% variance explained) using 500 modes. Similar reduction of NRMSEs can also be found for recovering salinity and temperature fields (magenta and green lines in Figure 8(f)).

Here the applicability of the MEOF method to construct SO nitrate maps is introduced. More results and the importance of this study are referred to Liang *et al.* (2018).

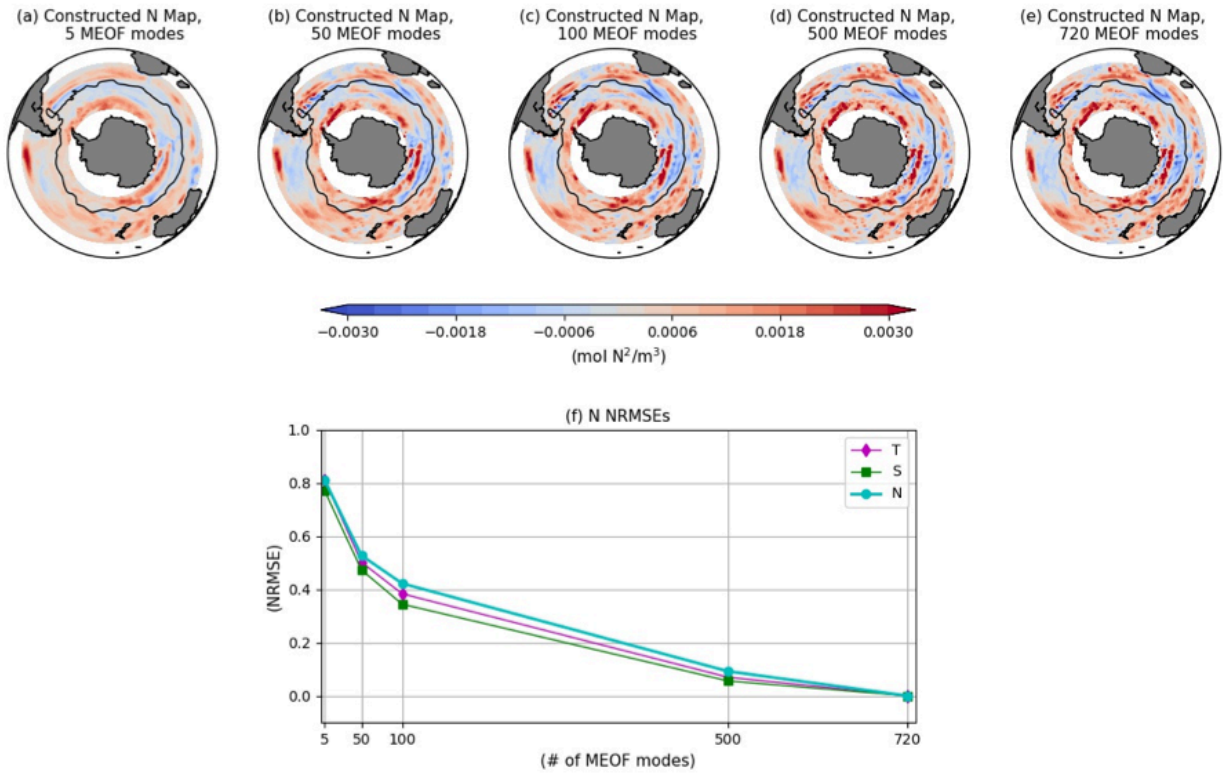

Figure A8 (a)-(e) show constructed nitrate anomaly maps using the first five, fifty, one-hundred, five-hundred, and 720 MEOF modes in August of a random model year. In panel (a)-(e), the black curve circling low-latitude oceans represents Subantarctic Front according to Orsi et al. (1995). As in Figure A7, the black curve circling low-latitude oceans represents Subantarctic Front. (f) shows the NRMSEs between each constructed nitrate map and the reference nitrate anomaly fields (cyan line). Also shown in (f) are the NRMSEs for salinity (green line) and temperature fields (magenta line).

Appendix B

Maximum Covariance Analysis

A.1 Introduction

Prohaska (1976) may be the first to apply Maximum Covariance Analysis (MCA) in meteorological research; however, it is until 1990s that the MCA gained it popularity among atmospheric and oceanographic studies (Bretherton *et al.*, 1992; Wallace *et al.*, 1992). The concept of MCA is rooted from the EOF analysis, but it extends to incorporating two fields and aims for extracting the common features of spatial patterns between two fields. Therefore, MCA has been used to find coupled mode in the atmosphere and ocean, or represent their co-variability mode.

Cautions have to be bear in mind when applying MCA analysis. MCA may have difficulties in revealing that which field is the cause and which field is the response, showing non-linear relationship between two fields (for example the streamfunction and vorticity fields), or distinguishing physical modes from artificial modes. Cherry (1996) suggested that a better strategy is to investigate the relationship between the PCs of these two fields obtained by performing separate EOF analysis before performing MCA. If the highly correlated relationship between two fields can be identified, MCA could also extract their coupling co-variability. It is also noted that the spatial domains chosen for the two fields should be largely consistent, avoiding the possibility that the co-variability mode captured by MCA only reflects pure coincidence.

The MCA is used in Chapters 4 and 5 to examine the possible Pacific-Atlantic climate variability modes over the 500-hPa geopotential height and sea surface temperature anomaly fields. Separate EOF and correlation analyses are also performed to support the findings from MCA alone following the suggestions of Cherry (1996).

A.2 Mathematical Formatting

Consider two anomaly fields X and Y arranged in matrix forms:

$$X = \begin{pmatrix} x_{11} & x_{12} & \cdots & x_{1n} \\ x_{21} & x_{22} & \cdots & x_{2n} \\ \vdots & \vdots & \vdots & \vdots \\ x_{m1} & x_{m2} & \cdots & x_{mn} \end{pmatrix}, \; Y = \begin{pmatrix} y_{11} & y_{12} & \cdots & y_{1p} \\ y_{21} & y_{22} & \cdots & y_{2p} \\ \vdots & \vdots & \vdots & \vdots \\ y_{m1} & y_{m2} & \cdots & y_{mp} \end{pmatrix}, \qquad \text{(B.1)}$$

where x_{ij} (y_{ij}) is a data component of X (Y) at discrete time i and spatial grid j. The column direction denotes the time advancement at one specific grid of the spatial domain, while the row assigns the spatial grids at a specific time. MCA first calculate the covariance matrix:

$$C_{XY} = \frac{1}{m} X^Y Y, \qquad \text{(B.2)}$$

Then MCA performs Singular Value Decomposition of C_{XY} to get:

$$C_{XY} = U \Lambda V^T, \qquad \text{(B.3)}$$

The U and V^T are used to represent the spatial structure of X and Y, i.e., the MCA modes. Finally projections of U and V onto X and Y give rise to their time information (i.e., principal components). And Λ is a diagonal matrix which elements are the corresponding singular values of each MCA mode. In general, the elements in Λ are arranged in decreasing order.

The relative importance of the MCA mode can be estimated in terms of squared covariance fraction, which is defined as:

$$f_k = \frac{\lambda_k^2}{\sum_{i=1}^{K} \lambda_i^2}, \tag{B. 4}$$

where K is the total number of the MCA modes and λ_k is the k'th element in Λ.

BIBLIOGRAPHY

Alexander, M. A., I. Bladé, M. Newman, J. R. Lanzante, N.-C. Lau, and J. D. Scott, 2002: The atmospheric bridge: The influence of ENSO teleconnections on air-sea interaction over the global oceans. *J. Climate*, **15**, 2205–2231, doi:10.1175/1520-0442(2002)015,2205:TABTIO.2.0.CO;2.

Alexeev, V. A., P. L. Langen, J. R. Bates, 2005: Polar amplification of surface warming on an aquaplanet in "ghost forcing" experiments without sea ice feedbacks. *Clim. Dynam.*, **24**, 655-666.

Alvera-Azcárate, A., A. Barth, J.-M. Beckers, and R. H. Weisberg, 2007: Multivariate reconstruction of missing data in sea surface temperature, chlorophyll, and wind satellite fields. *J. Geophys. Res.*, **112**.

Amante, C., and B. Eakins, 2009: ETOPO1 Global Relief Model converted to PanMap layer format. *NOAA-National Geophysical Data Center*, doi:10.1594/PANGAEA.769615.

Amaya, D. J., N. E. Bond, A. J. Miller, and M. J. DeFlorio, 2016: The evolution and known atmospheric forcing mechanisms behind the 2013-2015 North Pacific warm anomalies. *US CLIVAR Variations*, Vol. 14, No. 2, US CLIVAR, Washington, DC, 1-6, https://usclivar.org/newsletter/newsletters.

Ashok, K., S. K. Behera, S. A. Rao, H. Weng, and T. Yamagata, 2007: El Niño Modoki and its possible teleconnection, *J. Geophys. Res.*, **112**, C11007, doi:10.1029/2006JC003798.

Barandiaran D., S.-Y. Wang, K. Hilburn, 2013: Observed trends in the Great Plains low-level jet and associated precipitation changes in relation to recent droughts. *Geophys. Res. Lett.*, **40**, L058296.

Barnes, E. A. and I. R. Simpson, 2017: Seasonal Sensitivity of the Northern Hemisphere Jet Streams to Arctic Temperatures on Subseasonal Time Scales. *J. Climate*, **30**, 10117-10137.

Barnston, A. G., and R. E. Livezey, 1985: A high resolution roated EOF analysis of monthly and seasonally averaged 700 mb height, Proc. Ninth Conf. on Probability and Statistics in Atmospheric Science, Virginia Beach, *Amer. Meteor. Soc.*, 290-297.

Barnston, A. G., and R. E. Livezey, 1987: Classification, seasonality and persistence of low-frequency atmospheric circulation patterns. *Mon. Wea. Rev.*, **115**, 1083-1126, doi:10.1175/1520-0493(1987)115,1083:CSAPOL.2.0.CO;2.

Barnston, A. G., and M. S. Halpert, 1991: Modulation of Southern Oscillation-Northern Hemisphere mid-winter climate relationships by QBO. *J. Climate*, **4**, 203–217, doi:10.1175/1520-0442(1991)004,0203:MOSONH.2.0.CO;2.

Basara, J. B., J. N. Maybourn, C. M. Peirano, J. E. Tate, P. J. Brown, J. D. Hoey, B. R. Smith, 2013: Drought and associated impacts in the Great Plains of the United States - a review. *Int. J. Geosci.,* **4**, 72-81.

Behringer, D. W., M. Ji, and A. Leetmaa, 1998: An improved coupled model for ENSO prediction and implications for ocean initialization. Part I: The ocean data assimilation system. *Mon. Wea. Rev.*, **126**, 1013-1021, doi:10.1175/1520-0493(1998)126,1013:AICMFE.2.0.CO;2.

Berrisford, P., P. Kallberg, S. Kobayashi, D. P. Dee, S. M. Uppala, A. J. Simmons, and P. Poli, 2011: Atmospheric conservation properties in ERA-Interim, *ERA Report Series*, ECMWF: Reading, UK.

Bjerknes, J., 1969: Atmospheric teleconnections from the equatorial Pacific. *Mon. Wea. Rev.,* **97**, 163-172.

Bond, N. A., M. F. Cronin, H. Freeland, and N. Mantua, 2015: Causes and impacts of the 2014 warm anomaly in the NE Pacific. *Geophys. Res. Lett.*, **42**, 3414-3420, doi:10.1002/2015GL063306.

Bonner, W. D., J. Paegle, 1970: Diurnal variations in the boundary layer winds over the south central United States in summer. *Mon. Wea. Rev.,* **98**, 735-744.

Boyer, E. W., R. W. Howarth, J. N. Galloway, F. J. Dentener, P. A. Green, and C. J. Vörösmarty, 2006: Riverine nitrogen export from the continents to the coasts Glob. *Biogeochem. Cycles*, **20**, GB1S91.

Brayshaw, D., B. Hoskins, and M. Blackburn, 2009: The Basic Ingredients of the North Atlantic Storm Track. Part I: LandSea Contrast and Orography. *J. Atmos. Sci.*, **66**, 2539–2558.

Bretherton, C. S., C. Smith, J. M. Wallace, 1992: An intercomparison of methods for finding coupled patterns in climate data. *J. Climate,* **5**, 541-560.

Bretherton, C. S., M. Widmann, V. P. Dymnidov, J. M. Wallace, and I. Bladé, 1999: The effective number of spatial degrees of freedom of a time-varying field. *J. Climate*, **12**, 1990-2009, doi:10.1175/1520-0442(1999)012,1990:TENOSD.2.0.CO;2.

Byerle, L. A., J. Paegle, 2003: Modulation of the Great Plains low-level jet and moisture transports by orography and large-scale circulations. *J. Geophys. Res.*, **108**, D003005.

Capotondi, A., and Coauthors, 2015: Understanding ENSO diversity. *Bull. Am. Meteorol. Soc.*, **96**, 921-938.

Carroll, J. B., 1953: An analytical solution for approximating simple structure in factor analysis. *Psychometrika,* **18**, 23-38.

Chen, J., and P. Kumar, 2002: Role of terrestrial hydrologic memory in modulating ENSO impacts in North America. *J. Climate*, **15**, 3569–3585.

Chen, M., P. Xie, J. E. Janowiak, and P. A. Arkin, 2002: Global land precipitation: a 50-yr monthly analysis based on gauge observations. *J. Hydrometeor.*, **3**, 249-266.

Cherry, S., 1996: Singular value decomposition analysis and canonical correlation analysis. *J. Climate*, **9**, 2003-2009.

Cheung, H. H. N., N. Keenlyside, N.-E. Omrani, and W. Zhou, 2018: Remarkable link between projected uncertainties of Arctic sea-ice decline and winter Eurasian climate. *Adv. Atmos. Sci.,* **35**, 38-51.

Chiang, J.C.H., K. S. Tokos, S.-Y. Lee, and K. Matsumoto, 2018: Contrasting impacts of the wintertime South Pacific Split Jet and the Southern Annual Mode modulation on Southern Ocean circulation and biogeochemistry. Paleoceanography and Paleoclimatology, **33**, doi:10.1002/2017PA003229.

Chiew, F. H. S., and T. A. McMahon, 2002: Global ENSO-streamflow teleconnection, streamflow forecasting and interannual variability. *Hydrol. Sci. J.*, **47**, 505-522.

Church, J. A., N. J. White, and J. M. Arblaster, 2005: Significant decadal- scale impact of volcanic eruptions on sea level and ocean heat content. *Nature,* **438**, 74-77.

Cohen, J., J. Furtado, M. Barlow, V. Alexeev, and J. Cherry, 2012: Arctic warming, increasing fall snow cover and widespread boreal winter cooling. *Environ. Res. Lett.*, **7**, 014007, doi:10.1088/1748-9326/7/1/014007.

Cohen, J. and Coauthors, 2014: Recent Arctic amplification and extreme mid-latitude weather. *Nat. Geosci.*, **7**, 627–637, doi:10.1038/ngeo2234.

Cohen, J., K. Pfeiffer, and J. A. Francis, 2018: Warm Arctic episodes linked with increased frequency of extreme winter weather in the United States. *Nature commun.*, **9**, 869.

Cook, K. H., E. K. Vizy, Z. S. Launer, C. M. Patricola, 2008: Springtime intensification of the Great Plains low-level jet and Midwest precipitation in GCM simulations of the twenty-first century. *J. Climate,* **21**, 6321-6340.

Cowell, C. M., and R. T. Stoudt, 2002: Dam-induced modifications to upper Allegheny River streamflow patterns and their biodiversity implications. *J. Amer. Water Resour. Assoc.,* **38**, 187-196.

Chou, C., and M.-H. Lo, 2007; Asymmetric responses of tropical precipitation during ENSO. *J. Climate*, **19**, 3411–3433.

Daly, C., M. Halbleib, J. I. Smith, W. P. Gibson, M. K. Doggett, G. H. Taylor, J. Curtis, and P. P. Pasteris, 2008: Physiographically sensitive mapping of climatological temperature and precipitation across the conterminous United States. *Int. J. Climatol.*, **28**, 2031-2064.

Dai, A., and K. E. Trenberth, 2002: Estimates of freshwater discharge from continents: latitudinal and seasonal variations. *J. Hydrometeor.*, **3**, 660-687.

Dai, A., T. Qian, and K. E. Trenberth, 2009; Changes in continental freshwater discharge from 1948 to 2004. *J. Climate*, **22**, 2773–2792.

Davini, P., 2013: Atmospheric blocking and winter mid-latitude climate variability. Ph.D. thesis. *Università Ca' Foscari Venezia*, 141 pp. (Available online at http://hdl.handle.net/10579/2241).

Dawson, A., 2016: eofs: A Library for EOF Analysis of Meteorological, Oceanographic, and Climate Data. *J. Open Res. Softw.*, **4**, 14. DOI: http://doi.org/10.5334/jors.122.

Dee, D. P. and Coauthors, 2011: The ERA-Interim reanalysis: configuration and performance of the data assimilation system. *Q. J. Royal Meteorol. Soc.*, **137**, 553-397, doi: 10.1002/qj.828.

Delworth, T. L., F. Zenh, G. A. Vecchi, X. Yang, L. Zhang, and R. Zhang, 2016: The North Atlantic Oscillation as a driver of rapid climate change in the Northern Hemisphere. *Nat. Geosci.*, **9**, 509-512, doi:10.1038/ngeo2738.

Deser, C., R. A. Tomas, and L. Sun, 2015: The role of ocean-atmosphere coupling in the zonal-mean atmospheric response to Arctic sea ice loss. *J. Climate*, **28**, 2168-2186, doi:10.1175/JCLI-D-14-00325.1.

Dettinger, M. D., and H. F. Diaz, 2000: Global characteristics of stream flow seasonality and variability. *J. Hydrometeor.*, **1**, 289-310.

Di Lorenzo, E., and N. Mantua, 2016: Multi-year persistence of the 2014/15 North Pacific marine heatwave. *Nat. Climate Change*, **6**, 1042–1047, doi:10.1038/nclimate3082.

Di Lorenzo, E., G. Liguori, and N. Mantua, 2016: Climate interpretation of the North Pacific marine heatwave of 2013-2015. US CLIVAR Variations, Vol. 14, No. 2, US CLIVAR, Washington, DC, 13-18, https://usclivar.org/newsletter/newsletters.

Dommenget, D. and M. Latif, 2002: A cautionary note on the interpretation of EOFs. *J. Climate,* **15**, 216-225.

Duchez, A., D. Desbruyères, J. J.-M. Hirschi, E. Frajka-Williams, S. Josey, and D. G. Evan, 2016: The tale of a surprisingly cold blob in the North Atlantic. *US CLIVAR Variations*, Vol. 14, No. 2, US CLIVAR, Washington, DC, 19-23, https://usclivar. org/newsletter/newsletters.

Eltahir, E. A. B., and P. J. F. Yeh, 1999: On the asymmetric response of aquifer water level to floods and droughts in Illinois. *Water Resour. Res.*, **35**, 1199-1217.

Entin, J. K., A. Robock, K. Y. Vinnikov, S. E. Hollinger, S. Liu, and A. Namkhai, 2000: Temporal and spatial scales of observed soil moisture variations in the extratropics. *J. Geophys. Res.*, **105**, 11,865-11,877.

Esbensen, S. K., 1984: A comparison of intermonthly and interannual teleconnections in the 700 mb geopotential height field during the Northern Hemisphere winter. *Mon. Wea. Rev.*, **112**, 2016–2032, doi:10.1175/1520-0493(1984)112,2016: ACOIAI.2.0.CO;2.

Francis, J. A. and S. J. Vavrus, 2012: Evidence linking Arctic amplification to extreme weather in mid-latitudes. *Geophys. Res. Lett.,* **39**, L06801.

Francis, J. A., S. J. Vavrus, and J. Cohen, 2017: Amplified Arctic warming and mid-latitude weather: new perspectives on emerging connections. *WIREs Clim. Change*.

Franzke, C., and S. B. Feldstein, 2005: The continuum and dynamics of Northern Hemisphere teleconnection patterns. *J. Atmos. Sci.*, **62**, 3250–3267, doi:10.1175/JAS3536.1.

Fukunaga, K. and W. L. G. Koontz, 1970: Application of the Karhunen-Loève expansion to feature selection and ordering. *IEEE Trans. Comput.,* **C-19**, 311-318.

Fukuoka, A., 1951: *A Study of 10-day Forecast (A Synthetic Report)*, Vol. XXII. The Geophysical Magazine: Tokyo; 177-218.

Galbraith, E. D., A. Gnanadesikan, J. P. Dunne, and M. R. Hiscock, 2010: Regional impacts of iron-light colimitation in a global biogeochemical model. *Biogeosciences*, **7**.

Garcia, H. E., R. A. Locarnini, T. P. Boyer, J. I. Antonov, O. Baranova, M. M. Zweng, J. R. Reagan, and D. R. Johnson, 2014a: World ocean atlas 2013 volume 3: Dissolved oxygen, apparent oxygen utilization, and oxygen saturation. *NOAA Atlas NESDIS 75*, 27.

Garcia, H. E., R. A. Locarnini, T. P. Boyer, J. I. Antonov, O. Baranova, M. M. Zweng, J. R. Reagan, and D. R. Johnson, 2014b: World ocean atlas 2013 volume 4: Dissolved inorganic nutrients (phosphate, nitrate, silicate). *NOAA Atlas NESDIS 76*, 25.

Gent, P.R. and Coauthors, 2011: The community climate system model version 4. *J. Climate,* **24**, 4973-4991.

Gentemann, C. L., M. R. Fewings, and M. García-Reyes, 2017: Satellite sea surface temperatures along the West Coast of the United States during the 2014–2016 northeast Pacific marine heat wave. *Geophys. Res. Lett.*, **44**, 312–319, doi:10.1002/ 2016GL071039.

Gerten, D., S. Rost, W. von Bloh, and W. Lucht, 2008: Causes of change in 20th century global river discharge. *Geophys. Res. Lett.,* **35**, L20405.

Gillett, N. P. and Coauthors*,* 2008: Attribution of polar warming to human influence. *Nature Geosci*., **1,** 750-754.

Goolsby, D. A., and Coauthors, 1999: Flux and sources of nutrients in the Mississippi-Atchafalaya River basin: Topic 3 Report for the Integrated Assessment if Hypoxia in the Gulf of Mexica. NOAA Coastal Ocean Office, Series No. 17.

Goss, M., S. B. Feldstein, and S. Lee, 2016: Stationary wave interference and its relation to tropical convection and Arctic warming. *J. Climate*, **29**, 1369-1389.

Graversen, R. G., T. Mauritsen, M. Tjernström, E. Källén, and G. Svensson, 2008: Vertical structure of recent Arctic warming. *Nature,* 451, 53-56, doi:10.1038/nature06502.

Golub, G. H., and C. F. van Loan, 1996: *Matrix Computation*. John Hopkins University Press: Baltimore, MD.

Hammond, M. D. and D. C. Jones, 2016: Freshwater flux from ice sheet melting and iceberg calving in the Southern Ocean. *Geosci. Data J.*, **3**, 60-62.

Hannachi, A., I. Joliffe, and D. Stephenson, 2007: Empirical or- thogonal functions and related techniques in atmospheric science: A review. *Int. J. Climatol.*, **27**, 1119-1152, doi:10.1002/joc.1499.

Hannah, H., 2015: 'Warm blob' in Pacific Ocean linked to weird weather across the U.S. *University of Washington News* (http://www.washington.edu/news/2015/04/09/warm-blob-in-pacific-ocean-linked-to-weird-weather-across-the-u-s/).

Hartmann, D., 2015: Pacific sea surface temperature and the winter of 2014. *Geophys. Res. Lett.*, **42**, 1894-1902, doi:10.1002/ 2015GL063083.

Held, I. M., 1983: Stationary and quasi-stationary eddies in the extratropical troposphere: Theory, in *Large-Scale Dynamical Processes in the Atmosphere*, edited by B. J. Hoskins and R. P. Pearce, pp. 127–168, Academic Press, London, U. K.

Held, I., M. Ting, and H. Wang, 2002: Northern winter stationary waves: theory and modeling. *J. Climate,* **15,** 2125-2144.

Henson, B., 2016: The North Atlantic blob: A marine cold wave that won't go away. WunderBlog, Weather Underground, https://www.wunderground.com/blog/JeffMasters/the-north- atlantic-blob-a-marine-cold-wave-that-wont-go-away.html.

Hobday, A. J. and Coauthor, 2016: A hierarchical approach to defining marine heatwaves. *Prog. Oceanogr.,* **141,** 227-238.

Holton, J., 2004: An introduction to dynamic meteorology, Vol. 1. *Academic Press*.

Horel, J. D., 1981: A rotated principal component analysis of the interannual variability of the Northern Hemisphere 500 mb height field. *Mon. Wea. Rev.,* **109**, 2080-2092.

Horel, J. D. and J. M. Wallace, 1981: Planetary-scale atmospheric phenomena associated with the Southern Oscillation. *Mon. Wea. Rev.*, **109**, 813–829, doi:10.1175/1520-0493(1981)109<0813:PSAPAW>2.0.CO;2.

Hoerling, M., A. Kumar, and M. Zhong, 1997: El Niño, La Niña, and the nonlinearity of their teleconnections. *J. Climate*, **10,** 1769-1786.

Hoskins, B. and D. Karoly, 1981: The steady linear response of a spherical atmosphere to thermal and orographic forcing. *J. Atmos. Sci*., **38**, 1179-1196.

Hoskins, B., 1983: Modelling of the transient eddies and their feedback on the mean flow, in *Large-Scale Dynamical Processes in the Atmosphere*, edited by B. Hoskins and R. P. Pearce, pp. 169-199, Academic Press, London, U.K.

Hoskins, B., I. James, and G. White, 1983: The shape, propagation and mean-flow interaction of large-scale weather systems. *J. Atmos. Sci.*, **40**, 1595-1612.

Hotelling, H., 1933: Analysis of a complex of statistical variables into principal components. *J. Educa. Psychol.,* **24**, 417-520.

Hu, Q., J. A. Torres-Alavez, and M. S. Van Den Broeke, 2018: Land-cover change and the "Dust Bowl" drought in the U.S. Great Plains. *J. Climate*, doi:10.1175/JCLI-D-17-0515.1.

Hu, Z.-Z., A. Kumar, B. Jha, J. Zhu, and B. Huang, 2017: Persistence and predictions of the remarkable warm anomaly in the northeastern Pacific Ocean during 2014-16. *J. Climate*, **30**, 689-702, doi:10.1175/JCLI-D-16-0348.1.

Huber, D. B., D. B. Mechem, N. A. Brunsell, 2014: The effects of Great Plains irrigation on the surface energy balance, regional circulation, and precipitation. *Climate,* **2**, 103-128.

Iles, C. E., and G. C. Hegerl, 2015: Systematic change in global patterns of streamflow following volcanic eruptions. *Nat. Geosci.*, **8**, 838-842.

Inatsu, M., and B. J. Hoskin, 2006: The seasonal and wintertime interannual variability of the split jet and the storm-track activity minimum near New Zealand. *J. Meteor. Soc. Japan*, **84**, 433-445.

IPCC, 2013: Climate Change 2013: The Physical Science Basis. Contribution of Working Group I to the Fifth Assessment Report of the Intergovernmental Panel on Climate Change (Stocker, T.F., D. Qin, G.-K. Plattner, M. Tignor, S.K. Allen, J. Boschung, A. Nauels, Y. Xia, V. Bex and P.M. Midgley (eds.)). *Cambridge University Press*, Cambridge, United Kingdom and New York, NY, USA, 1535pp, doi:10.1017/CBO9781107415324.

Jaffe, D. A., and L. Zhang, 2017: Meteorological anomalies lead to elevated O3 in the western U.S. in June 2015. *Geophys. Res. Lett.*, **44**, 1990-1997, doi:10.1002/2016GL072010.

Jiménez-Esteve, B. and D. I. Domeisen, 2018: The Tropospheric Pathway of the ENSO-North Atlantic Teleconnection. *J. Climate*, doi:10.1175/JCLI-D-17-0716.1.

Johnstone, J. A., and N. J. Mantua, 2014: Atmospheric controls on northeast Pacific temperature variability and change, 1900-2012. *Proc. Natl. Acad. Sci. USA*, **111**, 14,360–14,365, doi:10.1073/pnas.1318371111.

Jolliffe, I.T., 1987: Rotation of principal components: some comments. *J. Climatol,* **7**, 507-510.

Jolliffe, I. T., 2002: *Principal Component Analysis*, 2nd edn. Springer: New York.

Kahya, E., and J. A. Dracup, 1993; U.S. streamflow patterns in relation to the El Niño/Southern Oscillation, *Water Resour. Res.*, **42**, 2491-2503.

Kaiser, H. F., 1958: The varimax criterion for analytic rotation in factor analysis. *Psychometrika,* **23**, 187-200.

Kalnay, E., and Coauthors, 1996: The NCEP/NCAR 40-Year Re- analysis Project. *Bull. Amer. Meteor. Soc.*, **77**, 437-471, doi:10.1175/1520-0477(1996)077,0437:TNYRP.2.0.CO;2.

Kao, H.-Y., and J.-Y. Yu, 2009; Constrasting eastern-Pacific and central-Pacific types of ENSO. *J. Climate*, **22**, 615-632, doi:10.1175/2008JCLI2309.1.

Kaplan, A., Y. Kushnir, M. A. Cane, and M. B. Blumenthal, 1997: Reduced space optimal analysis for historical data sets: 136 years of Atlantic sea surface temperatures. *J. Geophys. Res.*, **102**, 27,835-27,860.

Karori, M. A., J. Li, and F.-F. Jin, 2013; The asymmetric influence of the two types of El Niño and La Nina on summer rainfall over southeast China. *J. Climate*, **26**, 4567-4582.

Kay, J. E. and Coauthors, 2015: The community earth system model (CESM) large ensemble project: A community resource for studying climate change in the presence of internal climate variability. *Bull. Am Met. Soc.,* **96**, 1333-1349.

Key, R. M. and Coauthors, 2015: Global Ocean Data Analysis Project, Version 2 (GLODAPv2). Carbon Dioxide Information Analysis Center, Oak Ridge Nat Lab, doi:10.3334/CDIAC/OTG. NDP093 GLODAPv2.

Kim, B.-M., S.-W. Son, S.-K. Min, J.-H. Jeong, S.-J. Kim, X. Zhang, T. Shim, and J.-H. Yoon, 2014: Weakening of the stratospheric polar vortex by Arctic sea-ice loss. *Nat. Commun.*, **5**, 4646, doi:10.1038/ncomms5646.

Kim, J.-S. and Coauthors, 2017: Reduced North American terrestrial primary productivity linked to anomalous Arctic warming. *Nat. Geosci.,* **10**, 572-576.

Kim, S. T., J.-Y. Yu, 2012: The two types of ENSO in CMIP5 models. *Geophys. Res. Lett.,* **39**, L11704, doi: 10.1029/2012GL052006.

Kim, K.-W. and G. R. North, 1999: EOF-based linear prediction algorithm: examples. *J. Climate,* **12**, 2076-2092.

Kug, J.-S., F.-F. Jin, and S.-I. An, 2009: Two types of El Niño events: Cold Tongue El Niño and Warm Pool El Niño. *J. Climate*, **22**, 1499-1515, doi:10.1175/2008JCLI2624.1.

Kug, J.-S. and Coauthors, 2015: Two distinct influences of Arctic warming on cold winters over North America and East Asia. *Nat. Geosci.,* **8**, 759-762.

Kumar, A., and Z.-Z. Hu, 2012: Uncertainty in the ocean- atmosphere feedbacks associated with ENSO in the re- analysis products. *Climate Dyn.*, **39**, 575-588, doi:10.1007/ s00382-011-1104-3.

Kumar, A., H. Wang, W. Wang, Y. Xue, and Z.-Z. Hu, 2013: Does knowing the oceanic PDO phase help predict the atmospheric anomalies in subsequent months? *J. Climate*, **26**, 1268-1285, doi:10.1175/JCLI-D-12-00057.1.

Kunz, T., K. Fraedrich, and F. Lunkeit, 2009: Impact of Synoptic-Scale Wave Breaking on the NAO and Its Connection with the Stratosphere in ERA-40. *J. Climate*, **22**, 5464-5480.

Kurtzman, D., and B. R. Scanlon, 2007: El Niño-Southern Oscillation and Pacific Decadal Oscillation impacts on precipitation in the southern and central United States: Evaluation of spatial distribution and predictions, *Water Resour. Res.*, **43**, W10427, doi:10.1029/2007WR005863.

Labat, D., 2010: Cross wavelet analyses of annual continental freshwater discharge and selected climate indices. *J. Hydrol.*, **385**, 269-278.

Larkin, N. K. and D. E. Harrison, 2005: On the definition of El Niño and associated seasonal average U.S. weather anomalies. *Geophys. Res. Lett.,* **32**, L13705.

Lauvset, S. K. and Coauthors, 2016: A new global interior ocean mapped climatology: the 1× 1 GLODAP version 2. *Earth Syst. Sci. Data Discuss.*, **8**, 325.

Lee, H.J., M. O. Kwon, S.-W. Yeh, Y.-O. Kwon, W. Park, J.-H. Park, Y. H. Kim, and M. A. Alexander, 2017: Impact of poleward moisture transport from the North Pacific on the acceleration of sea-ice loss in the Arctic since 2002, *J. Clim.*, **30**, 6757–6769.

Lee, M.-Y., C.-C. Hong, and H.-H. Hsu, 2015: Compounding effects of warm sea surface temperature and reduced sea ice on the extreme circulation over the extratropical North Pacific and North America during the 2013–2014 boreal winter. *Geophys. Res. Lett.*, **42**, 1612-1618, doi:10.1002/ 2014GL062956.

Lee, S.-K., R. Atlas, D. B. Enfield, C. Wang, H. Liu, 2013: Is there an optimal ENSO pattern that enhances large-scale atmospheric processes conducive to major tornado outbreaks in the U. S.? *J. Climate,* **26**, 1626-1642.

Lee, T. and M. J. McPhaden, 2010: Increasing intensity of El Niño in the central-equatorial Pacific. *Geophys. Res. Lett.*, **37**, L14603.

Li, W., P. Zhang, J. Ye, L. Li, and P. A. Baker, 2011: Impact of two different types of El Niño events on the Amazon climate and ecosystem productivity. *J. Plant Ecol.*, **4**, 91-99, doi:10.1093/jpe/rtq039.

Liang, Y.-C., M.-H. Lo, and J.-Y. Yu, 2014: Asymmetric responses of land hydroclimatology to two types of El Niño in the Mississippi River basin. *Geophys. Res. Lett.*, **41**, 582–588.

Liang, Y.-C., J.-Y. Yu, M.-H. Lo, and C. Wang, 2015: The changing influence of El Niño on the Great Plains Low-Level Jet, *Atmos. Sci. Lett.*, 16, 512-517, doi:10.1002/asl.590.

Liang, Y.-C., C.-C. Chou, J.-Y. Yu, and M.-H. Lo, 2016: Mapping the Locations of Asymmetric and Symmetric Discharge Responses in Global Rivers to the Two Types of El Niño*, Environ. Res. Lett.*, 11, doi:10.1088/1748-9326/11/4/044012.

Liang, Y.-C., J.-Y. Yu, E. S. Saltzman, and F. Wang, 2017: Linking the Tropical Northern Hemisphere pattern to the generation of the Pacific warm blob and Atlantic cold blob, *J. Climate,* 30, 9041-9057, doi:10.1175/JCLI-D-17-0149.1.

Liang, Y.-C., M. R. Mazloff, I. Rosso, S.-W. Fang, and J.-Y. Yu, 2018: A multi-variate Empirical Orthogonal Function method to construct nitrate maps in the Southern Ocean, *J. Atmos. Oceanic Technol.* (under review).

Liang, Y.-C. and J.-Y. Yu, 2018: Arctic warming intensifies the climate connectivity between the North Pacific and North Atlantic, *Geophys. Res. Lett.* (in preparation).

Lo, M.-H., P. J.-F. Yeh, and J. S. Famiglietti, 2008: Using baseflow to constrain water table depth simulations in the NCAR Community Land Model (CLM). *Adv. Water Resour.*, **31**, 1552-1564, doi:10.1016/j.advwatres.2008.06.007.

Lo, M.-H., and J. S. Famiglietti, 2010: The effect of water table dynamics on land surface hydrologic memory. *J. Geophys. Res.*, **115**, D22118,doi:10.1029/2010JD014191.

Lo, M.-H., and J. S. Famiglietti, 2011: Precipitation response to land subsurface hydrologic processes in atmospheric general circulation model simulations. *J. Geophys. Res.*, **116**, D05107, doi:10.1029/2010JD015134.

Lo M.-H., and J. S. Famiglietti, 2013: Irrigation in California's Central Valley strengthens the southwestern U.S. water cycle. *Geophys. Res. Lett.,* **40**, L50108.

Loève, M., 1978: *Probability Theory*, Vol. 2, 4th edn. Springer Verlag: New York.

Lorenz, E. N., 1956: Empirical Orthogonal Functions and Statistical Weather Prediction. *Technical report, Statistical Forecast Project Report 1*, Dep of Meteor, MIT: 49.

Losch, M., D. Menemenlis, J.-M. Campin, P. Heimbach, and C. Hill, 2010: On the formulation of sea-ice models. Part 1: Effects of different solver implementations and parameterizations. *Ocean Modell.*, **33**, 129-144.

Manabe, S. and R. T. Wetherald, 1975: The effects of doubling the CO_2 concentration on the climate of a general circulation model. *J. Atmos. Sci.*, **32**, 3-15.

Mantua, N. J., S. R. Hare, Y. Zhang, J. M. Wallace, and R. C. Francis, 1997: A Pacific decadal climate oscillation with impacts on salmon production. *Bull. Amer. Meteor. Soc.*, **78**, 1069-1079, doi:10.1175/1520-0477(1997)078,1069: APICOW.2.0.CO;2.

Marshall, J., A. Adcroft, C. Hill, L. Perelman, and C. Heisey, 1997: A finite-volume, incompressible Navier Stokes model for studies of the ocean on parallel computers. *J. Geophys. Res.*, **102**, 5753-5766, doi:10.1029/96JC02775.

McIntyre, M. E. and T. Palmer, 1983: Breaking Planetary Waves in the Stratosphere. *Nature*, **305**, 593-600.

McPhaden, M., T. Lee, and D. McClurg, 2011: El Niño and its relationship to changing background conditions in the Tropical Pacific. *Geophys. Res. Lett.,* **38**, L15709.

Medred, C., 2014: Unusual species in Alaska waters indicate parts of Pacific warming dramatically. *Alaska Dispatch News*, 14 September, http://www.adn.com/article/20140914/unusual-species-alaska-waters-indicate-parts-pacific-warming-dramatically.

Milliman, J. D., K. L. Farnsworth, P. D. Jones, K. H. Xu, and L. C. Smith, 2008: Climatic and anthropogenic factors affecting river discharge to the global ocean 1951–2000. *Glob. Planet. Change*, **62**, 187-194.

Milly, P. C. D., K. A. Dunne, and A. V. Vecchia, 2005: Global pattern of trends in sreamflow and water availability in a changing climate. *Nature*, **438**, 347-350.

Mo, K. C., 1985: Interhemisphere correlations statistics during the Northern Hemisphere winter. *Proc. Ninth Conf. on Probability and Statistics in Atmospheric Sciences*, Virginia Beach, VA, Amer. Meteor. Soc., 283–289.

Mo, K. C., and R. E. Livezey, 1986: Tropical-extratropical geopotential height teleconnections during the Northern Hemi- sphere winter. *Mon. Wea. Rev.*, **114**, 2488–2515, doi:10.1175/1520-0493(1986)114,2488:TEGHTD.2.0.CO;2.

Mo, K. C. and E. H. Berber, 2004: Low-level jets and the summer precipitation regimes over North America. *J. Geophys. Res.,* **109**, D06117.

Mo, K. C., 2010: Interdecadal modulation of the impact of ENSO on precipitation and temperature over the United States. *J. Climate*, **23**, 3639–3656, doi:10.1175/2010JCLI3553.1.

Monahan, A. H., J. C. Fyfe, M. H. Ambaum, D. B. Stephenson, and G. R. North, G. R., 2009: Empirical orthogonal functions: The medium is the message. *J. Climate*, **22**, 6501-6514.

Mori, M., M. Watanabe, H. Shiogam, J. Inoue, and M. Kimoto, 2014: Robust Arctic sea-ice influence on the frequent Eurasian cold winters in past decades. *Nat. Geosci*. **7,** 869-873.

Nakamura, T. and Coauthors, 2015: A negative phase shift of the winter AO/NAO due to the recent Arctic sea-ice reduction in late autumn. *J. Geophys. Res.,* **120**, 3209-3227.

Newman, M., G. P. Compo, and M. A. Alexander, 2003: ENSO-forced variablity of the Pacific decadal oscillation. *J. Climate*, **16**, 3853–3857, doi:10.1175/1520-0442(2003)016,3853:EVOTPD.2.0.CO;2.

Nikolaidis, A., G. Georgiou, D. Hadjimitsis, and E. Akylas, 2014: Filling in missing sea-surface temperature satellite data over the Eastern Mediterranean sea using the DINEOF algorithm. *Open Geosci.*, **6**, 27-41.

Nilsson, C., C. A. Reidy, M. Dynesius, and C. Revenga, 2005: Fragmentation and flow regulation of the world's large river systems. *Science,* **308**, 405-408.

Ning, L. and R. S. Bradley, 2015: Influence of eastern Pacific and central Pacific El Niño events on winter climate extremes over the eastern and central United States. *Int. J. Climatol.*, **35**, 4756-4770.

Niu, G.-Y., Z.-L. Yang, R. E. Dickinson, and L. E. Gulden, 2005: A simple TOPMODEL-based runoff parameterization (SIMTOP) for use in GCMs. *J. Geophys. Res.*, **110**, D21106, doi:10.1029/2005JD006111.

North, G.R., T. L. Bell, R. F. Cahalan, F. J. Moeng, 1982: Sampling errors in the estimation of empirical orthogonal functions. *Mon. Weather Rev.,* **110**, 699-706.

Obukhov, A. M., 1947: Statistically homogeneous fields on a sphere. *Uspethi Mathematicheskikh Nauk,* **2**, 196-198.

Oki, T. and Y. C. Sud, 1998: Design of total runoff integrating pathways (TRIP)-a global river channel network. *Earth Interact.*, **2**, 1–37.

Oki, T. and S. Kanae, 2006: Global hydrological cycles and world water resources. *Science*, **313**, 1068-1072.

Oleson, K. W. and Coauthors, 2010: Technical description of version 4.0 of the community land model (CLM). *NCAR Technical Note*, NCAR/TN-478+STR Natl. Cent. for Atmos. Res. Boulder Colo, **257**.

Orsi, A. H., T. Whitworth, and W. D. Nowlin, 1995: On the meridional extent and fronts of the Antarctic Circumpolar Current. *Deep-Sea Res. I*, **42**, 641-673.

Overland, J. E., J. A. Francis, R. Hall, E. Hanna, S.-J. Kim, and T. Vihma, 2015: The melting Arctic and midlatitude weather patterns: Are they connected? *J. Climate*, **28**, 7917–7932, doi:10.1175/JCLI-D-4-00822.1.

Overland, J. E. and Coauthors, 2016: Nonlinear response of mid-latitude weather to the changing Arctic. *Nat. Climate Change*, **6**, 992– 999, doi:10.1038/nclimate3121.

Pal, I., E. Towler, and B. Livneh, 2015: How can we better understand low river flows as climate changes? *Eos*, 96.

Panagiotopoulos, F., M. Shahgedanova, and D. B. Stephenson, 2002: A review of Northern Hemisphere winter-time teleconnection patterns. *J. Phys. IV France*, **12**, 10–27, doi:10.1051/ jp4:20020450.

Pavan, V, and S. Tibaldi, C. Brankovich, 2000: Seasonal prediction of blocking frequency: results from winter ensemble experiments. *Q. J. Royal Meteorol. Soc.,* **126**, 2125-2142.

Payne, A. E. and G. Magnusdottir, 2014: Dynamics of landfalling atmospheric rivers over the North Pacific in 30 years of MERRA reanalysis. *J. Climate*, **27**, 7133–7150, doi:10.1175/ JCLI-D-14-00034.1.

Pearson, K., 1902: On lines and planes of closest fit to systems of points in space. *Philos. Mag.,* **2**, 559–572.

Peings, Y., E. Brun, V. Mauvais, and H. Douville, 2013: How stationary is the relationship between Siberian snow and Arctic Oscillation over the 20th century? *Geophys. Res. Lett.*, **40**, 183-188, doi:10.1029/2012GL054083.

Peings, Y., and G. Magnusdottir, 2014: Response of the wintertime northern hemisphere atmospheric circulation to current and projected Arctic sea ice decline: A numerical study with CAM5. *J. Climate*, **27**, 244–264, doi:10.1175/JCLI-D-13-00272.1.

Peng, P., and A. Kumar, 2005: A large ensemble analysis of the influence of tropical SSTs on seasonal atmospheric variability. *J. Climate*, **18**, 1068–1085, doi:10.1175/JCLI-3314.1.

Peterson, W., M. Robert, and N. Bond, 2015: The warm Blob continues to dominate the ecosystem of the northern California Current. *PICES Press*, Vol. 23, No. 2, North Pacific Marine Science Organization, Sidney, BC, Canada, 44–46, https://www.pices.int/publications/pices_press/volume23/ PPJuly2015.pdf.

Pinto, J. G., M. Reyers, and U. Ulbrich, 2011: The variable link between PNA and NAO in observations and in multi-century CGCM simulations. *Clim. Dyn.*, **36**, 337–354, doi:10. 1007/s00382-010-0770-x.

Pithan, F. and T. Mauritsen, 2014: Arctic amplification dominated by temperature feedbacks in contemporary climate models. *Nature Geosci.,* **7**, 181-184.

Plumb, R. A., 1985: On the Three-Dimensional Propagation of Stationary Waves. *J. Atmos. Sci.*, **42**, 217-229, doi:10.1175/1520-0469(1985)042h0217:OTTDPOi2.0.CO;2.

Prohaska, J., 1976: A technique for analyzing the linear relationships between two meteorological fields. *Mon. Wea. Rev.*, **104**, 1345-1353

Rahmstorf, S., E. B. Jason, G. Feulner, M. E. Mann, A. Robinson, S. Rutherford, and E. J. Schaffernicht, 2015: Exceptional twentieth-century slowdown in Atlantic Ocean overturning circulation. *Nat. Climate Change*, **5**, 475-480, doi:10.1038/ nclimate2554.

Rayner, N. A., D. E. Parker, E. B. Horton, C. K. Folland, L. V. Alexander, D. P. Rowell, E. C. Kent, and A. Kaplan, 2003: Global analyses of sea surface temperature, sea ice, and night marine air temperature since the late nineteenth century. *J. Geophys. Res.*, **108**, 4407, doi:10.1029/2002JD002670.

Richman, M. B., 1981: Obliquely rotated principal components: an improved meteorological map typing technique. *J. Appl. Meteorol. Climatol.,* **20**, 1145-1159.

Riviere, G. and I. Orlanski, 2007: Characteristics of the Atlantic Storm-Track Eddy Activity and Its Relation with the North Atlantic Oscillation. *J. Atmos. Sci*., **64**, 241-266.

Robson, J., P. Ortega, and R. Sutton, 2016: A reversal of climatic trends in the North Atlntic since 2005. *Nat. Geosci.*, **9**, 513-517, doi:10.1038/ngeo2727.

Rodwell, M. J., B. J. Hoskins, 2001: Subtropical anticyclones and summer monsoon. *J.Climate,* **14**, 3192-3211.

Rodell, M., and Coauthor, 2004: The Global Land Data Assimilation System. *Bull. Am. Meteorol. Soc.*, **85**, 381-394, doi:10.1175/BAMS-85-3-381.

Rogers, J. C., 1981: The North Pacific Oscillation. *J. Climatol.*, **1**, 39–57, doi:10.1002/joc.3370010106.

Rogers, J. C., and J. S. M. Coleman, 2004: Ohio winter precipitation and stream flow associations to Pacific atmospheric and oceanic teleconnection patterns. *Ohio J. Sci.*, **104**, 51–59.

Ropelewski, C. F., and M. S. Halpert, 1986: North America precipitation and temperature patterns associated with the El Niño/Southern Oscillation (ENSO). *Mon. Weather Rev.*, **114**, 2352-2362.

Ross, T. and N. Lott, 2003: A climatology of 1980-2003 extreme weather and climate events. Technical Report 2003-01, NOAA/NESDIS National Climate Data Center, Asheville, NC.

Rosso, I., M. R. Mazloff, A. Verdy, and L. D. Talley, 2017: Space and time variability of the Southern Ocean carbon budget. *J. Geophys. Res.*, 112, 7407-7432, doi:10.1002/2016JC012646.

Rossby, C. and Coauthors, 1939: Relation between variations in the intensity of the zonal circulation of the atmosphere and the displacements of the semi-permanent centers of action. *J. Mar. Res.*, **2**, 38-55.

Sacks, W. J., B. I. Cook, N. Buenning, S. Levis, and J. H. Helkowski, 2009: Effects of global irrigation on the near-surface climate. *Climate Dyn.,* **33**, 159-175.

Sampe, T., H. Nakamura, A. Goto, and W. Ohfuchi, 2010: Significance of a midlatitude sst frontal zone in the formation of a storm track and an eddy-driven westerly jet. *J. Climate*, **23**, 1793-1814.

Schmittner, A., P. Bakker, R. L. Beadling, J. T. M. Lenaerts, S. Mernild, O. Saenko, and D. Swingedouw, 2016: Greenland ice sheet melting influence on the North Atlantic. *US CLIVAR Variations*, Vol. 14, No. 2, US CLIVAR, Washington, DC, 32–37, https://usclivar.org/newsletter/newsletters.

Schneider, N., and B. Cornuelle, 2005: The forcing of the Pacific decadal oscillation. *J. Climate*, **18**, 4355–4373, doi:10.1175/ JCLI3527.1.

Schneider, T., 2006: The general circulation of the atmosphere. *Annu. Rev. Earth Planet. Sci.*, **34**, 655-688.

Screen, J. A. and I. Simmonds, 2010: The central role of diminishing sea ice in recent Arctic temperature amplification. *Nature,* **464***,* 1334-1337.

Screen, J. A., C. Deser, and I. Simmonds, 2012: Local and remote controls on observed Arctic warming. *Geophys. Res. Lett.*, **39**, L10709, doi:10.1029/2012GL051598.

Screen, J. A., 2014: Arctic amplification decreases temperature variance in northern mid- to high-latitudes. *Nat. Clim. Change,* **4**, 577-582.

Screen, J. A. and I. Simmonds, 2014: Amplified mid-latitude planetary waves favour particular regional weather extremes. *Nat. Clim. Change*, **4**, 704-709, doi:10.1038/nclimate2271.

Screen, J. A. and J. A. Francis, 2016: Contribution of sea-ice loss to Arctic amplification is regulated by Pacific Ocean decadal variability. *Nat. Clim. Change*, **6**, 856-860.

Seager, R., M. Hoerling, S. Schubert, H. Wang, B. Lyon, A. Kumar, J. Nakamura, and N. Henderson, 2014: Causes and predictability of the 2011-14 California drought. Assessment Rep., NOAA/OAR/Climate Program Office, 42 pp., http://cpo.noaa. gov/MAPP/californiadroughtreport.

Seager, R., M. Hoerling, S. Schubert, H. Wang, B. Lyon, A. Kumar, J. Nakamura, and N. Henderson, 2015: Causes of the 2011–14 California drought. *J. Climate*, **28**, 6997-7024, doi:10.1175/JCLI-D-14-00860.1.

Seager, R., and N. Henderson, 2016: Tropical ocean forcing of the persistent North American west coast ridge of winter 2013/14. *J. Climate*, **29**, 8027-8048, doi:10.1175/JCLI-D-16-0145.1.

Serreze, M. C. and R. G. Barry, 2011: Processes and impacts of Arctic amplification: a research synthesis. *Glob. Planet. Change,* **77**, 85-96.

Shannon, H. D. and R. P. Motha, 2015: Managing weather and climate risks to agriculture in North America, Central America and the Caribbean. *Weather Clim. Extremes*, **10**, 50-56.

Shaw, T. A. and Coauthors, 2016: Storm track processes and the opposing influences of climate change. *Nat. Geosci.,* **9**, 656-664.

Sheffield, J., G. Goteti, and E. F. Wood, 2006: Development of a 50-yr high-resolution global dataset of meteorological forcings for land surface modeling. *J. Climate*, **19**, 3088–3111.

Shindell, D. and G. Faluvegi, 2009: Climate response to regional radiative forcing during the twentieth century. *Nat. Geosci.,* **2,** 294-300.

Serreze, M., A. Barrett, J. Stroeve, D. Kindig, and M. Holland, 2009: The emergence of surface based Arctic amplification. *Cryosphere*, **3**, 11-19.

Siedlecki, S., E. Bjorkstedt, R. Feely, A. Sutton, J. Cross, and J. Newton, 2016: Impact of the Blob on the Northeast Pacific Ocean biogeochemistry and ecosystems. US CLIVAR Variations, Vol. 14, No. 2, *US CLIVAR, Washington*, DC, 7–12, https://usclivar.org/newsletter/newsletters.

Smith, T. M., R. W. Reynolds, R. E. Livezey, and D. C. Stokes, 1996: Reconstruction of historical sea surface temperatures using empirical orthogonal functions. *J. Climate*, **9**, 1403-1420.

Smith, T. M. and R. W. Reynolds, 2003: Extended reconstruction of global sea surface temperatures based on COADS data (1854-1997). *J. Climate,* **16**, 1495-1510.

Sung, M.-K. and Coauthors, 2016: Arctic-North Pacific coupled impacts on the late autumn cold in North America. *Environ. Res. Lett.,* **11**, 084016.

Stroeve, J. C., M. C. Serreze, M. M. Holland, J. E. Kay, J. Malanik, and A. P. Barrett, 2012: The Arctic's rapidly shrinking sea ice cover: a research synthesis. *Clim. Chang.*, **110**, 1005-1027, doi:10.1007/s10584-011-0101-1.

Strong, C. and G. Magnusdottir, 2008: Tropospheric Rossby Wave Breaking and the NAO/NAM. *J. Atmos. Sci.*, **65**, 2861-2876.

Swain, D. L., M. Tsiang, M. Haugen, D. Singh, A. Charland, B. Rajaratnam, and N. S. Diffenbaugh, 2014: The extraordinary California drought of 2013/2014: Character, context, and the role of climate change. *Bull. Amer. Meteor. Soc.*, **95** (Suppl.), S3–S7, doi:10.1175/1520-0477-95.9.S1.1.

Swain, D. L., 2015: A tale of two California droughts: Lessons amidst record warmth and dryness in a region of complex physical and human geography. *Geophys. Res. Lett.*, **42**, 9999-10,003, doi:10.1002/2015GL066628.

Swain, D. L., D. E. Horton, D. Singh, and N. S. Diffenbaugh, 2016: Trends in atmospheric patterns conducive to seasonal precipitation and temperature extremes in California. *Sci. Adv.*, **2**, doi:10.1126/sciadv.1501344.

Takaya, K. and H. Nakamura, 2001: A Formulation of a Phase-Independent Wave-Activity Flux for Stationary and Migratory Quasigeostrophic Eddies on a Zonally Varying Basic Flow. *J. Atmos. Sci.*, **58**, 608-627, doi:10.1175/1520-0469(2001)058h0608:AFOAPIi2.0.CO;2.

Thiiébaux, H. J., F. W. Zwiers, 1984: The interpretation and estimation of effective sample sizes. *J. Appl. Meteorol. Climatol.,* **23**, 800-811.

Thompson, D. W. J. and J. M. Wallace, 1998: The Arctic Oscillation signature in the wintertime geopotential height and temperature fields. *Geophys. Res. Lett.,* **25**, 1297-1300.

Ting, M., H. Wang, 2006: The role of the North American topography on the maintenance of the Great Plains summer low-level jet. *J. Atmos. Sci.*, **63**, 1056-1068.

Trenberth, K. E. and C. J. Guillemot, 1996: Physical processes involved in the 1988 drought and 1993 floods in North America. *J. Climate,* **9**, 1288-1298.

Trenberth, K. E., G. W. Branstator, D. Karoly, A. Kumar, N. C. Lau, and C. Ropelewski, 1998: Progress during TOGA in understanding and modeling global teleconnections associated with tropical sea surface temperatures. *J. Geophys. Res.*, **103**, 14291-14324.

Trenberth, K. E. and D. P. Stepaniak, 2001: Indices of El Niño evolution. *J. Climate,* **14**, 1697-1701.

Twine, T. E., C. J. Kucharik, and J. A. Foley, 2005: Effects of El Niño-Southern Oscillation on the climate, water balance, and streamflow of the Mississippi River Basin. *J. Climate*, **18**, 4840-4861.

Uccellini, L. W., 1980: On the role of upper tropospheric jet streaks and leeside cyclogenesis in the development of low level jet in the Great Plains. *Mon. Wea. Rev.,* **108**, 1689-1696.

Vallis, G. K., 2017: Atmospheric and oceanic fluid dynamics. Cambridge, UK: Cambridge University Press.

Vecchi, G. A., T. L. Delworth, and B. Booth, 2017: Origin of Atlantic decadal swings. *Nature,* **548**, 284-285.

Verdy, A., and M. R. Mazloff, 2017: A data assimilating model for estimating Southern Ocean biogeochemistry. *J. Geophys. Res.*, **112**, 6968-6988, doi:10.1002/2016JC012650.

von Storch, H., 1995: Spatial Patterns: EOFs and CCA. In *Analysis of Climate Variability: Application of Statistical Techniques*, von Storch H, Navarra A (eds). Springer Verlag: Berlin; 227-257.

von Storch, H., F. W. Zwiers, 1999: *Statistical Analysis in Climate Research*. Cambridge University Press: Cambridge.

Wallace, J. M., and D. S. Gutzler, 1981: Teleconnections in the potential height field during the Northern Hemisphere winter. *Mon. Wea. Rev.*, **109**, 784-812, doi:10.1175/1520-0493(1981)109,0784: TITGHF.2.0.CO;2.

Wallace, J. M., C. Smith, and C. S. Bretherton, 1992: Singular value de- composition of wintertime sea surface temperature and 500-mb height anomalies. *J. Climate*, **5**, 561-576, doi:10.1175/ 1520-0442(1992)005,0561:SVDOWS.2.0.CO;2.

Wallace, J. M. and D. W. J. Thompson, 2002: The Pacific center of action of the Northern Hemisphere annular mode: Real or artifact? *J. Climate*, **15**, 1987-1991.

Wallace, J. M., I. M. Held, D. W. J. Thompson, K. E. Trenberth, and J. E. Walsh, 2014: Global warming and winter weather. *Science,* **343**, 729-730.

Wang, B., R. Wu, and X. Fu, 2000: Pacific-East Asian teleconnection: how does ENSO affect east Asian climate. *J. Climate*, **13**, 1517-1536.

Wang, C., 2007: Variability of the Caribbean low-level jet and its relations to climate. *Climate Dyn.,* **29**, 411-422.

Wang, C., S.-K. Lee, and D. B. Enfield, 2007: Impact of the Atlantic warm pool on the summer climate of the Western Hemisphere. *J. Climate,* **20**, 5021-5040.

Wang, C., S.-K. Lee, and D. B. Enfield, 2008: Climate response to anomalously large and small Atlantic warm pools during the summer. *J. Climate,* **21**, 2437-2450.

Wang, K., T. Zhang, X. Zhang, G. D. Clow, E. E. Jafarov, I. Overeem, V. Romanovsky, X. Peng, and B. Cao, 2017: Continuously amplified warming in the Alaskan Arctic: Implications for estimating global warming hiatus. *Geophys. Res. Lett.,* **44**, 9029-9038.

Wang, L., J.-Y Yu, and H. Paek, 2017: Enhanced biennial variability in the Pacific due to Atlantic capacitor effect. *Nature Commun.,* **8**, 14887.

Wang, S.-Y., L. Hipps, R. R. Gillies, and J.-H. Yoon, 2014: Probable causes of the abnormal ridge accompanying the 2013-2014 California drought: ENSO precursor and anthropogenic warming footprint. *Geophys. Res. Lett.*, **41**, 3220-3226, doi:10.1002/2014GL059748.

Wang, X., X. Jiang, S. Yang, and Y. Li, 2013: Different impacts of the two types of El Niño on Asian summer monsoon onset. *Environ. Res. Lett.*, **8**, 044053.

Ward, P. J., W. Beets, L. M. Bouwer, C. J. C. H. Aerts, and H. Renssen, 2010: Sensitivity of river discharge to ENSO. *Geophys. Res. Lett.*, **37**, L12402.

Ward, P. J., S. Eisner, M. Flörke, M. D. Dettinger, and M. Kummu, 2014a: Annual flood sensitivities to El Niño-Southern Oscillation at the global scale. *Hydrol. Earth Syst. Sci.*, **18**, 47-66.

Ward, P. J., B. Jongman, M. Kummu, M. D. Dettinger, F. C. S. Weiland, and H. C. Winsemius, 2014b: Strong influence of El Niño Southern Oscillation on flood risk around the world. *Proc. Natl Acad. Sci. USA*, **111**, 15659-15664.

Weaver, S. J. and S. Nigam, 2008: Variability of the Great Plains low-level jet: large-scale circulation context and hydroclimate impact. *J. Climate,* **21**, 1532-1551.

Weaver, S. J., S. Schubert, and H. Wang, 2009: Warm season variations in the low-level circulation and precipitation over the central United States in observations, AMIP simulations, and idealized SST experiments. *J. Climate,* **22**, 5401-5420.

Weaver, S.J., S. Baxter, and A. Kumar, 2012: Climatic role of north American low-level jets on U.S. regional tornado activity. *J. Climate,* **25**, 6666-6683.

Whitney, F. A., 2015: Anomalous winter winds decrease 2014 transition zone productivity in the NE Pacific. *Geophys. Res. Lett.*, **42**, 428-431, doi:10.1002/2014GL062634.

Winton, M., 2006: Amplified Arctic climate change: What does surface albedo feedback have to do with it? *Geophys. Res. Lett*., **33**, L03701, doi:10.1029/2005GL025244.

Woodgate, R. A., T. J. Weingartner, and R. Lindsay, 2010: The 2007 Bering Strait oceanic heat flux and anomalous Arctic sea-ice retreat. *Geophys. Res. Lett.*, **37**, L01602, doi:10.1029/2009GL041621.

Woodgate, R. A., T. J. Weingartner, and R. Lindsay, 2012: Observed increases in Bering Strait oceanic fluxes from the Pacific to the Arctic from 2001 to 2011 and their impacts on the Arctic Ocean water column. *Geophys. Res. Lett.*, **39**, L24603, doi:10.1029/2012GL054092.

Xie, J., and M. Zhang, 2017: Role of internal atmospheric variability in the 2015 extreme winter climate over the North America Continent. *Geophys. Res. Lett.*, **44**, 2464-2471, doi:10.1002/2017GL072772.

Xie, S.-P., K. Hu, J. Hafner, Y. Du, G. Huang, and H. Tokinaga, 2009: Indian ocean capacitor effect on Indo-western Pacific climate during the summer following El Niño. *J. Climate*, **22**, 730-747.

Xue, Y., B. Huang, Z.-Z. Hu, A. Kumar, C. Wen, D. Behringer, and S. Nadiga, 2011: An assessment of oceanic variability in the NCEP Climate Forecast System Reanalysis. *Climate Dyn.*, **37**, 2511–2539, doi:10.1007/s00382-010-0954-4.

Yang, X.-Y., J. C. Fyfe, and G. M. Flato, 2010: The role of poleward energy transport in Arctic temperature evolution. *Geophys. Res. Lett.*, **37**, L14803, doi:10.1029/2010GL043934.

Ye, B., D. Yang, and D. L. Kane, 2003: Changes in Lena River streamflow hydrology: Human impacts versus natural variations. *Water Resour. Res.*, **39**, 1200, doi:10.1029/2003WR001991.

Yeager, S. G., W. M. Kim, and J. Robson, 2016: What caused the Atlantic cold blob of 2015. *US CLIVAR Variations*, Vol. 14, No. 2, US CLIVAR, Washington, DC, 24-31, https://usclivar.org/newsletter/newsletters.

Yeh, P. J.-F., and E. A. B. Eltahir, 2005: Representation of water table dynamics in a land surface scheme. Part I: Model development. *J. Climate*, **18**, 1861-880.

Yeh, S.-W., J.-S. Kug, B. Dewitte, M.-H. Kwon, B. P. Kirtman, and F.-F. Jin, 2009: El Niño in a changing climate. *Nature*, **461**, 511-514, doi:10.1038/nature08316.

Yu, B., Z. W. Wu, and W. J. Merryfield, 2017: Relationship between North American winter temperature and large-scale atmospheric circulation anomalies and its decadal variation. *Environ. Res. Lett.*, **11**, 074001, doi:10.1088/1748-9326/11/7/ 074001.

Yu, J.-Y. and D. L. Hartmann, 1993: Zonal flow vacillation and eddy forcing in a simple GCM of the atmosphere. *J. Atmos. Sci.,* **50**, 3244-3259.

Yu, J.-Y., and H.-Y. Kao, 2007: Decadal changes of ENSO persistence barrier in SST and ocean heat content indices: 1958–2001. *J. Geophys. Res.*, **112**, D13106, doi:10.1029/2006JD007654.

Yu, J.-Y., and S. T. Kim, 2011: Relationships between extratropical sea level pressure variations and the central Pacific and eastern Pacific types of ENSO. *J. Climate*, **24**, 708-720, doi:10.1175/2010JCLI3688.1.

Yu, J.-Y., and Y. Zou, S. T. Kim, and T. Lee, 2012a: The changing impact of El Niño on US winter temperatures. *Geophys. Res. Lett.*, **39**, L15702, doi:10.1029/2012GL052483.

Yu, J.-Y., M.-M. Lu, and S. T. Kim, 2012b: A change in the relationship between tropical central Pacific SST variability and the extratropical atmosphere around 1990, *Environ. Res. Lett.*, **7**, 034025, doi:10.1088/1748-9326/7/3/034025.

Yu., J.-Y. and S. T. Kim, 2013: Identifying the Types of Major El Nino Events since 1870. *Int. J. Climatol.*, **33**, 2105-2112. doi: 10.1002/joc.3575.

Yu, J.-Y., and Y. Zou, 2013: The enhanced drying effect of central-Pacific El Niño on US winter. *Environ. Res. Lett.*, **8**, 014019, doi:10.1088/1748-9326/8/1/014019.

Yu, J.-Y. and H. Paek, 2015: Precursors of ENSO beyond the tropical Pacific. *US CLIVAR Variations,* **13**, 15-20.

Yu, J.-Y., H. Paek, E. S. Saltzman, and T. Lee, 2015: The early-1990s change in ENSO-PSA-SAM relationships and its impacts on Southern hemisphere climate. *J. Climate*, **28**, 9393-9408.

Yu, J.-Y., X. Wang, S. Yang, H. Paek, and M. Chen, 2017: Changing El Nino-Southern Oscillation and Associated Climate Extremes, Book Chapter in *Climate Extremes: Patterns and Mechanisms*, Wang, S.-Y., Jin-Ho Yoon, Chris Funk, and R. R. Gillies (Ed.), *AGU Geophysical Monograph Series*, **226**, 3-38.

Zaba, K. D. and D. L. Rudnick, 2016: The 2014–2015 warming anomaly in the Southern California Current System observed by underwater gliders. *Geophys. Res. Lett.*, **43**, 1241-1248, doi:10.1002/2015GL067550.

Zhang, R., 2015: Mechanisms for low-frequency variability of summer Arctic sea ice extent, *Proc. Natl. Acad. Sci. U.S.A.*,**112**, 4570-4575.

Zhang, W., F.-F. Jin, and A. Turner, 2014: Increasing autumn drought over southern China associated with ENSO regime shift. *Geophys. Res. Lett.*, **41**, 4020-4026.

Zou, Y., J.-Y. Yu, T. Lee, M.-M. Lu, and S. T. Kim, 2014: CMIP5 model simulations of the impacts of the two types of El Niño on the U.S. winter temperature. *J. Geophys. Res. Atmos.*, **119**, 3076-3092, doi:10.1002/2013JD021064.